

**Marine Physical Laboratory**

**AD-A265 961**

(4)



## **Shear, Strain and Thermohaline Vertical Shear in the Upper Ocean**

**Steven Paul Anderson**

**DTIC  
ELECTE  
JUN 17 1993  
S A D**

**SIO Reference 93-3**

**MPL-U-4/93  
January 1993**

This document has been approved  
for public release and sale; its  
distribution is unlimited.



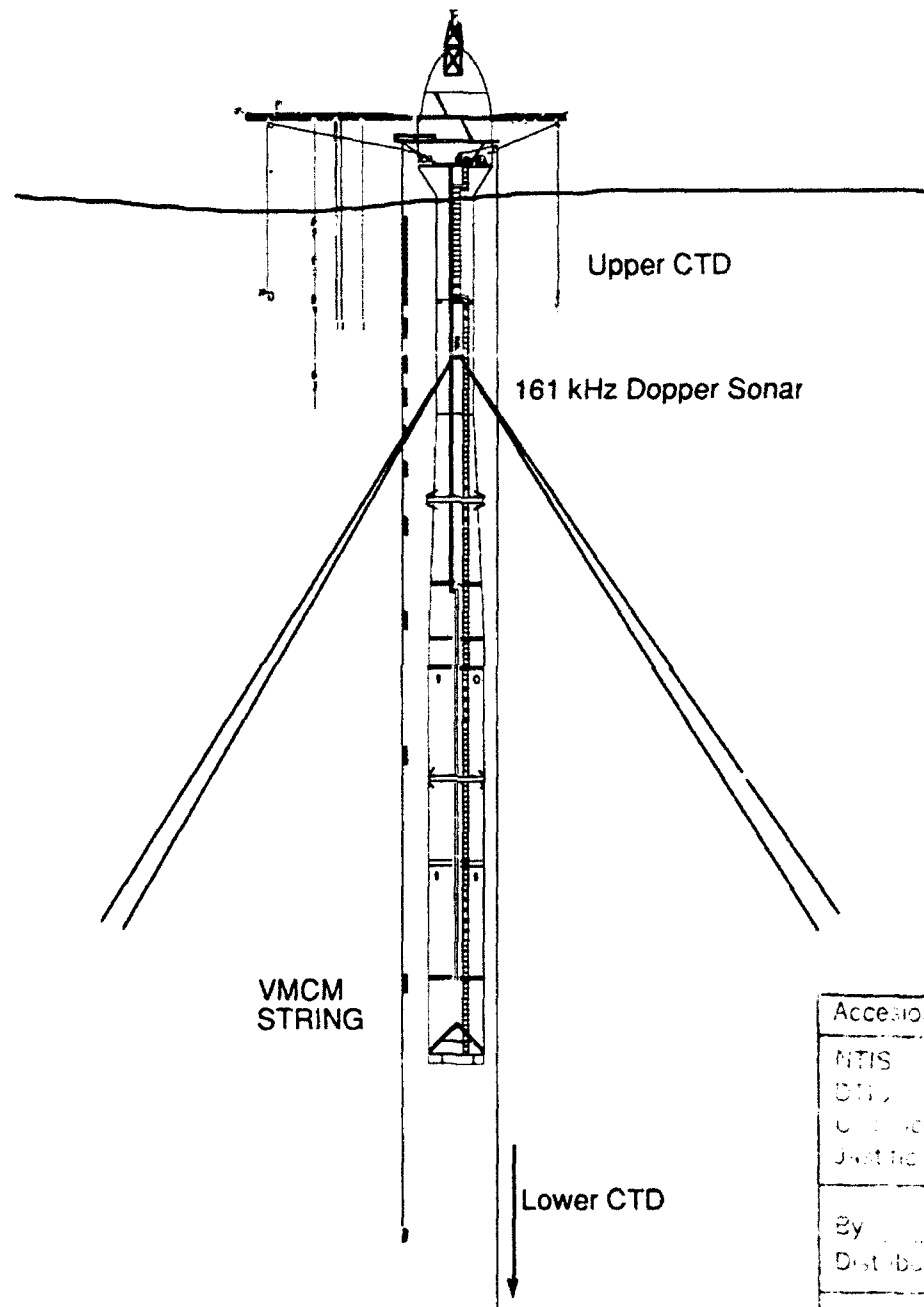
**University of California, San Diego  
Scripps Institution of Oceanography**

**93-13596**



UNIVERSITY OF CALIFORNIA, SAN DIEGO

Shear, Strain and Thermohaline Vertical Fine Structure in the  
Upper Ocean.



Steven Paul Anderson

1992

Accession For:	
NTIS	CR&I
DTIC	TAD
CD-ROM	CD
Joint Tech. Areas	
By _____	
Distribution	
Availability Codes	
Dist	Avail and/or Special
A-1	

REPORT DOCUMENTATION PAGE			Form Approved OMB No. 0704-0188
<p>Public reporting burden for this collection of information is estimated to average 1 hour per response, including the time for reviewing instructions, searching existing data sources, gathering and maintaining the data need ed., and completing and reviewing the collection of information. Send comments regarding this burden estimate or any other aspect of this collection of information, including suggestions for reducing this burden, to Washington Headquarters Services, Directorate for Information Operations and Reports, 1215 Jefferson Davis Highway, Suite 1204, Arlington, VA 22202-4302, and to the Office of Management and Budget, Paperwork Reduction Project (0704-0188), Washington, DC 20503.</p>			
1. Agency Use Only (Leave Blank).	2. Report Date. January 1993	3. Report Type and Dates Covered. Thesis	
4. Title and Subtitle.  <b>Shear, Strain and Thermohaline Vertical Fine Structure in the Upper Ocean</b>			5. Funding Numbers.  <b>N00014-90-J-1099</b>
6. Author(s).  <b>Steven Paul Anderson</b>			Project No. Task No.
7. Performing Monitoring Agency Name(s) and Address(es).  University of California, San Diego Marine Physical Laboratory Scripps Institution of Oceanography San Diego, California 92152			8. Performing Organization Report Number.  MPL-U-4/93 SIO Reference 93-3
9. Sponsoring/Monitoring Agency Name(s) and Address(es).  Office of Naval Research Department of the Navy 800 North Quincy Street Arlington, VA 22217-5000			10. Sponsoring/Monitoring Agency Report Number.
11. Supplementary Notes.			
12a. Distribution/Availability Statement.  Approved for public release; distribution is unlimited.	12b. Distribution Code.		
<b>13. Abstract (Maximum 200 words).</b> <p>Observations of fine scale (1-100m) vertical shear, strain and thermohaline structure are interpreted in terms of internal wave and frontal zone dynamics. The data were collected with the Marine Physical Laboratory 161 kHz Doppler sonar and a pair of CTD's. The two systems were operated from R/P FLIP for 18 days during February-March, 1990, as part of the SWAPP (35°N, 127°W) experiment. These simultaneous measurements of velocity and density provide an unique opportunity to study the vertical advection of shear layers. The observed shear variance is dominated by near inertial waves, with 35 m vertical wavelengths. These inertial waves propagate down from the mixed layer and are vertically advected by higher frequency waves. Vertical wavenumber-frequency spectral of shear and strain are examined in Eulerian (fixed depth) and semi-Lagrangian (isopycnal following) coordinates. The semi-Lagrangian shear and strain variances are more consistent with variances modeled by a linear superposition of internal waves. The p.d.f.'s of buoyancy frequency and Froude number (buoyancy normalized shear) are determined using the kinematic strain model of Pinkel and Anderson (1992). The Froude number distribution shows good agreement with data presented here and historical data (PATCHEX; Kunze et al., 1990). The advection of a frontal zone past the experiment site yielded detailed observations of frontal interleaving. Two vertical interleaving scales are observed. Five to fifteen meter scales appear to be double diffusively driven and are consistent with the laboratory model of Ruddick and Turner (1979), 40 m to 60 m scales are likely determined by internal wave of sub-mesoscale frontal dynamics. The observed front appears to be in near geostrophic balance.</p>			
14. Subject Terms. upper ocean dynamics, internal wave structure, wavenumber spectra, vertical frequency spectra			15. Number of Pages. 143
16. Price Code.			
17. Security Classification of Report. Unclassified	18. Security Classification of This Page. Unclassified	19. Security Classification of Abstract.. Unclassified	20. Limitation of Abstract. None

UNIVERSITY OF CALIFORNIA, SAN DIEGO

Shear, Strain and Thermohaline Vertical Fine Structure  
in the Upper Ocean.

A dissertation submitted in partial satisfaction of the  
requirements for the degree Doctor of Philosophy in  
Oceanography

by

Steven Paul Anderson

Committee in charge:

Professor Robert Pinkel, Chair  
Professor Charles Cox  
Professor Morteza Gharib  
Professor George Sugihara  
Professor William Young

1992

## Table of Contents

List of Figures.....	iv
List of Tables.....	vi
Acknowledgments.....	vii
Abstract.....	viii
<b>1 Introduction.....</b>	<b>1</b>
<b>2 Vertical Advection of Fine Scale Shear and Strain.....</b>	<b>5</b>
2.1 Introduction and Background.....	5
2.2 Stratification and Current Measurements.....	7
2.3 Strain Spectral Analysis.....	8
2.4 Shear Spectral Analysis.....	9
2.5 GM76 Model Variance.....	10
2.6 Rotary Shear Spectral Analysis.....	12
2.7 WKB approximation.....	12
2.8 Inertial Wave Vertical Advection Model.....	13
2.9 Counterclockwise to Clockwise Shear Variance Ratio.....	15
2.10 Strain Variance to Shear Variance Ratio.....	16
2.11 Summary and Conclusions.....	17
<b>3 Fine Scale Thermohaline Structure and Horizontal Mixing Across an Oceanic Front.....</b>	<b>45</b>
3.1 Introduction.....	45
3.2 Description of Data.....	46
3.3 Geopotential Anomalies.....	47
3.4 Vertical Interleaving.....	49
3.5 Fine Structure at the Frontal Interface.....	56
3.6 Estimates of Horizontal Heat and Salt Fluxes.....	57
3.7 Summary.....	60
<b>4. Froude Number Distribution.....</b>	<b>79</b>
4.1 Introduction.....	79
4.2 Buoyancy Frequency and Vertical Shear Distributions.....	81
4.3 Froude Number Distribution.....	83
4.4 Conclusions.....	85

<b>Appendices.....</b>	<b>95</b>
A. The Surface Wave Processes Program (SWAPP) Overview.....	95
B. Review of Linear Theory.....	102
C. CTD Data Processing.....	106
D. Velocity Biasing Due to Horizontal Beam Separation.....	112
E. Sonar Data Processing.....	115
E.1 Doppler Sonar Background	115
E.2 The MPL 161 kHz Doppler Sonar System.....	117
E.3 Variable Gain Correction.....	118
E.4 Noise Correction.....	120
E.5 Platform Motion correction.....	120
E.5.1 Platform Tilt and Accelerometer Measurements.....	121
E.5.2 Transform Matrix.....	121
E.5.3 Rotation Correction.....	124
E.5.4 Translation Correction.....	125
E.5.5 Mechanical Alignment Correction.....	126
E.5.6 Heading Correction.....	128
<b>References.....</b>	<b>141</b>

## List of Figures

### Chapter 2

2.1	East Velocity Shear on yearday 65.....	19
2.2	Schematic of W.H.O.I. aft Current Meter Sting.....	20
2.3	Depth Calibration Using W.H.O.I. Current Meter.....	21
2.4	Eulerian and Semi-Lagrangian Velocity Profiles.....	22
2.5	Strain Vertical Wavenumber spectra.....	23
2.6	Eulerian Strain Vertical Wavenumber Spectra.....	25
2.7	Semi-Lagrangian Strain Vertical Wavenumber Spectra.....	26
2.8	Eulerian Strain Vertical Frequency Spectra.....	27
2.9	Semi-Lagrangian Strain Vertical Frequency Spectra.....	28
2.10	Eulerian Shear Vertical Wavenumber--Frequency Spectrum.....	29
2.11	Semi-Lagrangian Shear Vertical Wavenumber--Frequency Spectrum.....	30
2.12	Mean Buoyancy Frequency Profile.....	31
2.13	Eulerian Rotary Shear Spectra Vs. Vertical Wavenumber.....	32
2.14	Semi-Lagrangian Rotary Shear Spectra Vs. Vertical Wavenumber.....	33
2.15	Eulerian Rotary Shear Spectra Vs. Frequency.....	34
2.16	Semi-Lagrangian Rotary Shear Spectra Vs. Frequency.....	35
2.17	WKB Eulerian Rotary Shear Spectra.....	36
2.18	WKB Semi-Lagrangian Rotary Shear Spectra.....	37
2.19	Displacement Frequency Spectrum.....	38
2.20	Measured CCW to CW Shear Ratio.....	39
2.21	Measured CCW to CW Shear Ratio Fit to Linear Theory.....	40
2.22	Measured Strain to Shear Variance Ratio.....	41
2.23	Noise Corrected Strain to Shear Ratio.....	42
2.24	Eulerian and Semi-Lagrangian Cumulative shear spectra.....	43
2.25	Shear Frequency Spectrum.....	44

### Chapter 3

3.1	T- S Diagram from 200-420m.....	62
3.2	Isopycnal Temperatures.....	63
3.3	T and S at Constant Potential Density.....	64
3.4	Integrated Current Trajectory.....	65
3.5	Geopotential Anomalies.....	66
3.6	Typical Temperature and Salinity Profile from Yearday 67.....	67
3.7	Typical Turner Angle Profile from Yearday 67.....	68
3.8	Percent of Profile that is Subject to Double Diffusive Convection.....	69
3.9	$\sigma_t$ - S Diagram from 200-420m. S.....	70
3.10	$\sigma_t$ - T Diagram from 200-420m.....	71
3.11	Internal Wave Temperature Anomalies.....	72
3.12	Variance of Vertical Gradients of Salinity and Temperature Differences.....	73
3.13	Vertical Wavenumber Spectra of Temperature and Salinity Anomalies.....	74
3.14	Vertical Wavenumber Spectra of Gradient Temperature and Salinity Anomalies.....	75

<b>3.15</b>	Temperature Difference Cascade Plot .....	76
<b>3.16</b>	Temperature Anomalies on Isopycnals During Yeardays 66.7 to 67.5. ....	77
<b>3.17</b>	Turner Angles on Isopycnals During Yeardays 66.7 to 67.5. ....	78
<b>3.18</b>	Sloping Temperature Gradient Anomaly Wavenumber Spectrum. ....	79

#### Chapter 4

<b>4.1</b>	Joint Histograms of Vertical Shear and Buoyancy Frequency. ....	87
<b>4.2</b>	Probability Distribution of Independent Shear and Buoyancy Frequency. ....	88
<b>4.3</b>	Difference Between Independent and Sampled Joint Distributions. ....	89
<b>4.4</b>	Histograms of Buoyancy Frequency. ....	91
<b>4.5</b>	Histograms of Vertical Shear. ....	92
<b>4.6</b>	Histograms of Froude Number .....	93
<b>4.7</b>	Distributions of Froude Number from a Neutrally Buoyant Float. ....	94

#### Appendix A

<b>A.1</b>	The SWAPP site. The Surface Waves Processes Program (SWAPP).....	97
<b>A.2</b>	SWAPP Meteorological Data. ....	98
<b>A.3</b>	Depth Averaged Temperature Contours. ....	99
<b>A.4</b>	Historic Hydrographic data and Cruise Averaged Potential Density. ....	100
<b>A.5</b>	Cruise Averaged Potential Density.....	101

#### Appendix C

<b>C.1</b>	High Frequency Pressure Filtering. ....	108
<b>C.2</b>	Temperature and Conductivity response matching. ....	109
<b>C.3</b>	Uncorrected Density Profiles. ....	110
<b>C.4</b>	Corrected Density Profiles. ....	111

#### Appendix B

<b>D.1</b>	Estimated Spectral Variance Bias Due to Beam Pair Separation. ....	114
------------	--------------------------------------------------------------------	-----

#### Appendix E

<b>E.1</b>	Repeat Sequence Coded Transmit Pulse. ....	129
<b>E.2</b>	161 kHz Beam Directions and Accelerometer Tilt Axis Directions. ....	130
<b>E.3</b>	Variable Gain Correction. ....	131
<b>E.4</b>	1 Hour Averaged Intensity Profile. ....	132
<b>E.5</b>	Hour averaged Intensity and Variable Gain First Differenced in Range. ....	133
<b>E.6</b>	1 Hour Averaged Covariance Magnitude Squared. ....	134
<b>E.7</b>	Wave Wire and Horizontal Acceleration Spectra. ....	135
<b>E.8</b>	Geophysical and titled coordinate systems. ....	136
<b>E.9</b>	Low Pass Filtered Tilt Angles and Depth Averaged Velocities. ....	137
<b>E.10</b>	Translation Corrected Slant Velocities. ....	138
<b>E.11</b>	Contour of Correlation Ratio vs. Mechanical Misalignment Angles. ....	139

## List of Tables

<b>2.1</b>	<b>Shear and Strain Variances.</b>	<b>24</b>
<b>4.1</b>	<b>Probability Distribution Parameters.</b>	<b>90</b>
<b>E.1</b>	<b>MPL 161 kHz Incoherent Doppler Sonar System Configuration Parameters.</b>	<b>130</b>

### **Acknowledgments**

I wish to express my gratitude to my advisor, Dr. Robert Pinkel, for all the encouragement, direction and support he has given me. I would like to thank my committee for providing useful comments and advice.

I am indebted to the Upper Ocean Physics Group for their expertise and dedication to excellence that made the collection of such high quality data sets possible. My work with engineers Mike Goldin, Lloyd Green and Eric Slater was a valuable part of my education. I wish to thank Mary Sisti and Chris Neely for their useful services. I also wish to thank the crew of R/P FLIP, headed by Dewitt Efird, for their valuable assistance.

I would like to thank all my friends at Scripps for making my graduate studies an enjoyable experience. In particular, I offer many thanks to Timothy Boyd, David Jacobs, Mark Merrifield, Jeffrey Sherman, and Jerome Smith for many simulating conversations and encouragement. I also wish to thank fellow students Greg Bullard, Diana Lewis and Hans Ramm.

Special thanks go to Britt Eilers for her encouragement and understanding. And thanks to my family for their constant support.

This research work was supported by the Office of Naval Research under grant N00014-90-J-1099.

## ABSTRACT OF THE DISSERTATION

Shear, Strain and Thermohaline Vertical Fine Structure in the Upper Ocean.

by

Steven Paul Anderson

University of California, San Diego, 1992

Professor Robert Pinkel, Chairman

Observations of fine scale (1-100m) vertical shear, strain and thermohaline structure are interpreted in terms of internal wave and frontal zone dynamics. The data were collected with the Marine Physical Laboratory 161 kHz Doppler sonar and a pair of CTD's. The two systems were operated from R/P FLIP for 18 days during February-March, 1990, as part of the SWAPP ( $35^{\circ}$  N,  $127^{\circ}$  W) experiment.

These simultaneous measurements of velocity and density provide an unique opportunity to study the vertical advection of shear layers. The observed shear variance is dominated by near inertial waves, with 35 m vertical wavelengths. These inertial waves propagate down from the mixed layer and are vertically advected by higher frequency waves. Vertical wavenumber-frequency spectra of shear and strain are examined in Eulerian (fixed depth) and semi-Lagrangian (isopycnal following) coordinates. The semi-Lagrangian shear and strain variances are more consistent with variances modeled by a linear superposition of internal waves.

The p. d. f.'s of buoyancy frequency and Froude number (buoyancy normalized shear) are determined using the kinematic strain model of Pinkel and Anderson (1992). The Froude number distribution shows good agreement with data presented here and historical data (PATCHEX; Kunze et al., 1990).

The advection of a frontal zone past the experiment site yielded detailed observations of frontal interleaving. Two vertical interleaving scales are observed. Five to fifteen meter scales appear to be double diffusively driven and are consistent with the laboratory model of Ruddick and Turner (1979), 40 m to 60 m scales are likely determined by internal wave or sub-mesoscale frontal dynamics. The observed front appears to be in near geostrophic balance.

## Chapter 1

### Introduction

This dissertation consists of three investigations of fine scale (2-300m) upper ocean dynamics. These investigations are presented in the following three chapters. Each chapter is largely self contained. Chapter 2 examines observations of vertical shear and strain in the context of linear internal wave dynamics. Chapter 3 presents observations of thermohaline fine structure associated with an oceanic frontal zone. Chapter 4 examines the probability distribution of shear instabilities. An extensive data set unifies these investigations. This chapter outlines the principal results from each investigation.

This dissertation presents data collected primarily by two systems during February and March, 1990, as part of the Surface Wave Processes Program (SWAPP; Appendix A). The experiment was located approximately 500 miles west of central California ( $35^{\circ} 8.2' N$ ,  $126^{\circ} 59.0' W$ ; Figure A.1) where the instrumentation was deployed from R/P FLIP (Figure 1.1). The Marine Physical Laboratory 161 kHz coded-pulse Doppler sonar system is used to profile the ocean currents from 50 m to 325 m depth. The processing of the sonar data involved several steps before reliable velocity profiles were obtained. The processing (see Appendix E) includes variable gain correction, band limited noise removal, estimation of mechanical alignment errors and tilt and heading correction. The resulting velocity profiles are one minute averages of east and north components of horizontal velocity from 50 m to 325 m. The acoustic pulse length smoothing is 5.5 m in depth. The Marine Physical Laboratory yo-yo CTD system profiled the ocean density and thermohaline structure from the surface to 420 m every 130 seconds. A pair of CTD's operated in tandem with the upper CTD profiling from the surface to 220 m and the second from 200 m to 420 m. The CTD data processing (see Appendix C) involves phase matching the temperature and conductivity data to remove salinity spiking, filtering the pressure signal and merging the data from both CTD's. This results in profiles of temperature, salinity and density with a vertical resolution of 1.5 m. The need to properly align the depth information is key to the merging to the sonar and CTD data sets. Depths are inferred from acoustic travel time for the sonar and pressure for the CTD. It is possible to cross check these very different indicators of depth using a vertical string of vector measuring current meters (VMCM) provided by R. Weller. The two systems were operated simultaneously from R/P FLIP for 12 days.

I. Chapter 2, observations of vertical advection of fine scale shear and strain are presented. The observed shear variance is dominated by near inertial waves that propagate down from the mixed layer with 35 meter vertical wavelengths. The near inertial shear layers are vertically advected by the internal semi-diurnal tide and higher

frequency waves and appear to ride up and down with isopycnal layers. Vertical wavenumber-frequency spectra of shear and strain are examined in Eulerian (fixed depth) and semi-Lagrangian (isopycnal following) coordinates. This is the first analyses of the true evolution of velocity in isopycnal following coordinates. Strain spectra show energy propagating towards the surface in the semi-diurnal tidal band. Eulerian vertical wavenumber spectra display a vertical wavenumber dependence which changes significantly with frequency. This contrasts the spectral models of Garrett and Munk (1972, 1975) which propose a vertical wavenumber dependence that is independent of frequency. Interpretation of Eulerian rotary shear is confused by "Doppler" shifting of the fine scale shear layers to higher frequencies. The semi-Lagrangian spectra of shear and strain appear more separable in vertical wavenumber and frequency. The comparison of shear and strain variances exhibit better agreement with linear theory in the semi-Lagrangian coordinates. Estimates of semi-Lagrangian counterclockwise to clockwise rotating shear variance ratios agree well with linear theory. The main conclusion is that the internal wave field appears more consistent with a linear superposition of internal waves when observed in semi-Lagrangian coordinates.

Chapter 3 presents observations of the vertical structure of temperature and salinity near a frontal zone. During the SWAPP experiment, an oceanic front was advected past the experiment site. The front was characterized below 200 m by warm, salty water encountered at the start of the experiment and a transition in the middle of the time series to colder, fresher water with nearly the same density. The temperature and salinity change on an isopycnal located at 300 m is  $0.425^{\circ}\text{C}$  and  $0.0825\text{‰}$ . The front appears to be in a geostrophic balance. This is determined by comparing velocity estimates from the sonar to geopotential anomalies. To study the time and space scales of the intrusive interleaving associated with the front, a depth/time series of temperature and salinity anomalies is presented. The anomalies are calculated by removing the mean temperature and salinity at constant density for each CTD profile. Two vertical scales of interleaving are observed near the front. The small scale intrusions have vertical lengths of 5-15 meters, are double diffusively unstable on the top and bottom and slope upward from the warm side to the cold side of the front. The intrusions are consistent with scales predicted by Ruddick and Turner (1979). Larger scale interleaving is seen at 40 to 60 m. These larger scales are may driven by sub-mesoscale or internal wave forcing.

In Chapter 4, the probability density function (p. d. f.) of buoyancy normalized shear, or Froude number, is examined. It is conjectured that most of the turbulence observed in the ocean interior results from breaking internal waves. Shear instability is the hypothesized cause of breaking. The Froude number is a ratio of the inertial forces to the buoyancy forces. It is equal to the inverse square root of the gradient Richardson number. The potential for shear instabilities occurs when the Froude number is greater than 2.0 (Richardson number less than 0.25). The model p. d. f. of Froude numbers is determined using modeled distributions of shear and strain. The buoyancy frequency distribution is derived from the kinematic strain model of Pinkel and Anderson (1992). The model vertical shear distribution is given by a Rayleigh distribution under the

assumption that each component of shear is independent and normally distributed. By assuming that shear and buoyancy frequency are independent, the joint p. d. f. of vertical shear and buoyancy frequency is estimated. Actual data from the CTD and sonar suggest that even though there is detectable dependence, this is a reasonable approximation. The p. d. f. of Froude numbers is calculated from the joint p. d. f. of vertical shear and buoyancy frequency. The resulting p. d. f. successfully models histograms of Froude numbers estimated at 1 m to 10 m scales. The Froude number distribution scales with the mean buoyancy frequency normalized by the mean vertical shear. Little change in the Froude number distribution is seen from 125 m to 300 m. in depth.

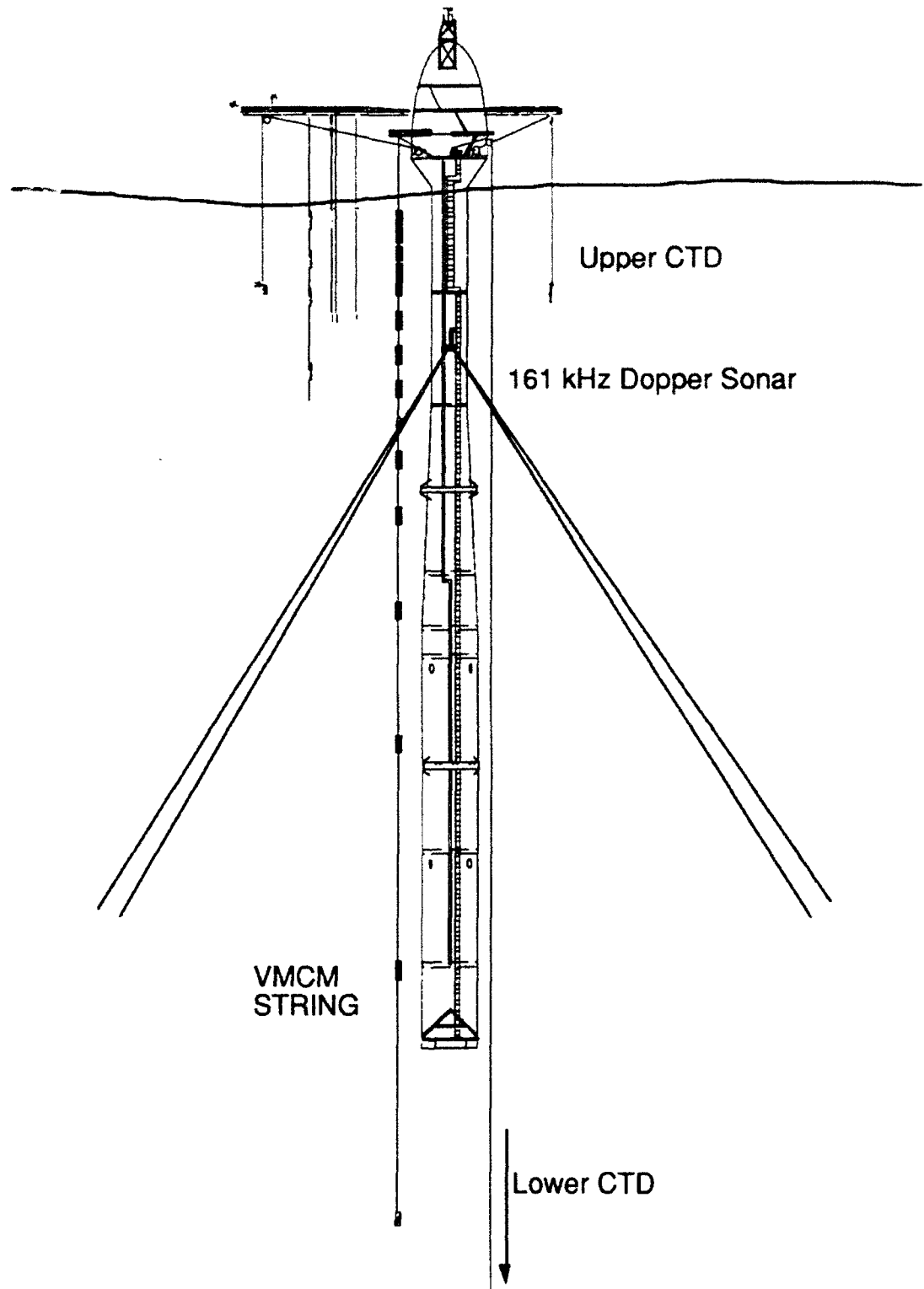


**Figure 1.1 R/P FLIP Instrumentation Diagram.** Upper ocean observations are made with the Marine Physical Laboratory 161 kHz Doppler sonar system and a pair of CTD's. This diagram shows the deployment configuration used during SWAPP.

## Chapter 2

### Vertical Advection of Near Inertial Shear Layers

#### 2.1. Introduction and Background.

Mixing in the ocean interior is thought to be caused by the fine scale vertical shear and strain of the internal wave field. Previous Eulerian estimates of internal wave statistics are difficult to interpret due to vertical advection (commonly referred to as finestructure contamination.) Phillips (1971) describes how the internal wave statistics at a fixed depth are altered by advection of "frozen" layers past an instrument at fixed depth. This can lead to "Doppler shifting" and aliasing of intrinsic wave frequencies. To examine the significance of internal wave self advection, shear and strain are studied here in semi-Lagrangian and Eulerian coordinates. Vertical wavenumber-frequency spectra are estimated and compared. Linear theory consistency tests of counterclockwise to clockwise shear variance and shear to strain variance ratios are studied in both coordinates. The results show that the semi-Lagrangian statistics give better agreement with linear internal wave theory than Eulerian statistics.

The new coordinate system, defined by isopycnal surfaces, is referred to as semi-Lagrangian. Finestructure contamination can be minimized by tracking isopycnal surfaces in depth and time (Pinkel et. al.; 1991). Fluid dynamics is classically formulated in either Eulerian or Lagrangian variables. Eulerian variables track the fluid flow from a particular point in three coordinate space. Lagrangian variables divide the fluid into macroscopically small parcels that are typically identified by their initial or undisturbed positions and track the position of each parcel. Most ocean observations and model studies (including the internal wave field) are made in terms of Eulerian variables. The semi-Lagrangian statistics are not true Lagrangian statistics since horizontal advection is neglected. Much of the Doppler shifting of the internal wave field can be removed in semi-Lagrangian coordinates, thus yielding a better estimate of the intrinsic wave frequencies.

Previous measurements of the oceanic internal gravity wave field have shown common spectral form. Garrett and Munk (1972, 1975, hereafter GM) developed a model of the internal wave variance spectrum by consolidating a variety of oceanic temperature and velocity measurements into a universal spectral structure. GM internal wave spectrum is an empirical model that assumes that the velocity and temperature fluctuations in the ocean are due to a random superposition of internal waves. The GM spectrum has been a valuable reference for comparing various internal wave measurements. It has had modifications for high wave number roll off (Munk, 1981 and Gregg and Kunze, 1991) in light of more recent observations. The GM hypothesize a

nearly white spectra of vertical shear and strain at low wave numbers and a roll off at vertical wavenumbers above 0.1 cpm. GM also assume that at all internal wave frequencies, shear and strain vertical wave number spectra have the same shape. However, not all observations fit the hypothesized spectral form and the model lacks a theoretical explanation for its spectral shape.

Recent studies suggest that self advection of the internal wave field may be significant, thus invalidating the assumption that the internal wave field is a linear superposition of waves. Allen and Joseph (1989) model the oceanic internal wave field as a superposition of linear internal waves in Lagrangian coordinates. By examining the spectra in Eulerian coordinates they find that many different spectral shapes in Lagrangian coordinates will result in the same Eulerian spectra. By using measured Eulerian spectra, the can not determine the underlying Lagrangian spectrum. Hines (1991a,1991b) has used Lagrangian coordinates to model the atmospheric internal wave spectrum with similar results. Observations of vertical wavenumber-frequency shear spectra by Pinkel (1985) and Sherman and Pinkel (1991) dispute the GM assumption of spectral separability of wavenumber and frequency in Eulerian coordinates. They observe red vertical wavenumber dependence of shear spectra at low frequency and white wavenumber dependence at high frequency. The vertical wavenumber-frequency spectrum of strain in semi-Lagrangian coordinates, as estimated by Sherman and Pinkel (1991), does appear to be more separable. The wavenumber dependence is nearly white out to the cutoff at all frequencies. Using the GM model spectrum in semi-Lagrangian coordinates, Sherman and Pinkel (1991) show that vertical advection can lead to the observed Eulerian shear spectrum.

Tests for consistency of shear and strain variances with linear theory often show more shear than expected at high frequencies and more strain than expected near the inertial band (Eriksen, 1978; Müller et al., 1978; Kunze et al., 1990). Holloway (1983) suggests that this discrepancy may be due to fine-scale potential vorticity anomalies. Kunze et al. (1990) using data taken with a neutrally buoyant float, claim that the excess shear and strain is due to Doppler shifting and aliasing of internal waves with intrinsic near inertial frequencies. Sherman (1989) compares observed counterclockwise to clockwise rotating shear variances to linear theory and finds excess counterclockwise shear in the inertial band. Sherman (1989) also reports that his estimates are distorted by vertical advection of the internal waves.

The data presented in this chapter were taking with the MPL rapid profiling CTD system and the 161 kHz Doppler sonar system. The 161 kHz Doppler sonar system is used to study the ocean currents from 50m to 325m depth. A pair of rapid profiling CTD's provided density profiles from the surface to 420 meters. The two systems were operated for 12 days during March, 1990 as part of the SWAPP experiment. The experiment was located approximately 500 miles west of central California ( $35^{\circ} 8.2' N$ ,  $126^{\circ} 59.0' W$ ;Figure A.1). The simultaneous measurement of velocity and density provides a unique opportunity to study the vertical advection of shear layers. Vertical wavenumber-frequency spectra of shear and strain are examined in Eulerian (fixed depth)

and semi-Lagrangian (isopycnal following) coordinates. Shear and strain statistics are then compared to linear internal wave theory.

## 2.2. Stratification and Current measurements.

This section describes the merging of the CTD and Doppler sonar data into one depth/time series. Two profiling CTD's measured density from ~5 to 420 meters in depth with a vertical resolution of 1.5 meters and a cycle period of 130 seconds (Appendix C). A Doppler sonar system measured velocity profiles from ~40 to 320 meters in depth with a vertical resolution of 5.5 meters every 60 seconds (Appendix E). The need to properly align the depth information is key to the merging to the data sets. Depths are inferred from acoustic travel time for the sonar and pressure for the CTD. It is possible to cross check these very different indicators of depth using a vertical string of vector measuring current meters (VMCM) provided by R. Weller.

The VMCM's were deployed from the aft boom of FLIP: 10 meters horizontally from the sonar, which was mounted on the thruster, and 15 meters from the upper CTD on the starboard boom. The VMCM data set consists of there 15 minute averaged temperature and vector averaged velocities (depths 72.5 m (vm12), 100.25 (vm13) and 132.5 m (vm20)) from February 25, 1990 to March 17, 1990. Hour averaged temperatures from vm12 and vm20 are compared with corresponding hour averaged temperature profiles from the upper CTD sampled at 1.0 meter increments. The CTD calibrated current meter depths are determined by using the depths of maximum correlation and are  $72 \pm 0.5$  and  $134 \pm 0.5$  meters for vm12 and vm20 respectively (Figure 2.3c). The VMCM calibrated sonar depths are found by comparing 15 minute averaged sonar velocity profiles with the corresponding current meter records. The vertical length of each acoustic range bin is 2.91 meters (Appendix E). Maximum East/West velocity correlations occur at range bin numbers,  $b_n$ , 20 (73.2 m), 31 (105.2 m) and 42 (137.2 m) for vm12, vm13 and vm20 respectively (Figure 2.3a). Maximum North/South velocity correlations occur at range bin numbers 21 (76.1 m), 31 (105.2 m) and 42 (137.2 m) for vm12, vm13 and vm20 respectively (Figure 2.3b). The vm12 is located directly between range bins 20 and 21 and the first depth bin is located at 15 meters depth. The CTD calibrated center depth of each range bin is then  $(12.1 + 2.91b_n) \pm 2$  meters where  $b_n$  is the range bin number.

Before combining the velocity and density profiles, the spatial resolution of each density profile is degraded to correspond to that of the velocity data. This is done using a running boxcar filter of length 5.5 meters in depth. Then both data sets are sampled using linear interpolation at integer meters from 40 m to 350 m. These are low pass filtered using a 5 pole Butterworth filter with a cutoff at 0.2 cpm and zero phase shift. The velocity data are then smoothed over 3 minutes in time and sampled 30 seconds after the start of the CTD profile using linear interpolation. This results in the combined velocity and density data which is sampled every 1 meter in depth from 40 to 350 meters

and every 130 seconds in time. The time when data was obtained on both systems is from yearday 63 through year day 75.

The Eulerian depth/time series used in the spectral analysis comes from the combined velocity and density data from yearday 63 to 75. Both velocity and density are sampled in depth every 2 meters from 50 meters to 306 meters using a cubic spline interpolation. Three profiles are averaged and missing data points at each depth are linearly interpolated in time to create a profile every 6.5 minutes. To create the Semi-Lagrangian (isopycnal following) depth/time series, 128 isopycnals are chosen that have a mean separation of 2 meters in depth from 50 meters to 306 meters. The instantaneous isopycnal depths and the velocity at each isopycnal depth are found by linear interpolation in depth for each profile. The Semi-Lagrangian velocities are then averaged over 3 profiles and missing data on an isopycnal is linearly interpolated in time.

### 2.3. Strain Spectra.

Eulerian and semi-Lagrangian strain are calculated from the density profiles obtained from the profiling CTD system. Eulerian strain is obtained by first differencing density in depth, normalizing each profile by the first differenced mean density profile and subtracting 1.0 (Appendix B). Semi-Lagrangian strain is calculated by first differencing the isopycnal displacements in depth, normalizing by the mean isopycnal separation and subtracting 1.0. Spectral variance is estimated from 9 blocks of data, each 128 points in depth and 512 points in time corresponding to 50-306 meters depth and 55.4 hours in time. The blocks are overlapped by 50% in time and tapered in space and time with a triangle window before fourier transforming.

To correct high wavenumber variances that are degraded by vertical smoothing, the spectra are multiplied in wavenumber by  $\text{sinc}^2(5.5*\pi m)$ . This is not the proper correction for the semi-Lagrangian strain since the depth smoothing is done in Eulerian coordinates. It is applied to the semi-Lagrangian spectra for comparison with the Eulerian spectra. The correction is approximately the same if straining is small at the scales considered. A strain vertical wavenumber spectrum with a vertical resolution of 1.5 meters (Figure 2.5) is calculated for comparison with the vertically smoothed spectrum. The high resolution spectrum is flat from low wavenumbers to  $\sim 0.1$  cpm. The vertical wavenumber, cumulative spectra, corrected at high wavenumber shows a similar spectral shape out to 0.1 cpm. Thus, the correction restores the true spectra shape.

The spectra are averaged into 6 frequency bands and plotted versus wavenumber out to 0.1 cpm (Figures 2.6 and 2.7). The Eulerian and semi-Lagrangian strain spectra look very similar to those of Sherman and Pinkel (1991). The Eulerian bands do not show a common spectral shape but do converge to a  $m^{-2}$  slope at high wavenumber. The two lowest frequency bands are red at all observed wavenumbers. The high frequency bands rise from low wavenumber then roll off as they meet the common high wavenumber slope. In contrast, the semi-Lagrangian spectrum is nearly white at all but the highest frequency bands. The high frequency bands rise up as they approach 0.1 cpm.

The frequency dependence of the spectrum can be seen by averaging into four vertical wavenumber bands. Each of the four wavenumber bands is smoothed over 3 frequency bands above 0.27 cph and 12 frequency bands between 0.27 and 0.52 cph before plotting versus frequency (Figures 2.8 and 2.9). The Eulerian wavenumber bands again do not show common spectral shape. The longest wave lengths (128-32m) are red and have a  $\omega^2$  slope. There is an upward energy peak in the 128-64m band at the semi-diurnal tide. Pinkel et al. (1987) also observed net upward tidal energy off the coast of California. The shortest wavelengths (32-10m) are nearly flat at low frequency with less variance than the longer waves and roll off at higher frequency with more variance. No semi-diurnal peak is present in the short wavelengths. The semi-Lagrangian spectra show congruent form at all wavenumbers. The longest waves resolved (128-32m) have an upward energy semi-diurnal peak. The cumulative spectrum has a  $\omega^{-1}$  slope at low frequencies and a  $\omega^2$  slope above 0.2 cph.

#### 2.4. Shear spectral analysis.

Eulerian and semi-Lagrangian shear are calculated from the velocity profiles obtained by the Doppler sonar system. Eulerian shear is obtained by first differencing the complex horizontal velocity ( $\mathbf{u} = u + iv$ ) at 2 meter depth intervals. Semi-Lagrangian shear is calculated by first differencing the complex velocity found on a previously selected set of isopycnals that are spaced 2 meters apart on average. Spectral variance is estimated from 9 blocks of data, each 128 points in depth and 512 points in time corresponding to 50-306 meters depth and 55.4 hours in time. The blocks are overlapped by 50% in time and tapered in space and time with a triangle window before Fourier transforming. Rotary spectra are found by averaging the spectra in each quadrant of wavenumber-frequency space.

The high wavenumber variances have been corrected in the same manner as the strain spectra. To correct high wavenumber variances that are degraded by vertical smoothing, the spectra are multiplied in wavenumber by  $\text{sinc}^2(5.5\pi m)$ . This is not the proper correction for the semi-Lagrangian strain since the depth smoothing is done in Eulerian coordinates. It is applied to the semi-Lagrangian spectra, however, for comparison to the Eulerian shear spectra and the corrected strain spectra.

The shear spectra are averaged into the same 6 frequency bands as the corresponding strain spectra and plotted versus wavenumber out to 0.1 cpm (Figures 2.10b and 2.11b). The Eulerian shear spectrum is similar to those of Pinkel (1985) and Sherman and Pinkel (1991). The highest frequency band (1-0.5 hours) is red. All the bands appear to have a slope change at  $\sim 0.3$  cpm. The lowest four frequency bands (55-4 hours) converge at high wave number to a  $m^{-5/2}$  dependence. All frequency bands appear to converge near 0.1 cpm. The semi-Lagrangian shear spectrum has some of the same characteristics as that of the modeled spectrum of Sherman and Pinkel (1991). The highest frequency bands (4-0.5 hours) rise slowly towards 0.1 cph. There is no convergence of the frequency bands at high wavenumber. The lowest frequency bands

(55-8), however, still show a peak at  $\sim 0.3$  cpm and roll off at higher wavenumber. As will be shown later, this variance peak is due to local forcing of near inertial waves at the surface.

To examine the frequency dependence, spectra are averaged into 4 vertical wavenumber bands and smoothed in frequency above 0.3 cph the same as the strain spectra (Figures 2.10a and 2.11a). The lowest wavenumbers (128-32m) in the Eulerian spectrum rise to a peak at the inertial frequency ( $f = .0478$  cph). Note that the 64-32m wave length band has a second peak at  $\omega = 0.13$  cph which is the sum of the inertial and semi-diurnal tide frequencies. Kunze et al. (1991) also report a vertical shear "super tidal" peak in data taken with the RiNo float during PATCHEX which took place  $1^\circ$  south of SWAPP. The shorter wave lengths have no inertial peak but instead are nearly flat until rolling off at higher frequency to a  $\omega^{-2}$  slope. This is the same general shape observed by Sherman and Pinkel (1991) where the low wavenumbers have a  $\omega^{-2}$  slope starting at the inertial frequency, while the higher wavenumbers appear more flat and have higher energy density at high frequency. The semi-Lagrangian spectra (Figure 2.11a) have quite a different shape. All but the shortest wavelengths have a similar shape and show an inertial peak. The spectrum falls with a  $\omega^{-4}$  slope until a slope change at  $\sim 0.3$  cph and the 64-32 meter wavelength band approaches a  $\omega^1$  slope. This is different from the modeled spectra of Sherman and Pinkel (1991) who observed a  $\omega^{-2}$  slope. There is no longer a super tidal peak. The highest wavenumbers (16-10m) exhibit no inertial peak.

## 2.5. Comparison with GM76 model variance.

In this section, measured shear and strain variances are compared with GM modeled variances. There is some question as to which version of the GM model to use. Gregg and Kunze (1991) show that shear and strain variances obtained by using Munk(1981) are  $2/\pi$  times smaller than those obtained from GM76 (Garrett and Munk, 1975 as modified by Carins and Williams, 1976). GM76 is used here since it appears to be the more commonly used of the models. From Gregg and Kunze (1991), the GM76 spectra of vertical strain,  $\phi_\lambda$ , and vertical shear,  $\phi_s$ , as functions of vertical wavenumber,  $\beta$  (given in rad/sec), are

$$\phi_\lambda(\beta) = \frac{Eb^3}{2j\pi} \left( \frac{N_o}{N} \right)^2 \frac{\beta_*^2}{(1 + \beta/\beta_*)^2} \left[ \frac{1}{\text{rad m}^{-1}} \right] \quad (2.1)$$

$$\phi_s(\beta) = \frac{3Eb^3 N_o^2}{2j\pi} \frac{\beta_*^3}{(1 + \beta/\beta_*)^2} \left[ \frac{s^{-2}}{\text{rad m}^{-1}} \right] \quad (2.2)$$

where  $N_o = .00524$  rad s $^{-1}$  is the reference buoyancy frequency,  $E = 6.3 \times 10^{-5}$  is the dimensionless energy level and  $b = 1300$  m is the scale depth of the thermocline. The vertical wavenumber,  $\beta$ , is related to the mode number,  $j$ , by

$$\beta = \frac{\pi j}{b} \left( \frac{N}{N_0} \right) \quad (2.3)$$

and for  $j_* = 3$  then  $\beta_* = 0.0073 (N/N_0) \text{ rad m}^{-1}$ . To compare the GM76 variances to the measured variance, (2.1) and (2.2) are integrated over the sampled wavenumber bandwidth yielding

$$\langle \lambda_{GM}^2 \rangle = \frac{Eb^3 \beta_*^3}{2j_*\pi} \left( \frac{N_0}{N} \right)^2 \left[ 1 + \frac{\beta}{\beta_*} - \left( 1 + \frac{\beta}{\beta_*} \right)^{-1} - 2 \ln \left( 1 + \frac{\beta}{\beta_*} \right) \right]_{\beta_l}^{\beta_u} \quad (2.4)$$

$$\langle S_{GM}^2 \rangle = \frac{3Eb^3 N_0^2 \beta_*^3}{2j_*\pi} \left[ 1 + \frac{\beta}{\beta_*} - \left( 1 + \frac{\beta}{\beta_*} \right)^{-1} - 2 \ln \left( 1 + \frac{\beta}{\beta_*} \right) \right]_{\beta_l}^{\beta_u} \quad (2.5)$$

where  $\beta_l$  and  $\beta_u$  are the lower and upper vertical wavenumber bandwidth limits respectively. The GM76 shear variance to strain variance ratio

$$\frac{\langle S_{GM}^2 \rangle}{\langle \lambda_{GM}^2 \rangle N^2} = 3 \quad (2.6)$$

is independent of vertical wavenumber bandwidth.

The Semi-Lagrangian and Eulerian variances are found by integrating the wavenumber-frequency spectra over vertical wavelength band 0.00391 to 0.1 cpm (256 to 10 meter wavelengths) and frequency band 0.0182 to 2.0 cph (55 to 0.5 hours) and are displayed in Table 2.1. Using the depth average  $\bar{N} = 4.4$  cph (Figure 2.12), (2.4) and (2.5) over estimate the both Eulerian and semi-Lagrangian total strain variance and under estimate the total shear variance. Eulerian and semi-Lagrangian strain variances are 85% and 75% of GM76 respectively. Eulerian and semi-Lagrangian shear variances are 130% and 116% of GM76. The excess shear and low strain in consistent with the observations of strong near inertial waves. The expected shear to strain variance ratio from linear theory for a near inertial wave is

$$\frac{\langle S^2 \rangle}{\langle \lambda^2 \rangle N^2} = \left[ \frac{\omega^2 + f^2}{\omega^2 - f^2} \right]. \quad (2.7)$$

Assuming the total variance is dominated by a single near inertial wave, the wave frequency can be estimated from the variance ratio using (2.6). Using  $\bar{N}$ , the Eulerian and semi-Lagrangian variance ratio can be accounted for by a near inertial wave frequency of  $1.26f$ . (It is not clear whether  $\bar{N}$  or the maximum buoyancy frequency,

$N_{\max} = 6.2$  cph., provides the appropriate scaling because of the large variation in the observed buoyancy frequency. Using  $N_{\max}$ , the frequency becomes  $1.61f$  which is slightly higher than the observed spectral frequency peaks.)

## 2.6. Rotary shear spectral analysis.

Rotary spectra are found by averaging the spectra found in each quadrant of wavenumber-frequency space. The spectra are divided into 4 quadrants: counter clockwise downward energy (CCWDN) ( $+m, -\omega$ ), clockwise downward energy (CWDN) ( $-m, +\omega$ ), counter clockwise upward energy (CCWUP) ( $-m, -\omega$ ) and clockwise upward energy (CWUP) ( $+m, +\omega$ ). The processing and averaging are the same as discussed with the strain and shear spectra. The Eulerian rotary shear spectra versus vertical wavenumber reveals the observed slope break at 0.03 cpm at all frequencies in the CWDN and CCWUP spectra (Figure 2.13a-d). This slope change is not apparent in the CWUP and CCWDN Eulerian spectra. The semi-Lagrangian spectra only have a peak at 0.03 cpm in the lowest wavenumber bands (55-8 hours).

Vertical wavenumber is averaged into 4 bands and plotted against frequency for the Eulerian and semi-Lagrangian spectra (Figures 2.15 and 2.16). The super tidal peak is only located in the 64-32 m band of the Eulerian CWDN spectra. At high frequency in the Eulerian spectra, the highest wavenumber bands have the largest spectral density. An inertial peak is observed in the CWDN and CWUP spectra in the low wavenumber bands (128-32m). The highest wavenumber band (16-10m) is white at low frequency and rolls off above 0.3-0.5 cph in all four quadrants. The wavenumber bands look much more similar in the semi-Lagrangian spectra. They have a  $\omega^{-1}$  power law at all frequencies in the CCWDN and CCWUP spectra with the lowest wavenumbers (128-64m) having slightly less spectral density at high frequency. An inertial peak occurs in all but the highest wavenumber bands in the CWDN and CWUP spectra.

The total shear variance is dominated by near-inertial waves propagating away from the surface. The CWDN contains 43% total Eulerian shear variance and 54% of the semi-Lagrangian shear variance (Table 2.1). The prominent wavelength associated with these waves is 35 meters. There is noticeably more CW semi-Lagrangian than Eulerian shear variance. Also evident is the decrease in CCWUP semi-Lagrangian variance where vertical advection of the near inertial waves has the largest effect (see Section 2.8).

## 2.7. WKB approximation.

Linear internal wave theory assumes that the background density gradient is constant. For cases where the buoyancy frequency varies slowly in depth, the vertical wavenumber,  $m$ , also becomes a slow function of depth. This approximation is called the Liouville-Green or WKB approximation (Gill, 1982). As a wave propagates from a region of large to small  $N$ , its characteristic vertical wavelength will grow and horizontal velocity amplitudes will shrink. Following the approach of Gill (1982), assuming that  $\omega$  is small compared with  $N$  and that the vertical scale  $m^{-1}$  is small compared with the scale

over which  $m$  varies, a new vertical coordinate can be found so that  $m$  is constant with depth. The vertically stretched vertical coordinate,  $z_m$ , is defined by

$$z_m(z) = \int_0^z \frac{\bar{N}(z)}{N_m} dz \quad (2.8)$$

where  $N_m$  is the maximum value of the buoyancy frequency and  $\bar{N}(z)$  is the mean buoyancy frequency profile. The horizontal velocity,  $\mathbf{u}$ , scales with depth according to

$$|\mathbf{u}_m| = \left( \frac{\bar{N}(z)}{N_m} \right)^{-\frac{1}{2}} |\mathbf{u}| \quad (2.9)$$

where  $\mathbf{u}_m$  is the WKB vertical velocity. This scaling allows the comparison of wave energy and vertical scales measured at different depths.

The WKB scaling is applied to the data using the mean buoyancy profile from the combined velocity and density data set (Figure 2.12). The amplitude of the velocity at each depth is adjusted using (2.9) then resampled at stretched depths,  $z_m$ . The scaling and stretching is applied to both the Eulerian and Semi-Lagrangian velocity field data sets. Using the same routines to calculate rotary shear spectra as described in Section 2.7 yields the WKB shear spectra (Figures 2.17 and 2.18). The high wavenumber correction has been applied to both the spectra.

One change in the vertical wavenumber spectra is in the inertial band. The clockwise downward near inertial energy from the non-WKB scaled Eulerian and Semi-Lagrangian spectra (Figures 2.13b and 2.14b; 55-16 hour period) has one peak at 0.009 cpm and a second peak at 0.03 cpm. In contrast, the WKB scaled spectra (Figures 2.17b and 2.18b; 55-16 hour period) have only one peak at 0.02 cpm. This difference suggests that the near inertial waves are to the stretching by the changing buoyancy frequency. (The vertical group velocity for these waves is 30 meters per day ( $\omega = 1.26f$ ) and it would take nearly 10 days for this near inertial wave group to reach 300 meters from the surface.) There is also a shape difference between the non-WKB and WKB spectra at high wavenumbers. This is expected since the vertical smoothing is nonlinear in stretched coordinates and has not been correctly removed. The non-WKB spectra will be used instead since there are no significant spectral shape changes at low wavenumber and the effects of vertical smoothing are better understood.

## 2.8. Inertial Wave Vertical Advection Model.

A simple model is presented here to illustrate inertial wave spectra distortion by vertical advection. Consider the complex velocity field of an inertial wave in vertically advective coordinates and given by

$$\mathbf{u} = U_0 e^{i(m\zeta - ft)} \quad (2.10)$$

where  $\zeta$  is defined to follow vertically advected layers (isopycnals),  $U_0$  is the velocity amplitude,  $m$  is the vertical wavelength and  $f$  is the inertial frequency. The layer vertical acceleration is found from the total derivative of the vertical velocity field on that layer,

$$\frac{Dw}{Dt} = \frac{\partial w}{\partial t} + u \frac{\partial w}{\partial x} + v \frac{\partial w}{\partial y} + w \frac{\partial w}{\partial x} \quad (2.11)$$

The term of the left hand side of the equation is the vertical acceleration of the layer. The first term on the right side is the local Eulerian acceleration of the water and the last 3 terms are the convective accelerations. Using the small amplitude wave assumption, the second order terms are dropped and the equation is then linearized. Thus, the acceleration of a layer is approximated by the acceleration found at its mean depth in Eulerian coordinates. Then the displacement of the layer is found by integrating the vertical velocity at a given depth. Using the mean depth of a layer as a Lagrangian label for that layer, the semi-Lagrangian coordinate,  $\zeta$ , for a single internal gravity wave is related to the Eulerian coordinates by

$$\zeta(z, t) = z - A \sin(\hat{m}z - \hat{\omega}t) = z - \eta \quad (2.12)$$

where  $\eta$  is the vertical displacement,  $\hat{m}$  and  $\hat{\omega}$  are the vertical wavenumber and frequency of the displacement wave and  $A$  is the amplitude of displacement. The Eulerian shear field is related to the semi-Lagrangian shear by

$$\mathbf{u}_z = \frac{\partial \zeta}{\partial z} \mathbf{u}_\zeta = (1 - \eta_z) \mathbf{u}_\zeta \quad (2.13)$$

If the strain is small ( $\eta_z \ll 1$ ), solving for the Eulerian shear yields

$$\mathbf{u}_z(z, t) = m U_0 e^{i(mz - ft)} e^{i(m\eta)} \quad (2.14)$$

If the vertical advection is small compared to the vertical wavelength of the inertial wave ( $A m^{-1} \ll 1$ ) then

$$\mathbf{u}_z(z, t) = m U_0 e^{i(mz - ft)} (1 + m\eta) \quad (2.15)$$

Using (2.12) and solving for the Eulerian vertical shear rotary spectrum yields

$$\begin{aligned} \Phi_E(\bar{m}, \bar{\omega}) &= \\ \Phi_{S.L.} + \frac{m^4}{4} U_0^2 A^2 &\left[ \delta(m + \hat{m} - \bar{m}) \delta(f + \hat{\omega} + \bar{\omega}) + \delta(m - \hat{m} - \bar{m}) \delta(f - \hat{\omega} + \bar{\omega}) \right] \end{aligned} \quad (2.16)$$

where the semi-Lagrangian or intrinsic wave spectrum is

$$\Phi_{S.L.}(\tilde{m}, \tilde{\omega}) = \frac{m^2}{2} U_0^2 \delta(m - \tilde{m}) \delta(\omega + \tilde{\omega}) \quad (2.17)$$

The Eulerian spectrum contains "Doppler" shifted frequencies and wavenumbers due to the vertical advection. The variance is shifted to the summed and differenced wavenumber and frequency and scales with the displacement variance normalized by the inertial vertical wavelength.

Assuming that the vertical wavelength of vertical advection is long compared to the inertial wave ( $m \gg \hat{m}$ ), the Eulerian rotary spectrum will be altered at the vertical wavenumber,  $m$ , in both the CWDN and CCWUP spectra for an inertial wave traveling downward. No energy from this wave is transferred to the CWUP and CCWDN spectra. The observed Eulerian rotary spectra show this to be the case (Figure 2.13). The inertial shear variance is dominated by  $m = 0.03$  cpm seen at all frequencies in Figures 2.13b and 2.13d corresponding to the CWDN and CCWUP spectra. The distortion is absent from the CCWDN and CWUP (Figures 2.13a and 2.13c).

The frequency dependence of the distortion will rely on the frequency spectrum of the displacement,  $\Phi_\eta$ . Modeling the displacement,  $\eta$ , as a spectrum of frequencies, the Eulerian shear rotary spectrum is written as

$$\Phi_E(\tilde{m}, \tilde{\omega}) = \Phi_{S.L.} + \frac{m^4}{4} U_0^2 [\Phi_\eta(-f - \tilde{\omega}) + \Phi_\eta(f + \tilde{\omega})] \delta(m - \tilde{m}). \quad (2.18)$$

Typical  $\Phi_\eta$  have a peak at the semi-diurnal tide,  $M_2$ , and fall as  $\omega^{-2}$  out to the buoyancy cutoff at  $N$  (Figure 2.19). The strongest distortion is expected at  $\tilde{\omega} = -(f + M_2)$  and  $\tilde{\omega} = -(f - M_2)$  which would lead to a super tidal and sub-inertial spectral peaks. The super tidal peak is observed in the Eulerian CWDN shear spectrum in the 64-32 m band (Figure 2.15b) as expected and not anywhere else. The sub-inertial peak can not be seen because the records are too short. At high frequency ( $\omega \gg f$ ), the distortion will have a slope of  $\omega^{-2}$ . The shear frequency spectrum also has a slope of nearly  $\omega^{-2}$  suggesting that observable distortion occurs at all frequencies.

## 2.9. Counter Clockwise to Clockwise Shear Variance Ratio.

The CCW to CW shear variance ratio is calculated by dividing the sum of CCWDN and CCWUP spectra by the sum of CWDN and CWUP spectra. From linear theory, the expected CCW/CW ratio is

$$\frac{\Phi_{ccw}}{\Phi_{cw}} = \left( \frac{\omega - f}{\omega + f} \right)^2 \quad \text{for } \omega > f \quad (2.19)$$

which is only a function of frequency. As  $\omega$  approaches the inertial frequency,  $f$ , the waves should be dominated by clockwise rotation (in the northern hemisphere) as the ratio approaches zero. At higher frequency, rotation becomes less important and CCW variance should equal CW variance.

The CCW/CW ratio is computed for the 4 wavenumber bands and smoothed in frequency as discussed for both Eulerian and semi-Lagrangian shear (Figure 2.20a-b). All the wavenumber bands in the semi-Lagrangian coordinates have greater CW rotation near  $\omega = f$ . Only the lowest wavenumbers in Eulerian coordinates appear to be affected by rotation and the CCW/CW ratio for the high wavenumbers does not deviate significantly from 1.0 at any frequency. To better illustrate the deviations from linear theory, the CCW/CW ratios are normalized by expected values (2.19) and plotted with 95% confidence limits (Figure 2.21). The semi-Lagrangian shear fits linear theory at all wavenumbers and frequencies better than the Eulerian shear. At high frequency ( $\omega > 1$  cph), CCW shear appears to be overestimated in both coordinates. One possibility for this discrepancy is measurement noise which would equally corrupt CW and CCW shear variance thus pushing the ratio closer to 1.0 as the signal to noise ratio gets small. At low frequencies, the CCW/CW shear ratio measured at low wavenumbers is better predicted by linear theory than higher wavenumbers. This also could be caused by measurement noise or failure to perfectly resolve the semi-Lagrangian coordinates.

## 2.10. Strain Variance To Shear Variance Ratio

The expected strain variance to shear variance ratio from linear theory is

$$\Psi(\omega) = N^2 \frac{\Phi_\lambda}{\Phi_s} = \frac{N^2}{N^2 - \omega^2} \left( \frac{\omega^2 - f^2}{\omega^2 + f^2} \right) \quad (2.20)$$

where  $\Phi_\lambda$  is the strain spectrum,  $\Phi_s$  is the shear spectrum,  $N$  is the buoyancy frequency and  $f$  is the inertial frequency. Independent of wavenumber, near inertial waves have excess shear variance and high frequency waves have excess strain variance. Observed ratios are found in Eulerian and semi-Lagrangian coordinates using the estimated shear and strain spectra from four wavenumber bands (Figure 2.22a-b). The Eulerian ratio exhibits excess shear at the two middle wavenumber bands (64-16m) except at the inertial frequency. This excess shear has been observed by Sherman (1989) and Kunze et al. (1990). They both claim that the vertical advection of low mode internal waves Doppler shifts the intrinsic wave frequency to higher frequencies.

The semi-Lagrangian strain variance to shear variance ratio fits ratios modeled by linear theory very well from  $\omega = f$  to  $\omega = 0.5$  cph at all but the highest wavenumber band. Above 0.5 cph, excess shear is found at all wavenumbers. This is associated with the break in slope of the semi-Lagrangian shear frequency spectrum (Figure 2.9a) since the semi-Lagrangian strain frequency spectrum has no observed slope change (Figure 2.7c). This excess shear is most likely due to possible errors in estimating the semi-Lagrangian

shear. First of all, the sonar overestimates the horizontal velocity associated with high frequency waves due to beam separation biasing (Appendix D). Secondly, the depth smoothing of the density profiles has removed high wavenumber straining. For a high strain event, the estimated isopycnals depths will under resolve the true semi-Lagrangian coordinates. Thirdly, the velocity profiles have been averaged in Eulerian coordinates for three minutes and interpolated to a single profile of density. This will cause aliasing of the true semi-Lagrangian velocities. By not fully resolving the semi-Lagrangian coordinates in depth and time, the high frequency semi-Lagrangian shear is still corrupted by vertical advection and Doppler shifting of the intrinsic wave frequencies. All of these may lead to excess shear at high frequency.

## 2.11. Discussion and Conclusions.

Vertical advection of high mode, near inertial waves by higher frequency ( $\omega > M_2$ ), low mode waves significantly distorts Eulerian measurements of shear and strain. The Eulerian shear to strain ratios reveal excess shear at all frequencies above the near inertial band. A simple model of a vertically advected, downward propagating, inertial wave demonstrates how the wave energy is moved to higher frequency when sampled in fixed depth coordinates. The predicted spectral distortion scales with the variance of the displacement normalized by the vertical wavelength of the inertial wave squared and is found at the sum and difference inertial frequency and advecting frequencies. A super tidal peak in the Eulerian shear spectrum is seen in the wavenumber band [0.0161-0.0313] cpm. The displacement variance is dominated by the semi-diurnal internal tide and this super tidal peak corresponds to the sum of the inertial frequency and the semi-diurnal tide. Both observed displacement spectrum and the Eulerian shear spectrum decay in frequency with a slope of  $\omega^2$  above the super tidal peak (Figure 2.25). This indicates distortion of the shear is important at all observed frequencies when sampled in Eulerian coordinates.

Semi-Lagrangian shear and strain ratios closely fit those predicted by linear theory for the frequency band [ $f - 0.5$ ] cph and vertical wavelengths [128-16] cpm. Excess shear is observed above 0.5 cph. The semi-Lagrangian shear frequency spectrum exhibits a slope change from  $\omega^3-\omega^4$  above  $f$  to  $\omega^{-1}-\omega^2$  above 0.5 cph which is not seen in the strain spectrum. Thus the excess shear may be due to Doppler shifting since the semi-Lagrangian coordinate is not fully resolved in time and space.

The total strain variance is 75-85% of GM76 strain variance and the total shear variance is 116-130% of GM76 shear variance. The deficiency in strain and excess shear can be accounted for assuming that the shear and strain is dominated by a near inertial wave of frequency  $1.26f$ . Semi-Lagrangian rotary shear spectrum show 54% of the shear variance in the CW downward energy corresponding to near inertial waves propagating away from the surface. The dominate vertical wavenumber of these waves is 0.03 cpm.

Since most internal wave spectra are from either single vertical profiles or from a moored instrument at fixed depth yielding a time series it is useful to look at cumulative

spectra for comparison (Figure 2.24). The cumulative Eulerian and semi-Lagrangian shear frequency spectra([128-10]m) have some distinct differences. The semi-Lagrangian spectrum reveals nearly twice energy at the inertial peak and much less energy at all frequencies above the Eulerian super tidal peak. The cumulative Eulerian and semi-Lagrangian shear vertical wavenumber spectra ([55-0.5] hours) are very similar (Figure 2.24). This is expected since the distortion by vertical advection does not shift intrinsic vertical wavenumber. The vertical wavenumber shear spectra do not fit the form of the composite shear spectrum presented by A. E. Gargett et al. (1981). The spectra appear more like those of Duda and Cox (1989) who measured vertical shear off the coast of California with the Cartesian Diver and found no reproducible power law in the band [0.02-0.1] cpm. The spectra rise from low wavenumber to a peak at 0.03 cpm. and then decay with a  $m^{-1.5}$  power law out to 0.1 cpm. The observed spectral shape is likely due to the local forcing of the near inertial waves.

Eulerian shear and strain vertical wavenumber and frequency spectra show similar characteristics and do not have the same wavenumber dependence at all frequencies as predicted by the GM model. The spectra are have red vertical wavenumber spectra at low frequency and blue wavenumber dependence at high frequency with all frequencies converging near 0.1 cpm. All frequency bands in the Eulerian shear spectrum show a break in slope at 0.03 cpm corresponding to Doppler shifting of a wave with near inertial intrinsic frequency to higher frequency. The semi-Lagrangian shear and strain vertical wavenumber and frequency exhibit more separability into wavenumber and frequency. Both spectra have slightly blue wavenumber dependence at high frequency, [0.25-2] cph. At low frequency, [.0182-0.0625] cph, the strain spectrum has white wavenumber dependence and the shear spectrum are slightly red with a peak at 0.03 cpm.

The results here show that self advection of the internal wave field is significant on vertical scales of 10 to 128 meters. The SWAPP experiment emphasis this fact since the dominant vertical scale of the shear variance is on the same order as vertical displacement. At longer wavelengths, advection should not be as important and Eulerian and Lagrangian statistics should be the same (Allen and Joseph, 1989). The observation that the waves obey linear internal wave dynamics best in semi-Lagrangian coordinate may be useful in developing new internal wave models.

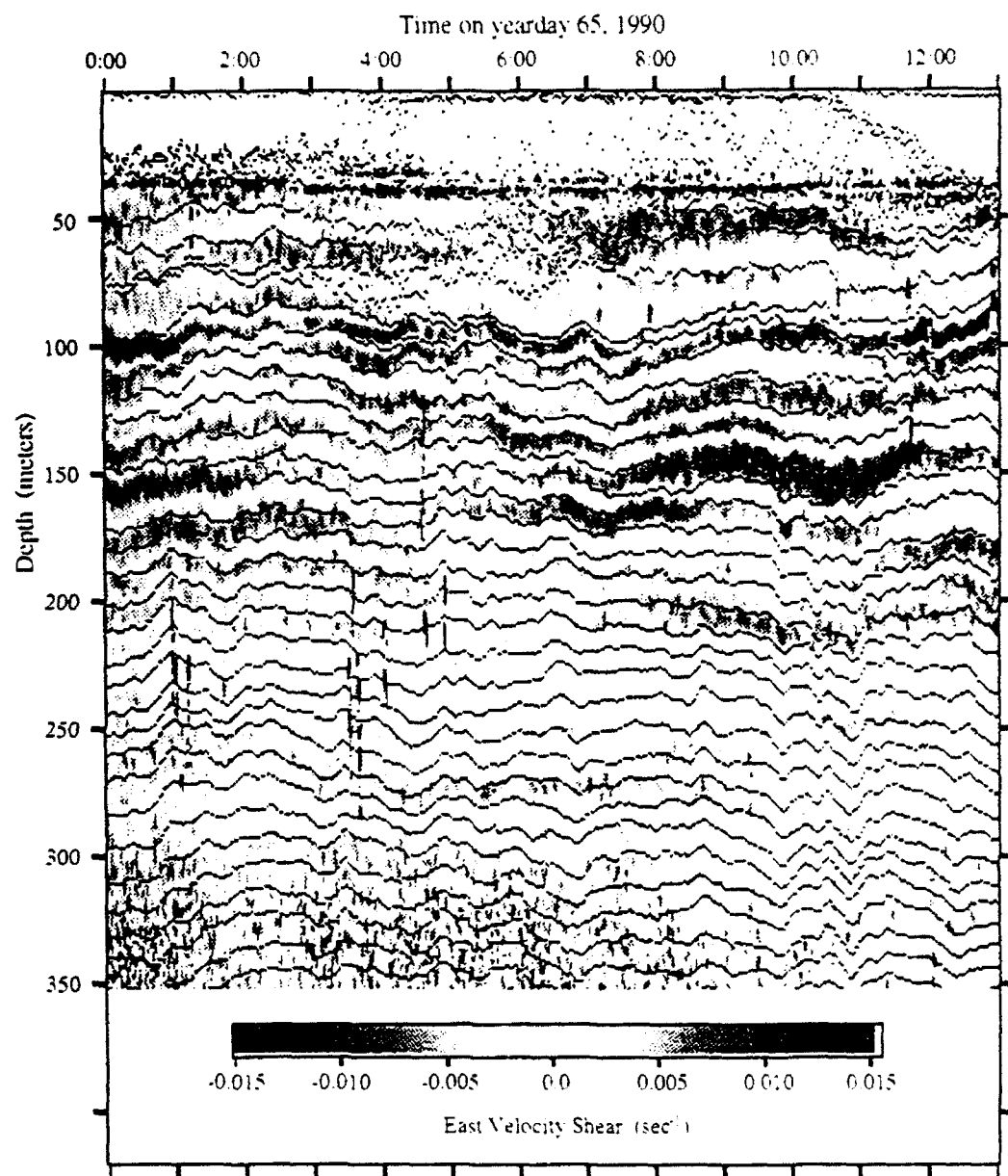


**Figure 2.1** East Velocity Shear on yearday 65. East velocity shear from the 161 kHz sonar averaged over 3 minutes is contoured to a depth of 350 meters from 0:00 to 12:00 (PST) on yearday 65, 1992. Overlaid (black curves) are isopycnals separated by 10 meters in depth on average. The lack of acoustic scatterers during the night and early morning limits the sonar range to 300 meters. After 7:00, reliable velocity estimates are made to 350 meters. Strong shear layers are visible in the 75 to 200 meters depth range. Note that the shear layers appear to "ride" up and down with the isopycnals.

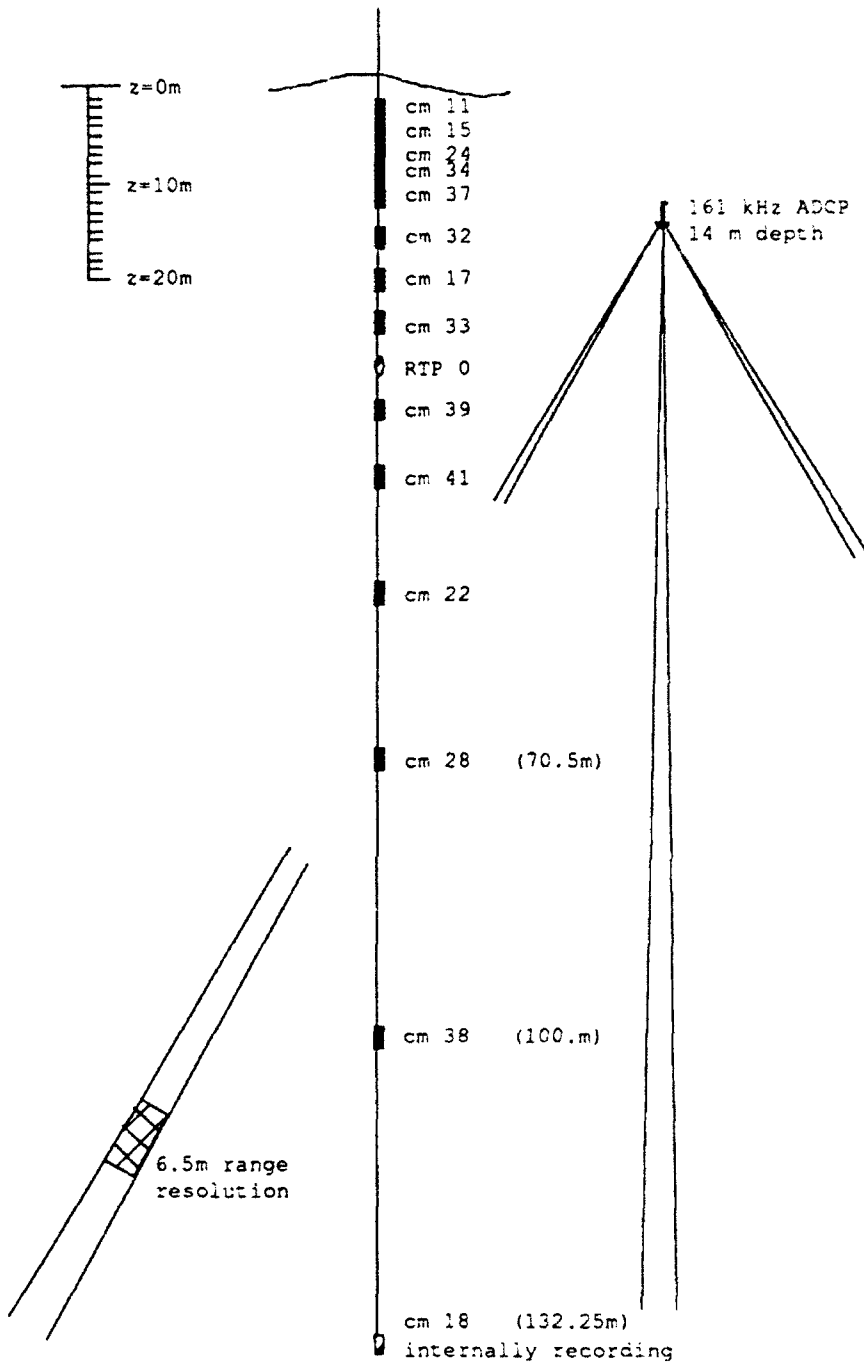


**Figure 2.2 Schematic of W.H.O.I. aft Current Meter Sting.** During the SWAPP experiment, W. H. O. I. deployed 19 current meters on 2 strings from two booms on FLIP. The port deployment extended to 41 meters and the aft deployment (shown in this schematic) extended to 132.25 meters depth. 15 minute averaged velocity time series for the three deepest current meters (cm 28, cm 38, and cm 18) was obtained from W. H. O. I. for comparison with the M. P. L. 161 kHz ADCP. Also shown in this diagram is the depth of the ADCP which was mounted on FLIP's directional thruster and has a 6.5 meter range resolution. The horizontal spacing between the current meter string and the ADCP was approximately 10 meters and is not drawn to scale on the schematic.

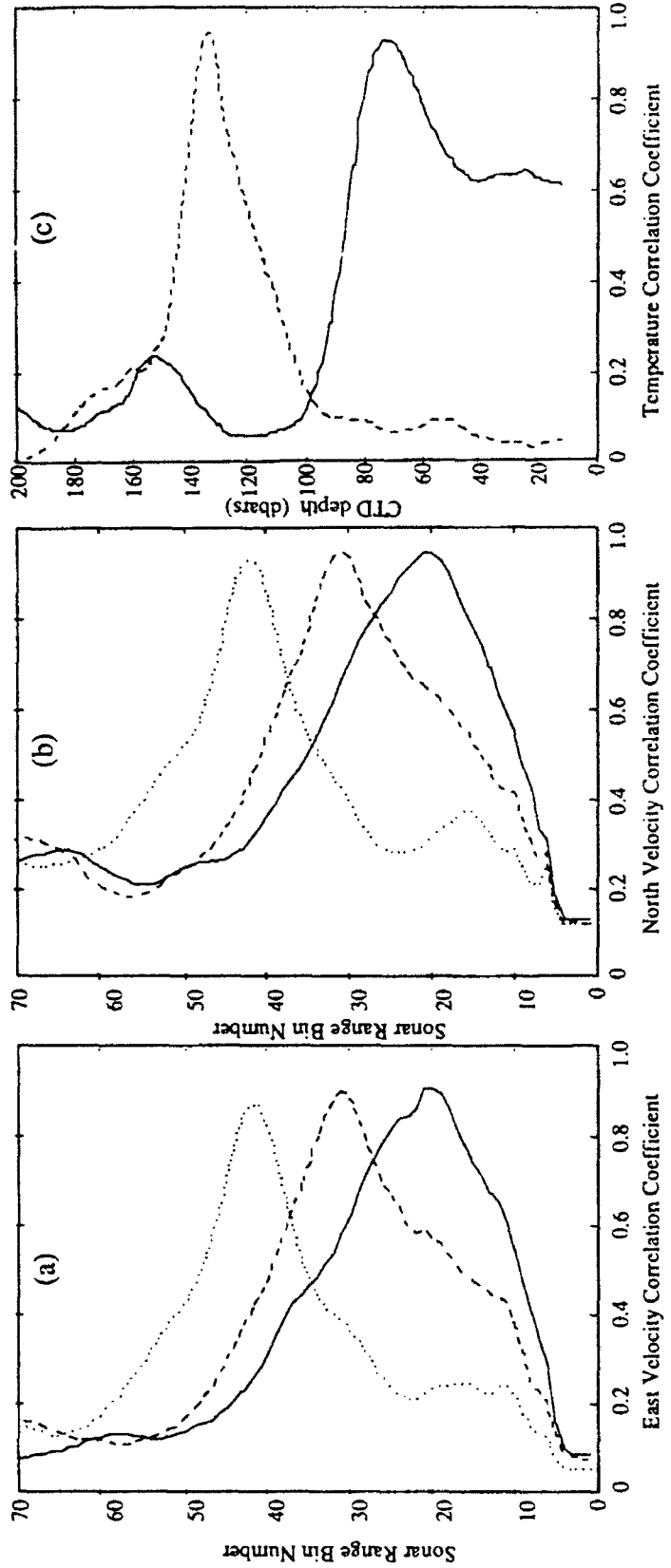


**Figure 2.3 Depth Calibration Using W.H.O.I. Current Meter.** (a) The time series used for the correlation calculations consisted of 15 minute averaged velocities during the 16 days that both systems were in operation. East velocity time series from the three deepest current meters are correlated with velocity time series from each depth bin from the ADCP. The correlation coefficient is plotted as a function of depth bin number for vm12 (solid line), vm13 (dashed line) and vm20 (dotted line). Maximum coefficients occur at bin numbers 20 (vm12), 31 (vm13) and 42 (vm20). (b) Same as (a) except North velocity component is used. Maximum coefficients occur at bin numbers 21 (vm12), 31 (vm13) and 42 (vm20). (c) Temperature time series from current meters vm12 and vm20 are correlated with temperature time series from the CTD. The time series used for the correlation calculations consist of 60 minute averaged temperatures during the 20 days that both systems were in operation. CTD temperature time series are taken at 1 meter depth intervals from 10 to 200 meters. The correlation coefficient is plotted as a function of depth bin number for vm12 (solid line) and vm20 (dashed line). Maximum coefficients occur at depths 72 meters (vm12) and 134 meters (vm20).

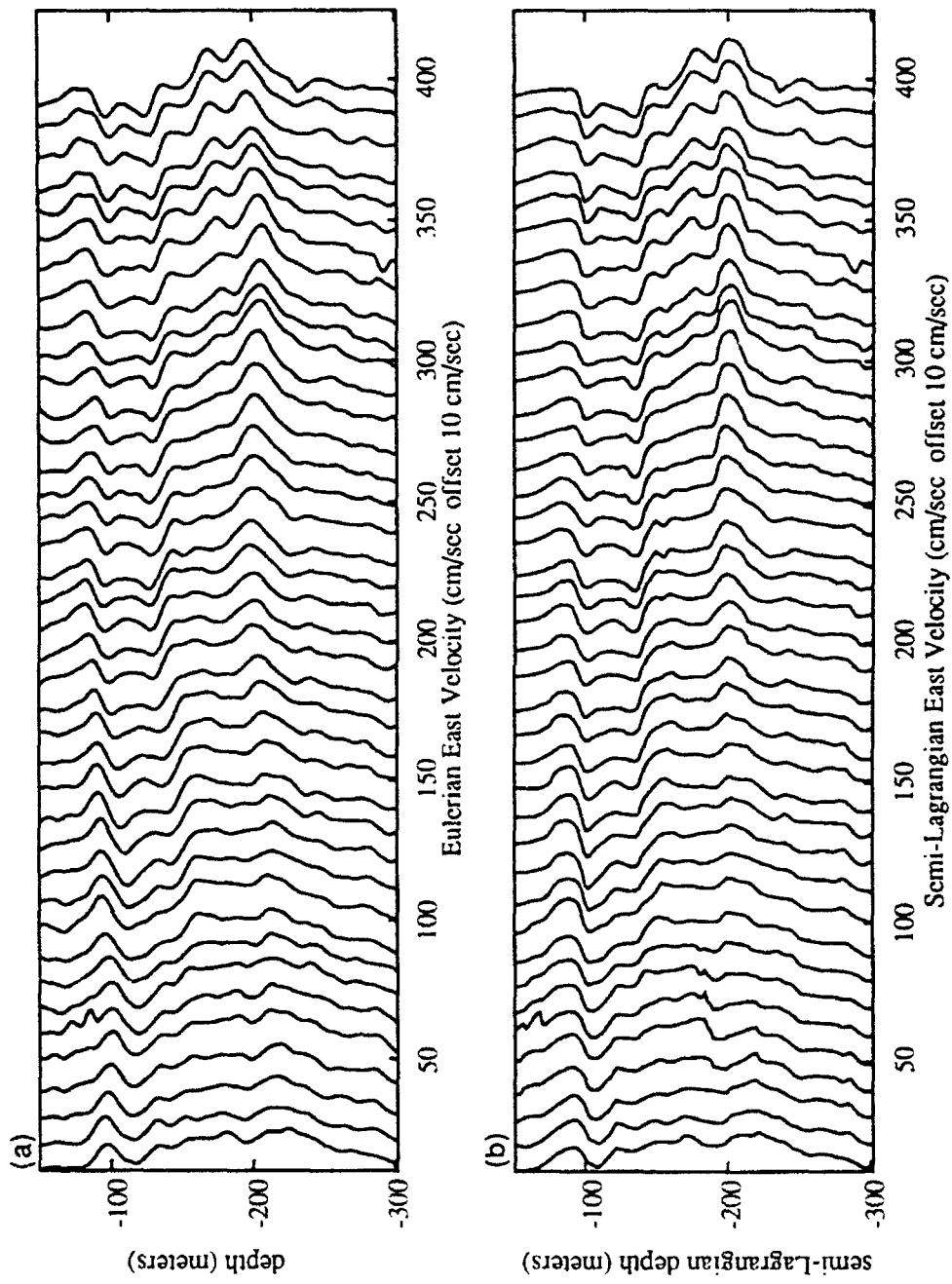


**Figure 2.4 Eulerian and Semi-Lagrangian Velocity Profiles.** (a) Eulerian profiles calculated in Eulerian (fixed depth) coordinates. Profiles are sequential 6.5 minute averages offset by 10 cm/sec and presented in cascade format representing ~4.3 hours of data. (b) East velocity profiles calculated in semi-Lagrangian (isopycnal following) coordinates. Same velocity profiles as plotted in (a) except data is sampled at isopycnal depths and plotted versus the isopycnal mean depth.

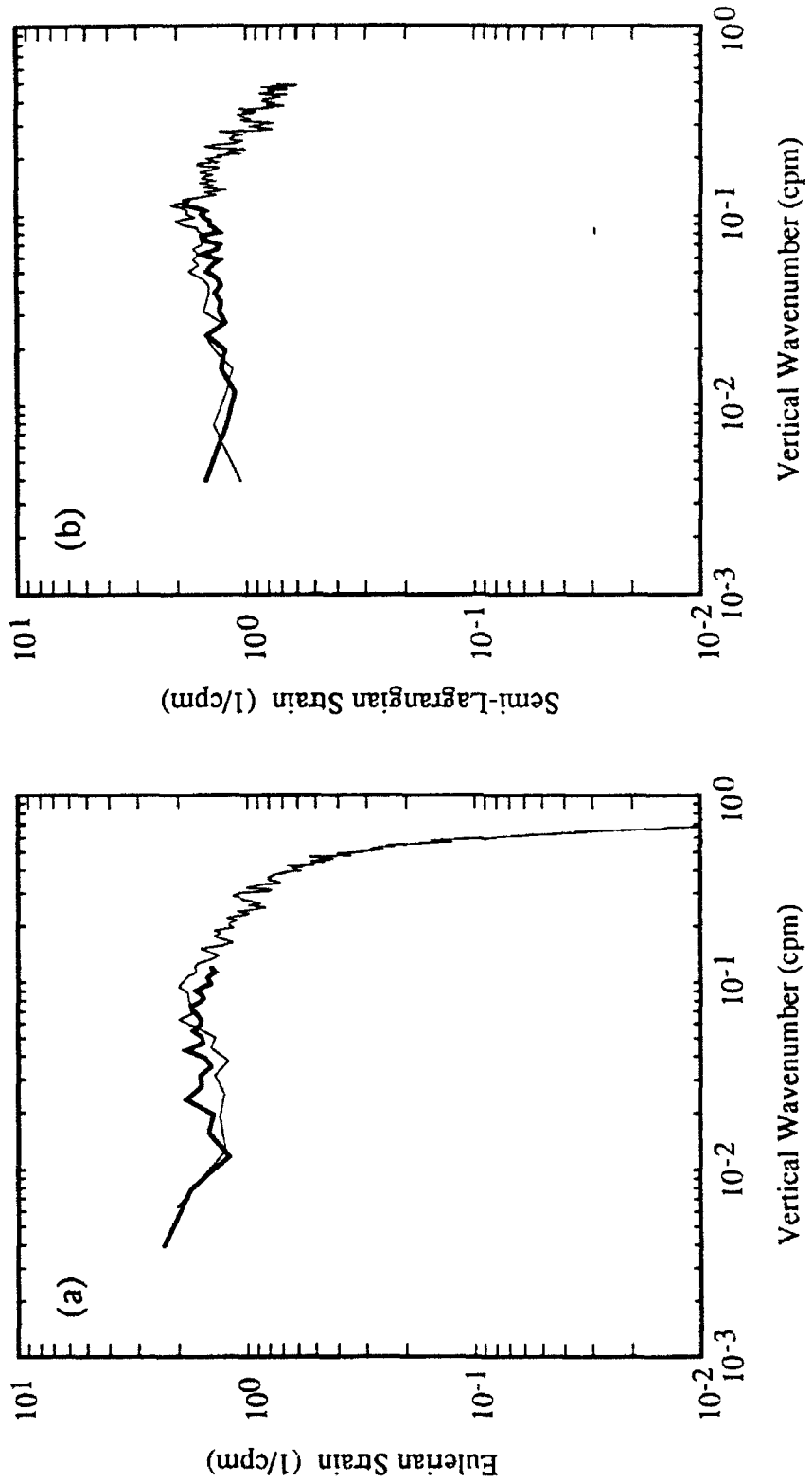


**Figure 2.5 Strain Vertical Wavenumber spectra.** The yo-yo CTD system has a vertical resolution of 1.5 meters and takes a profile every 130 seconds. The density profiles are smoothed in depth by 5.5 meters and in time over 390 seconds before merging with the velocity data. Vertical strain spectra calculated from the smoothed density data must be corrected at high wavenumber. Full resolution spectra and high wavenumber corrected spectra are plotted for comparison. (a) Full resolution Eulerian strain spectrum (light line) is calculated from 40 profiles spaced 10 hours apart in time and plotted with smoothed Eulerian strain spectrum (heavy line) summed over the frequency band [0.018-2.0] c.p.h. (b) 256 isopycnal depths, each separated by 1 meter in depth on average from 150 to 400 meters in depth, are first differenced in depth to calculate the full resolution semi-Lagrangian strain. 180 vertical strain spectra separated by 2 hours over 15 days are averaged together before plotting (light line). Also plotted in the smoothed semi-Lagrangian strain spectrum (heavy line) summed over the frequency band [0.018-2.0] c.p.h.

**Table 2.1 Shear and Strain Variances.** This table shows the shear and strain variance found by integrating the measured shear and strain spectra over the vertical wavelength band 0.00391 to 0.1 cpm (256 to 10 meter wavelengths) and frequency band 0.0182 to 2.0 cph (55 to 0.5 hours). Variances at high wavenumber have been amplified to compensate for roll off due to vertical smoothing. (Numbers in parentheses are percent of total.)  $\langle \lambda_{10}^2 \rangle$  and  $\langle S_{10}^2 \rangle$  are found by integrating the GM76 spectrum over the same wavenumber band. Shear to strain variance has been scaled by both the depth averaged buoyancy frequency ( $N=4.4$  cph) and the maximum buoyancy frequency ( $N_{\max}=6.2$  cph) for comparison.

	Eulerian		Semi-Lagrangian	
Strain Variance				
Upward Energy	0.0924	(51%)	0.0812	(51%)
Downward Energy	0.0893	(49%)	0.0801	(49%)
$\langle \lambda_{10}^2 \rangle$	0.181		0.161	
$\langle \lambda_{10}^2 \rangle / \langle \lambda_{GM}^2 \rangle$ N=4.4 cph	0.85		0.75	
Shear Variance (1/sec <sup>2</sup> )x10 <sup>-5</sup>				
CCW downward	0.650	(14%)	0.363	(9%)
CW downward	2.04	(43%)	2.30	(54%)
CCW upward	1.00	(21%)	0.435	(10%)
CW upward	1.08	(23%)	1.16	(27%)
$\langle S_{10}^2 \rangle$	4.76		4.25	
$\langle S_{10}^2 \rangle / \langle S_{GM}^2 \rangle$ N=4.4 cph	1.3		1.16	
$\frac{\langle S_{10}^2 \rangle}{N^2 \langle \lambda_{10}^2 \rangle}$ N=4.4 cph	4.45		4.47	
$\frac{\langle S_{10}^2 \rangle}{N_{\max}^2 \langle \lambda_{10}^2 \rangle}$ N=6.2 cph	2.25		2.26	

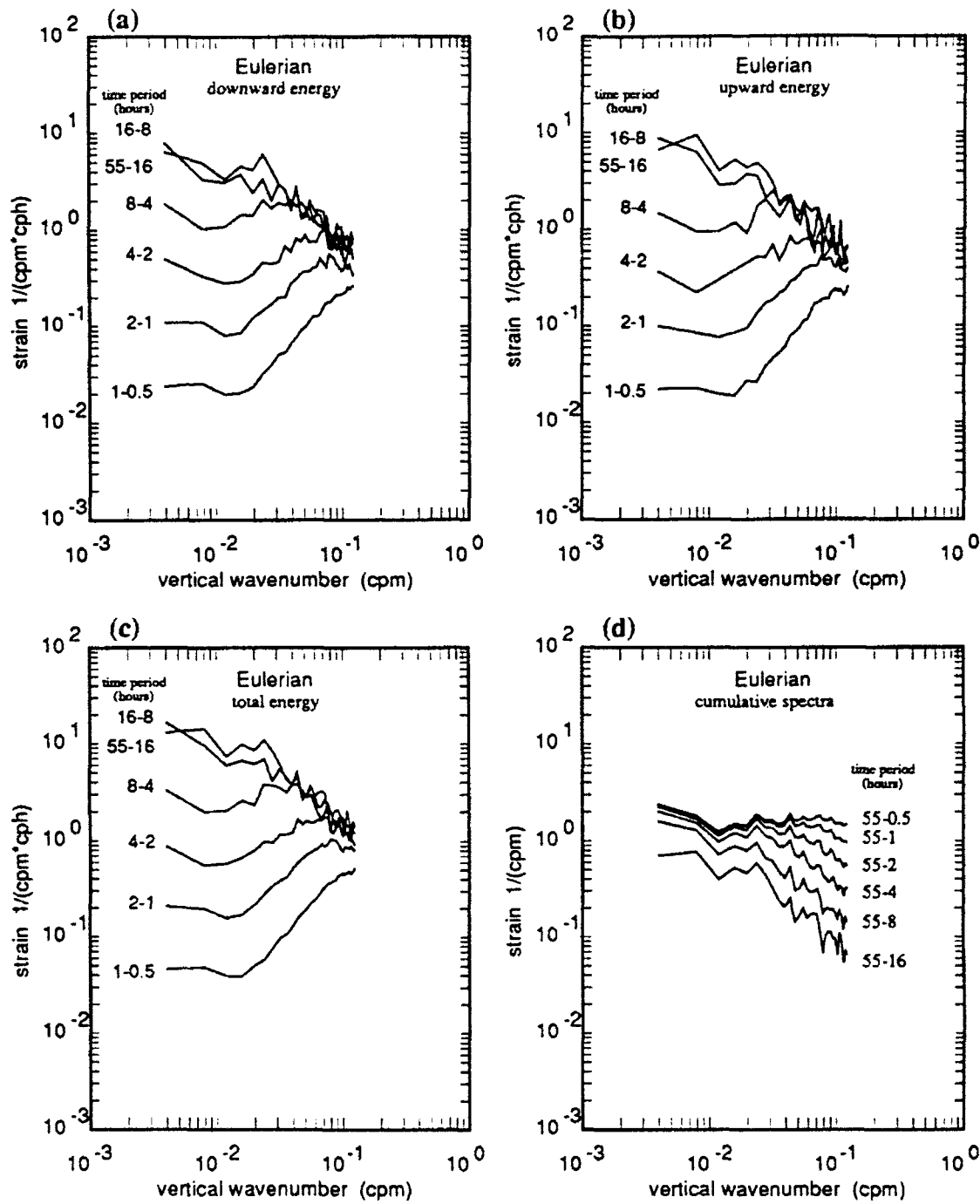


**Figure 2.6 Eulerian Strain Vertical Wavenumber Spectra.** Data used for these spectral estimates are from the combined velocity and density data. The spectra have been corrected at high wavenumbers for vertical smoothing. (a), (b), and (c) show variances in six frequency bands plotted against vertical wavenumber. (a) contains just the downward propagating energy. (b) contains the upward energy. (c) contains the total energy. (d) is the cumulative spectrum.

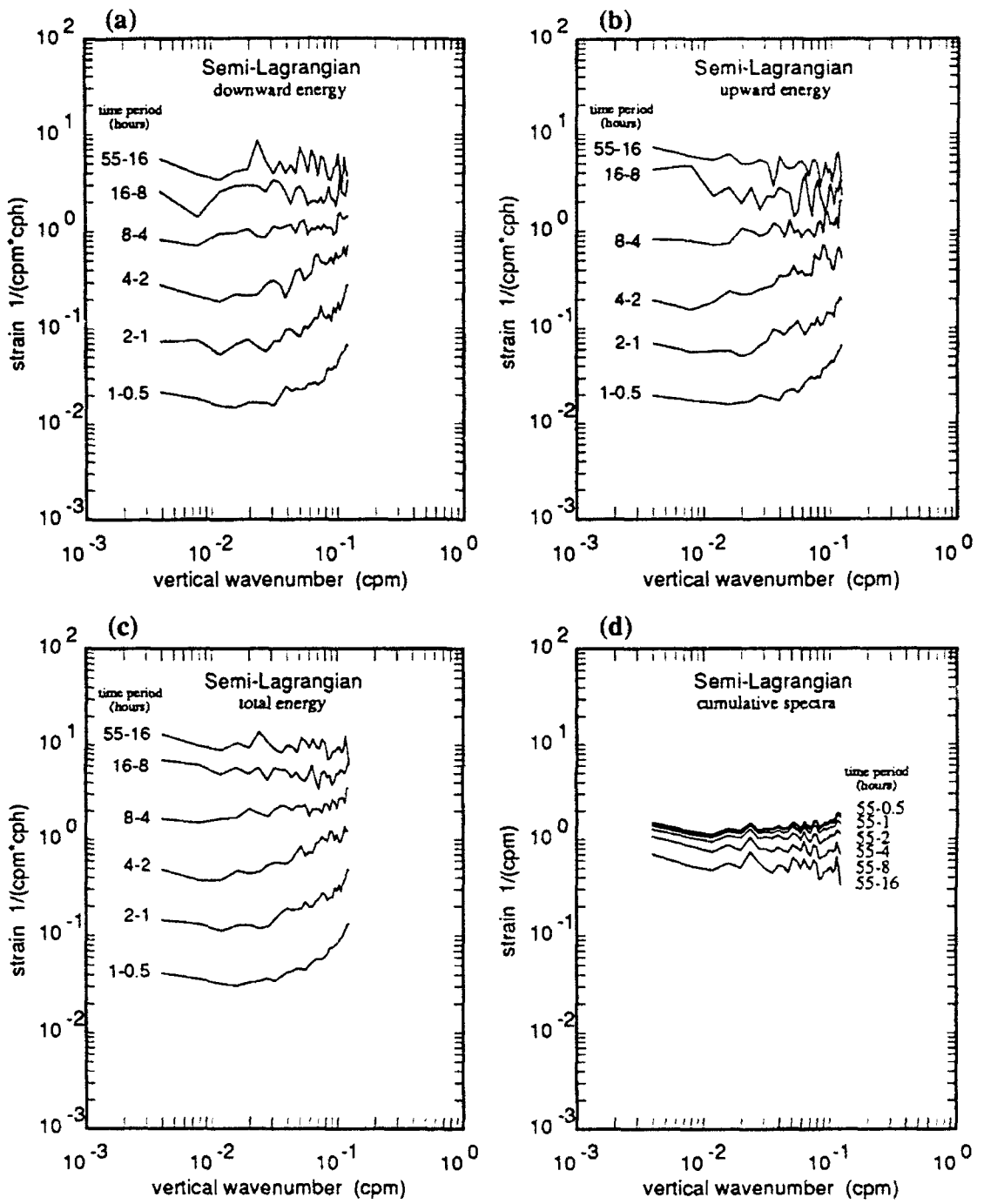


**Figure 2.7** *Semi-Lagrangian Strain Vertical Wavenumber Spectra.* Data used for these spectral estimates are from the combined velocity and density data. The spectra have been corrected at high wavenumbers for vertical smoothing. (a), (b), and (c) show variances in six frequency bands plotted against vertical wavenumber. (a) contains just the downward propagating energy. (b) contains the upward energy. (c) contains the total energy. (d) is the cumulative spectrum.

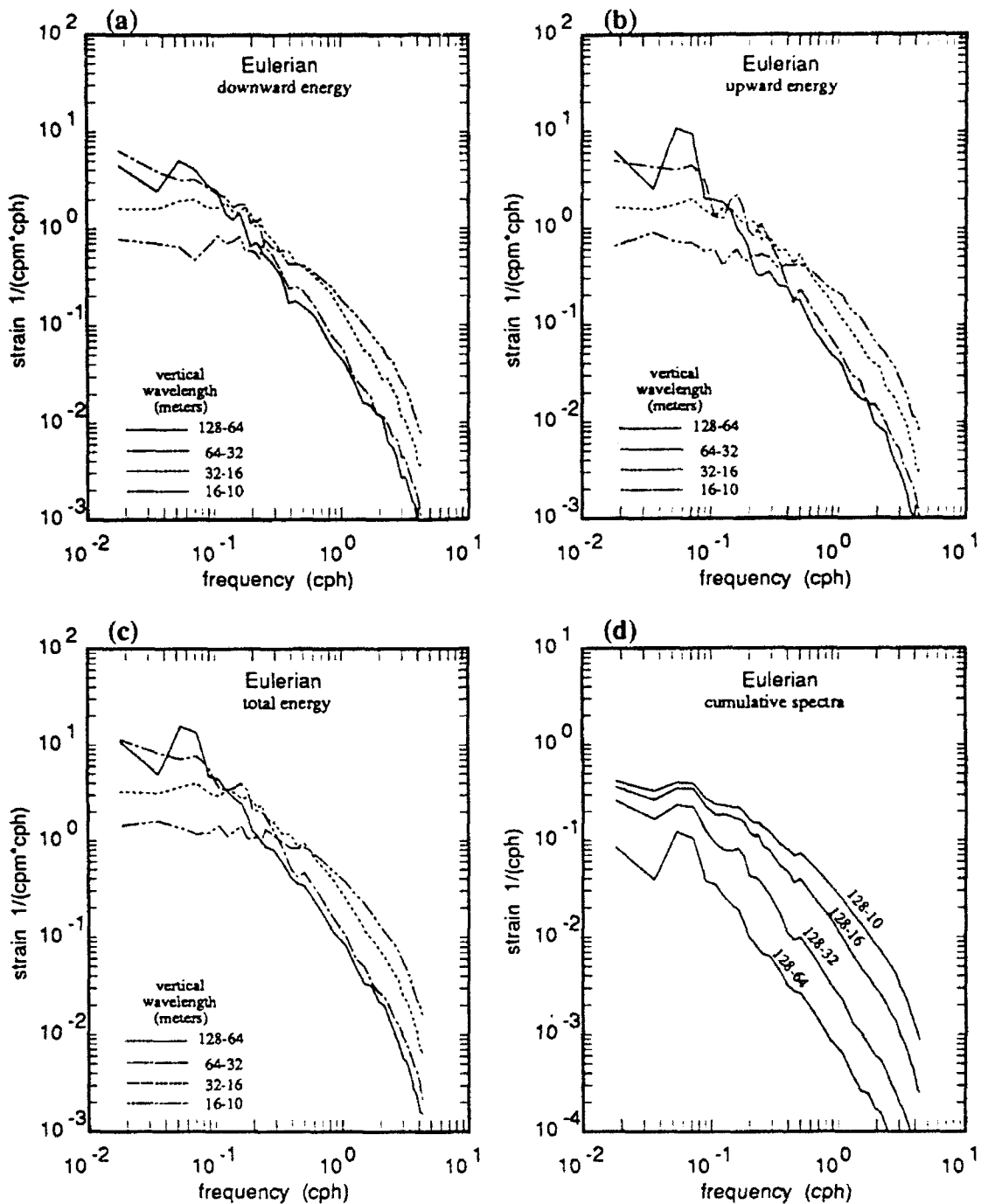


**Figure 2.8 Eulerian Strain Vertical Frequency Spectra.** Data used for these spectral estimates are from the combined velocity and density data. The spectra have been corrected at high wavenumbers for vertical smoothing. (a), (b), and (c) show variances in four wave vertical wavenumber bands plotted against frequency. (a) contains just the downward propagating energy. (b) contains the upward energy. (c) contains the total energy. (d) is the cumulative spectrum.

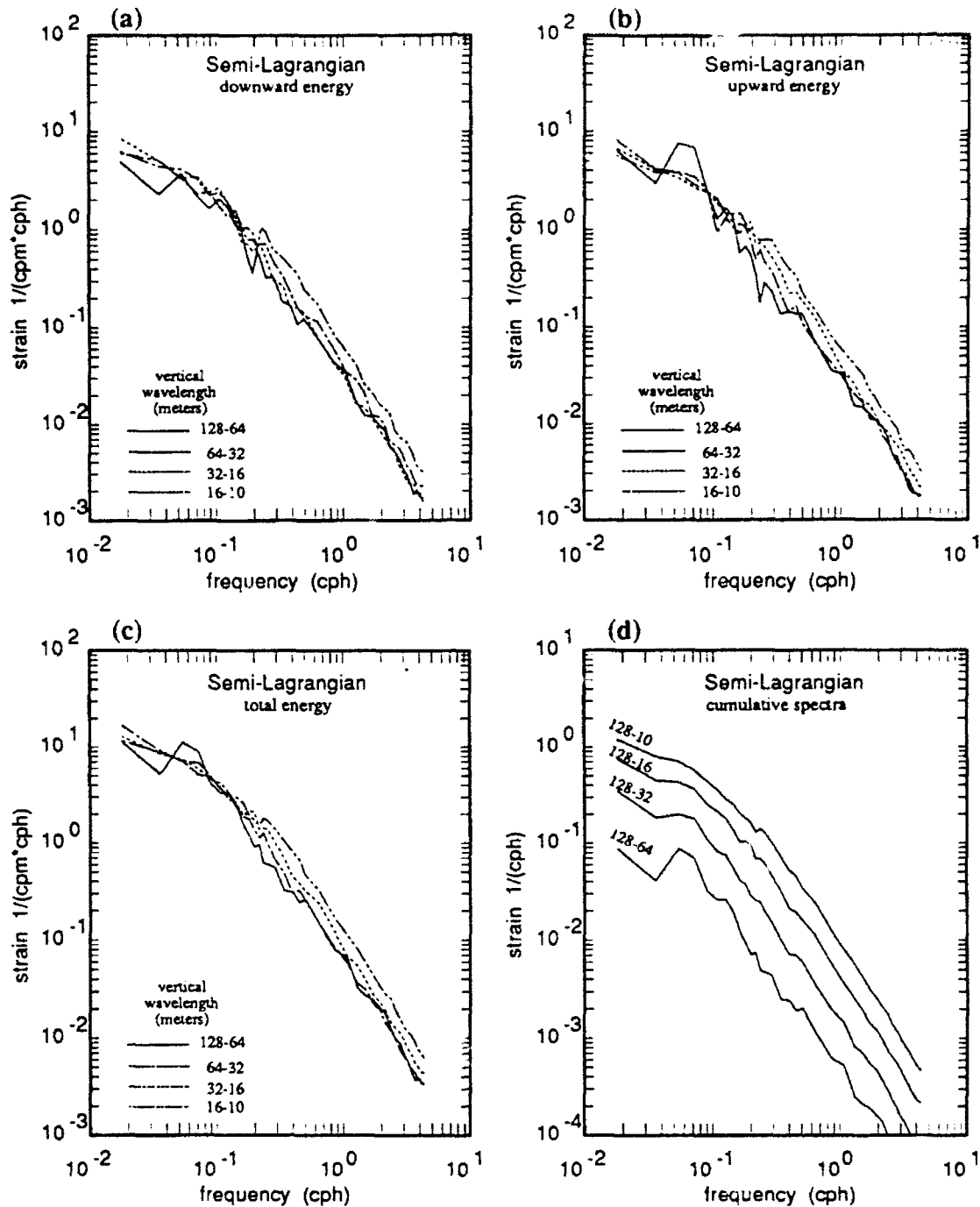


**Figure 2.9 Semi-Lagrangian Strain Vertical Frequency Spectra.** Data used for these spectral estimates are from the combined velocity and density data. The spectra have been corrected at high wavenumbers for vertical smoothing. (a), (b), and (c) show variances in four wave vertical wavenumber bands plotted against frequency. (a) contains just the downward propagating energy. (b) contains the upward energy. (c) contains the total energy. (d) is the cumulative spectrum.

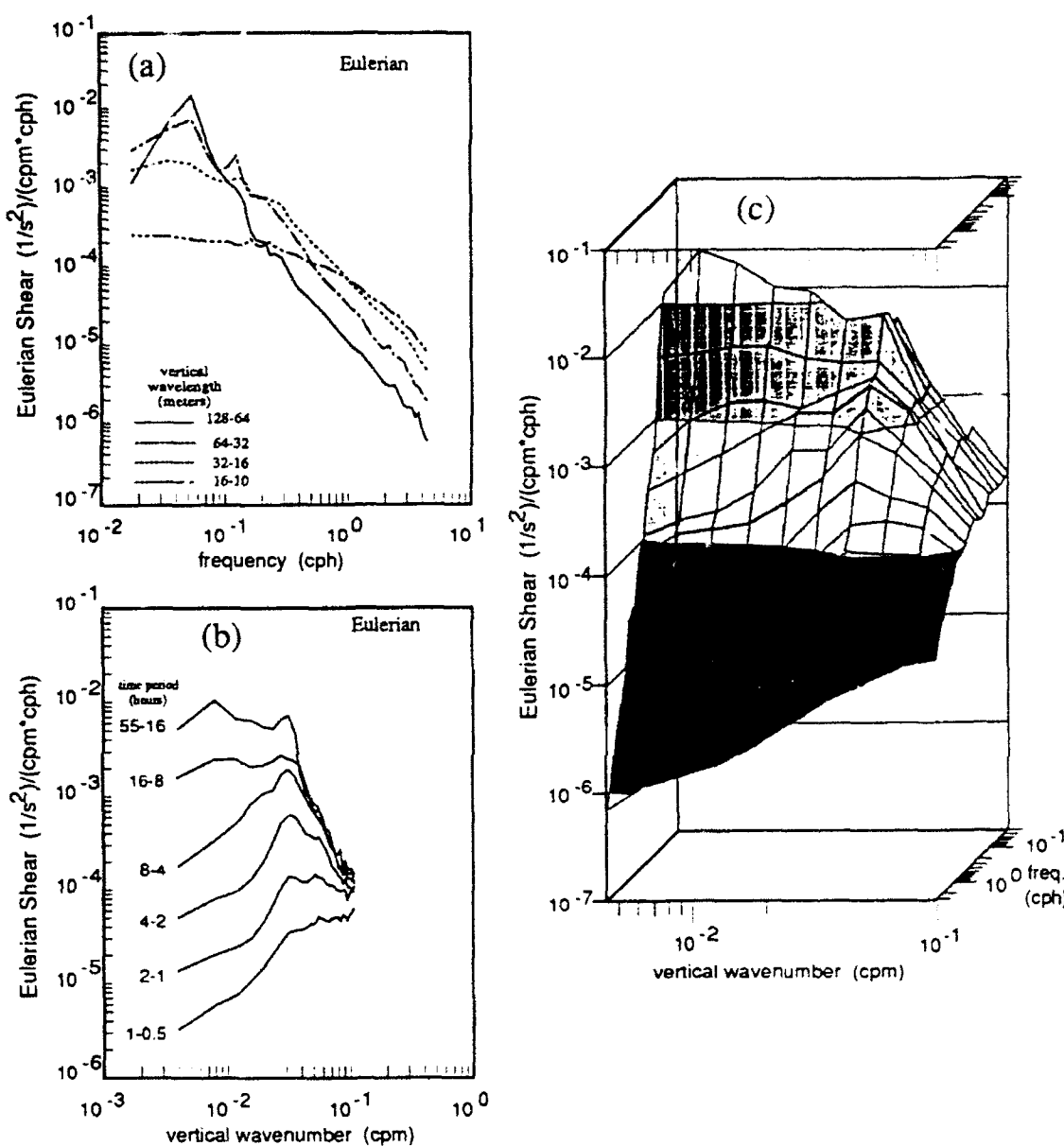


**Figure 2.10 Eulerian Shear Vertical Wavenumber--Frequency Spectrum.** Eulerian shear is found by first differencing the velocity profile over 2 meter depth intervals. (a) the average spectra density is calculated for 4 wavenumber bands and plotted against frequency. Spectra have been smoothed in frequency above 0.27 c.p.h. (b) the averaged spectral density is found for 6 frequency bands and plotted against wavenumber. (c) the spectrum shown in 3-D format.

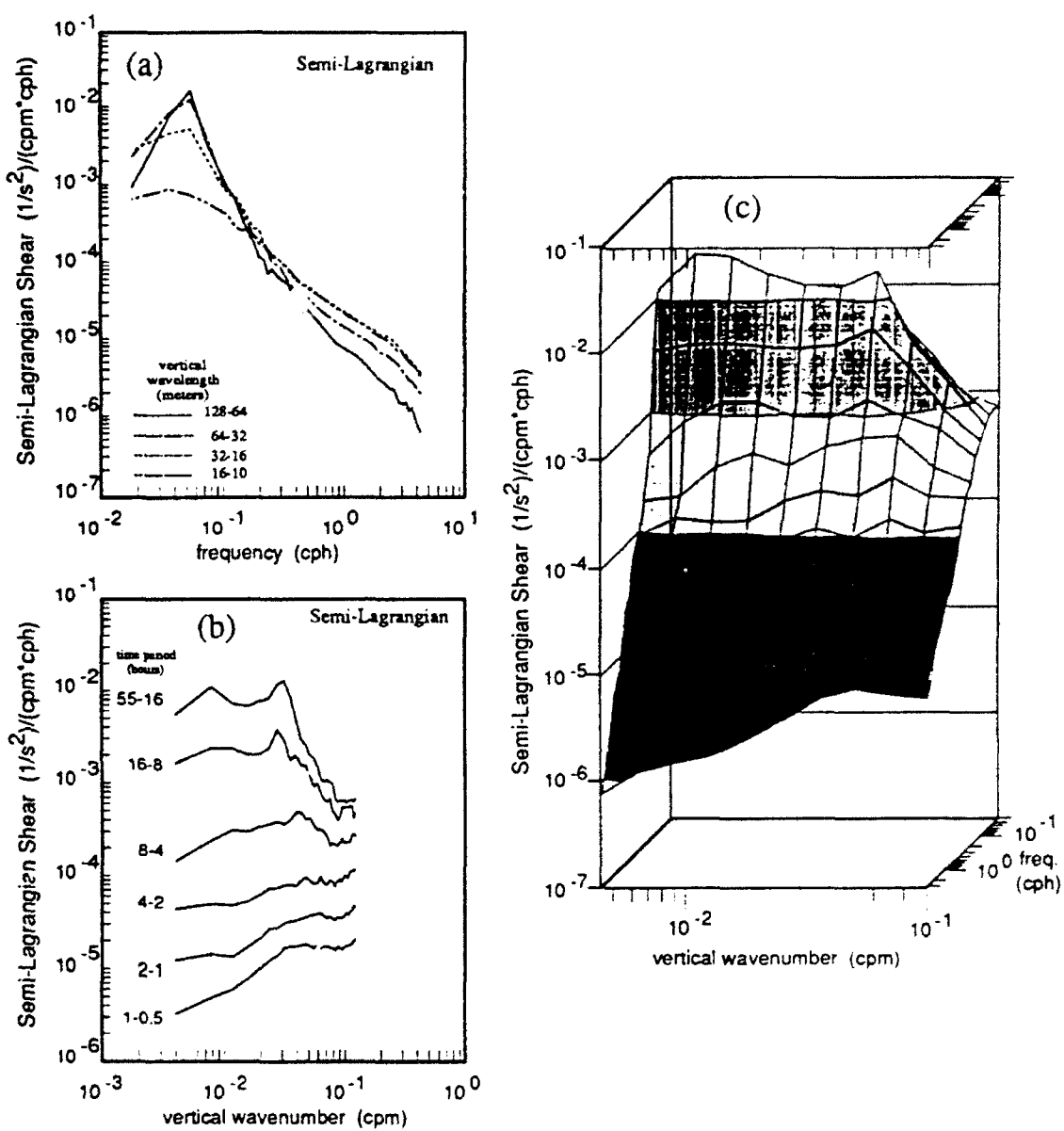


**Figure 2.11 Semi-Lagrangian Shear Vertical Wavenumber--Frequency Spectrum.** Semi-Lagrangian shear is found by first differencing in depth the velocity profile found on isopycnals separated by 2 meters on average. (a) the average spectra density is calculated for 4 wavenumber bands and plotted against frequency. Spectra have been smoothed in frequency above 0.27 c.p.h. (b) the averaged spectral density is found for 6 frequency bands and plotted against wavenumber. (c) the spectrum shown in 3-D format.

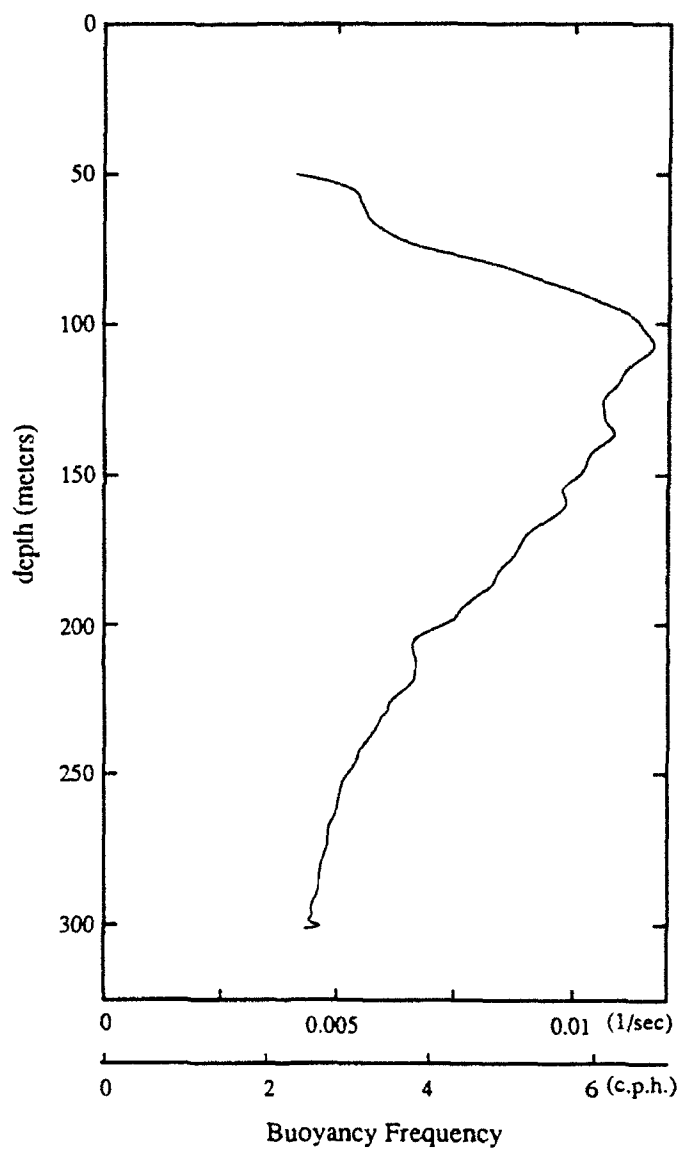


**Figure 2.12 Mean Buoyancy Frequency Profile.** Density profiles from yearday 63 to yearday 75 are averaged together. The mean buoyancy profile is found by first differencing the time averaged density profile.

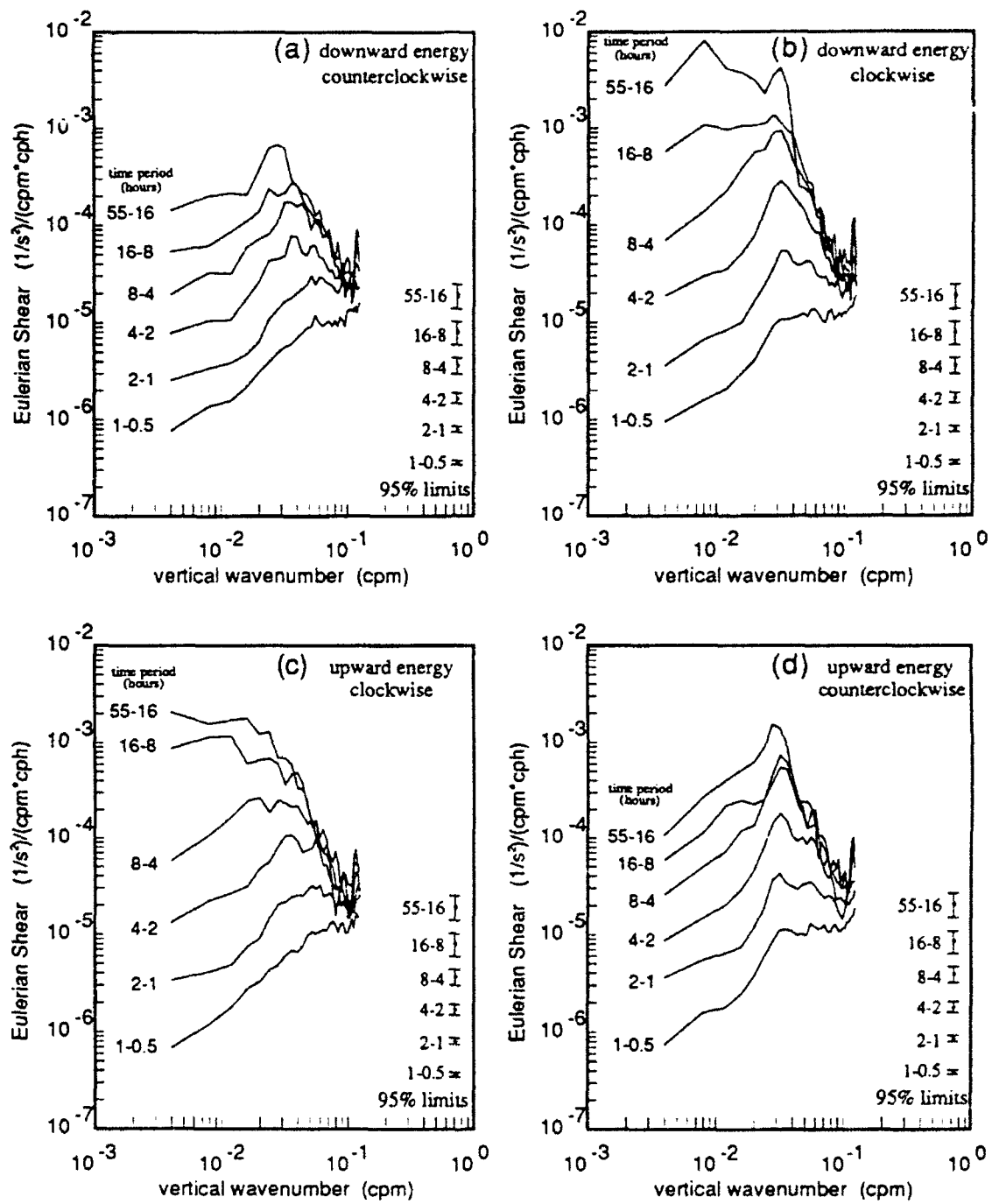


**Figure 2.13 Eulerian Rotary Shear Spectra Vs. Vertical Wavenumber.** The spectra have been corrected at high wavenumbers for vertical smoothing. Six frequency bands are plotted. (a) contains downward CCW propagating energy. (b) contains downward CW propagating energy. (c) contains upward CW propagating energy. (d) contains upward CCW propagating energy.

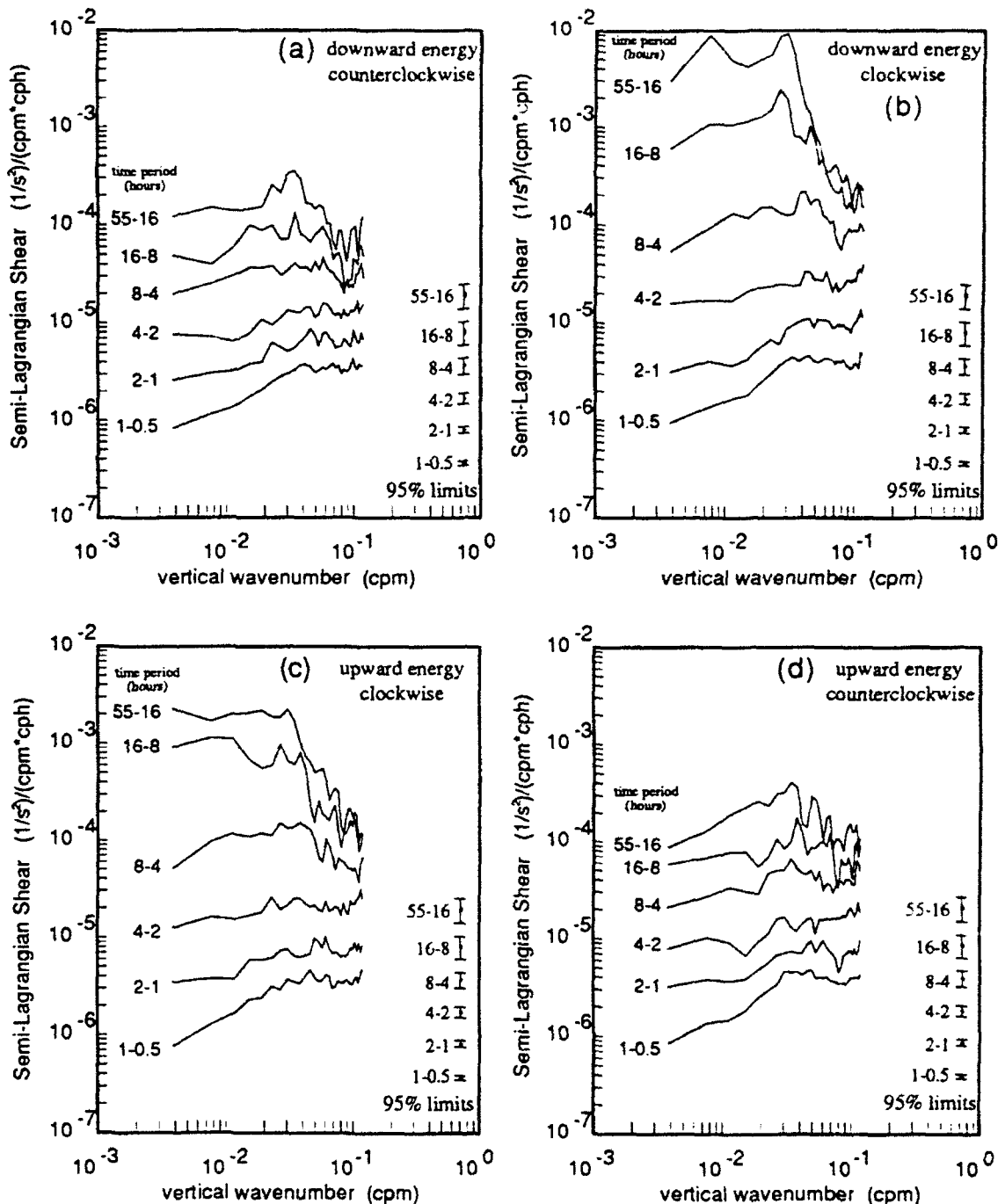


**Figure 2.14** *Semi-Lagrangian Rotary Shear Spectra Vs. Vertical Wavenumber.* Same as Figure 2.13 except semi-Lagrangian shear spectra are plotted.

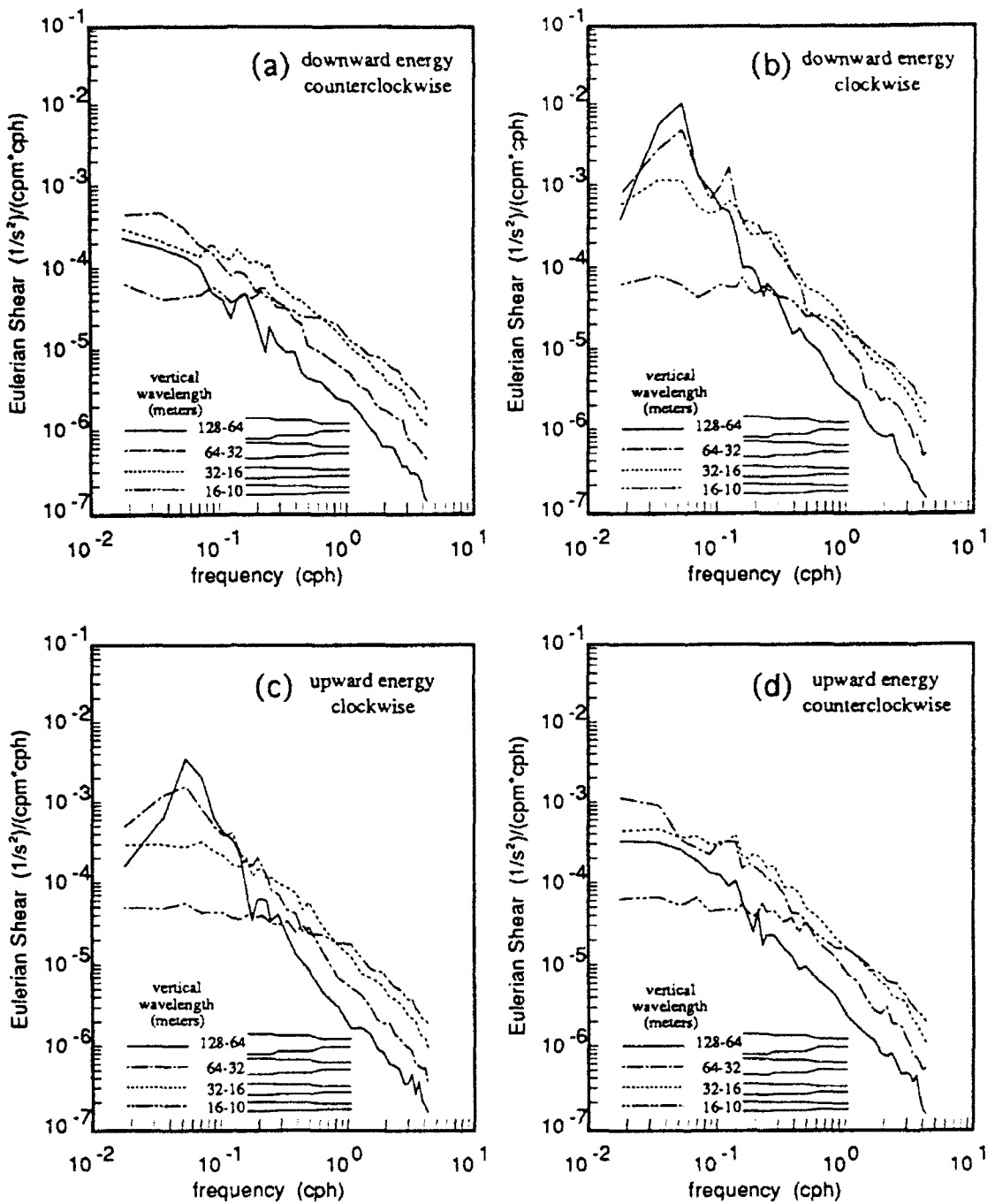


**Figure 2.15 Eulerian Rotary Shear Spectra Vs. Frequency.** The spectra have been corrected at high wavenumbers for vertical smoothing. Four wavenumber bands are plotted. Approximate 95% confidence limits scale with frequency smoothing. (a) contains downward CCW propaging energy. (b) contains downward CW propaging energy. (c) contains upward CW propaging energy. (d) contains upward CCW propaging energy.

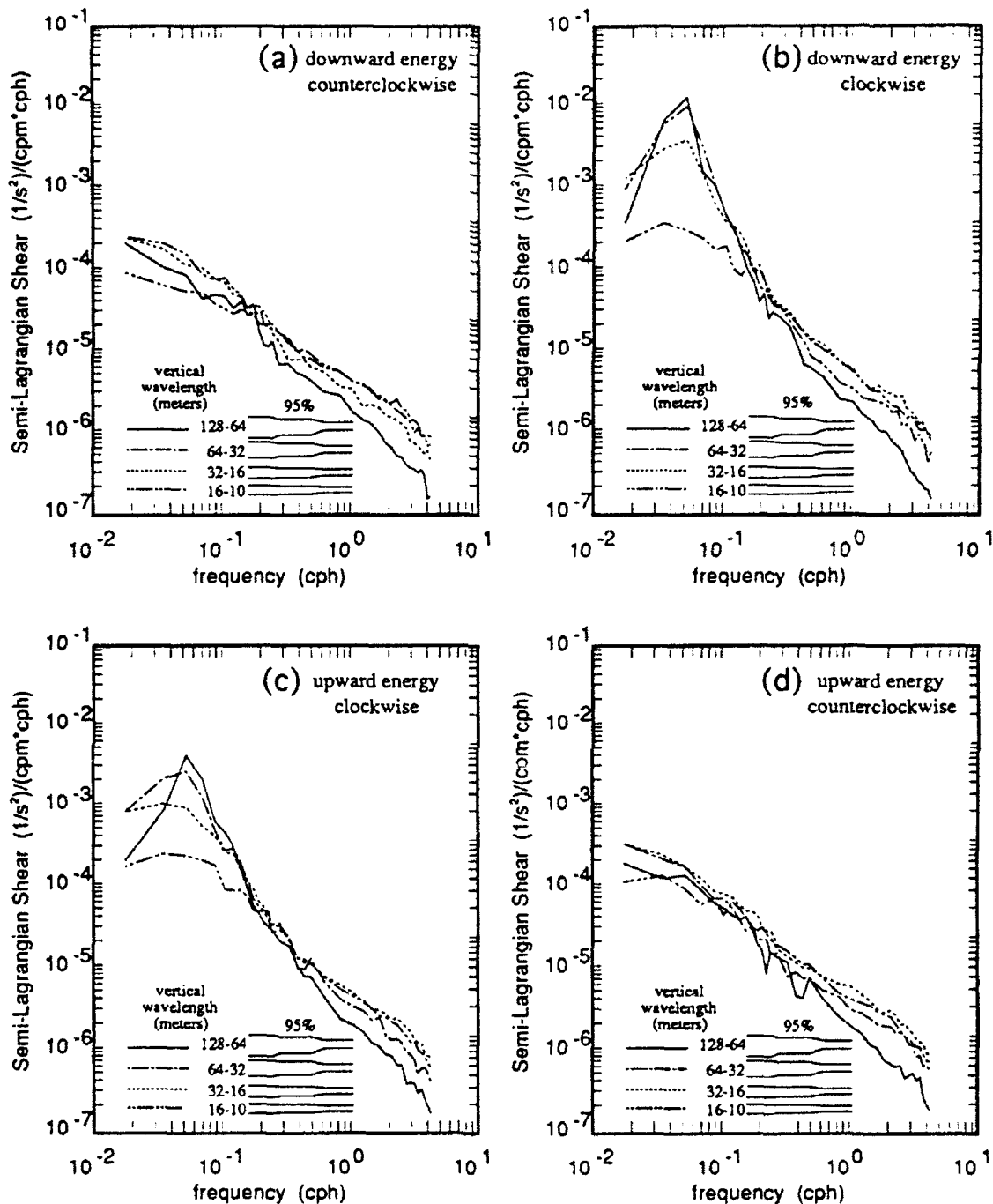


**Figure 2.16** *Semi-Lagrangian Rotary Shear Spectra Vs. Frequency.* Same as Figure 2.15 except semi-Lagrangian shear spectra are plotted.

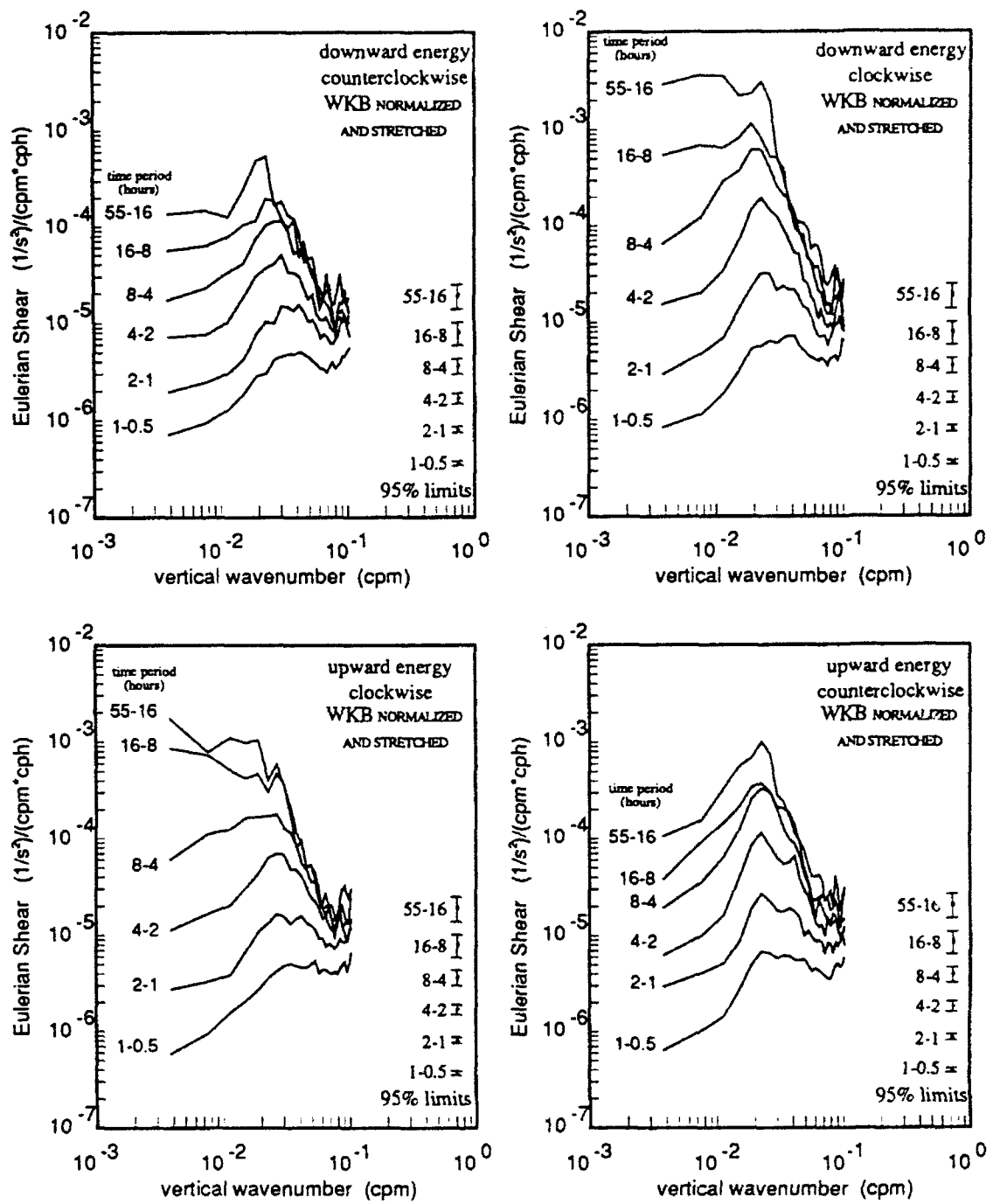


**Figure 2.17 WKB Eulerian Rotary Shear Spectra.** Velocity profiles are stretched and amplitude normalized according to WKB theory using the time averaged buoyancy frequency profile prior to shear spectra calculations. The spectra have been corrected at high wavenumbers for vertical smoothing. Four wavenumber bands are plotted. Approximate 95% confidence limits scale with frequency smoothing. (a) contains downward CCW propaging energy. (b) contains downward CW propaging energy. (c) contains upward CW propaging energy. (d) contains upward CCW propaging energy.

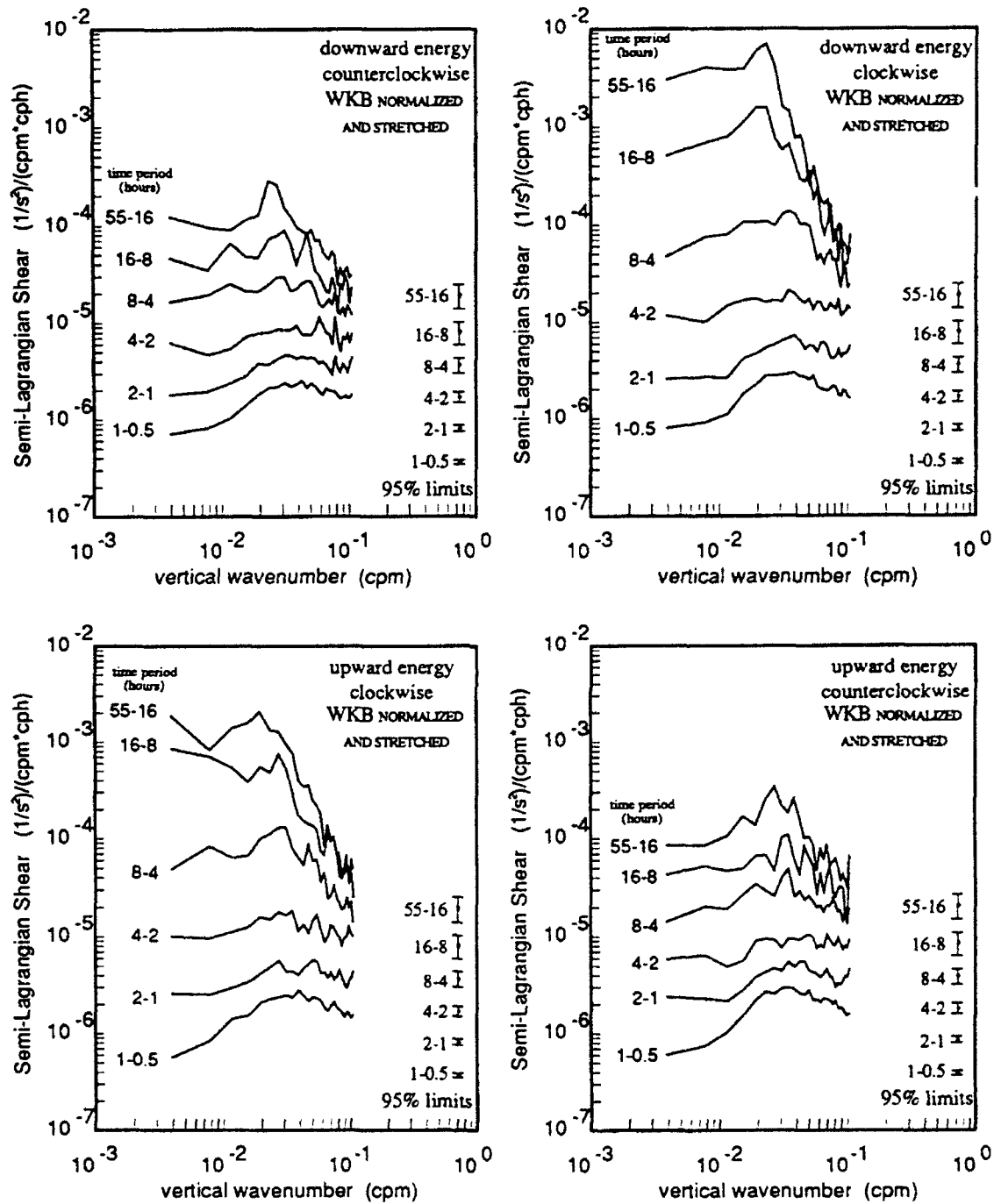


**Figure 2.18** WKB Semi-Lagrangian Rotary Shear Spectra. Same as Figure 2.17 except semi-Lagrangian velocity profiles are used.

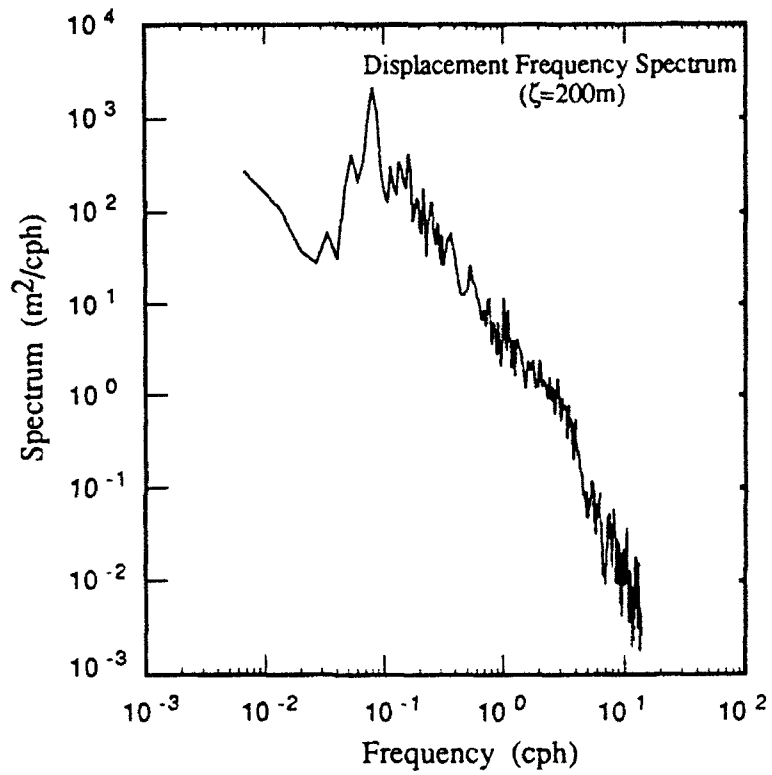


**Figure 2.19 Displacement Frequency Spectrum.** The displacement of an isopycnal whose mean depth is 200m is tracked for 15 days. Shown is the displacement frequency spectrum. The spectrum has been smoothed in frequency above 1.0 c.p.h. The spectrum has a peak at the semi-diurnal tidal frequency, has a slope of  $\omega^{-2}$  down to the buoyancy frequency cutoff at  $\sim 4.0$  c.p.h.

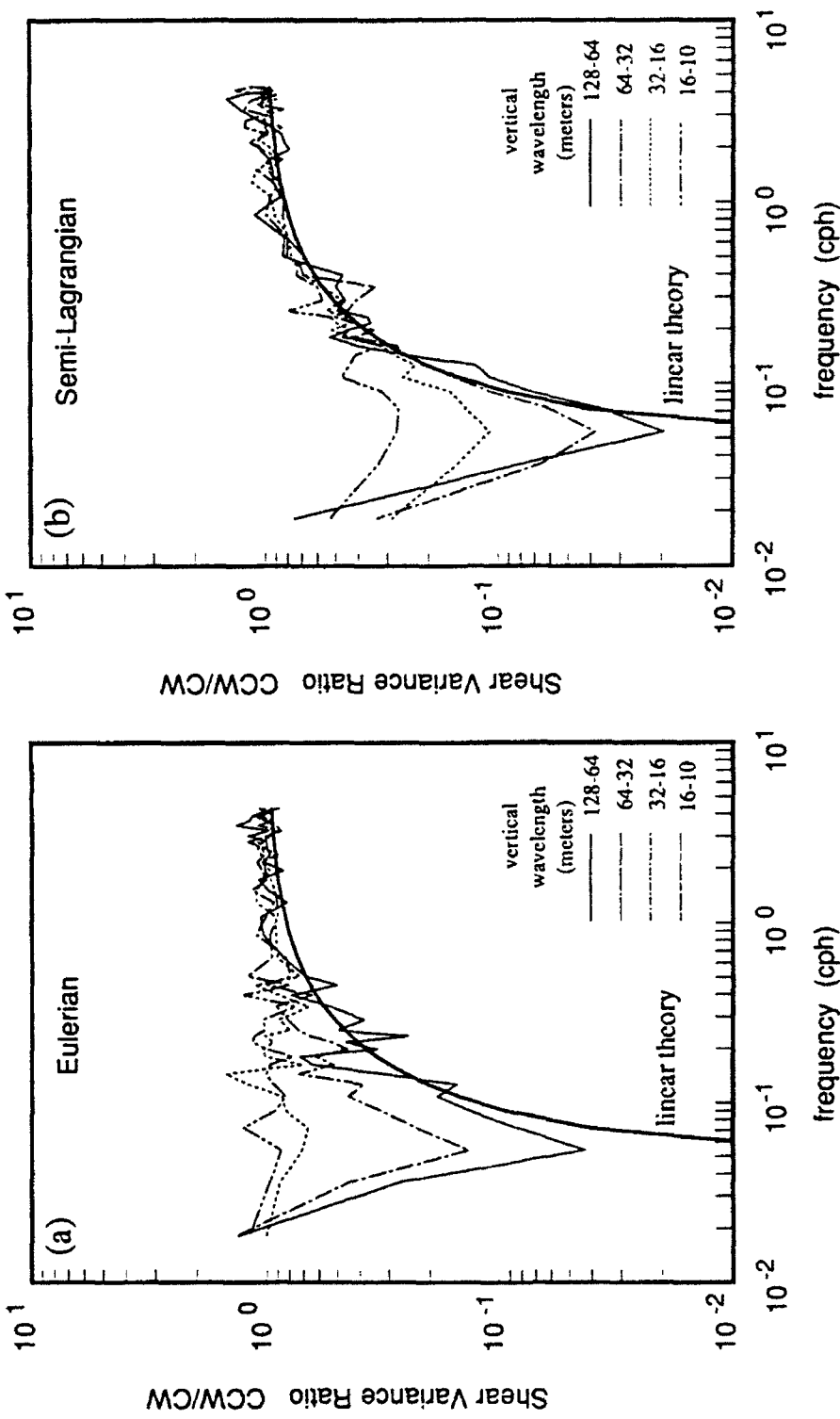


**Figure 2.20 Measured CCW to CW Shear Variance Ratio.** The ratio of counterclockwise (CCW) to clockwise (CW) shear variance found in the rotary shear spectra is plotted. The heavy line is predicted CCW/CW variance ratio using linear theory. (a) measured Eulerian CCW/CW shear ratio averaged over 4 wavenumber bands. (b) measured Semi-Lagrangian CCW/CW shear ratio averaged over 4 wavenumber bands.

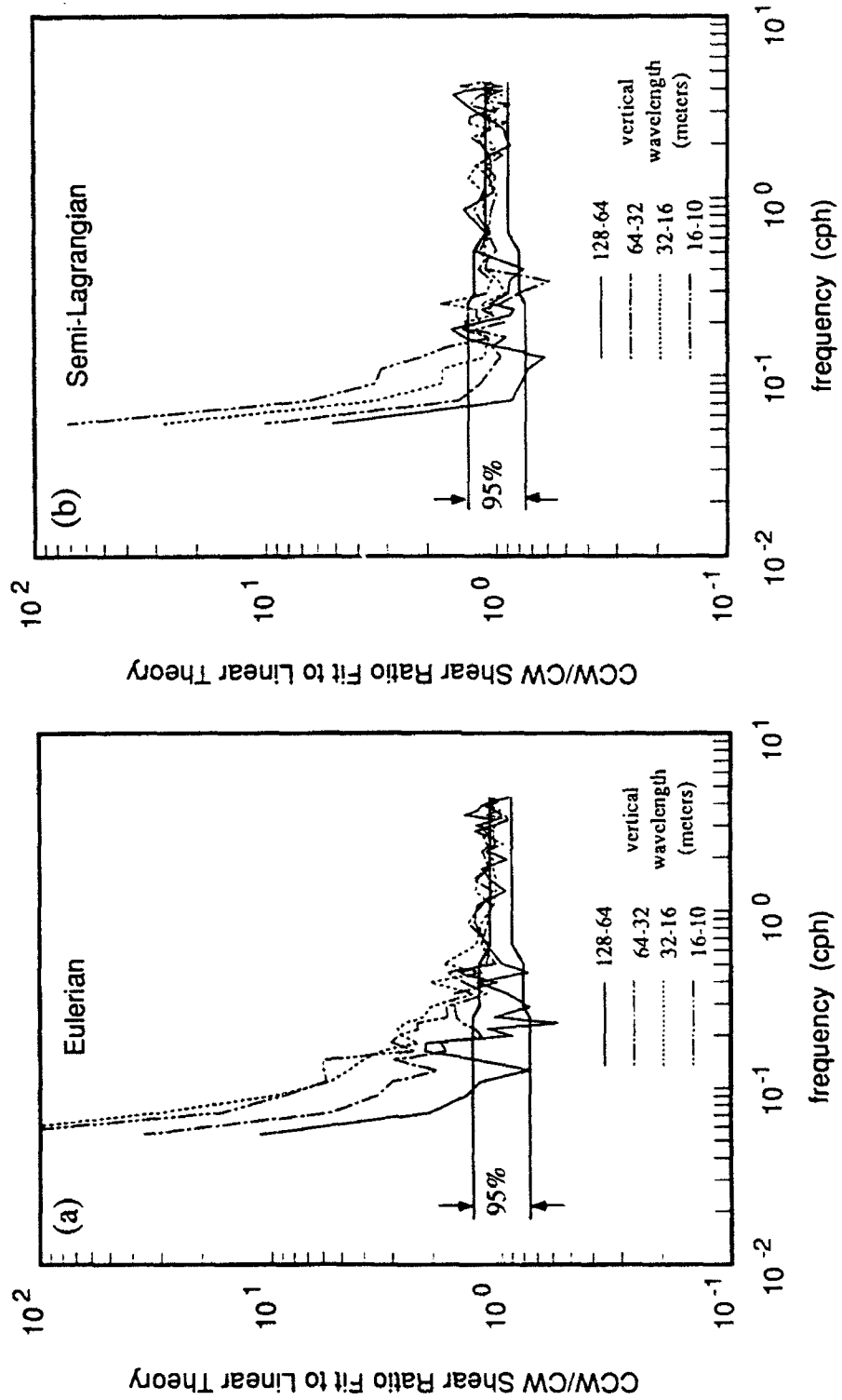


**Figure 2.21 Measured CCW to CW Shear Ratio Fit to Linear Theory.** The ratio of counterclockwise (CCW) to clockwise (CW) shear variance found in the rotary shear spectra normalized by that expected from linear theory is plotted. (a) normalized Eulerian CCW/CW shear ratio averaged over 4 wavenumber bands. (b) normalized Semi-Lagrangian CCW/CW shear ratio averaged over 4 wavenumber bands. Approximate 95% confidence interval for the longest wavelength band is drawn around 1.0 and tapers towards higher frequencies due to frequency smoothing.

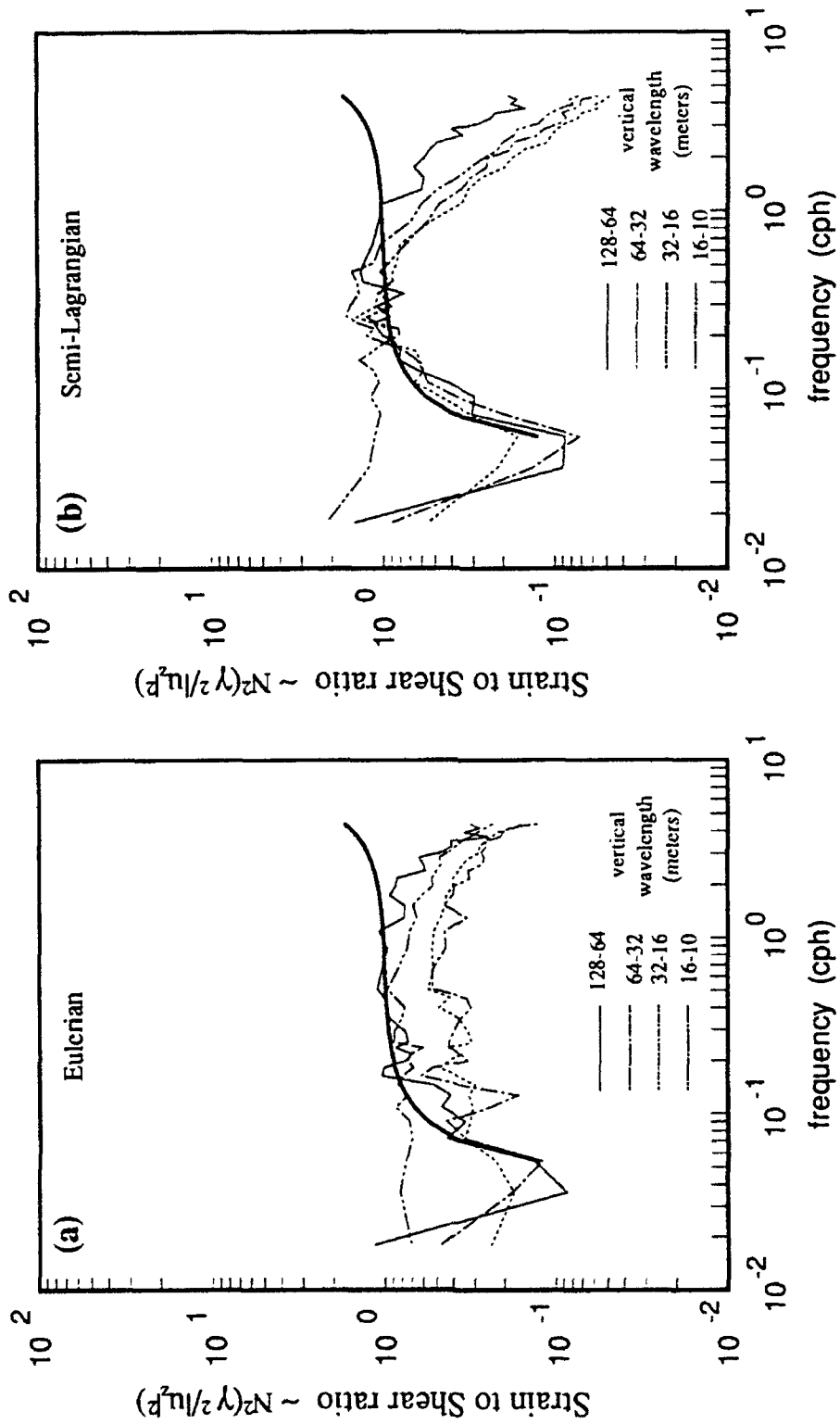


**Figure 2.22 Measured Strain to Shear Variance Ratio.** The ratio of measured strain variance to measured shear variance normalized by the average buoyancy frequency ( $N=6.15$  cph). The heavy line is predicted strain to shear ratio using linear theory. (a) measured Eulerian strain shear ratio averaged over 4 wavenumber bands. (b) measured Semi-Lagrangian strain to shear ratio averaged over 4 wavenumber bands.

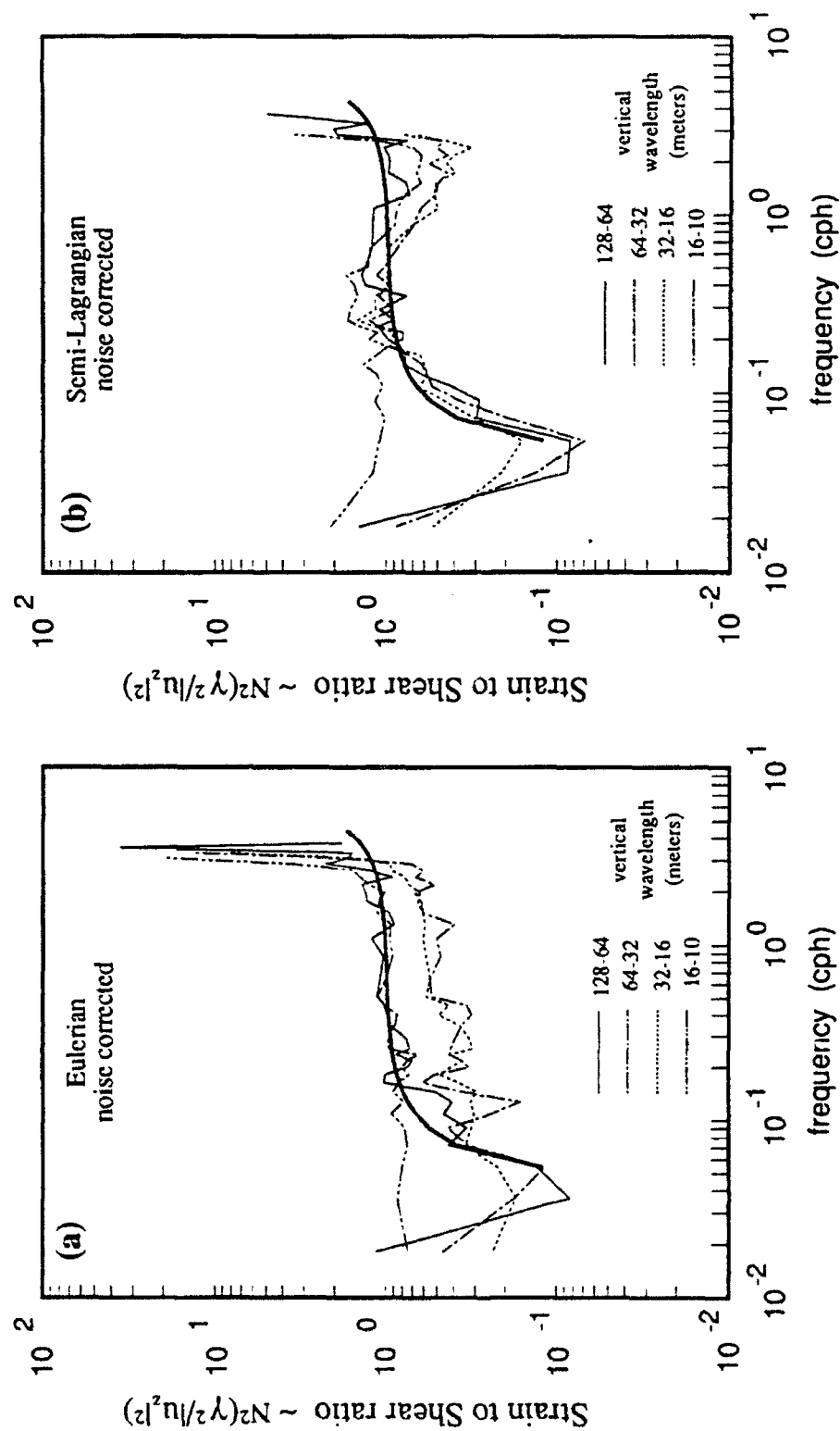


**Figure 2.23 Noise Corrected Strain to Shear Ratio.** Same as Figure 2.22 except that an assumed white noise frequency spectrum has been subtracted from each shear spectrum wavenumber band before calculating the strain to shear ratio. Removal of the noise decreases the shear variance at high frequencies (>0.4 cph) and measured Semi-Lagrangian strain to shear ratio is more closely approximated by linear theory.

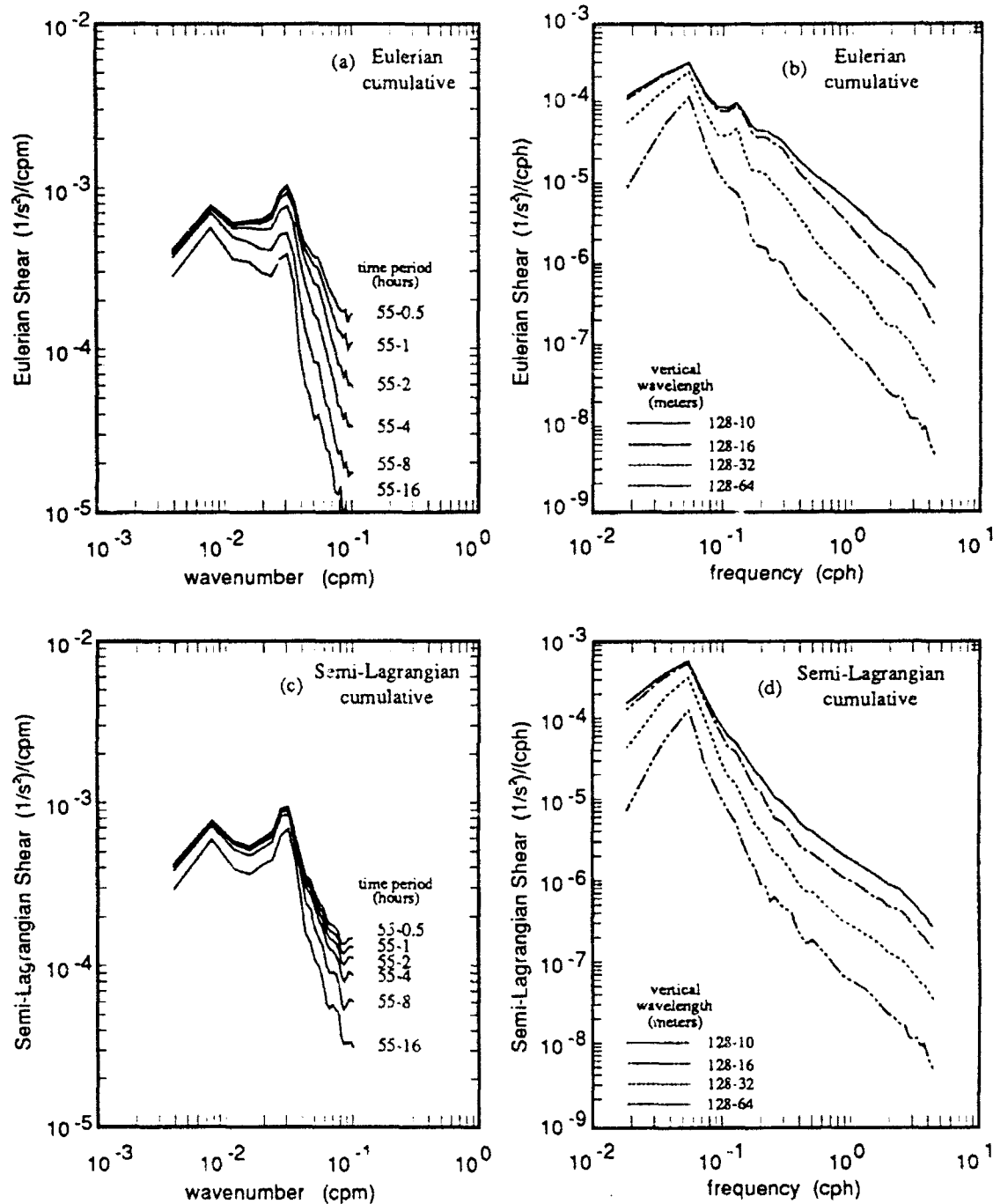


**Figure 2.24 Eulerian and Semi-Lagrangian Cumulative shear spectra.** Vertical wavenumber-frequency shear spectra are integrated from low frequency to successively higher frequency and plotted for (a) Eulerian shear and (c) semi-Lagrangian shear. Vertical wavenumber-frequency shear spectra are integrated from low wavenumber to successively higher wavenumber and plotted for (b) Eulerian shear and (d) semi-Lagrangian shear.

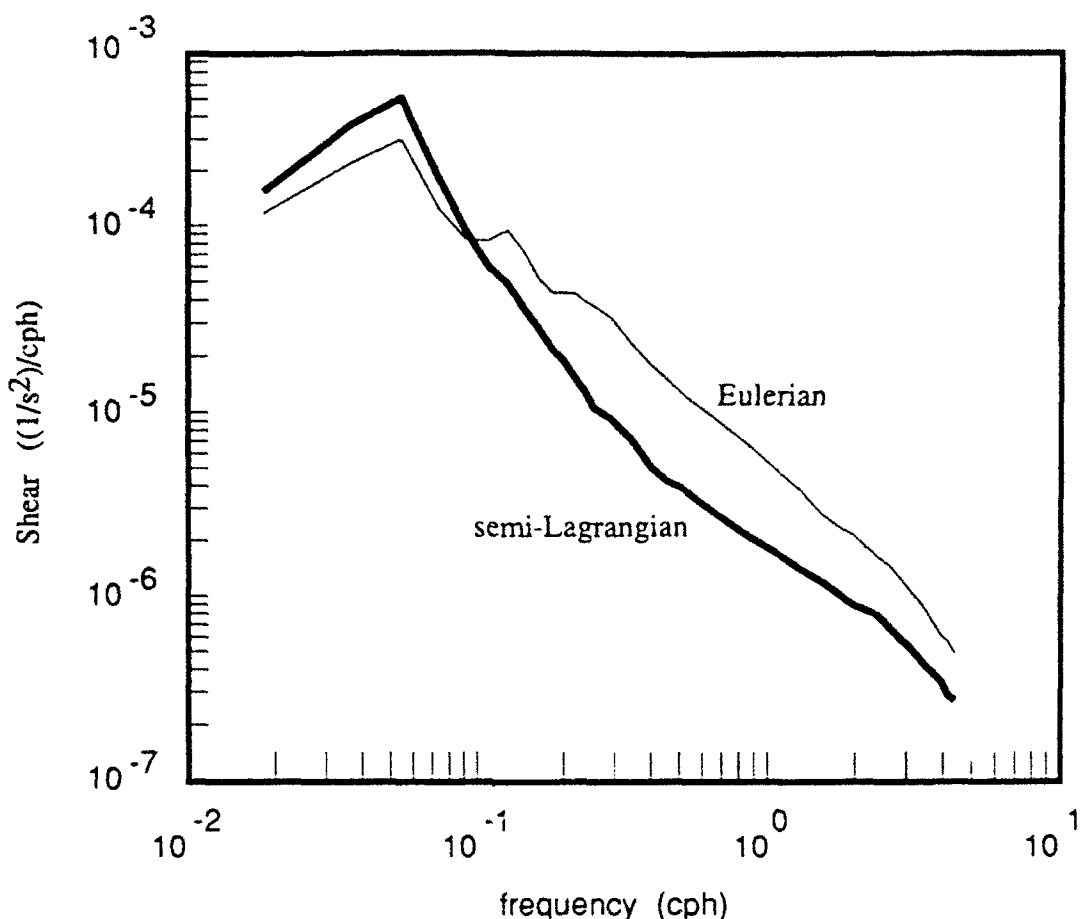


**Figure 2.25 Shear Frequency Spectrum.** Eulerian and semi-Lagrangian shear frequency spectra are found for the vertical wavenumber band [0.0078-0.1] c.p.m. The almost twice the variance is found in the semi-Lagrangian near inertial band than in the Eulerian. A super tidal peak is observed in the Eulerian spectrum and at higher frequencies more variance is found in the Euierian spectrum. Vertical advection has Doppler shifted waves with near inertial intrinsic frequency leading to contamination of the Eulerian frequency spectrum.

## Chapter 3

### Thermohaline Finestructure

#### 3.1. Introduction

In this chapter the fine scale vertical structure of temperature and salinity associated with an oceanic frontal zone is examined. An oceanic front is a boundary between two water masses with different thermohaline characteristics. Fronts play an important role in the transformation of mesoscale inhomogeneities into thermohaline finestructure. Intrusive layers (a layer of one water type surrounded by water with different thermohaline characteristics) as well as temperature and salinity inversions are commonly observed in thermohaline fine structure near oceanic fronts (Horne, 1978; Georgi, 1978; Joyce et al. 1978; Posmentier and Houghton, 1978, Fedorov, 1986). The formation of finestructure is an important process since the interleaving of the two water masses acts as stirring which enlarges the surface area between the two water masses and thus enhances cross frontal fluxes.

There are two driving mechanisms for interleaving near a frontal zone. Horizontal advection by internal waves may move a water parcel from one side of the front to the other. If horizontal temperature gradients are strong enough, this may lead the salinity or temperature inversion and double diffusive instabilities. Turner (1978) observed in laboratory models that double diffusion alone can drive interleaving at the interface of two water masses with different thermohaline characteristics.

The advection of a frontal zone past the SWAPP site during the operation of the CTD system provides a unique opportunity to study the finestructure associated with the front. The MPL rapid profiling CTD system profiles from the surface to 420 m every 130 seconds during yeardays 60 to 75, 1990 (Appendix C). The data are examined here in the context of traditional fine scale frontal analysis. The data are lacking in that they are only a time series, not a survey, and spatial gradients are not directly known. They are estimated by time integrating velocity data from the MPL 161 kHz Doppler sonar system. The time resolution of the CTD data allows the tracking of intrusive layers in isopycnal coordinates. The front is examined for a geostrophic balance by comparing geopotential anomalies to velocity shears from the Doppler sonar. Intrusions are tracked by removing the mean temperature and salinity on isopycnals yielding a depth/time series of thermohaline anomalies.

### 3.2. Description of Data

An XBT survey of the waters surrounding the SWAPP experiment site, taken on yearday 55, 1992 (see Appendix A), reveals a front in the 200 to 400 meter depth range. The front is initially located to the northwest of FLIP's location and is characterized by warm water to the southeast and cold water to the northwest. This is the only spatial survey available of the deep frontal structure. Sea surface temperature estimates from satellite data were limited by cloud cover and the surface water temperatures do not appear correlated with the deep water. The SWAPP experiment was not originally designed to be a study of local hydrographic features. However, the data from the lower of the two CTD's in operation provides a detailed observation of frontal structures as the water masses are advected past the experiment site. The rapid profiling CTD system provides a time series consisting of 9200 profiles from 200 to 420 meters with a cycle period of 130 seconds and was in operation from yearday 60 to 75.

The CTD profiles clearly show two different water masses. A scatter plot of temperature and salinity (Figure 3.1) from 200 to 420 m reveals a clustering of data points along two different characteristic T-S lines. Few data points are found to lie near the cruise averaged T - S curve. A picture of the frontal structure can be formed by tracking the temperature along an isopycnal in depth and time (Figures 3.2 and 3.3). It is useful at this point to divide the time series into three segments. The first segment contains yeardays 60 to 66 (drop numbers 0 to 3750). It is characterized by warmer and saltier water than average. The water mass is relatively free from intrusions except for a small intrusion of cold water that is found below 350 meters from day 60 to 63. The temperature (and salinity) along all the isopycnals slowly decreases in time. The second segment contains yeardays 66 to 70 (drop numbers 3750 to 6250). It is characterized by a rapid drop in temperature (and salinity) along isopycnals. The deepest isopycnals ( $420 > \bar{z} > 300$  m) continually decrease in temperature during this time while the shallower isopycnals ( $300 > \bar{z} > 200$  m) go from cold to warm to cold. Many temperature inversions occur at all depth ranges. The third segment contains yeardays 70 to 75 (drop numbers 6250 to 9500) and is characterized by colder and fresher water than average at all depth ranges. Many temperature inversions can still be seen. The temperature change along an isopycnal increases with depth and thus the average vertical gradients of temperature and salinity are larger at end of the experiment than at the beginning.

Estimating the horizontal gradients of temperature and salinity across the front can be done in two ways. The XBT survey revealed a horizontal temperature gradient in the 200-400 meter depth range (Appendix A). The estimated cross frontal temperature gradient is  $1.85 \times 10^{-5}$  °C/m. Assuming that the cross frontal density gradient is small, the salinity gradient can be estimated by

$$\frac{d\bar{S}}{dy} = \frac{\alpha}{\beta} \frac{dT}{dy} \quad (3.1)$$

where

$$\beta = \rho_o^{-1} \frac{\partial \rho}{\partial S} \Big|_{T,p} ; \quad \alpha = \rho_o^{-1} \frac{\partial \rho}{\partial T} \Big|_{S,p}$$

and  $y$  is the across front coordinate.  $\alpha$  and  $\beta$  are nearly constant from 200 to 420 meter and are equal to  $\alpha = 1.508 \times 10^{-4} \text{ } ^\circ\text{C}^{-1}$  and  $\beta = 7.712 \times 10^{-4} \text{ } \text{‰}^{-1}$ . Using (3.1), estimated salinity gradient is  $3.62 \times 10^{-6} \text{ } \text{‰}/\text{m}$ . This method may underestimate the horizontal gradients due to the low spatial resolution of the survey.

The second method is to compare a time series of temperature on an isopycnal with the time integrated velocity field. The temperature and salinity on three isopycnals with average depths of 250, 300 and 350 m are tracked (Figure 3.3). Between yeardays 66 and 68, the temperature and salinity decrease by approximately  $0.425^\circ\text{C}$  and  $0.0825 \text{ ‰}$  on the 300m isopycnal. The largest temperature change occurs on the deepest isopycnal which continues to decrease until yearday 70. The vertical temperature gradient becomes larger on the cold side of the front. The horizontal range of temperatures measured is still not as large as that seen in depth averaged temperatures from the XBT survey due to the temperature gradient change. The horizontal displacement is found by time integrating the depth averaged velocity from the 161 kHz sonar (Figure 3.4). The resulting trajectory assumes the velocities result from a frozen ocean moving past an anchored FLIP. The depth averaged velocities are dominated by a current of nearly 9 cm/s flowing towards the east. Using the displacement from yearday 66.7 to 67.2 ( $\sim 7.1 \text{ km}$ ) yields temperature and salinity gradients of  $5.27 \times 10^{-5} \text{ } ^\circ\text{C}/\text{m}$  and  $1.03 \times 10^{-5} \text{ } \text{‰}/\text{m}$ . It is unlikely that the velocity field is perpendicular to the front, so the width of the front is overestimated. Even though these cross frontal gradients are larger than those estimated from the XBT survey, they may still be smaller than the true cross frontal gradients.

### 3.3. Geopotential Anomalies

Often oceanic fronts are characterized by a horizontal density gradient across the front and an associated geostrophic velocity balance. Since no spatial survey was conducted of the potential density field, the only clue of a geostrophic balance comes from a time series of geopotential anomaly,  $\Phi'$ . The geopotential anomaly at some pressure,  $p$ , is defined by

$$\Phi' = - \int_0^p \delta \, dp \quad (3.2)$$

where the specific volume anomaly,  $\delta$ , is defined in terms of the specific volume,  $v_s$ ,

$$\delta = v_s(S, T, p) - v_s(35, 0, p). \quad (3.3)$$

Geopotential anomalies over four 100 meter depth ranges ([0-100], [100-200], [200-300], [300-400]) are found using hour averaged density profiles (Figure 3.5). The signal at all

depth ranges is dominated by the semi-diurnal internal tide vertically advecting the mean density profile. This tidal signal can be removed by time averaging  $\Phi'$ . Geopotential anomalies in the 0 to 100 meter depth ranges are much too large to be accounted for by a geostrophic balance and are likely due to local mixed layer dynamics. The [100-200]m water gets steadily more dense with time, the [200-300]m water does not have any net change in density across the front and the [300-400]m water gets steadily more dense with time. Thus the cold, fresh water encountered at the end of the experiment is more dense than the warm, salty water found at the same depths at the beginning of the cruise.

It is useful to estimate the geostrophic flow needed to support such a horizontal pressure gradient. The geostrophic velocity at pressure  $p_1$  relative to the velocity at  $p_2$  is calculated by

$$v_g(p_1) - v_g(p_2) = f^{-1} \frac{\partial}{\partial x} \{ \Phi'(p_1) - \Phi'(p_2) \}, \quad (3.4)$$

$$u_g(p_1) - u_g(p_2) = -f^{-1} \frac{\partial}{\partial y} \{ \Phi'(p_1) - \Phi'(p_2) \}. \quad (3.5)$$

where  $x$  and  $y$  are the east and north coordinates and  $u$  and  $v$  are the east and north velocity components. Using the time series of  $\Phi'$ , the magnitude of the relative velocity is estimated by

$$|v_{400} - v_{300}| = \frac{1}{f|\Delta X|} [(\Phi_{400}(t_2) - \Phi_{300}(t_2)) - (\Phi_{400}(t_1) - \Phi_{300}(t_1))] \quad (3.6)$$

where the  $\Delta X$  is the time integrated current trajectory determined by

$$\Delta X = \frac{-\int_{t_1}^{t_2} \mathbf{u} dt}{(t_2 - t_1)} \quad (3.7)$$

The depth average velocity vector,  $\mathbf{u}$ , is determined using velocity profiles obtained from the MPL 161 kHz sonar (Appendix E). Velocity estimates are averaged over 6.5 minutes in time and 100 to 350 meters in depth and integrated in time to get  $\Delta X$  (Figure 3.4). The velocities are dominated by an eastward flowing current of nearly 9 cm/sec from yearday 63 to yearday 73. The northward component of velocity changes direction on yearday 68. The total estimated displacement from yearday 63 to 73 is 85 km to the west with negligible southward displacement. The net change in geopotential anomaly from yearday 63 to 73 is approximately  $0.120 \text{ m}^2/\text{s}^2$  for  $[\Phi_{200} - \Phi_{100}]$ ,  $-0.0 \text{ m}^2/\text{s}^2$  for  $[\Phi_{300} - \Phi_{200}]$  and  $-0.024 \text{ m}^2/\text{s}^2$  for  $[\Phi_{400} - \Phi_{300}]$ . Since the total displacement is towards the west, the northward component of the current is calculated using (3.6). The geostrophic velocity at 100 m relative to 200 m is 1.7 cm/s northward, at 200 m relative to 300 m is 0.0 cm/s northward and at 300 m relative to 400 m is 0.4 cm/s southward. For

comparison, the northward component of sonar estimated currents at 100 m, 200 m, and 300 m are averaged from yearday 63 to 73. The mean velocity difference is 2.03 cm/s between 100 and 200 m and 0.03 cm/s between 200 and 300 m. These are consistent with the estimated geostrophic velocity calculations. Fedorov (1986) says that small-scale fronts are likely to be exceptions to geostrophic balance. Fedorov refers to this as "semi-geostrophic" phenomena and is the result of mesoscale forcing leading to the front formation (frontogenesis). Nothing is known about the history of this front but the northward component of velocity appears to be in geostrophic balance. Without a north/south section, it can not be determined if the strong eastward current observed is in a geostrophic balance.

### 3.4. Vertical Interleaving

Typical finestructure thermohaline profiles from the lower CTD reveal many temperature and salinity inversions on scales of 3 to 20 meters (Figure 3.6). Temperature and salinity inversions are matched such that the resulting density profile is hydrostatically stable. The energy stored in the inversions is released through double diffusive mixing processes.

The difference in the molecular diffusivity between salt and heat in the ocean which has a significant effect on vertical fluxes when both salinity and temperature increase or decrease with depth. The energy driving these fluxes comes from the thermohaline property that has a destabilizing effect on the density gradient. The diffusive case occurs when temperature and salinity increase with depth. It is characterized by convective layers and by more heat flux than salt flux through the layer. The salt fingering case occurs when temperature and salinity decrease with depth. It is characterized by intrusive 'fingers' propagating vertically across the interface with vertical salt fluxes dominating heat fluxes. The potential for one of these processes to take place is quantified by the density ratio

$$R_p = \frac{\alpha \frac{\partial T}{\partial z}}{\beta \frac{\partial S}{\partial z}} \quad (3.8)$$

or the Turner angle

$$Tu = \tan^{-1} \left( \frac{\alpha T_z - \beta S_z}{\alpha T_z + \beta S_z} \right) = \tan^{-1}(R_p) - 45^\circ. \quad (3.9)$$

where  $T$  is the temperature,  $S$  is the salinity and  $z$  is the vertical coordinate. The two cases are then described by

$$\left. \begin{array}{l} 0 \leq R_p \leq 1 \\ -90^\circ \leq Tu \leq -45^\circ \end{array} \right\} \rightarrow \text{Diffusive}$$

$$\left. \begin{array}{l} 1 \leq R_p \\ 45^\circ \leq Tu \leq 90^\circ \end{array} \right\} \rightarrow \text{Fingers.}$$

A typical profile of  $Tu$  reveals that much of the water column (200-420m) is subject to double diffusive processes (Figure 3.7).

The percent of the water column that is subject to salt fingering ( $Tu > 45^\circ$ ) is typically twice as large as the percentage of the water column that is subject to diffusive convection ( $Tu < 45^\circ$ ) (Figure 3.8). During the first part of the time series (yeardays 60 to 65), diffusively unstable water occurs less than 3% of the time, whereas fingering occurs in 10% to 20% of the time. On yearday 65 occurrences of temperature and salinity inversion increases dramatically. This increase takes place before the large isopycnal temperature drop that takes place at yeardays 66 to 67 (Figure 3.3). The incidents of temperature and salinity inversions reach a maximum at the time of the large temperature drop (yeardays 66-67) and again at yearday 69 when the isopycnals in the 200 to 300 meter depth range warm up for a half a day. As much as 50% of the water column from 200 to 420 meters is double diffusively unstable. After yearday 70, the percentage of temperature inversions decreases to 5% then slowly rises to 10% at yearday 75 and the percentage of salinity inversions stays large at 30% to 35%.

The likely cause for the large number of temperature and salinity inversions cross frontal advection. With the small vertical mixing rates typically found in the ocean interior, these intrusions can carry some of the thermohaline characteristics of their source waters for a long time. This may be why the number of inversions rises before the actual front is encountered. There are two kinematic effects which would cause the horizontal displacement of water parcels across a front. The first is horizontal velocities from the internal wave field. The second is horizontal intrusions or noses that are driven by the vertical flux of heat and salt by double diffusion. To study the intrusions and possible driving mechanisms, the salinity and temperature signals associated with mesoscale as well as internal wave advection and straining must be removed leaving just the finestructure thermohaline anomalies associated with the intrusions.

Following Joyce (1977) and Fedorov (1986), three scales are considered to resolve the finestructure thermohaline anomalies. Thus any scalar quantity,  $\phi$ , is described by

$$\phi = \bar{\phi} + \tilde{\phi} + \phi' \quad (3.10)$$

where

$$\bar{\phi} = \tilde{\phi}' = 0$$

The overbar denotes the mean field and is associated with the large (mesoscale) features. The tilde indicates those fine scale fluctuations associated with vertical interleaving which are anisotropic. The accent denotes the micro scale fluctuations associated with dissipation which are turbulent and isotropic in nature. Temperature and salinity anomalies,  $\tilde{T}$  and  $\tilde{S}$ , are determined by removing the cruise averaged mean temperatures and salinity,  $\bar{T}$  and  $\bar{S}$  (Figures 3.9 and 3.10). To eliminate the effects of vertical advection due to internal waves,  $\tilde{T}$  and  $\tilde{S}$  are found as functions of potential density using a cubic fit to the cruise average. The cruise averaged functions used are

$$\bar{T}(\sigma_i) = a_3(26 - \sigma_i)^3 + a_2(26 - \sigma_i)^2 + a_1(26 - \sigma_i)^1 + a_0 \quad (3.11)$$

$$\bar{S}(\sigma_i) = b_3(26 - \sigma_i)^3 + b_2(26 - \sigma_i)^2 + b_1(26 - \sigma_i)^1 + b_0 \quad (3.12)$$

where

$$a_0 = 8.5861; a_1 = 4.285; a_2 = -12.72; a_3 = 5.438;$$

$$b_0 = 33.491; b_1 = 2.143; b_2 = -2.651; \text{ and } b_3 = 1.264.$$

The scale of the turbulent fluctuations is not resolved by the CTD. Thus, the turbulent fluctuations are assumed to be zero. The temperature and salinity anomalies,  $\tilde{T}$  and  $\tilde{S}$ , are then determined for each hydrographic profile by

$$\tilde{T}_n(z) = T_n(z) - \bar{T}(\sigma_{i,n}(z))$$

and

$$\tilde{S}_n(z) = S_n(z) - \bar{S}(\sigma_{i,n}(z))$$

where  $T_n$ ,  $S_n$ , and  $\sigma_{i,n}$  and the temperature, salinity and density profiles for profile number  $n$ . This technique uses density as a semi-Lagrangian coordinate to remove the effects of internal wave vertical advection and straining leaving only the temperature and salinity signals associated with intrusions of different water masses.

Horizontal displacement, due to internal waves, of water parcels from two different water masses is a possible cause of vertical interleaving near a front. Joyce et al. (1978) and Georgi (1978) relate the intrusion temperature signal,  $\tilde{T}$ , to the horizontal displacement across the front by internal waves and the horizontal temperature gradient. This relationship can be written in vertical wavenumber frequency space as

$$\tilde{T}(\omega, m) = \frac{\partial \bar{T}}{\partial y} \frac{\hat{V}(\omega, m)}{i\omega} \quad (3.13)$$

where  $y$  is the cross frontal coordinate and  $\hat{V}$  is the cross frontal velocity. An upper bound on the vertical wavenumber spectrum of  $\tilde{T}$  is found by assuming the velocity variance is at the inertial frequency. The vertical wavenumber spectrum of  $\tilde{T}$  is then

$$\begin{aligned}\Phi_{\tilde{T}}(m) &\leq f^{-2} \left( \frac{\partial \bar{T}}{\partial y} \right)^2 \Phi_{\hat{V}}(m) \\ &\leq (4.9 \times 10^{-2} \text{ } ^\circ\text{C}^2 / (\text{m/s})^2) \Phi_{\hat{V}}(m)\end{aligned}\quad (3.14)$$

where  $\Phi_{\tilde{T}}$  is the spectrum of  $\tilde{T}$  and  $\Phi_{\hat{V}}$  is the spectrum of  $\hat{V}$ . Since the internal wave field is nearly horizontally isentropic, the velocity spectrum can be calculated from one component of velocity estimated from the 161 kHz Doppler sonar system (Appendix E). The velocity spectrum is determined using 6.5 minute averaged Eulerian east velocity, from depths 50 to 306 meters and ensemble averaged from yeardays 63 to 78. For comparison, the temperature anomaly spectrum (instantaneous temperature minus the strain corrected, mean temperature profile) from depths 200-420 meters is ensemble averaged from yeardays 60 to 75. Since internal wave velocities should scale with buoyancy frequency, a velocity spectrum calculated from shallower depths will over estimate the velocity variance at 200-420 m. Comparing the temperature anomaly spectrum and the velocity spectrum reveals that internal wave horizontal advection can only account for up to 5% of the total observed temperature anomaly signal (Figure 3.11). This calculation is sensitive to the horizontal temperature gradient estimate. If the true gradient is twice as large as the estimated gradient, displacements from internal waves could still account for only 20% of the temperature variance. Thus, the internal wave field is not strong enough to account for the observed interleaving unless the horizontal gradients are much larger than estimated. This is the same conclusion reached by Joyce et al. (1978) and Georgi (1978).

Since the vertical interleaving is not a result of internal waves advection, it is suggested that the interleaving is double diffusively driven. The potential for the double diffusive processes to occur has been shown, but no direct measurements of salt fingering or diffusive convection were made. Two typical features of double diffusively active intrusions can be compared to observations for consistency. These are the expected vertical scale of the intrusion and the slope of the intrusion across isopycnals.

Ruddick and Turner (1979) used a laboratory model to study mixing at an oceanic front across which there are large T-S anomalies but a small net horizontal density difference. They found that the vertical scales of the intrusions formed is directly proportional to the horizontal concentration gradient and inversely proportional to the vertical density gradient. They conclude that the vertical length scale of cross-frontal intrusions,  $H$ , can be determined to within a factor of two by

$$H = \frac{3}{2}(1-n) \frac{\beta \Delta \bar{S}}{\frac{1}{\rho} \frac{d\rho}{dz}} \quad (3.15)$$

where  $n$  is the density flux ratio (0.56 for heat/salt fingers),

$\Delta\tilde{S}$  is the salinity contrast measured across the front along an isopycnal,  
 $\frac{1}{\rho} \frac{d\rho}{dz}$

is the vertical density gradient and  $\beta = \frac{1}{\rho} \frac{\partial \rho}{\partial S}$ .

Ruddick and Turner (1979) successfully predict historical intrusion scales near frontal zones. Using the mean density gradient from 200 to 400 meters ( $2.36 \times 10^{-6} \text{ m}^{-1}$ ) and the salinity change across the front, the expected vertical length scale of the intrusions from (3.15) is 17.8 m.

Toole and Georgi (1981) contend that it is incorrect to extrapolate the laboratory results of Ruddick and Turner (1979). Their argument is that in the laboratory, the interleaving takes on the same vertical scales as the salt fingers suggesting the intrusion scale is determined by the energy in the salt fingering. In the ocean, the expected scales of the interleaving is much larger than the vertical scale of the salt fingers (which may be as large as 1 m (Williams, 1975)) and thus are unimportant to the behavior of large intrusions.

Toole and Georgi (1981) use linear stability analysis of intrusions in a frontal zone and look for the fastest growing mode. Their model predicts the fastest growing mode as a function of lateral salinity gradient, the vertical density gradient of the mean field, the vertical viscosity, haline diffusivity and flux and the local value of the Coriolis acceleration. The model uses the dimensionless salinity gradients,  $\varepsilon_x$  and  $\varepsilon_y$ , and vertical wavenumber,  $m$ , defined by

$$\varepsilon_x = \frac{(1 - \gamma)g\beta\tilde{S}_x}{N^2} \quad (3.16)$$

$$\varepsilon_y = \frac{(1 - \gamma)g\beta\tilde{S}_y}{N^2} \quad (3.17)$$

$$m^2 = \hat{m}^2 \frac{A^s}{N} \quad (3.18)$$

where  $\gamma$  is the ratio of the buoyancy contributions of the heat and salt fluxes,  $A^s$  is the haline vertical eddy diffusivity and  $\hat{m}$  is the vertical wavenumber with dimensions  $\text{m}^{-1}$ . The fastest growing wavenumber is given by

$$f(\varepsilon_z) = \frac{m_z^2 \sigma^{\frac{1}{2}}}{\varepsilon_z} \quad (3.19)$$

where  $f(\varepsilon_z)$  is obtained from Fig. 7. in Toole and Georgi (1981) and  $\sigma$  is the ratio of the haline to density vertical eddy diffusivities. Unlike the model of Ruddick and Turner (1979) which assumes a step function in salinity across the front, Toole and Georgi (1981) use the horizontal salinity gradient which is not well known for the SWAPP

experiment. Only the lower bound on the horizontal salinity gradient is known. The gradients

$$\begin{aligned}\beta\bar{S}_x &= 7.94 \times 10^{-9} \text{ m}^{-1}, \\ \beta\bar{S}_z &= -9.25 \times 10^{-7} \text{ m}^{-1} \text{ and} \\ N &= 5.24 \times 10^{-3} \text{ s}^{-1}\end{aligned}$$

and the constants suggested by Toole and Georgi (1981)

$$\begin{aligned}A^* &= 1.0 \times 10^{-4} \text{ m}^2/\text{s} \\ \sigma &= 0.1 \\ A^s &= \sigma A^* = 1.0 \times 10^{-3} \text{ m}^2/\text{s} \\ \gamma &= 0.6\end{aligned}$$

are used to obtain dimensionless variables

$$\begin{aligned}\varepsilon_x &= 1.13 \times 10^{-3}, \\ \varepsilon_z &= -1.32 \times 10^{-1} \text{ and} \\ f(\varepsilon_z) &= 0.6.\end{aligned}$$

Solving for the dominate vertical wavelength of the intrusions yields.

$$H = \frac{2\pi}{\hat{m}_c} = 2\pi\sigma^{\frac{1}{2}} \left( \frac{A^s}{\varepsilon_x f(\varepsilon_z) N} \right)^{\frac{1}{2}} = 58 \text{ meters.} \quad (3.20)$$

This vertical scale is more than twice as large as those estimated using Ruddick and Turner. There are two parameters in question when using the Toole and Georgi (1981) interleaving model which may lead to this overestimation. The first is the cross frontal salinity gradient which may be underestimated. The second is the vertical eddy diffusivity,  $A^*$ . Measurements taking by Gregg (1989) suggest that  $A^*$  may be as small as  $5 \times 10^{-6} \text{ m}^2/\text{s}$ . Using

$$A^* = 1 \times 10^{-5} \text{ m}^2/\text{s},$$

the Toole and Georgi (1981) model yields a vertical intrusion scale of

$$H = 18.3 \text{ meters.}$$

This scale is nearly the same as the 17.8 meter scale predicted by the model of Ruddick and Turner (1979) in spite of the complaint by Toole and Georgi (1981).

The observed intrusion scales are estimated using vertical wavenumber spectra. Half day ensemble averaged spectra are calculated for  $\tilde{T}$  and  $\tilde{S}$  over the depth range 220 to 420 meters using triangle windowing on two overlapping 128 meter depth segments (Figure 3.13). These are converted to gradient spectra by multiplying by  $(2\pi m)^2$ , where  $m$  is the vertical wavenumber, and corrected for high wavenumber smoothing by the finite CTD resolution. The temperature and salinity anomaly variance fluctuates

throughout the cruise (Figure 3.12) reaching a maximum on yearday 68. The spectra from the half day averages corresponding to the times of maximum (yearday 62-62.5) and minimum (yearday 68.5-69) variance are plotted along with the 15 day averaged spectrum for comparison (Figure 3.14). The cruise average spectra are nearly white out to 0.1 cpm and then fall off slightly out to 0.7 c.p.m. The minimum variance spectrum is red at all wavenumbers except for a slight rise at 0.2 c.p.m. The maximum spectrum rises out to 0.1 c.p.m. then falls off at higher wavenumber. The maximum spectrum has excess variance in the wavenumber band [0.05-0.2] c.p.m. while the minimum spectrum lacks variance in the same band relative to the mean. The expected wavelength of the intrusions, as predicted by Ruddick and Turner (1979) and Toole and Georgi (1981), falls within this band. Thus the observed excess variance in the expected wavenumber band associated with the intrusions is consistent with double diffusive driving of the intrusions.

The slope of the intrusions across isopycnals can also be an indication of active double diffusive processes. Turner (1978) used laboratory experiments to show that cross frontal intrusions will slope across isopycnal surfaces. His laboratory experiments demonstrate that for diffusively unstable intrusions, the increase in density below a salt fingering region dominates the decrease above the diffusive regime. Thus warm salty intrusions will tend to rise when surrounded by cold, less salty waters. The opposite is true as well: cold, fresh intrusions will tend to sink when surrounded by warm, salty waters. Similar conclusions were reached theoretically by Stern (1967). Ocean observations by Joyce, Zenk and Toole (1978) and Gregg (1979) have shown intrusions crossing isopycnals in the predicted manner.

Tracking intrusions along isopycnals is done here by sampling temperature anomalies on isopycnal surfaces. This is the semi-Lagrangian, or isopycnal following, coordinate system (Appendix B). Here, isopycnals that are spaced 0.5 m apart on average are tracked. The temperature anomaly on an isopycnal is then just the difference between the average temperature on that isopycnal and the instantaneous temperature. A cascade plot of temperature anomalies reveals many intrusions which propagate across isopycnals (Figure 3.15). Without a cross section of profiles directly across the front, it is difficult to say whether the intrusions are sloping across the front in the correct sense. The horizontal advection of intrusions below FLIP confuses the orientation of intrusion slopes. Assuming the intrusions slope up from the warm water encountered at the beginning of the cruise to the cold water encountered at the end of the cruise, any mean water velocity reversal will change the direction of the slope in time. For this reason, only a subset of the data where the temperature anomalies change most rapidly during yeardays [66.7-67.5] is investigated for intrusion slope (Figure 3.16). By eye, there appears to be equal signal from upward and downward propagating intrusions so Fourier analysis is used to investigate the slopes. Only the sense of the slope can be determined from the time series. The depth range [300-464] m. is used since temperatures decrease steadily during this time. A depth/time series consisting of 128 points in depth and 512 points in time is windowed with a triangle taper in both directions before two dimensional Fourier transformation. Upward and downward sloping phase contributions

are separated and summed over all frequency bands to make vertical wavenumber temperature anomaly spectra. Gradient spectra are found by multiplying the anomaly spectra by  $(2\pi m)^2$  (Figure 3.18). The 'upward sloping' spectrum corresponds to intrusions sloping upward from the warm, salty water to the cold, fresh water (the expected result). The upward sloping intrusions contain two thirds of the total variance,  $\langle \tilde{T}^2 \rangle$ . The upward sloping vertical wavenumber spectrum shows more variance than that downward sloping spectrum at all wavenumber below 0.225 c.p.m. This is the wavenumber band predicted to contain the scales of the interleaving intrusions. These results are consistent with the hypothesis that the intrusions are actively double diffusive.

### 3.5. Finestructure at the Frontal Interface

It is worth while to take a closer look at the structure of the intrusions during the yeardays [66.7-67.5] when the temperature and salinity characteristics change most rapidly. There appear to be two vertical scales associated with the temperature anomalies on isopycnals (Figure 3.16). The larger scale is 40-60 meters and takes the form of noses of warm water protruding into cold water. Two of the warm noses can be seen at depths 220-270m, day 66 , hour 18:00-22:00 and at depths 310-360 m, day 67; hour 2:00-4:00. The cold noses lie above and below the warm noses. The small scale comprises the structure on the noses which has vertical scales of 5 to 15 meters.

The potential for double diffusion to occur is mapped using Turner angle,  $T_u$ , calculated during yeardays [66.7-67.5]. Following the same isopycnals (separated by 0.5 m. in depth on average),  $T_u$  is calculated for each isopycnal from the temperature and salinity differences across isopycnals that are separated by 3.0 meters in depth on average. This yields a time/depth series of  $T_u$  (Figure 3.17). The characteristic scale for the diffusive and fingering interfaces is 5 to 15 meters. Alternating diffusive and fingering interfaces are observed at the edges of the larger scales noses which appear at nearly constant density or rise slightly with time. Diffusive and fingering layers are absent at depths 200 to 270 meters from 5:00-12:00; day 67 where the temperature anomalies suggest only one water mass is present ( $\tilde{T} = -0.3^\circ\text{C}$ ). Away from the noses, the alternating layers are not as apparent and diffusive and fingering interfaces tend to rise and fall across isopycnals (depths 300-420, before to 2:00 hours ;day67). The smaller layers seen in the temperature anomalies (5-15m) are double diffusively active above and below and their scales are likely set by the processes as described by Ruddick and Turner (1979) and Toole and Georgi (1981).

The physics governing the larger noses (40-60m) is not as clear. One possibility is that the noses are driven by submesoscale dynamics. The dynamics that created the front in the first place may have led to this larger scale distortion on its interface. A second possibility is that strong shears for near inertial internal waves are distorting the front. Schmitt (198?) shows that salt fingers still form in the presence of strong vertical shear so the smaller layers are still double diffusively active in the presence of larger scale inertial shears. The shear analysis performed in Chapter 2 shows that the vertical

shear variance is dominated by near inertial waves with vertical wavelengths of 35-45 m which is nearly consistent with the scale of the noses.

A third possibility is that larger scales are linked in some way to the double diffusive processes. Fedorov (1986) performed an interesting experiment. He placed a single (warm and salty) intrusive wedge into a surrounding body of cold water. Salt fingers began to form at the bottom interface of the wedge and, in time a counter flow (opposite to the direction of the moving wedge) was observed. This led to the formation of a second wedge below the original. Eventually the intrusion split into several laminae. The resulting structure was characterized by the upper most layer protruding the farthest from the source and deeper layers protruding successively less. This has many of the characteristics of the two scales observed here. Two larger scale noses (located at [220-280]m and [310-370]m) are warm and salty, the top of the nose protrudes the deepest into the cold, fresh side of the front. Beneath, several smaller layers are found with the general shape of the nose sloping away from the cold water. This process still needs an outside force to define the larger scale noses but may explain the generation of the smaller scale layers and their link to the larger scales.

Newly formed intrusive lenses, referred to as 'calving' by Fedorov (1986), are another feature seen during yeardays [66.7-67.5]. Calving is the separation of an intrusive tongue from the frontal interface and its transformation into an isolated lens. Several lenses can be seen in Figure 3.16. One such feature occurs at 300 m. at 20:00; day 66; where a lens of warm water is surrounded by colder water. Without a three dimensional survey it is impossible to tell whether this lens is completely separated from its origin. Separated lenses near frontal zones have been observed before (Fedorov, 1986). These lenses are likely formed from motions in the horizontal plane. The calving of interleaving layers will lead to increased variability in isopycnal temperatures near a front and lead to enhanced horizontal and vertical mixing.

### 3.6. Estimates of Horizontal Heat and Salt Fluxes

In order to maintain a statistically steady state of interleaving temperature and salinity fields in the presence of small-scale dissipation, fluxes of heat and salt must be supplied. The interleaving acts as stirring which enlarges the surface area between the two water masses. Inversions in temperature and salinity due to the interleaving permit small scale enhanced vertical transfer of heat and salt by double diffusive processes. Horizontal temperature and salinity fluxes,  $F_T$  and  $F_S$ , across the front are estimated by

$$F_T \equiv -\langle \tilde{V} \tilde{T} \rangle = A_T^v \langle \tilde{T}_z^2 \rangle \bar{T}^{-1} \quad (3.21)$$

$$F_S \equiv -\langle \tilde{V} \tilde{S} \rangle = A_S^v \langle \tilde{S}_z^2 \rangle \bar{S}^{-1}. \quad (3.22)$$

where  $\tilde{V}$  is the cross frontal velocity and  $A_T^v$  and  $A_S^v$  are vertical eddy diffusivities of temperature and salt (Joyce, 1977).  $\langle \tilde{T}_z^2 \rangle$  and  $\langle \tilde{S}_z^2 \rangle$  are the variances of vertical

gradients of salinity and temperature associated with vertical interleaving. (There is a slight confusion as to which scales to use. Gargett (1978) asserts that Joyce's model uses the microscale fluctuations of T and S. However, Joyce (1977) and Fedorov (1986) clearly state that the balance is with the interleaving scales. Joyce et. al (1978) use the interleaving scales to estimate horizontal fluxes with Joyce's (1977) model.) At some small vertical scale it is expected that dissipation scales will become important and using a vertical eddy diffusivity is no longer valid. Measurements by Gregg (1975) suggest that dissipation dominates at scales smaller than 0.5 c.p.m. The CTD deployed during SWAPP has a vertical resolution of 0.7 c.p.m (Appendix C).  $\langle \tilde{S}_z^2 \rangle$  and  $\langle \tilde{T}_z^2 \rangle$  over the wavenumber band [0.0078- 0.5] c.p.m. are estimated from half day ensemble averaged spectra of  $\tilde{T}$  and  $\tilde{S}$  (Figure 3.12). Using the maximum values

$$\begin{aligned}\langle \tilde{S}_z^2 \rangle_{\max} &= 2.72 \times 10^{-5} \left( \frac{\%}{m} \right)^2 \\ \langle \tilde{T}_z^2 \rangle_{\max} &= 8.81 \times 10^{-4} \left( \frac{^\circ C}{m} \right)^2\end{aligned}$$

and  $A_v^T = A_v^S = .1 \text{ cm}^2/\text{s}$  (the value suggested by Joyce et al. (1978)), the corresponding horizontal temperature and salt fluxes are

$$F_T = 1.67 \times 10^{-4} \left( \frac{^\circ C}{m/s} \right) \quad (3.23)$$

and  $F_S = 2.62 \times 10^{-5} \left( \frac{\%}{m/s} \right).$  (3.24)

These estimates are considered as upper bounds on the fluxes since the cross frontal gradients are likely underestimated and  $\langle \tilde{S}_z^2 \rangle$  and  $\langle \tilde{T}_z^2 \rangle$  are taken at their maximums. The temperature and salt fluxes are 20% and 4% respectively of those found at the Antarctic polar front. The uncertainty of the size of the vertical eddy diffusivities raises some question as to the proper bound of the horizontal fluxes.

Assuming all the dissipation is from shear instabilities, the vertical eddy diffusivity of density,  $K_\rho$ , can be estimated using Gregg's (1989) ten meter shear variance scaling of dissipation.  $K_\rho$  is estimated by

$$K_\rho \leq \frac{.2 \langle \varepsilon_{rw} \rangle}{N^2} = 1.4 \times 10^{-10} N_0^{-2} \frac{\langle S_{10}^4 \rangle}{\langle S_{GM}^4 \rangle} \left( \frac{m^2}{s} \right) \quad (3.25)$$

where  $\varepsilon_{rw}$  is the estimated dissipation,  $N$  is the buoyancy frequency,  $S_{10}$  is the measured ten meter shear,  $S_{GM}$  is the GM76 shear and  $N_0$  is the normalized buoyancy frequency ( $5.2 \times 10^{-3} \text{ 1/sec}$ ). Using the shear variance estimates from the 161 kHz Doppler sonar system (Table 2.1), yields  $K_\rho \leq 8.7 \times 10^{-6} \text{ m}^2/\text{s}$ . This value is nearly equal to the eddy diffusivities suggested by Joyce et al. (1978). The ten meter shear scaling does not include double diffusively driven mixing. For individual intrusions,  $A_v^T$  and  $A_v^S$  may be as large as  $1.0 \times 10^{-3} \text{ m}^2/\text{s}$  (Fedorov; 1986; Horne 1978) and assuming that 50% of the

water column is subject to double diffusive fluxes (Figure 3.8) at the peak of interleaving, the vertically averaged vertical diffusivities might be as large as  $5.0 \times 10^{-4} \text{ m}^2/\text{s}$ . (It is important to note that if the double diffusive fluxes are dominating then it is likely that  $A_v^s > A_v^T$  as reflected by the intrusion slopes across isopycnals.) Thus it is possible that the upper bounds on the horizontal fluxes may be even larger but since the cross frontal temperature and salinity gradients are underestimated, (3.23) and (3.24) are taken as conservative upper bounds.

The calculation of  $\tilde{T}$  and  $\tilde{S}$  presented here effectively removes the mean temperature and salinity on isopycnals. If the water was horizontally homogeneous,  $\tilde{T}$  and  $\tilde{S}$  would always be zero. Joyce et al. (1978) removes the mean temperature and salinity at depth and doing so still leaves a signal from internal wave straining and advection of the mean profile. Even in a horizontally homogeneous ocean, Joyce et al. (1978) would have non zero  $\tilde{T}$  and  $\tilde{S}$  and would predict a 'cross front' flux.

The question of buoyancy fluxes across a frontal interface has been a subject of some confusion. Joyce et al. (1978) used the above model (Equations (3.21) and (3.22)) to estimate salt and heat fluxes across the polar front at Drakes passage. In turn, they estimated the buoyancy flux by

$$F_\rho = -\langle \tilde{V}\tilde{T} \rangle = \rho_0(\beta F_s - \alpha F_T). \quad (3.26)$$

and found that the buoyancy flux was dominated by the salt flux working against the mean horizontal density gradient. Toole and Georgi (1981) argue that these results are just an artifact of overestimating the salinity variance due to uncertainties in the CTD sensor responses. The dynamical model of Toole and Georgi (1981) can not yield steady state fluxes across a front but their results suggest that the density flux must be down gradient in the Antarctic Polar Front. Fedorov (1986) disputes the results of Joyce et al. (1978) suggesting that the whole concept of eddy diffusivities is inappropriate. Using the upper bounds on the horizontal fluxes, (3.26) yields

$$\begin{aligned} F_\rho &= \rho_0(2.0 \times 10^{-8} - 2.5 \times 10^{-8}) \text{ kg/m}^2 \text{ sec} \\ &= -5 \times 10^{-6} \text{ kg/m}^2 \text{ sec} \end{aligned} \quad (3.27)$$

Here, the buoyancy flux is dominated by the heat flux contribution. The water in the 300 to 400 meter depth range got steadily more dense as well as colder with time. Thus the net buoyancy flux is up gradient rather than down gradient yielding the same results reached by Joyce et al. (1978) at the Antarctic Polar Front. This result does not seem physically realistic since the horizontal density gradient appears to be supported by a geostrophic balance. The buoyancy flux calculation is presented here just as an illustration. It is not taken as a physically meaningful result.

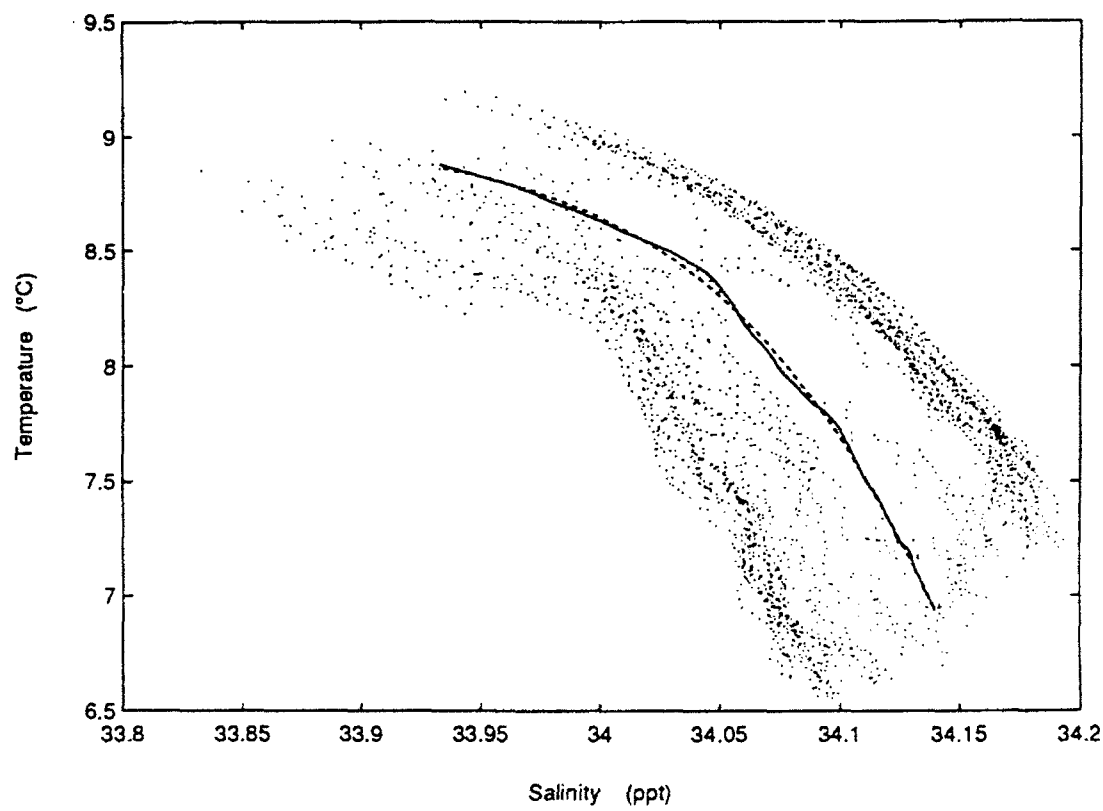
This raises some question about the appropriateness of using (3.26). The assumption that  $A_v^T = A_v^S$  is likely incorrect especially if there is significant double diffusively driven vertical fluxes. For diffusive interfaces on intrusions, heat fluxes are larger than salt fluxes ( $A_v^T > A_v^S$ ), and for salt fingering interfaces, salt fluxes are larger than heat fluxes ( $A_v^T < A_v^S$ ). Since salt fingering interfaces occur at least twice as often as diffusive ones (Figure 3.8), it is likely that the average vertical haline eddy diffusivity is larger ( $A_v^T < A_v^S$ ). It would not take much more haline vertical diffusivity to change the up gradient buoyancy flux to a down gradient flux. Consider a case where semi-Lagrangian (isopycnal) coordinates are used to track temperature and salinity anomalies. The ratio of  $\beta F_S$  to  $\alpha F_T$  is equal to one since  $\alpha \Delta T = \beta \Delta S$  on constant density surfaces and the horizontal buoyancy flux must be zero. Assuming that  $A_v^T \neq A_v^S$ , would lead to a net buoyancy transport along isopycnals which is physically impossible. Only in the case of using depth coordinates with sloping isopycnals can a net buoyancy flux exist. This is because the depth coordinates cross isopycnals themselves and the model correctly reflects this 'flux' of isopycnals.

### 3.7. Summary

Observations of increased variance in thermohaline finestructure during the SWAPP experiment is linked physical processes associated with a frontal zone. The front appears to be in geostrophic balance. The front is characterized in the depth range [200-420] m. by warm water to the southeast and warm water to the northwest. Horizontal salinity and temperature gradients across the front are at least  $1.0 \times 10^{-5} \text{‰}/\text{m}$  and  $5.3 \times 10^{-5} \text{°C}/\text{m}$ .

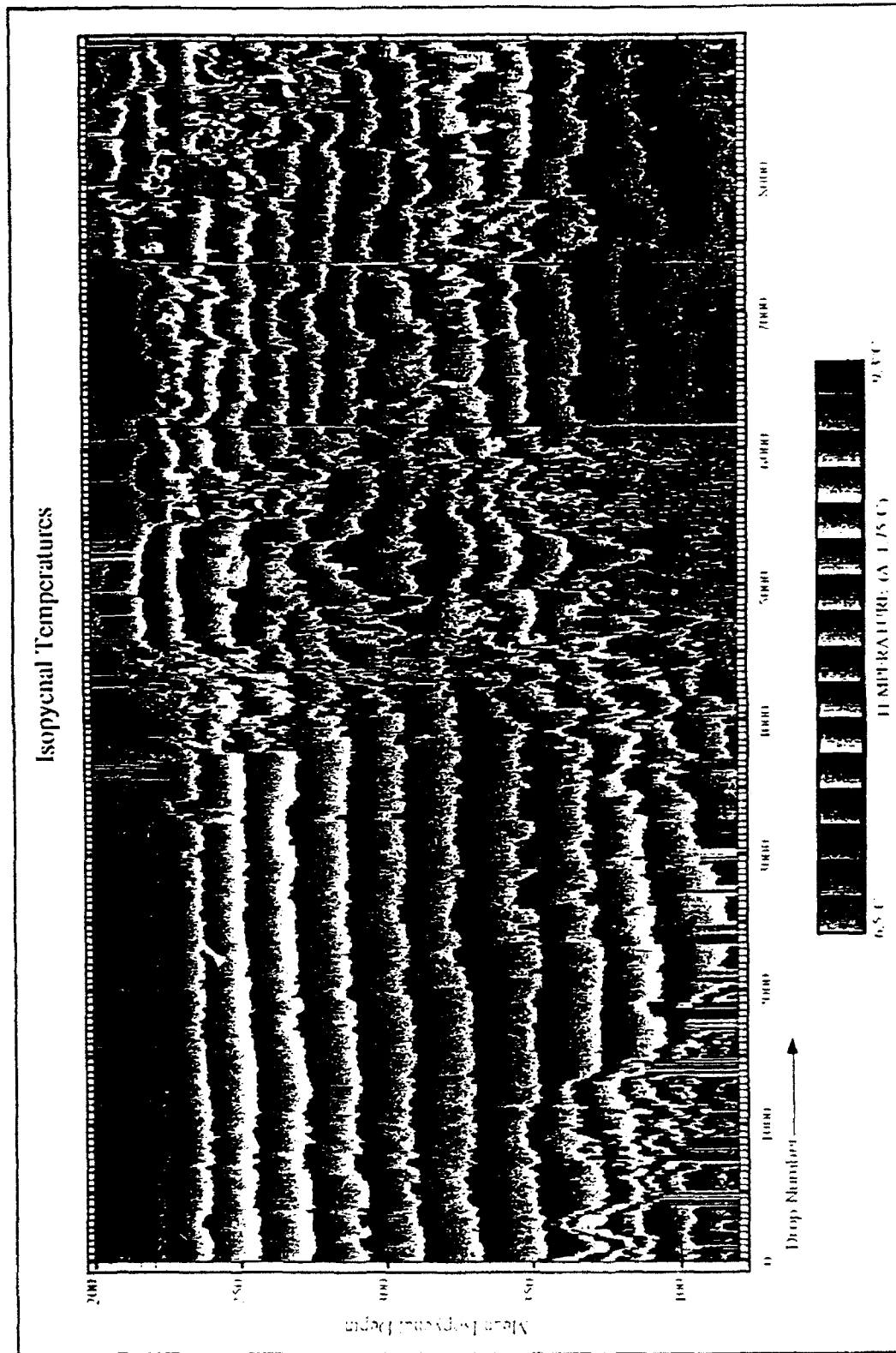
The fine scale thermohaline structure is sampled as a CTD time/depth series taken from a moored FLIP while the frontal zone is advected past the sampling location. The time series is characterized by warm, salty water starting at yearday 60, 1990. A rapid drop in isopycnal temperatures occurs near yearday 67 as the water characteristics become colder and fresher. Individual temperature and salinity profiles are characterized by many salinity and temperature inversions. Estimates of Turner angles suggest the presence of double diffusive processes. The potential for salt fingering ( $Tu > 45^\circ$ ) is larger than the potential for diffusive instabilities ( $Tu < -45^\circ$ ) and the number of temperature and salinity inversions rises yearday 67 and thus precedes the front.

Temperature and salinity anomalies are calculated by removing the mean temperature and salinity on isopycnals. This technique allows the tacking of intrusions. The intrusions have two dominant vertical scales near the front. The small scale intrusions have vertical lengths of 5-15 meters, are driven by double diffusive processes, slope upward from the warm side to the cold side of the front and is consistent with scales predicted by Ruddick and Turner (1979) and Toole and Georgi (1981). The larger scale is 40-60 m and is likely determined by submesoscale or internal wave forcing.



**Figure 3.1** *T-S Diagram from 200-420m.* Scatter plot of salinity plotted versus potential temperature. A point is plotted for every 3 meters from 200-420m. One profile from the lower CTD is plotted every 6 hours. Two distinct water masses can be seen. The cruise averaged profile (solid line) and a cubic curve fit (dashed line) are also plotted.

Figure 3.2 *Isopycnal Temperatures*. Isopleths of temperature in the deep ocean. The contours are plotted versus mean isopycnal depth for the period 1960-61, made no more than 10 m apart. The contours are continuous, plotted every 0.1°C deep interval.



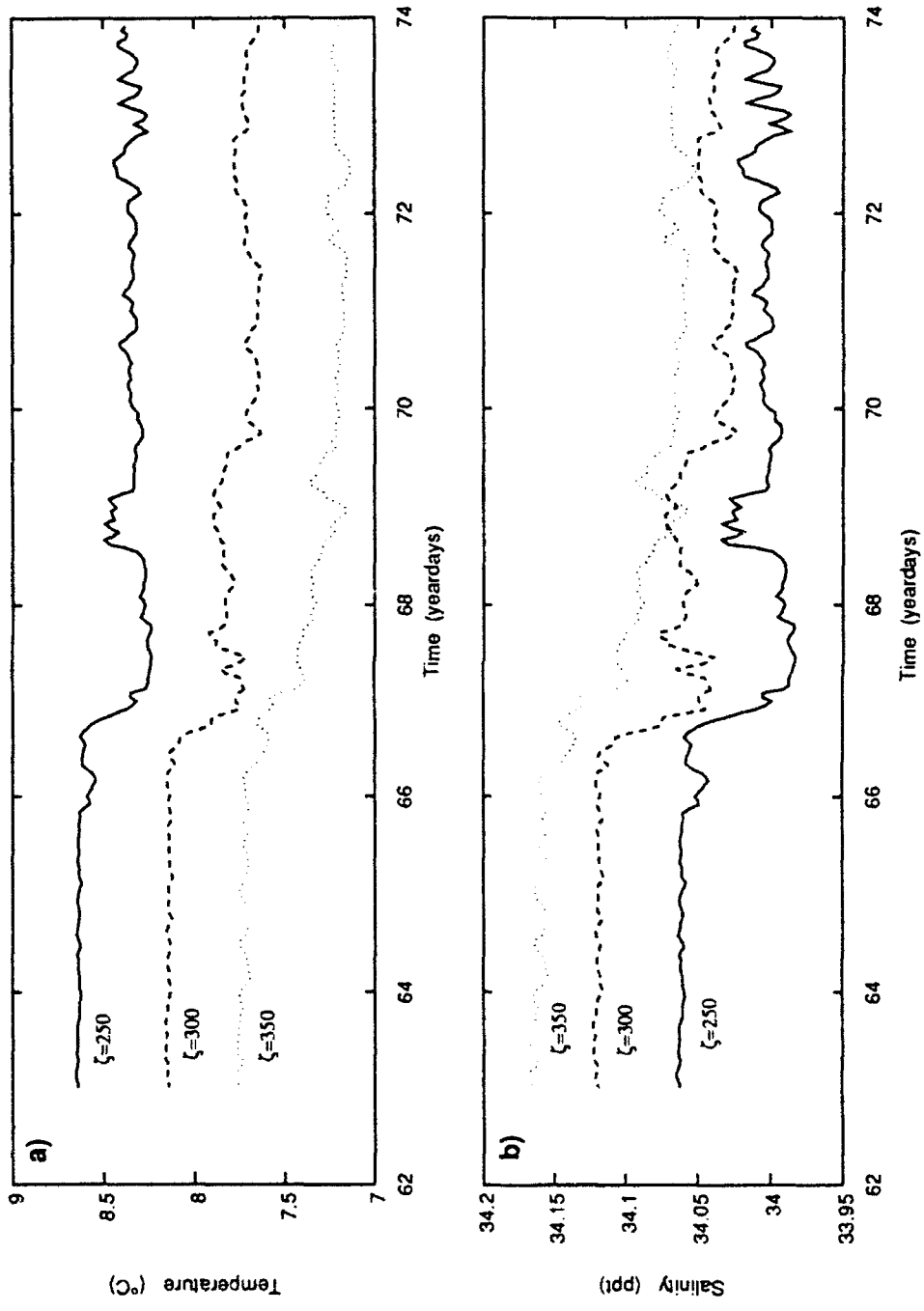
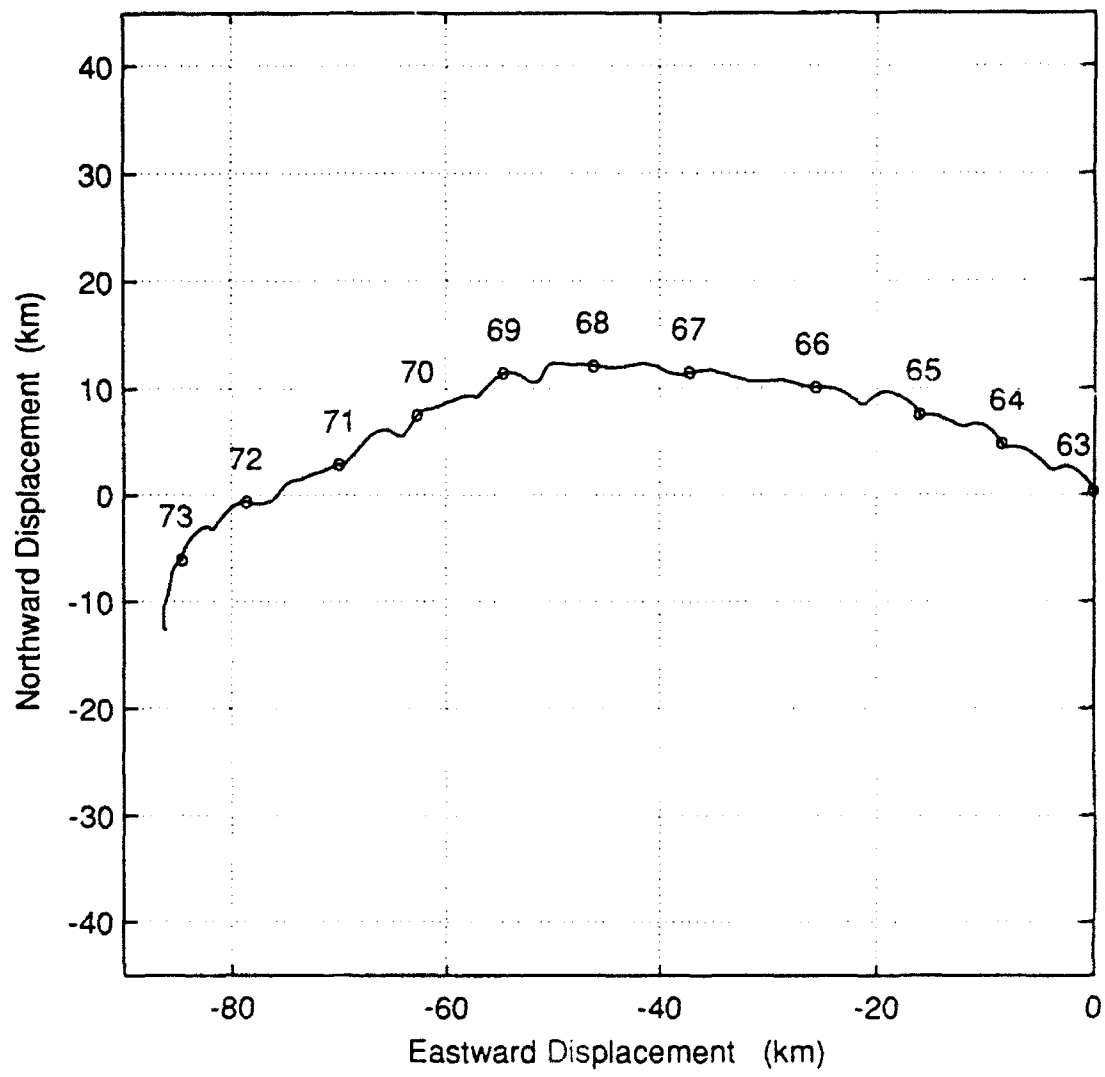
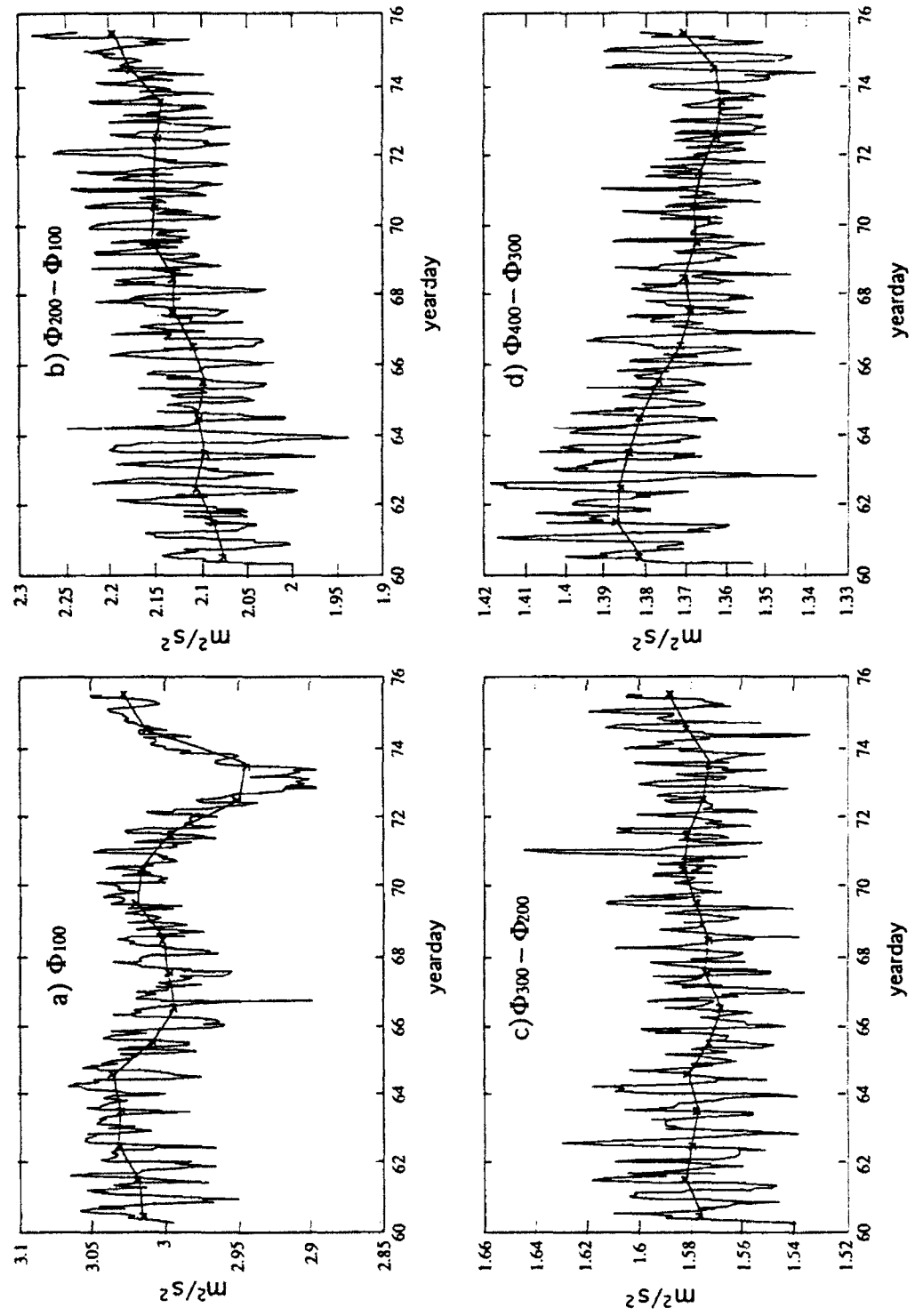


Figure 3.3  $T$  and  $S$  at Constant Potential Density Hour averaged temperature(a) and salinity(b) are found along three isopycnals ( $\tau = 250, 300$  and  $350\text{m}$ ) and plotted versus time.



**Figure 3.4 Integrated Current Trajectory** Hour averaged velocity profiles are depth averaged from 200 to 350 m depths and integrated in time.



**Figure 3.5 Geopotential Anomalies.** Hour averaged (light line) and daily averaged (dark line) geopotential anomalies are plotted versus time. The anomalies are calculated over 4 separate depth ranges: [0-100]m, [100-200]m, [200-300]m and [300-400]m.

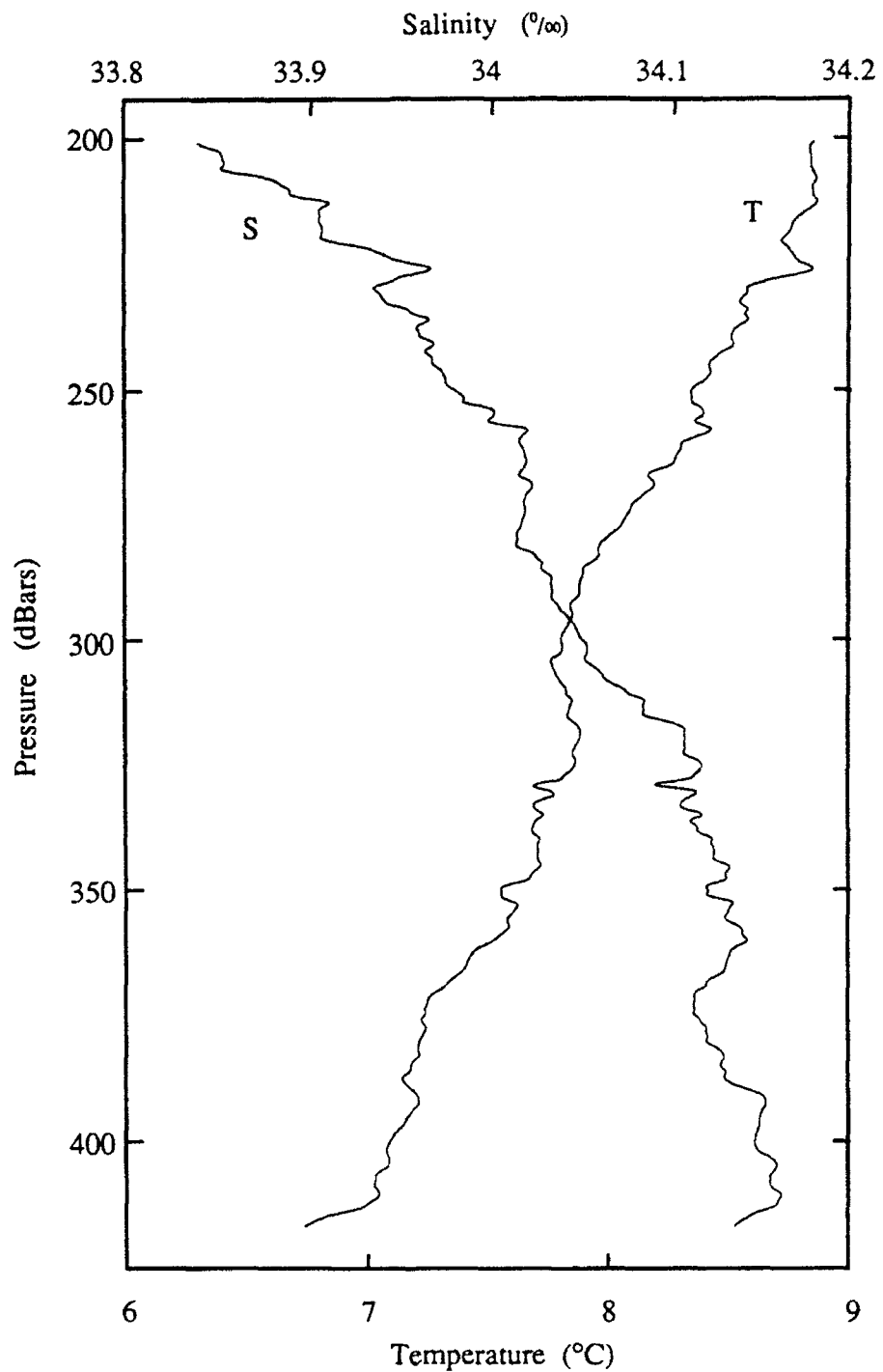


**Figure 3.6** Typical Temperature and Salinity Profile from Yearday 67. A typical temperature and corresponding salinity profile are plotted versus pressure. Temperature inversions are matched by salinity inversions to yield a stable density profile. Typical scales of temperature inversions are 5 to 15 meters.

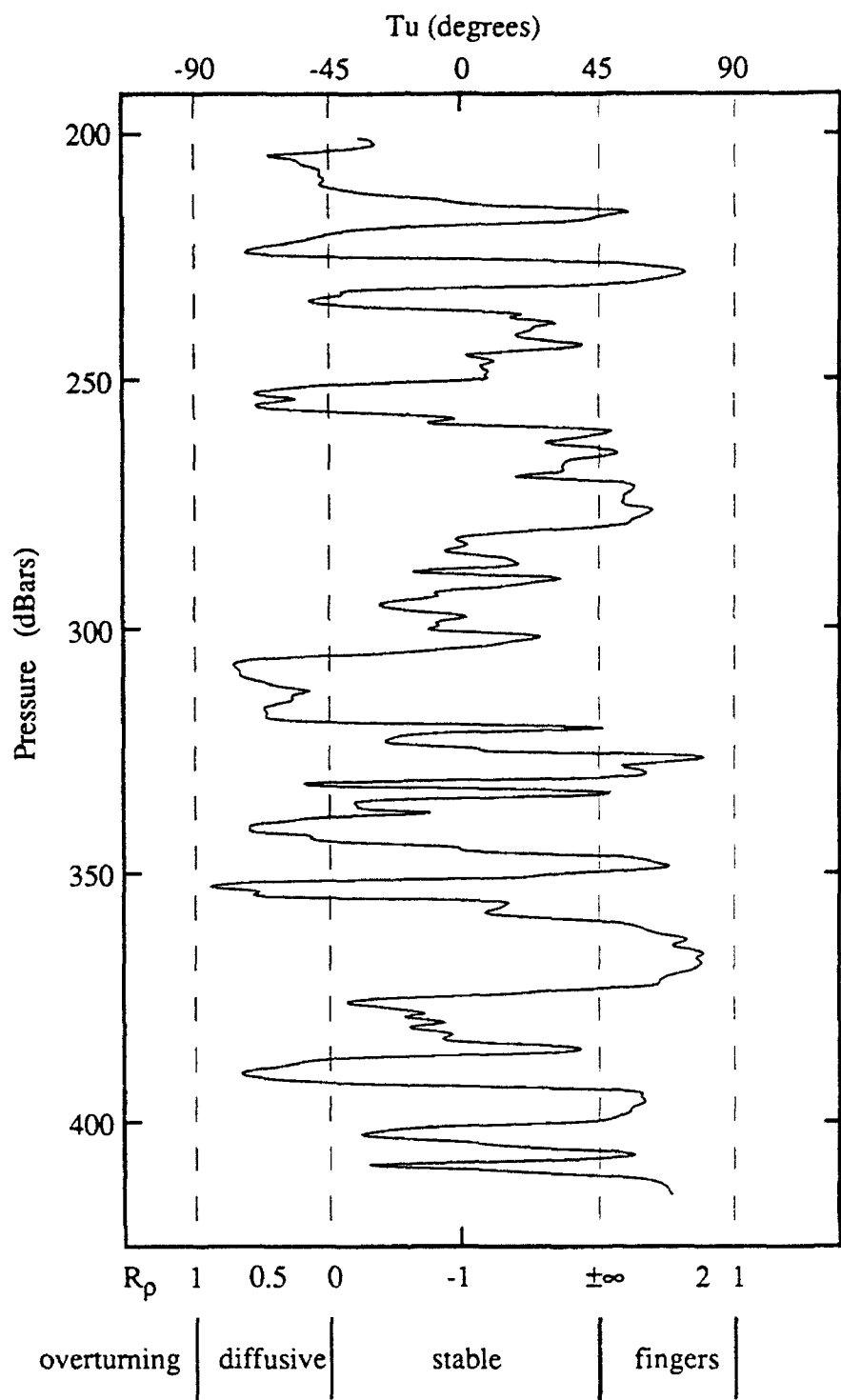


**Figure 3.7** Typical Turner Angle Profile from Yearday 67. Same Figure 3.6 except Turner angle,  $T_u$ , is plotted.  $T_u$  is computed from temperature and salinity differences taken over 5 meters in depth.

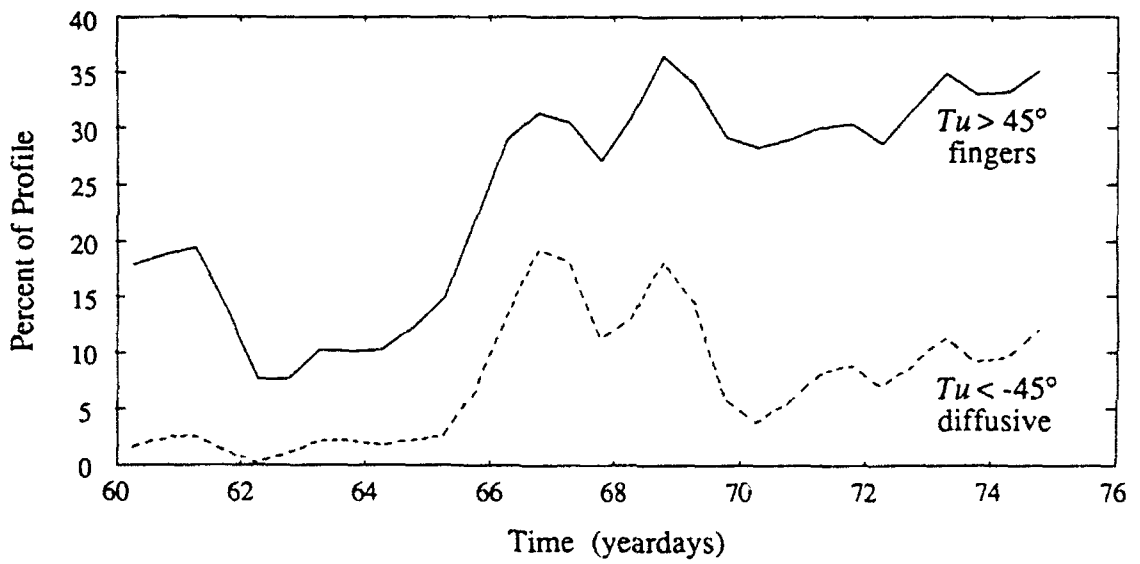


**Figure 3.8 Percent of Profile that is Subject to Double Diffusive Convection.** Turner angle,  $Tu$ , is computed from temperature and salinity differences taken over 5 meters in depth. The percent of each profile that is subject to diffusive instabilities ( $Tu < -45^\circ$ ; dashed line) and salt fingering ( $Tu > 45^\circ$ ; solid line) is averaged over half day intervals and plotted versus time. During strong interleaving on yeardays 66 to 70, as much as 50% of the water column is subject to double diffusive fluxes.

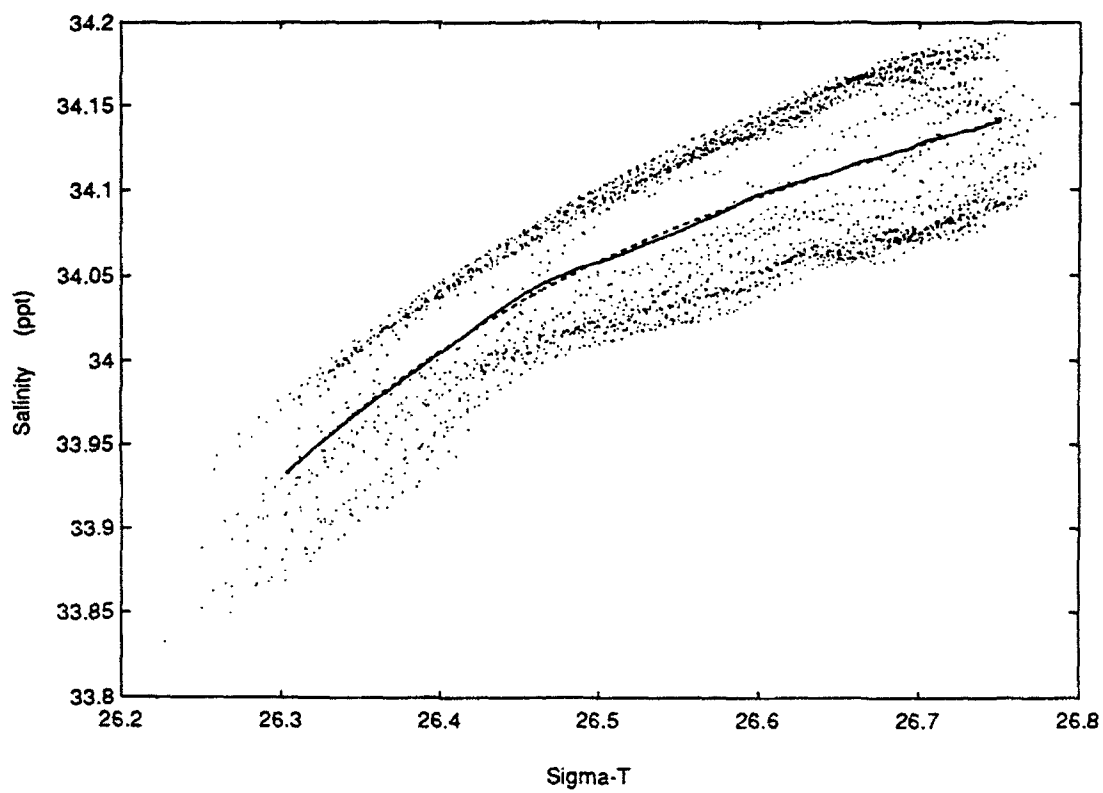


**Figure 3.9  $\sigma_T$  - S Diagram from 200-420m.** Scatter plot of salinity plotted versus potential density. A point is plotted for every 3 meters from 200-420m. One profile from the lower CTD is plotted every 6 hours. Two distinct water masses can be seen. The cruise averaged profile (solid line) and a cubic curve fit (dashed line) are also plotted.

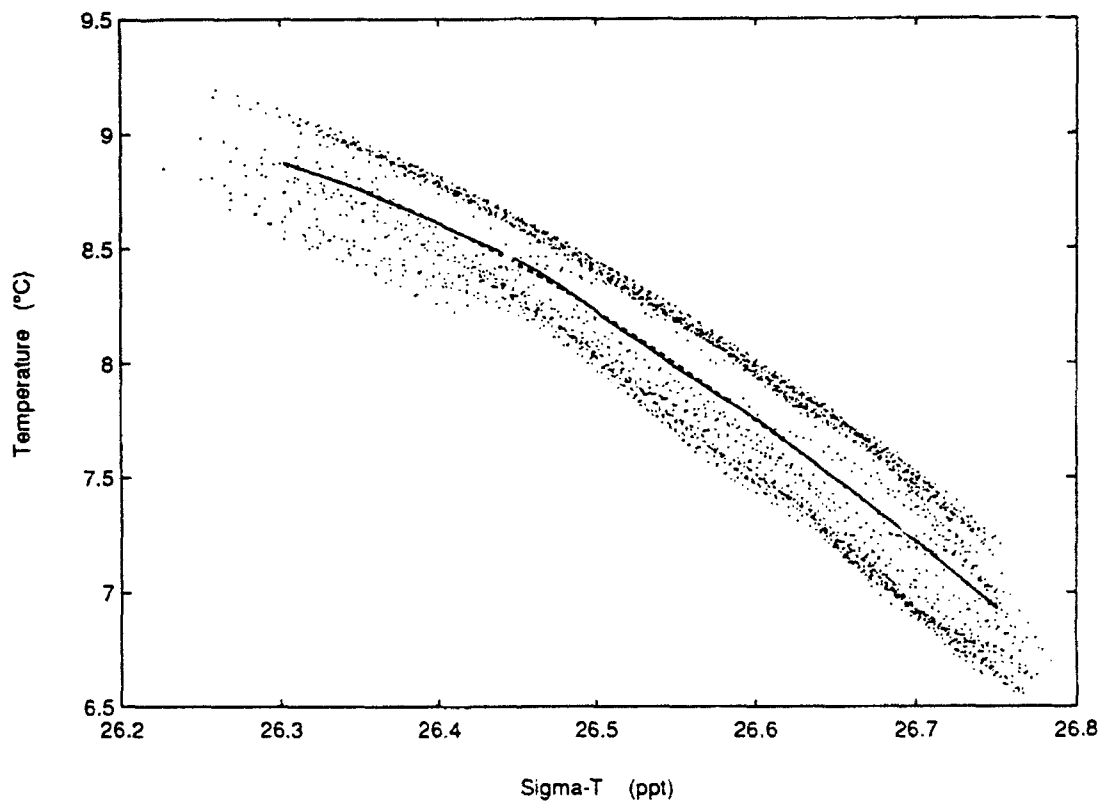


**Figure 3.10**  $\sigma_T$  -  $T$  Diagram from 200-420m. Scatter plot of temperature plotted versus potential density. A point is plotted for every 3 meters from 200-420m. One profile from the lower CTD is plotted every 6 hours. Two distinct water masses can be seen. The cruise averaged profile (solid line) and a cubic curve fit (dashed line) are also plotted.

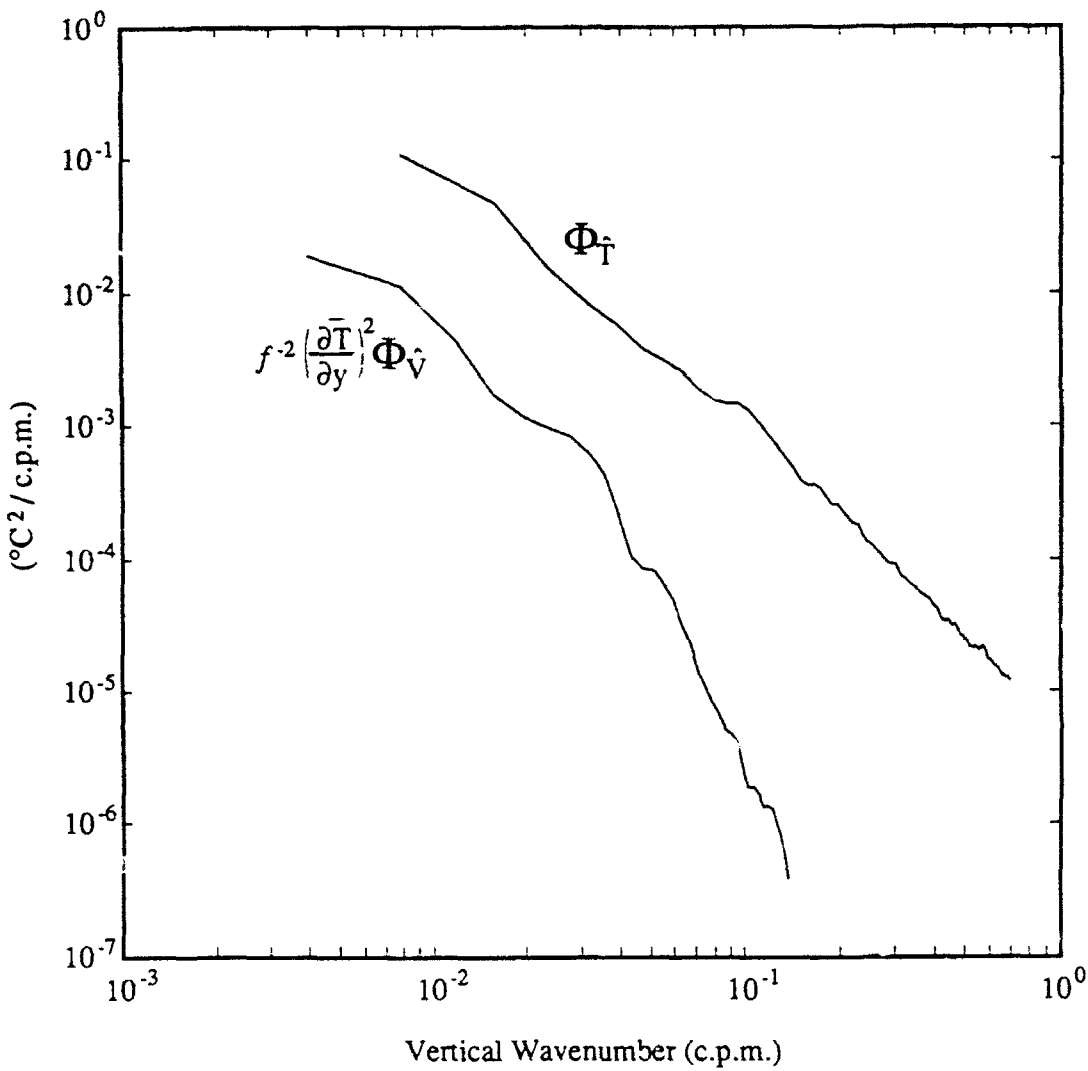


**Figure 3.11 Internal Wave Temperature Anomalies.** Temperature anomaly spectrum,  $\Phi_{\hat{T}}$ , is calculated using temperature fluctuations from depth ranges 220-420 meters and ensemble averaged over yeardays [60-75]. Maximum internal wave temperature anomaly spectrum is calculated using horizontal displacement spectrum (from 6.5 minute averaged velocity profiles, over depth ranges 50-300 m and ensemble averaged over yeardays [63-77]) and scaling by the cross frontal temperature gradient squared. Internal waves can only account for up to 5% of observed vertical interleaving.

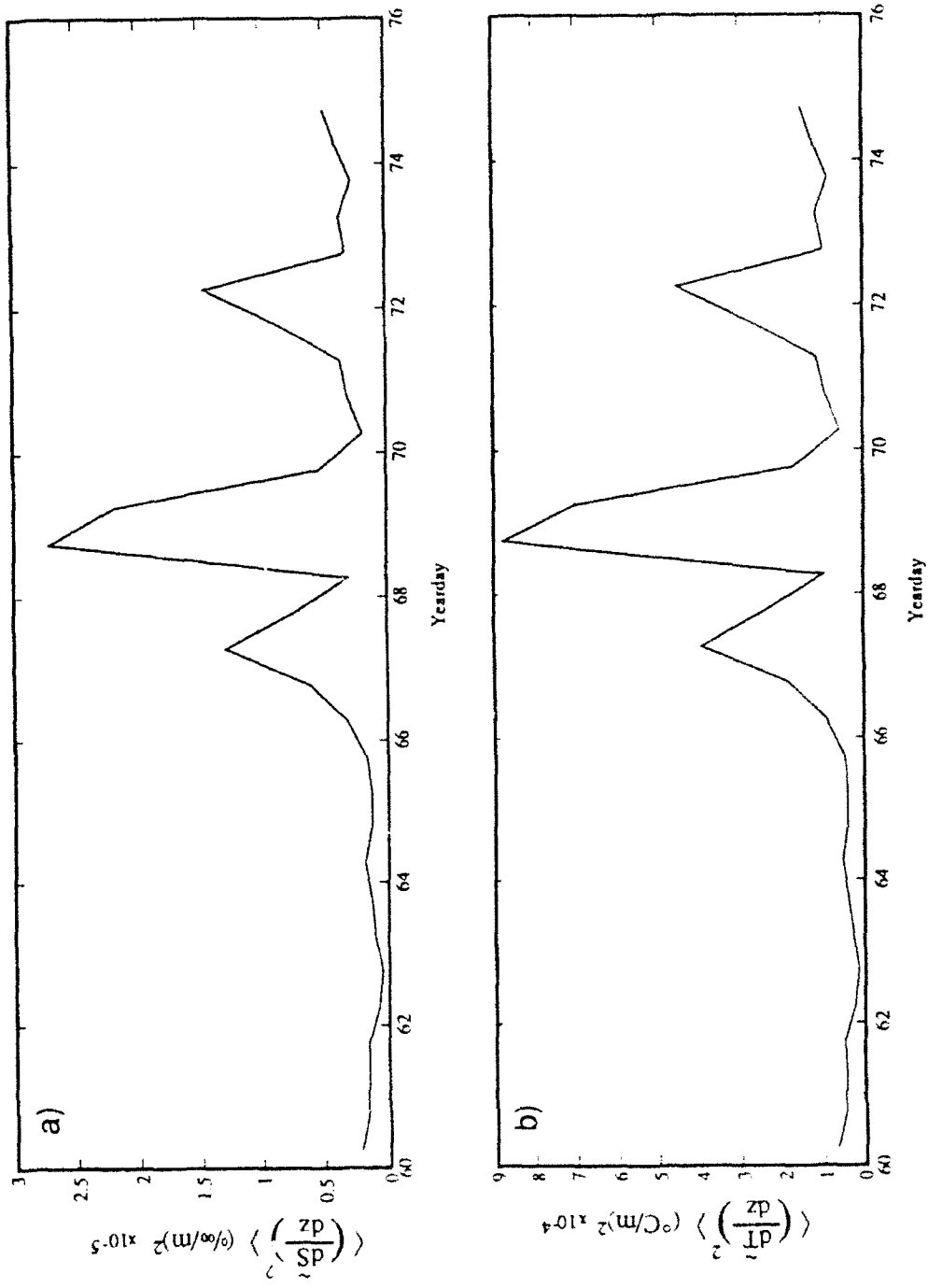


**Figure 3.12 Variance of Vertical Gradients of Salinity and Temperature Anomalies.** Salinity (a) and temperature (b) gradient variances are calculated from half day ensemble averaged spectra over the wavenumber band [0.0167-0.7] c.p.m. and plotted versus time.

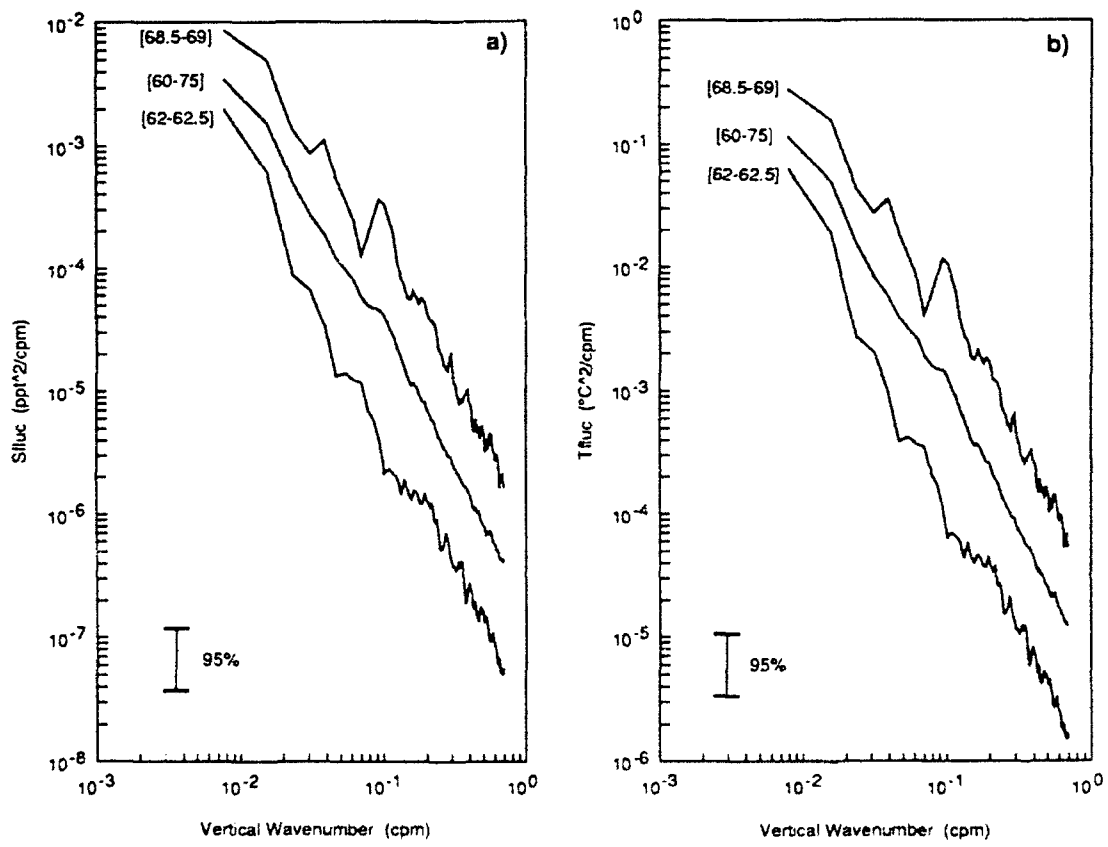


**Figure 3.13 Vertical Wavenumber Spectra of Temperature and Salinity Anomalies.** Spectra are calculated over the depth ranges 220-420 meters. Three ensemble averaged spectra are shown. Two half day averages from yeardays [62-62.5] and [68.5-69] and a 15 day average. Confidence intervals are approximate for half day ensembles.

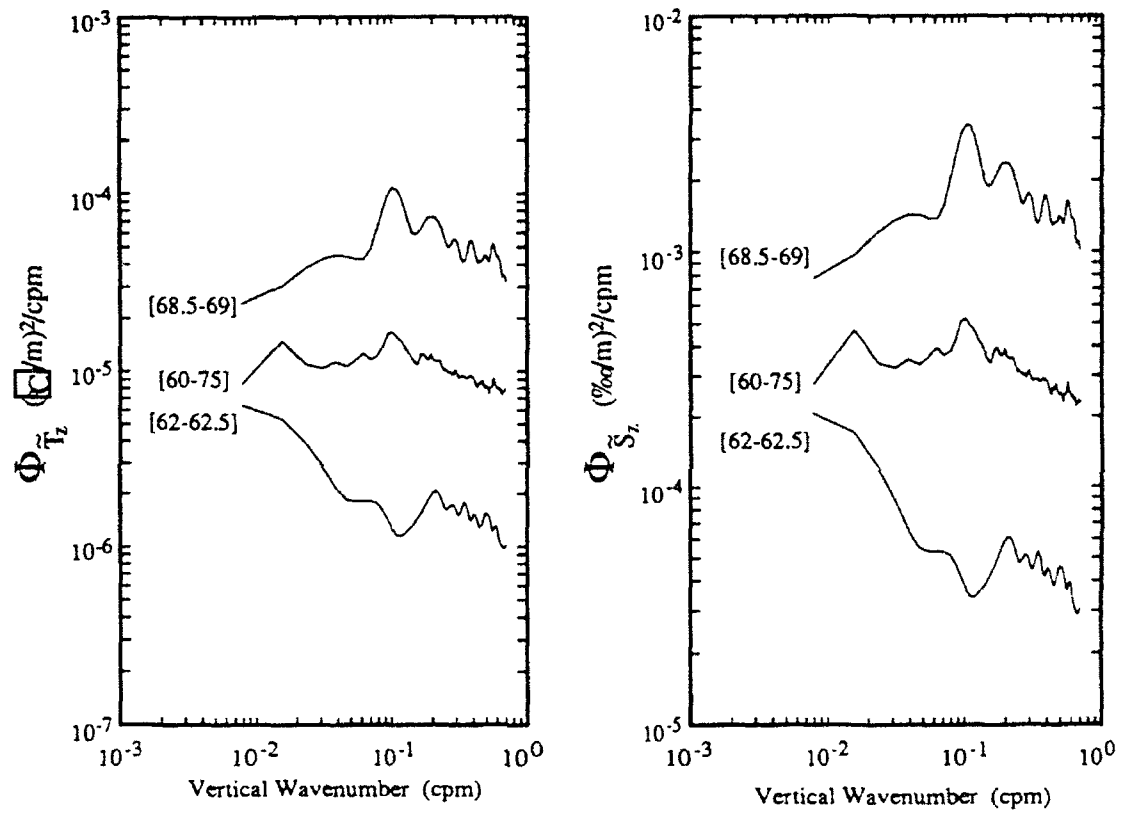


**Figure 3.14 Vertical Wavenumber Spectra of Gradient Temperature and Salinity Anomalies.** Spectra are calculated over the depth ranges 220-420 meters. Three ensemble averaged spectra are shown: yeardays [62-62.5], [68.5-69] and a 15 day average. Half day ensembles are smoothed in frequency with 5 pL triangle window.

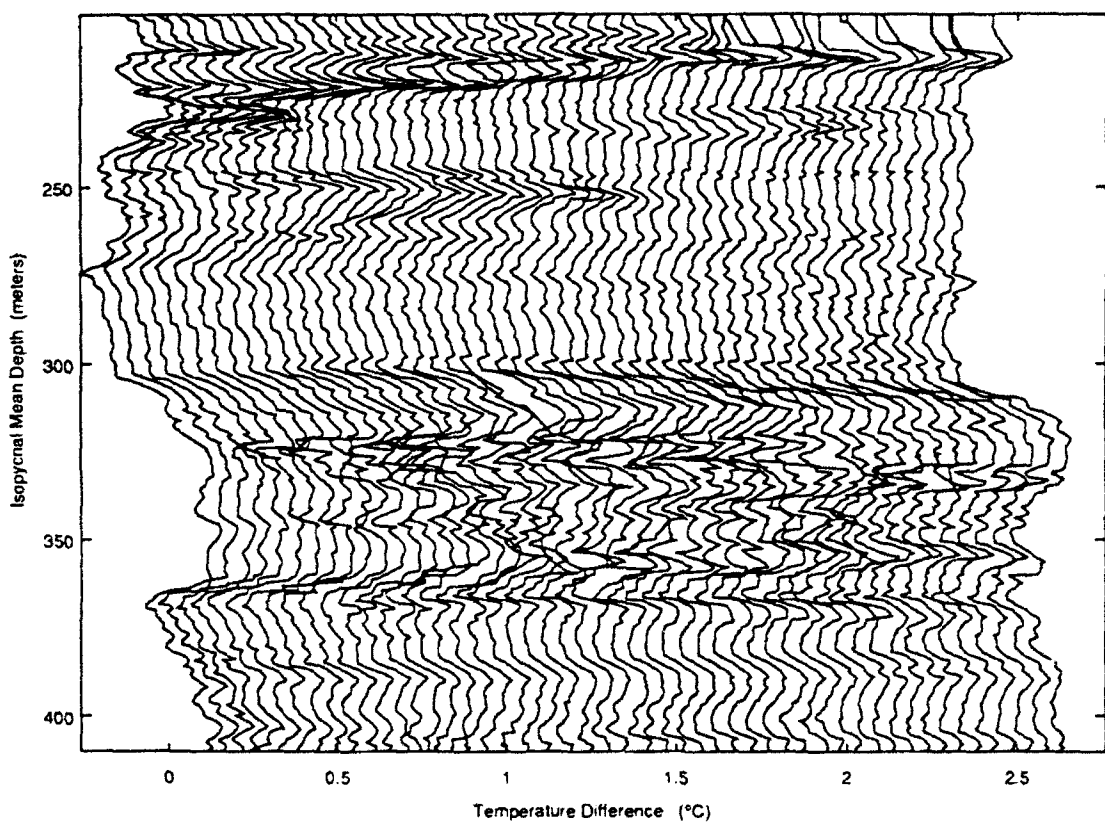


**Figure 3.15 Temperature Anomaly Cascade Plot .** Temperature anomaly on an isopycnal is plotted versus mean isopycnal depth. Cascade represents 1.8 hours in time.

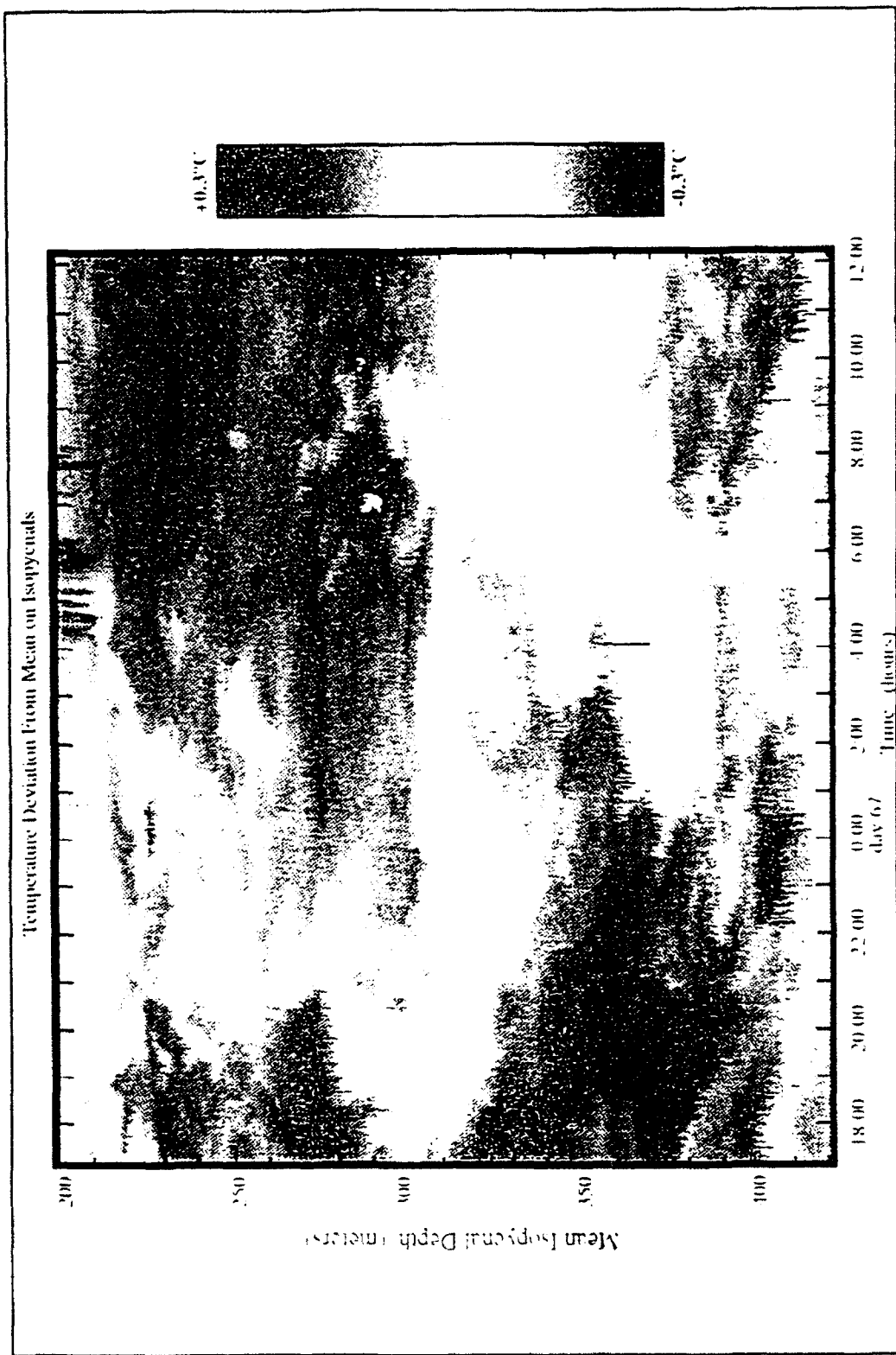
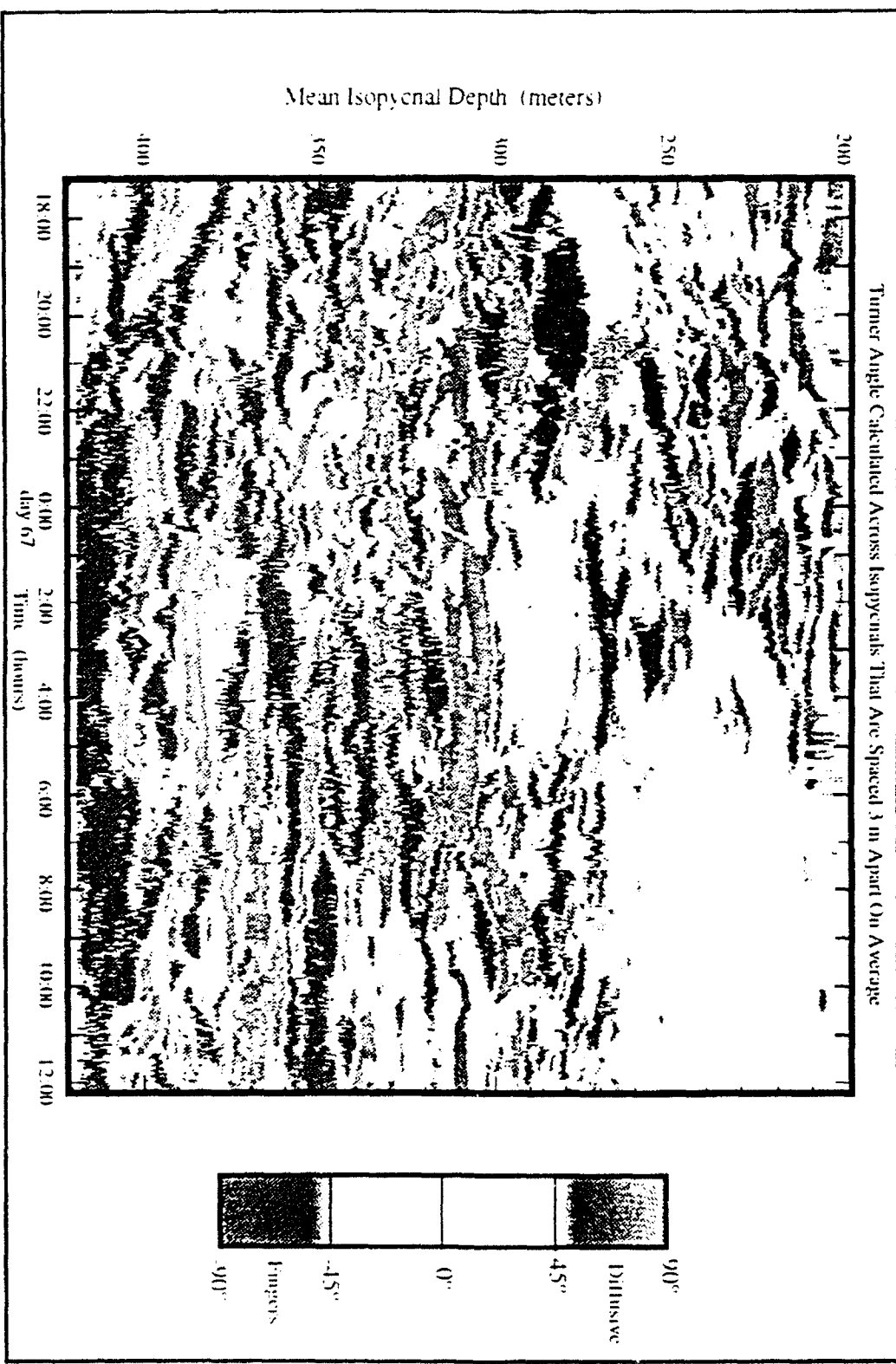
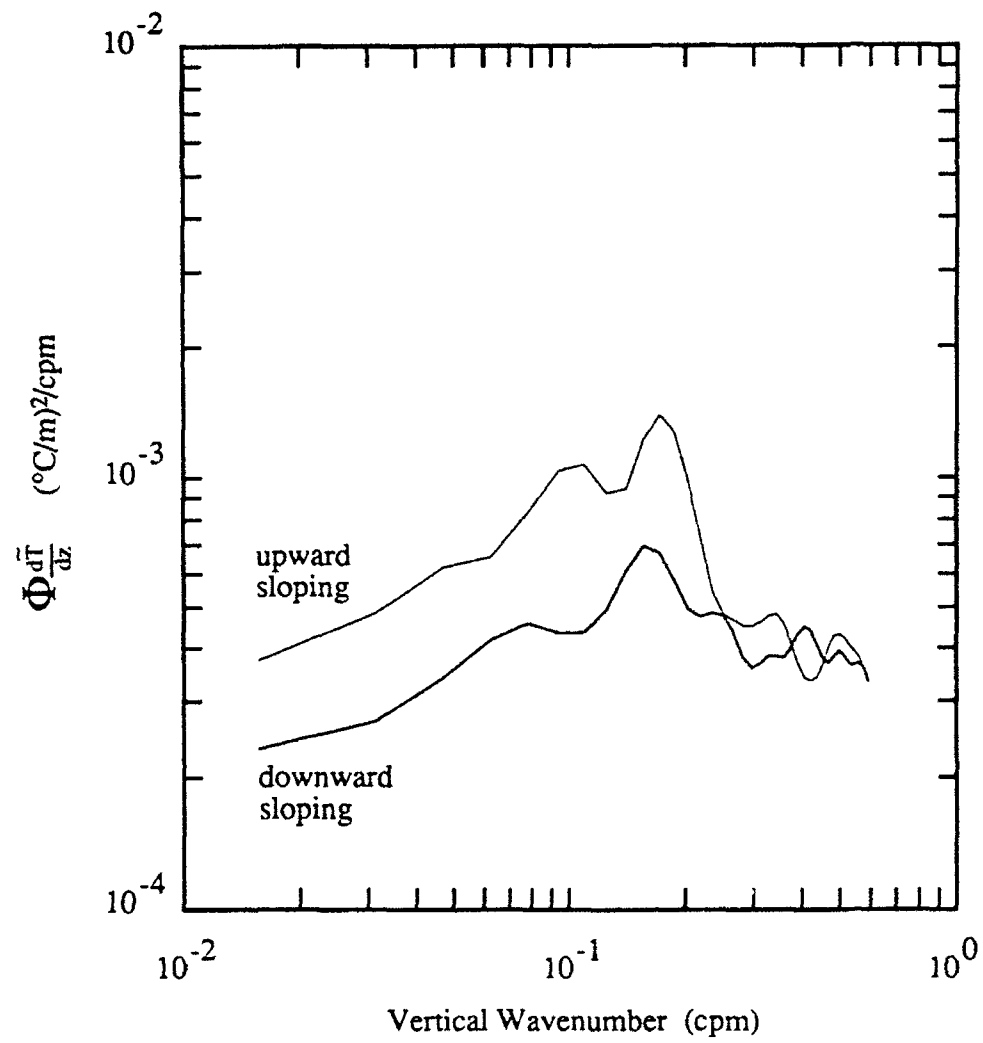


Figure 3.16. Temperature Anomalies on Isopycnals During Days 66.7 to 67.5. Temperature anomalies are tracked on isopycnals that are spaced in depth 0.5 m apart on average. The anomalies are contours plotted versus mean isopycnal depth and time from years days 66.7 to 67.5.





**Figure 3.18 Sloping Temperature Gradient Anomaly Wavenumber Spectrum.** Temperature anomalies on isopycnals are tracked. Upward and downward phase wavenumber spectra are extracted from vertical wavenumber/ frequency spectra. Wavenumber temperature gradient anomaly spectrum corresponding to upward (heavy line) and downward (light line) propagating phases are plotted. Data is from yeardays [66.7-67.5] and depths [300-364] meters. Upward sloping intrusions correspond to warm, salty (cold, fresh) water intrusions rising (sinking) across isopycnals and they move into cold, fresh (warm, salty) water.

## Chapter 4

### Froude Number Distribution

#### 4.1. Introduction

Turbulence observed in the ocean interior is thought to be caused by breaking internal waves. Shear instability is the hypothesized cause of breaking (Garrett and Munk, 1972; Eriksen, 1978; Munk, 1981, Kunze, 1990). A linear superposition of internal waves will lead to local vertical shearing and vertical straining of the water column. Shear and strain levels are occasionally sufficient to cause a shear instability. The distribution of these shear instabilities is not well known. Slow profiling microstructure instruments may undersample the underlying distribution of turbulent events due to the intermittency of wave breaking events (Baker, 1985). This undersampling will likely lead to an underestimate of vertical mixing due to internal wave breaking. This chapter examines the underlying probability density functions of shear and strain and presents a simple statistical model for the distribution of shear instabilities, or more specifically, Froude and Richardson numbers.

The gradient Richardson number,  $Ri$ , is often used to describe ratio of buoyancy forces to inertial forces. It is typically defined by

$$Ri = -\frac{g\rho_z}{\rho_0 V_z^2} = \frac{N^2}{S^2}. \quad (4.1)$$

where  $g$  is the local acceleration of gravity,  $\rho_0$  is the mean density,  $\rho_z$  is the vertical potential density gradient,  $V_z$  or  $S$  is the absolute value of the vertical shear and  $N$  is the buoyancy frequency. For  $Ri < 0.25$ , a fluid has the potential for a shear instability leading to turbulence. Since shear variance is typically larger than  $N$  variance, it is useful to use to buoyancy normalized shear or Froude Number,  $Fr$ , defined by

$$Fr = Ri^{-\frac{1}{2}} = \frac{V_z}{N} \quad (4.2)$$

to reduce the variance in the dimensionless ratio of inertial to buoyancy forces.

The Froude number distribution model is formed here using the known distributions of shear and strain. This is very similar to the derivation of a pdf of  $Ri$  by Desaubies and Smith (1982). The main difference is the underlying distribution of buoyancy frequency used. Desaubies and Smith (1982) assume that  $N$  is normally

distributed. However, this assumption is not consistent with recent observations. Pinkel and Anderson (1992) show that fine scale strain statistics can be modeled using Poisson statistics. From this model, the probability density of  $N$  is estimated and compared to histograms derived from the SWAPP CTD observations. Thus, the pdf of  $N$  is not a normal distribution. The shear distribution used here is the same as that assumed by Desaubies and Smith (1982). Individual horizontal components of vertical shear as seen by the sonar appear normally distributed and independent. This suggests a Rayleigh distribution of  $S$ . is the appropriate model. Joint histograms of  $S$  and  $N$  show that they are nearly independent which allows the direct estimation of the Froude number distribution. The modeled Froude number distribution is compared to histograms of  $Fr$  derived from the SWAPP data.

The density and velocity data presented in this chapter are collected with the MPL rapidly profiling CTD and 161 kHz Doppler sonar systems deployed from R/P FLIP during the SWAPP (1990) experiment (Appendix A). The CTD system provides density profiles from the surface to 420 m. every 130 seconds with a vertical resolution of 1.5 m (Appendix C). The sonar system yields 1 minute averaged velocity profiles from 50 to 325 m. with a vertical pulse length of 5.5 m (Appendix E). The data sets are depth calibrated as described in Section 2.2. After depth calibration, the velocity profiles are smoothed in time with a 3 minute running mean filter and resampled at the 30 seconds after the start of each CTD profile. Then both data sets are combined yielding more than 9200 profiles of simultaneous velocity and density estimates from 50 to 325 m. every 130 seconds from yearday 63 to 75. In this study, nine 25 m. depth ranges are investigated from 75 to 300 m. Vertical shear and buoyancy frequency are estimated from this combined data set. Shear,  $S$ , is defined as

$$S = |\mathbf{u}_z| = \frac{1}{\Delta z} \left[ \left( u\left(z + \frac{\Delta z}{2}\right) - u\left(z - \frac{\Delta z}{2}\right) \right)^2 + \left( v\left(z + \frac{\Delta z}{2}\right) - v\left(z - \frac{\Delta z}{2}\right) \right)^2 \right]^{\frac{1}{2}} \quad (4.3)$$

where  $z$  is the vertical coordinate (zero at the surface and increasing with depth),  $\Delta z$  is the vertical differencing interval,  $u$  is the east component of velocity and  $v$  is the north component of velocity. The buoyancy frequency,  $N$ , is defined as

$$N = \left[ \frac{g}{\rho_0} \frac{\partial \rho}{\partial z} \right]^{\frac{1}{2}} = \left[ \frac{g}{\rho_0 \Delta z} \left( \rho\left(z + \frac{\Delta z}{2}\right) - \rho\left(z - \frac{\Delta z}{2}\right) \right) \right]^{\frac{1}{2}} \quad (4.4)$$

where  $\rho$  is the density profile,  $g$  is the acceleration of gravity and  $\rho_0$  is the average density.  $Fr$  is calculated from the combined velocity and density profiles at depth  $z$  by

$$Fr = \frac{S}{N} \quad (4.5)$$

where  $S$  and  $N$  are taken as defined in (4.3) and (4.4).

#### 4.2. Distribution of Buoyancy Frequency and Vertical Shear

Joint histograms of shear,  $S$ , and buoyancy frequency,  $N$ , are constructed for nine 25 m depth ranges from 75 to 300 m.  $S$  and  $N$  are calculated using (4.3) and (4.4) and a difference interval,  $\Delta z$ , of 10 m. Each histograms contains 5 estimates of  $S$  and  $N$  in depth, and 9200 estimates in time. The joint histograms,  $f(N_i, S_j)$ , are normalized such that

$$\sum_{i=0}^{i_{\max}} \sum_{j=0}^{j_{\max}} f(N_i, S_j) \Delta N \Delta S = 1 \quad (4.6)$$

where

$$N_i = (i + \frac{1}{2}) \Delta N, \quad S_j = (j + \frac{1}{2}) \Delta S$$

and  $i$  and  $j$  are the bin numbers. The joint histogram,  $f(N_i, S_j)$ , are contour plotted for each of the nine depth ranges (Figure 4.1). It appears that the total variance in the histograms decreases with depth. The mean shear and buoyancy frequency decreases with depth below 125 m. A tilting of the contours from low  $S$  and  $N$  to high  $S$  and  $N$  can bee seen in the histograms above 250 m. This suggests some dependence of shear on buoyancy frequency.

Histograms of buoyancy frequency,  $f_N(N)$ , are found by integrating the joint histogram over all the shear bins,

$$f_N(N_i) = \sum_{j=0}^{j_{\max}} f(N_i, S_j) \Delta S, \quad (4.7)$$

and plotted for each of the nine depth ranges (Figure 4.4). The mean and variance of the distributions are given in Table 4.1. The mean has a maximum at [100-125] m. depth range and the variance decreases steadily with depth below 75 m.

Histograms of vertical shear,  $f_s(S)$ , are found by integrating the joint histogram over all the buoyancy frequency bins.  $f_s(S)$  is calculated by

$$f_s(S_j) = \sum_{i=0}^{i_{\max}} f(N_i, S_j) \Delta N \quad (4.8)$$

and plotted for each of the depth ranges (Figure 4.5). The mean and variance (Table 4.1), like the buoyancy frequency, reaches a maximum at [100-125] m. and decreases steadily with depth. An increase in shear is seen at [275-300] m. ranges where velocity estimates have reduced signal to noise at the far range of the sonar.

The dependence of shear and buoyancy can be tested using the joint histograms. Some dependence is anticipated since both the mean shear and buoyancy frequency decrease with depth. Vertical advection through the fixed depth range bins will cause some dependence due to the vertical gradients of  $\bar{S}$  and  $\bar{N}$ . Since both decrease with depth, a positive correlation is expected.  $S$  and  $N$  are said to be independent if

$$f(N, S) = f^N(N)f^S(S) \quad (4.9)$$

Contour plots of  $f^N(N)f^S(S)$  for the nine depth ranges looks qualitatively nearly the same as those of  $f(N, S)$  except for the slight tilt in the contours (Figure 4.2). The differences are better illustrated by subtracting the independent distribution from the true distribution. By contouring only the regions where  $f(N, S) > f^N(N)f^S(S)$ , the positive correlation between  $S$  and  $N$  is clearly illustrated (Figure 4.3). Typically a Chi-squared test can be applied to determine if two variables are independent but these tests are extremely sensitive to oversampling of a distribution which is the case here (Pinkel and Anderson, 1992). The correlation coefficients are low (<0.15) but positive for all the depth ranges. Clearly there is a slight dependence of  $S$  and  $N$ , however this dependence appears to be very small. Kunze (1990) find that shear and strain are uncorrelated and suggest that most of the fine scale shear comes from near inertial waves.

The distribution of  $N$  can be modeled from statistics of fine scale strain. From Pinkel and Anderson (1992), strain,  $\gamma$ , sampled in fixed depth coordinates, is modeled as a Poisson process. The resulting distribution of  $\gamma$  is

$$p^E(\gamma | \bar{\Delta z}) = \frac{(\lambda^* \gamma)^{\lambda^*} e^{-\lambda^*}}{\Gamma(\lambda^*)} \quad (4.10)$$

where

$$\lambda = 1.1 \text{ m}^{-1}, \quad \lambda^* = \bar{\Delta z} \lambda, \quad \gamma = \frac{\Delta z}{\bar{\Delta z}} = \eta_z + 1$$

and  $\eta_z$  is the Eulerian strain (Appendix B). To estimate the corresponding buoyancy frequency distribution, the strain is defined by

$$\gamma = \eta_z + 1 = \frac{\rho_z}{\bar{\rho}} \approx \left( \frac{N}{\bar{N}} \right)^2 \quad (4.11)$$

where  $\bar{N}$  is the mean buoyancy frequency and  $N$  is calculated from (4.4). This transformation assumes the  $\bar{N}$  does not vary with depth. This yields the distribution

$$p_t(N | \bar{\Delta z}) = \frac{2}{\Gamma(\lambda^*)} \frac{N}{\bar{N}^2} \left( \lambda^* \left( \frac{N}{\bar{N}} \right)^2 \right)^{\lambda^*} e^{-\lambda^* \left( \frac{N}{\bar{N}} \right)^2}. \quad (4.12)$$

Note that  $\bar{\Delta}z$  is the differencing interval used in (4.4). Taking  $\bar{N}$  from each of the depth ranges (Table 4.1) and  $\bar{\Delta}z=10.0$  m.,  $p_N$  is fit to the histograms of  $N$  (Figure 4.4). Good qualitative agreement with sampled distributions at almost all depths can be seen by plotting the modeled pdf's with the histograms of  $N$ . The [75-100] m. depth range does not yield good agreement to the Poisson model. Apparently, mixed layer dynamics are significantly different than those in the thermocline. The [125-150] m. depth range does not appear to fit well with the model. This is likely due to rapid changes in  $\bar{N}$  at these depths.

To model the distribution of  $S$  it is useful to examine the individual components of shear,  $S_x$  and  $S_y$ , where

$$S = |\mathbf{u}_z| = (S_x^2 + S_y^2)^{\frac{1}{2}} \quad (4.13)$$

The two components of shear sampled by the sonar have normal distributions, have small correlation coefficients and are thus independent. This independence and normal distribution of the shear components has been seen by Gregg (1991) and was assumed in the Garret and Munk internal wave models. The square root of the sum of two independent and normally distributed variables is described by the Chi distribution with 2 degrees of freedom (Papoulis, p.105 & p.250). The Chi distribution for the case 2 degrees of freedom (also called the Rayleigh distribution) is defined for  $S$  as

$$p^S(S) = \frac{S}{\alpha^2} e^{-\frac{S^2}{2\alpha^2}} \quad (4.14)$$

where

$$\bar{S} = \alpha \sqrt{\frac{\pi}{2}} \quad \text{and} \quad \sigma_s^2 = \frac{\alpha^2}{2}.$$

The shear distribution,  $p^S$ , is calculated for each of the nine depth ranges using the mean from the corresponding histograms (Figure 4.5). Good qualitative agreement to the sampled shear histograms can be seen at all but the [75-100] m. depth range where mixed layer dynamics may be playing an important role in shear statistics.

#### 4.3. Froude Number Distribution

Histograms of  $Fr$  are calculated over the same nine depth ranges as used for the shear and buoyancy frequency distributions (Figure 4.6). Between 100 and 250 meters, the distributions of  $Fr$  appear nearly identical with little change in mean and variance (Table 4.1). Increased mean and variance is observed below 250 m. and above 100 m.

The distribution of  $Fr$  is determined using the joint distribution of  $S$  and  $N$ . For two variables,  $x$  and  $y$ , for which the joint distribution,  $f(x,y)$ , is known, the distribution of the ratio of the two variables,  $v$ , is given by (Papoulis, p. 197)

$$f_v(v) = \int_{-\infty}^{\infty} |y| f(vy, y) dy \quad \text{where } v = \frac{x}{y}. \quad (4.15)$$

Since the Froude number is the ratio of  $S$  and  $N$ , its distribution is given by

$$p^{Fr}(Fr) = \int_0^{\infty} N p(FrN, N) dN \quad (4.16)$$

where  $p(S, N)$  is the joint distribution of  $S$  and  $N$ . Assuming that  $S$  and  $N$  are independent, the joint distribution is

$$\begin{aligned} p(S, N) &= p^S(S)p^N(N) \\ &= \left( \frac{2}{\alpha^2 \bar{N}^2 \Gamma(\lambda^*)} \right) \left( \frac{\lambda^*}{\bar{N}^2} \right)^{\lambda^*} N^{2\lambda^*+1} S e^{-\left( \lambda^* \left( \frac{N}{\bar{N}} \right)^2 + \frac{S^2}{2\alpha^2} \right)} \end{aligned} \quad (4.17)$$

The joint histograms demonstrated that these variables are not completely independent, but the dependence, especially below 125 m., appears to be small and correlation factors estimated for  $S$  and  $N$  at constant depth are less than 0.15. Substituting (4.17) into (4.16) yields

$$p^{Fr}(Fr) = \left( \frac{2}{\alpha^2 \bar{N}^2 \Gamma(\lambda^*)} \right) \left( \frac{\lambda^*}{\bar{N}^2} \right)^{\lambda^*} Fr \int_0^{\infty} N^{2\lambda^*+3} e^{-N^2 \left( \frac{\lambda^*}{\bar{N}^2} + \frac{Fr^2}{2\alpha^2} \right)} dN \quad (4.18)$$

By solving the integral in (4.18) and reducing, we obtain

$$p^{Fr}(Fr) = \frac{2qFr(\lambda^*+1)}{(qFr^2+1)^{\lambda^*+2}} \quad (4.19)$$

where

$$q = \frac{\bar{N}^2}{2\alpha^2 \lambda^*} = \frac{\pi}{4\lambda^*} \frac{\bar{N}^2}{\bar{S}^2} = \frac{1}{4\lambda^*} \frac{\bar{N}^2}{\sigma_s^2}. \quad (4.20)$$

The probability density distribution function  $p^{Fr}$ , is controlled by the parameters  $\lambda^*$  and  $q$ . The  $\lambda^*$  parameter (Pinkel and Anderson; 1991) determines the general shape of the distribution and contains an strain scale factor  $\lambda = 1.1 \text{ m}^{-1}$ , and the vertical differencing interval,  $\Delta z$ . The  $q$  parameter scales the distribution and is a function of  $\lambda^*$ , the mean buoyancy frequency,  $\bar{N}$ , and the shear variance,  $\sigma_s^2$ . The probability of the exceeding the shear instability threshold is found by integrating (4.19)

$$\begin{aligned}
 P(Fr \geq 2) &= \int_2^{\infty} p^{Fr}(Fr) dFr \\
 &= (4q + 1)^{-(\lambda + 1)}
 \end{aligned} \tag{4.21}$$

From (4.21) it can be seen that increasing the shear variance or decreasing the differencing interval will increase the likelihood of a shear instability.

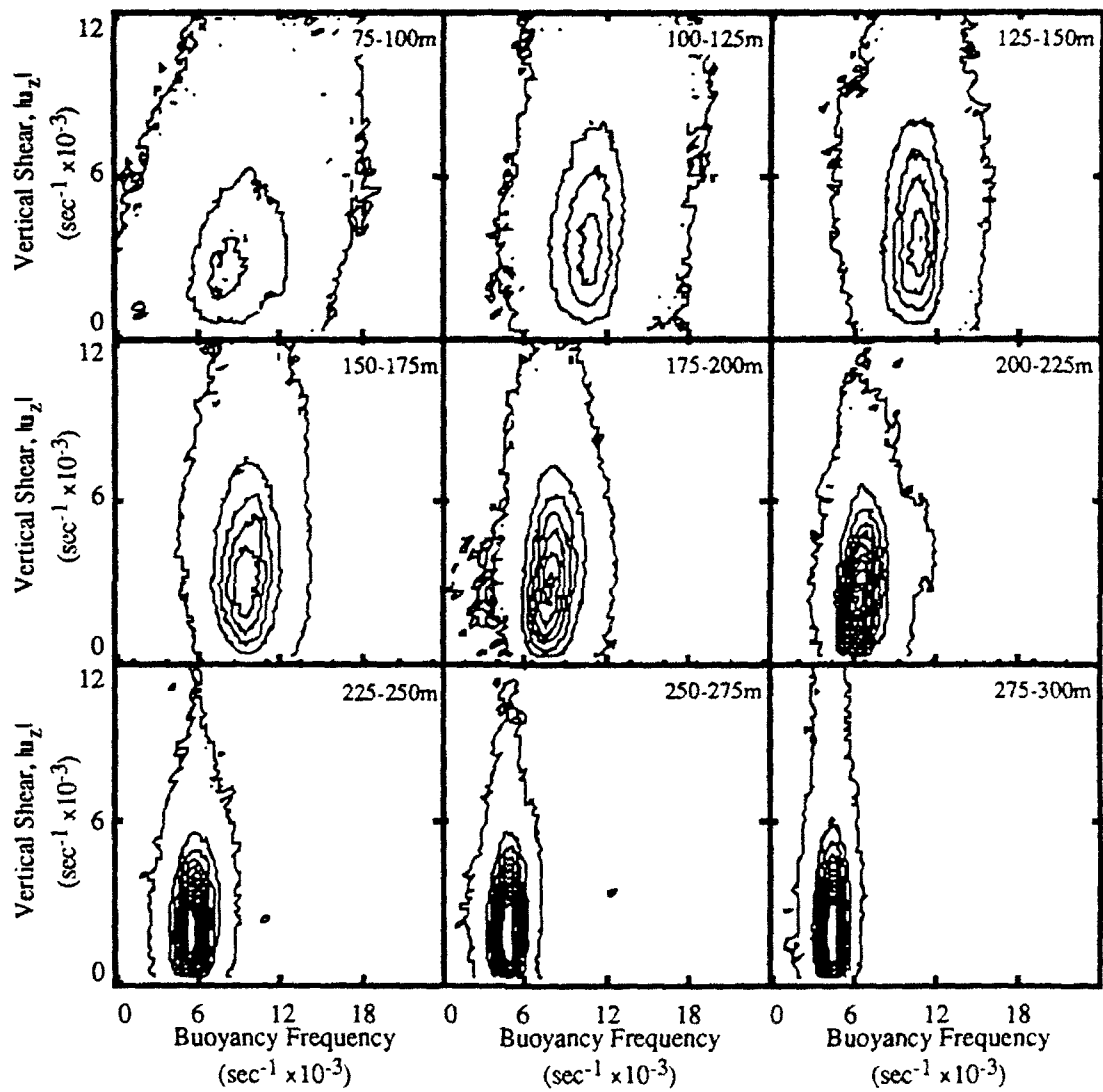
The modeled Froude number distributions are fit to the histograms in the nine depth ranges using the mean Froude numbers estimated from the histograms (Table 4.1 and Figure 4.6). Good model agreement can be seen from 125 to 275 meters, and the Froude number and shape of the distributions are nearly constant with depth. At shallower depths, [75-125] m., the model fails since shear and strain depart from their modeled distributions and have increased dependence.

The model should be valid for different scales assuming that shear and strain estimates are independent. The model distribution from Pinkel and Anderson (1992) includes scales down to 2 m. The individual components of shear are still likely to be independent and normally distributed over a broad range of scales. To demonstrate this scaling, the model is compared to data collected by Kunze (1990) using the neutrally buoyant float, RiNo, during PATCHEX (1985) of the coast of central California. The float, deployed at depths 180-200 m from October 12 to 22, yielded simultaneous shear and strain estimates calculated over 1 m, 2.5 m, and 5 m. separations. Using the shear and strain, Kunze (1990) calculate Froude Numbers and present histograms corresponding to 1 m, 2.5 m, and 5 m separations. Kunze (1990) shows that the distribution of Froude numbers changes form during the presence of an inertial wave group. The model distribution is fit to those of Kunze (1990) by using Figure 13 (from Kunze) to estimate the mean shear to mean buoyancy frequency ratio for each separation and then calculating the corresponding  $q$  parameter. The separations,  $\bar{\Delta}z$ , are 1 m, 2.5 m, and 5 m and  $\lambda = 1.1$  (Pinkel and Anderson, 1992). It is not clear whether averages reported by Kunze (1990) are from the full duration of the deployment, however, good model agreement can be seen from the distributions on 18-22 October (Figure 4.7). Kunze (1990) report 11% of the estimates of  $Fr$  at 1 m spacing are greater than 2 and unstable. From (4.21) with  $\bar{\Delta}z = 1$  and  $q = 0.4425$ , the model estimates that  $P(Fr \geq 2) = 0.125$ . The model is consistent with the observations.

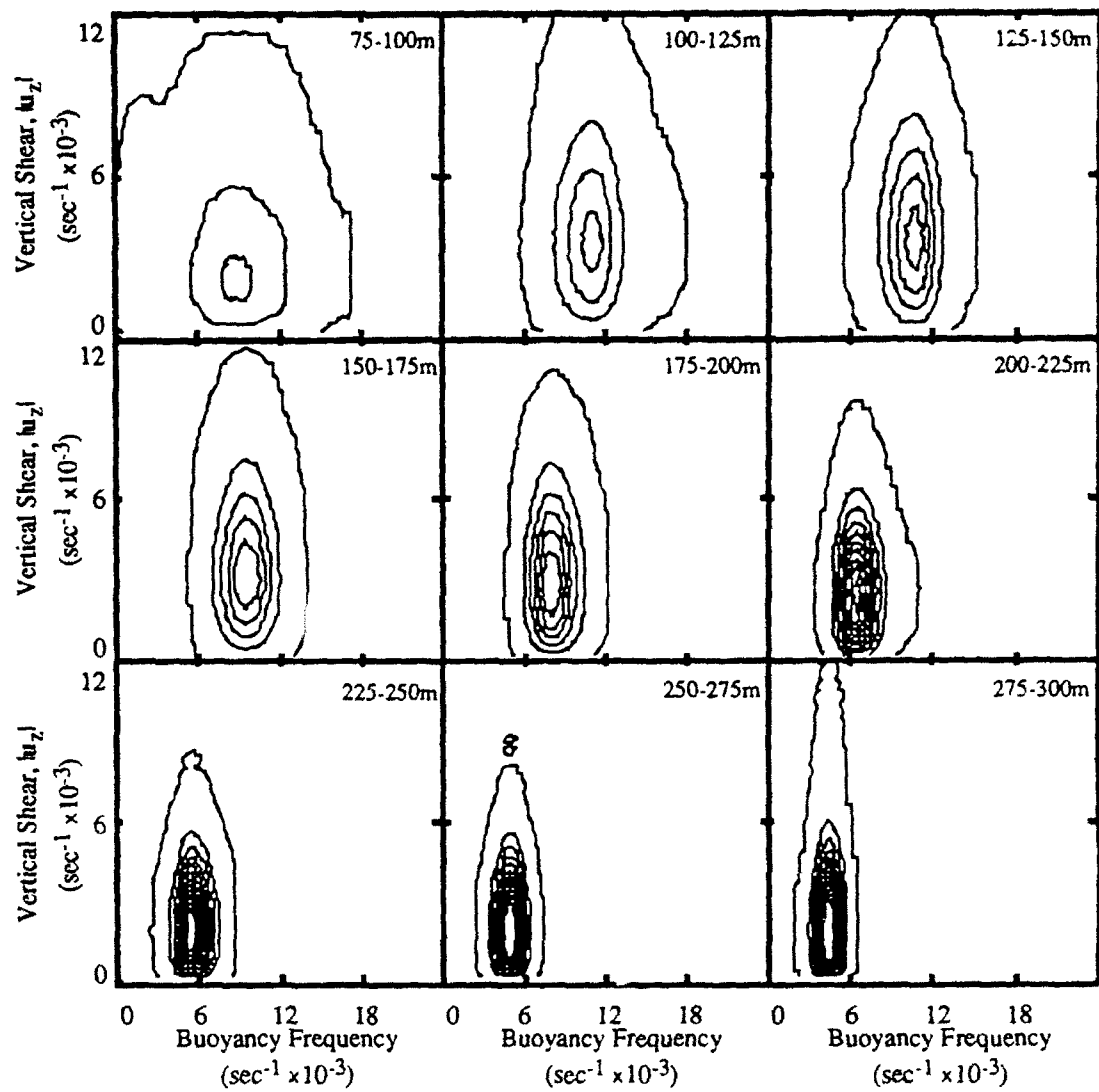
#### 4.4. Conclusions

The probability distribution function of Froude number is modeled using known distributions of vertical strain and vertical shear. The derivation assumes that shear and buoyancy are independent variables. Joint histograms of buoyancy frequency and shear demonstrate that there is small dependence on buoyancy frequency of shear with a positive correlation but that the assumption of independence is an appropriate approximation. The distribution of strain is Poisson as modeled by Pinkel and Anderson

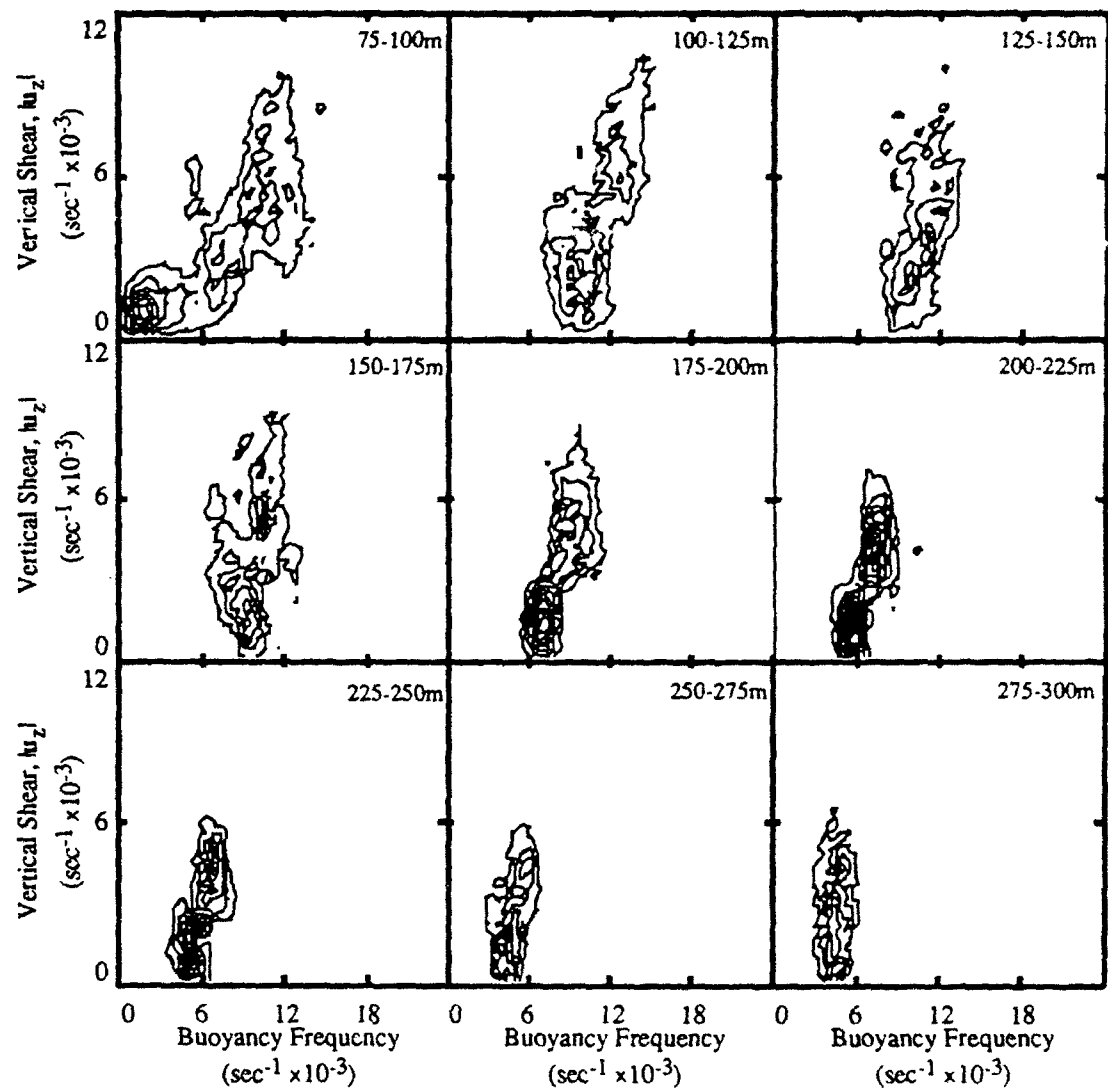
(1991) and related directly to the distribution of buoyancy frequency. The distribution of the absolute value of shear is Rayleigh distribution with each component of shear having a normal distribution and being independent. The resulting Froude number distribution has two parameters. The first is  $\lambda^* = \lambda \bar{\Delta z}$  from the Pinkel and Anderson (1992) model where  $\lambda = 1.1$  and  $\bar{\Delta z}$  is the vertical scales over which the Froude number is calculated. The second parameter,  $q$ , scales with the square of the ratio of the mean buoyancy frequency to the mean shear.



**Figure 4.1** Joint Histograms of Vertical Shear and Buoyancy Frequency. Shear and buoyancy frequency calculations are made over 10 meter depth intervals and histograms represent nine 25 m. depth bin ranges. Normalized histograms are contour plotted for each depth range. Each histogram represents approximately 50000 estimates of shear and strain.



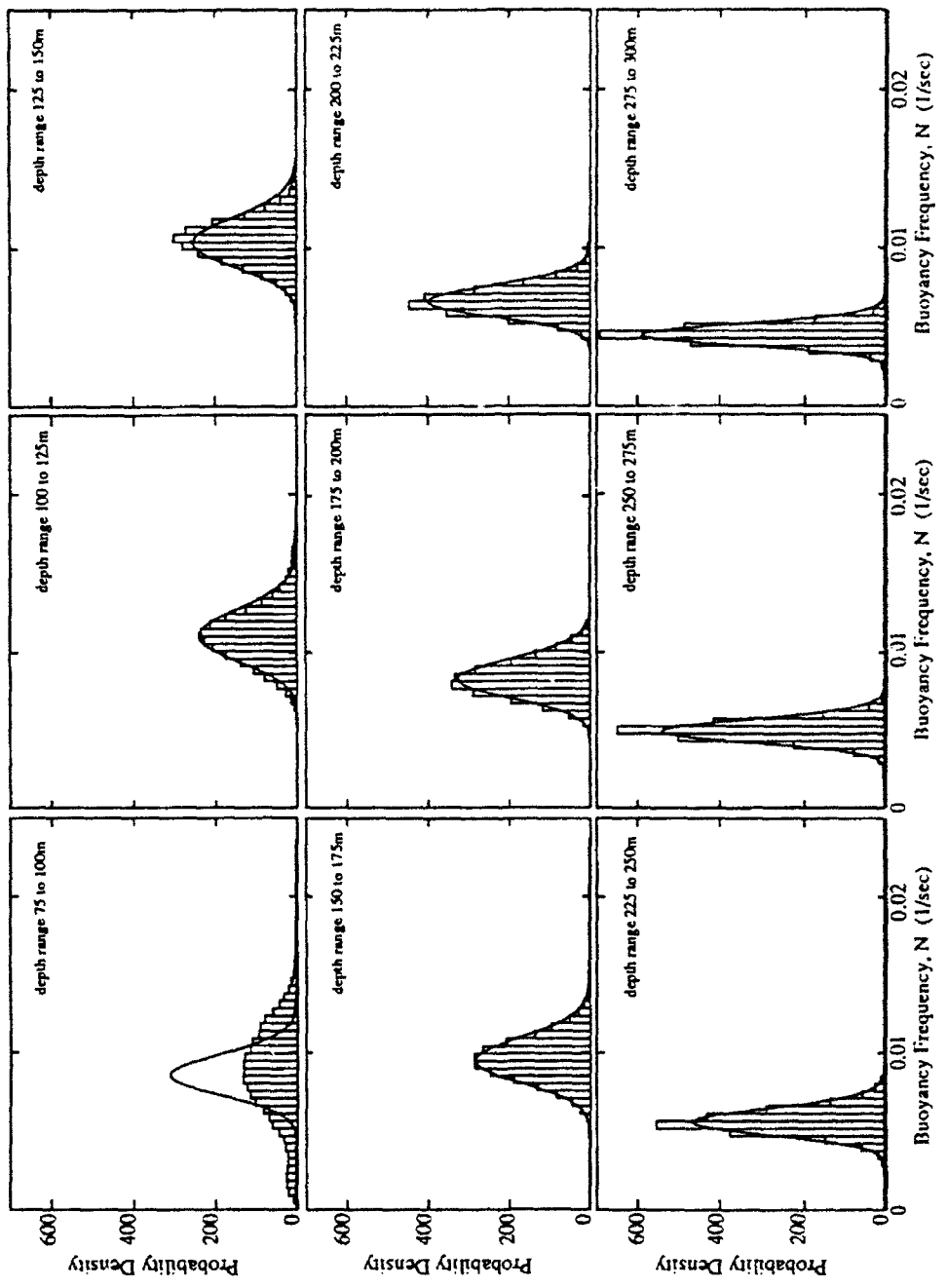
**Figure 4.2** Probability Distribution of Independent Shear and Buoyancy Frequency.



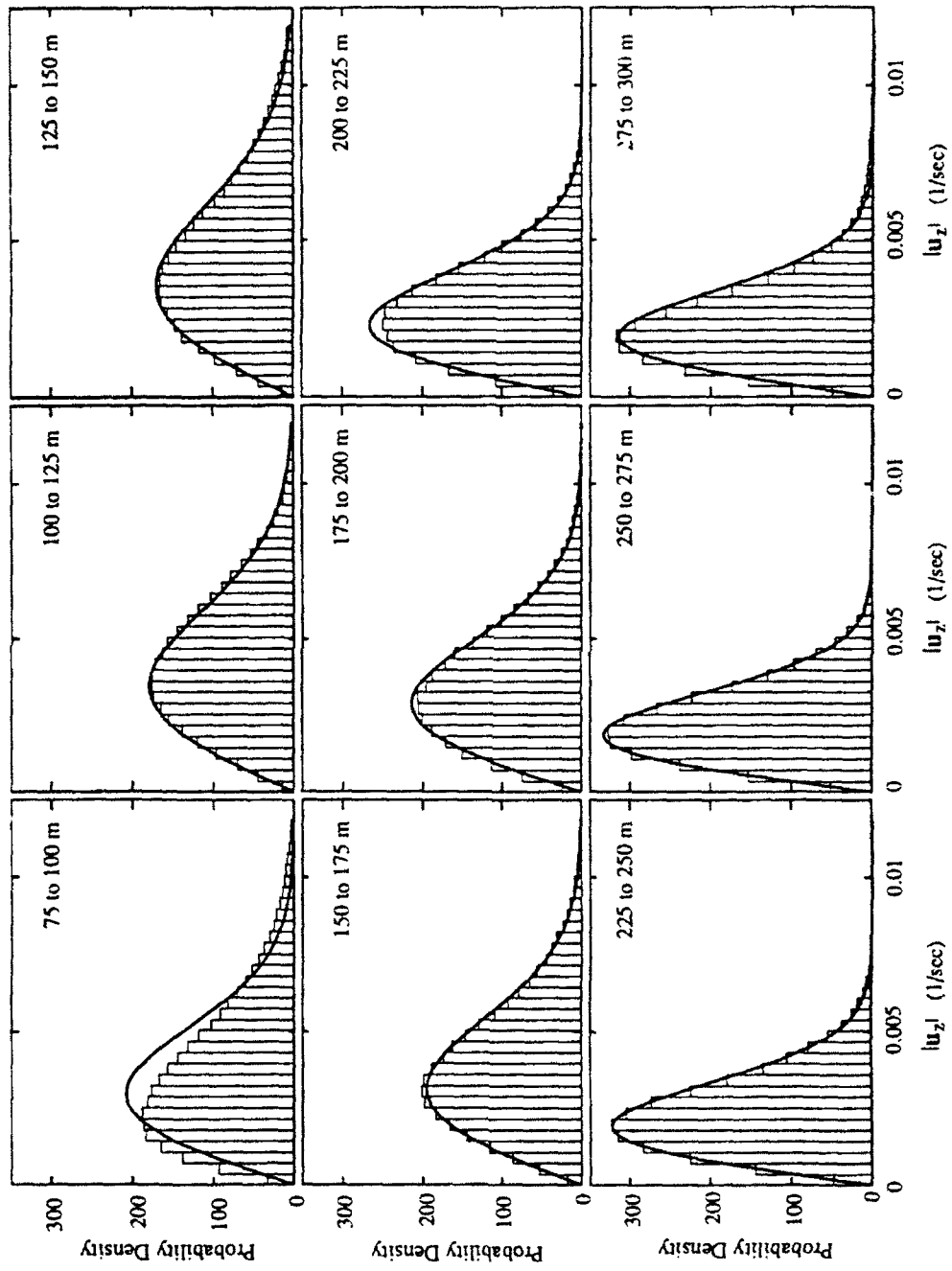
**Figure 4.3** Difference Between Independent and Sampled Joint Distributions.

Table 4.1 *Probability Distribution Parameters*.

Depth range (meters)	ave( $N$ ) (sec $^{-1}$ )	var( $N$ ) (sec $^{-2}$ )	ave( $S$ ) (sec $^{-1}$ )	var( $S$ ) (sec $^{-2}$ )	ave(Fr)	var(Fr)	q	ave( $S$ )/ ave( $N$ )
50-75	4.40x10 $^{-3}$	9.28x10 $^{-6}$	3.34x10 $^{-3}$	6.16x10 $^{-6}$	1.01	0.548	0.070	0.759
75-100	8.70x10 $^{-3}$	9.68x10 $^{-6}$	3.67x10 $^{-3}$	5.13x10 $^{-6}$	0.466	0.122	0.329	0.422
100-125	1.10x10 $^{-2}$	3.54x10 $^{-6}$	4.45x10 $^{-3}$	5.69x10 $^{-6}$	0.400	0.054	0.446	0.405
125-150	1.05x10 $^{-2}$	2.00x10 $^{-6}$	4.27x10 $^{-3}$	4.73x10 $^{-6}$	0.427	0.057	0.392	0.407
150-175	9.60x10 $^{-3}$	1.95x10 $^{-6}$	3.88x10 $^{-3}$	4.27x10 $^{-6}$	0.404	0.052	0.437	0.405
175-200	8.20x10 $^{-3}$	1.44x10 $^{-6}$	3.54x10 $^{-3}$	3.70x10 $^{-6}$	0.430	0.059	0.386	0.432
200-225	6.70x10 $^{-3}$	9.13x10 $^{-7}$	2.88x10 $^{-3}$	2.48x10 $^{-6}$	0.425	0.062	0.395	0.430
225-250	5.70x10 $^{-3}$	6.37x10 $^{-7}$	2.38x10 $^{-3}$	1.71x10 $^{-6}$	0.420	0.063	0.405	0.417
250-275	4.90x10 $^{-3}$	4.00x10 $^{-7}$	2.29x10 $^{-3}$	1.58x10 $^{-6}$	0.477	0.091	0.313	0.468
275-300	4.50x10 $^{-3}$	3.31x10 $^{-7}$	2.43x10 $^{-3}$	2.22x10 $^{-6}$	0.568	0.167	0.221	0.541



**Figure 4.4 Histograms of Buoyancy Frequency.** Buoyancy frequency histograms are found by integrating joint histograms. Buoyancy frequency calculations are made over 10 meter depth intervals and represent nine 25 m. depth bin ranges. The solid curves are corresponding model distributions from Pinkel and Anderson (1991).



**Figure 4.5 Histograms of Vertical Shear.** Shear histograms are found by integrating joint histograms over buoyancy frequency. Shear calculations are made over 10 meter depth intervals and represent nine 2.5 m. depth bin ranges. The solid curves are the corresponding Rayleigh probability distributions.

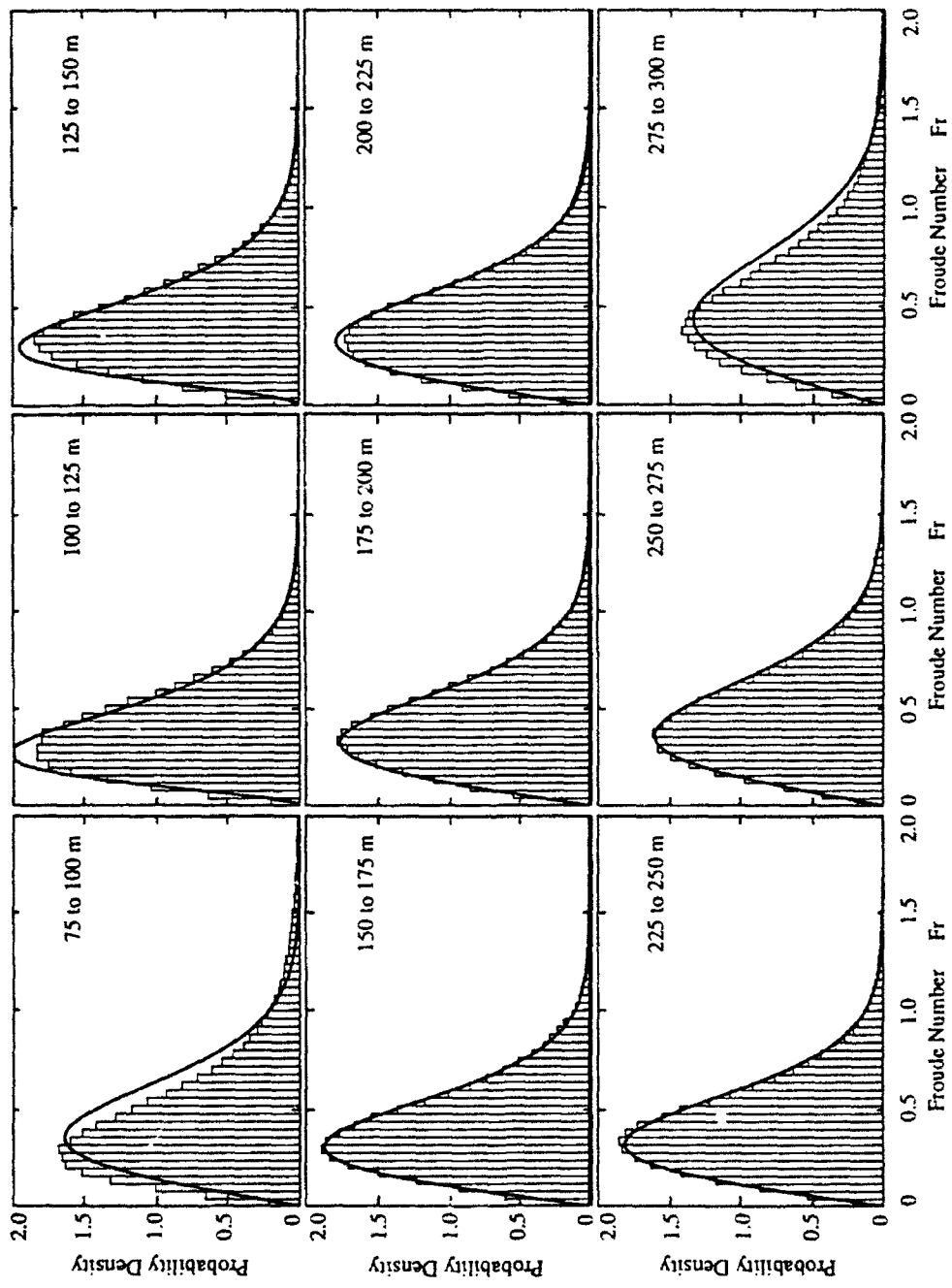


**Figure 4.6 Histograms of Froude Number** Froude number calculations are made over 10 10 meter depth intervals and represent nine 25 m. depth bin ranges.. The solid curves are corresponding modeled distribution. The model distribution assumes that shear and strain are independent.

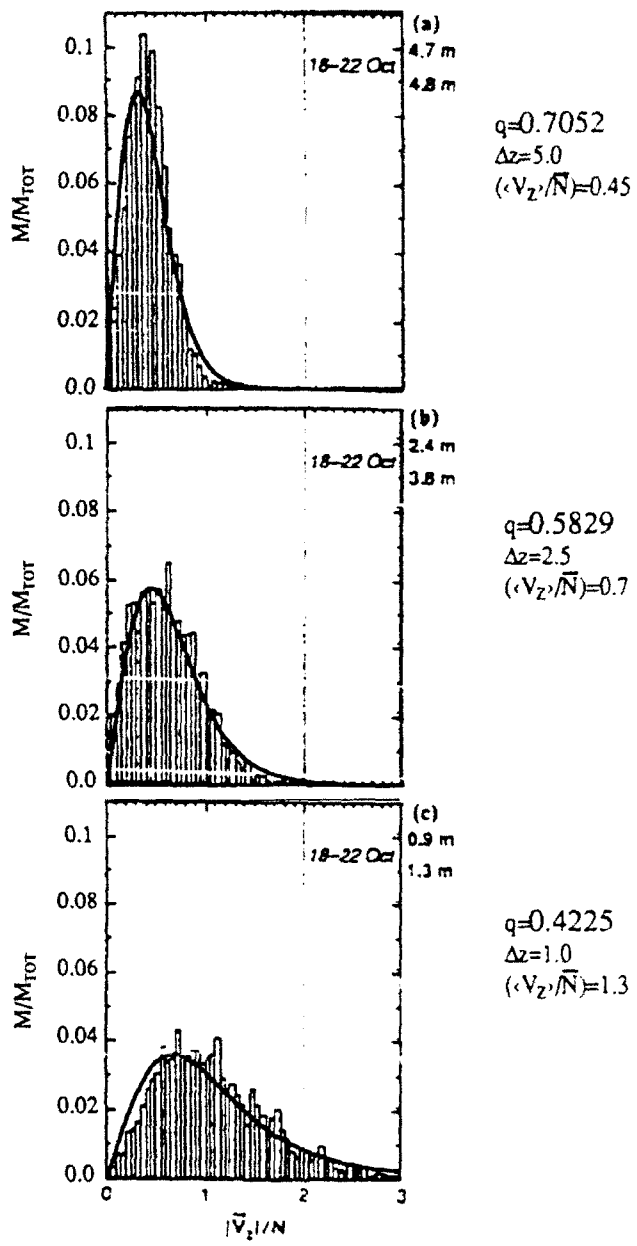


**Figure 4.7 Distributions of Froude Number from a Neutrally Buoyant Float (Kunze et al.; 1990).** Froude histograms are from Kunze et al. (1990) and were collected the RiNo float during PATCHEX (October, 1986). The instrument was deployed at a depth of 180-200m. The histograms are from 18 -22 Oct. and represent 3 vertical differencing intervals: 1 m, 2.5 m, and 5 m. The solid line overlaid on the histograms is the modeled distribution using mean shear to buoyancy frequency ratio estimated from Figure 13.b, Kunze et al. (1990).

## Appendix A

### Surface Wave Processes Program (SWAPP) Overview

The Surface Wave Processes Program (SWAPP) was conceived as an experiment to study mixed layer dynamics, Langmuir circulation and surface wave growth. The SWAPP experiment was located at 35° 8.2' N, 126° 59.0' W (Figure A.1) where FLIP was moored from February 22 to March 18, 1990. The CSS PARIZEAU was in the region from February 26 to March 18, 1990.

Principle investigators participating in the experiment included J. Smith (SIO), R. Pinkel (SIO), A. Plueddemann (WHOI), R. Weller (WHOI), W. Crawford (IOS) and D. Farmer (IOS). Mixed layer current measurements were made from FLIP using two strings of Vector Measuring Current Meters (WHOI). Surface currents and waves were sampled using a surface scattering acoustic Doppler array and a resistance wave wire array (SIO). Two down looking Doppler sonar systems (161 kHz and 67/80 kHz) mounted on FLIP monitored the internal wave activity (SIO). Density measurements were made with two continuously profiling CTD's (SIO). Profiles of turbulence in the mixed layer were made with the Fast Light Yo-yo II (FLY II; IOS) deployed from the CSS PARIZEAU. Meteorological measurements were taken from FLIP using a Vector Averaging Wind Recorder (VAWR; WHOI), an Improved Meteorological (IMET; WHOI) system and sonic anemometers (WHOI).

Meteorological Data was compiled by the group from W. H. O. I. (Figure A.2). Wind speed data was taken from the mast of FLIP. Wind velocities greater than 10 m/s occurred on yeardays 60, 64, 67 and 70. During the experiment, the sea surface temperature stayed between 13° and 14°C while the air temperature ranged from 9° to 14°C. The total heat flux was dominated by a diurnal cycle with daytime heating matched by nighttime cooling.

Strong frontal activity in the upper ocean occurred during the experiment. Satellite IR-imaging of the area, although hindered by cloud cover, showed strong fronts in surface temperature to the north and south of the SWAPP location. An extensive expendable bathy-thermogram (XBT) survey taken from the USS NAVAJO from February 20 to February 28, 1990 also shows strong frontal activity in the area. Thirty out of fifty XBT temperature profiles yielded reliable data to 400m depth and were used in the contour plots in Figure A.3. The survey covered a 100 km square area around FLIP. The average temperature from the surface to 20m (Figure A.3a) reveals a "S" shaped front with temperatures decreasing 1.6° from the northwest to the southeast. The average temperature from the surface to 20-100m (Figure A.3b) shows a similar shape with temperatures decreasing 2.0° from the northwest to the southeast. This near surface

front is not apparent at 100-200m (Figure A.3c) where temperatures range from 9.5° to 10.1°. At 200-400m (Figure A.3d), a deep front occurs with temperatures decreasing 1.0° from the southeast to the northwest, opposing the surface temperature gradient. Temperature-salinity scatter plots also show evidence of two distinct water masses in the 200-400m near the experiment site depth range (Figure 3.1).

The vertical density structure measured during SWAPP is typical of that historically found in the area (Figure A.4). The depth of the mixed layer is ~100 meters which is deeper than found in PATCHEX(Oct.-Nov., 1986) and MILDEX(Oct., 1983); two upper ocean studies conducted in the area (Figure A.5). This is expected since SWAPP occurred in the spring when the mixed layer has nearly reached its maximum depth. However, cruise averaged density profiles from MILDEX, PATCHEX and SWAPP all converge at about 200 meters depth.

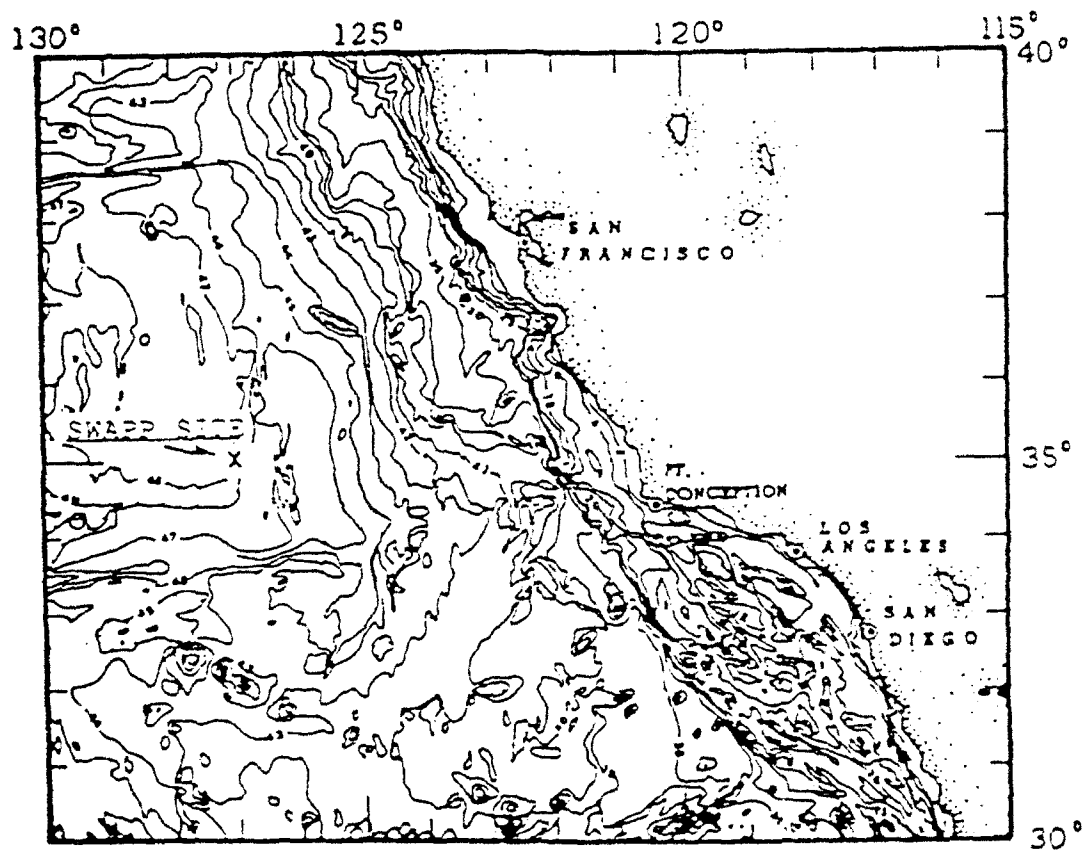


**Figure A.1** The SWAPP site. The Surface Waves Processes Program (SWAPP) experiment took place approximately 500 miles off the coast of California southwest of San Francisco. R/P FLIP was moored at  $35^{\circ} 8.2' N$ ,  $126^{\circ} 59.0' W$  from February 22 to March 18, 1990. Depth contours are in hundreds of meters.

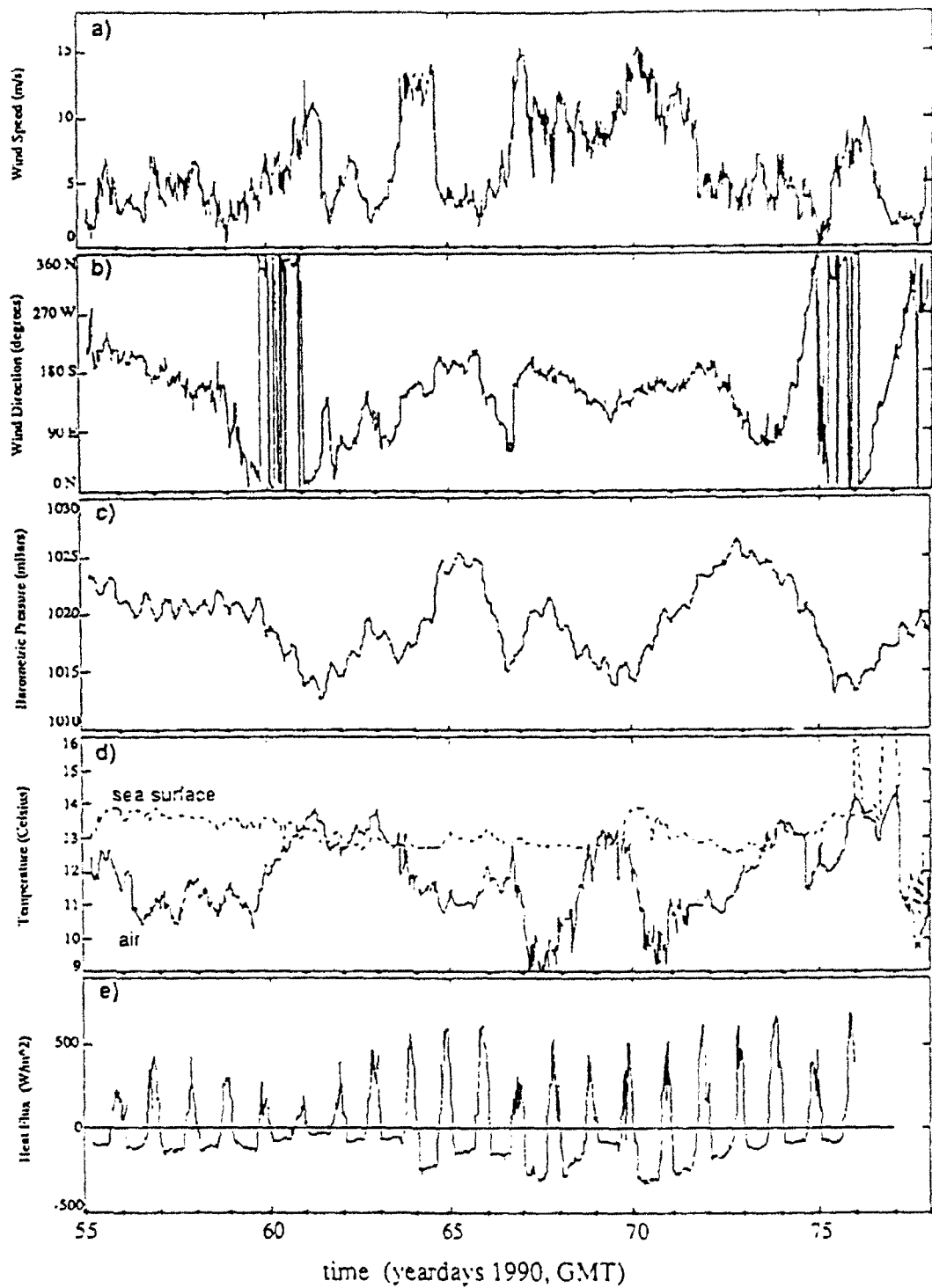


**Figure A.2a-e SWAPP Meteorological Data.** During the SWAPP experiment, the meteorological data was collected by the W. H. O. I. group led by R. Weller. Wind speed (a) and wind direction (b) were collected with the Vector Averaging Wind Recorder (VAWR). Barometric pressure is shown in (c). Sea Surface temperature (d; dashed line) is from the VMCM at 2.25m depth and is plotted along with air temperature (d; solid line). The total heat flux (e) is the sum of the estimated short-wave radiation, long-wave radiation, sensible heat flux and latent heat flux.

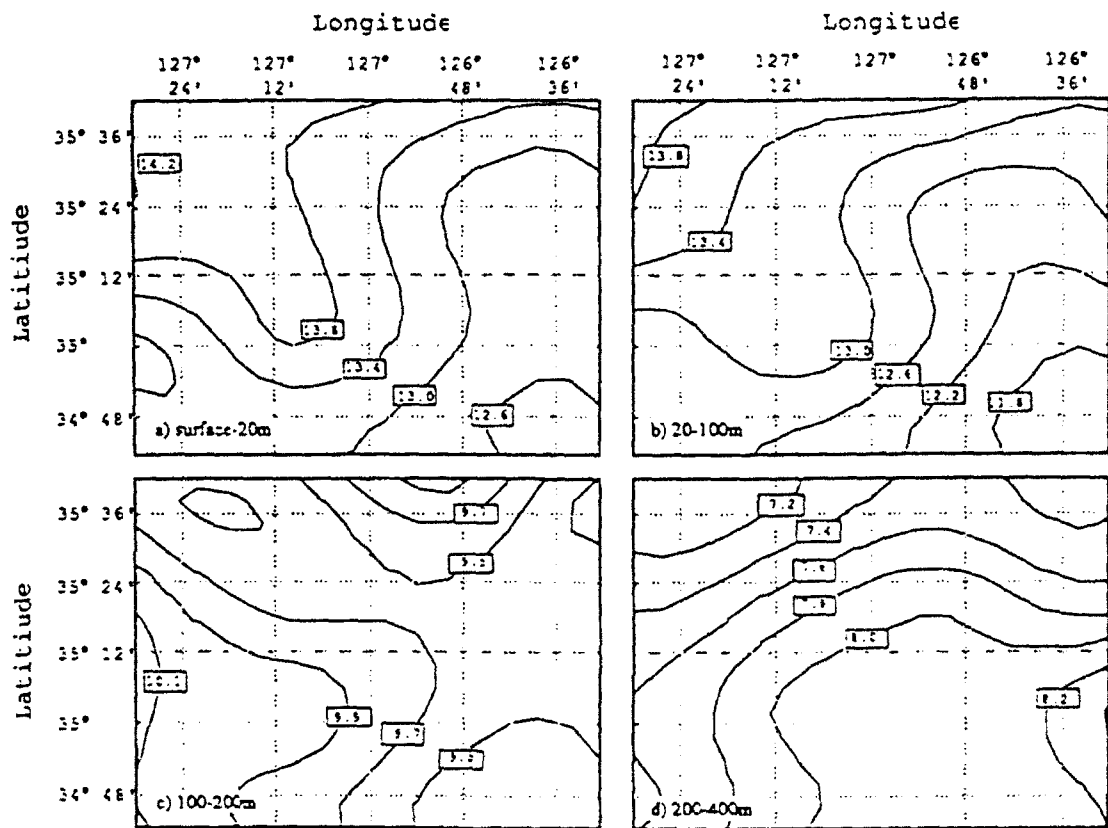


**Figure A.3a-d Depth Averaged Temperature Contours.** From February 20 to February 25 1990, Weller's Group from W. H. O. I. performed an XBT survey from the Navajo. From 57 temperature profiles taken, 30 are selected here which appear reliable down to 400 meters. For the contour plots, temperature profiles from the XBT survey are averaged in four depth ranges: (a) surface to 20 meters, (b) 20 to 200 meters, (c) 100 to 200 meters and (d) 200 to 400 meters. These depth averaged temperatures are contoured with labels in degrees Celsius. The survey reveals a strong front. Near surface water temperature increases by 2° C from southeast to northwest, while the water temperature below 200 meters decreases by 1° C.

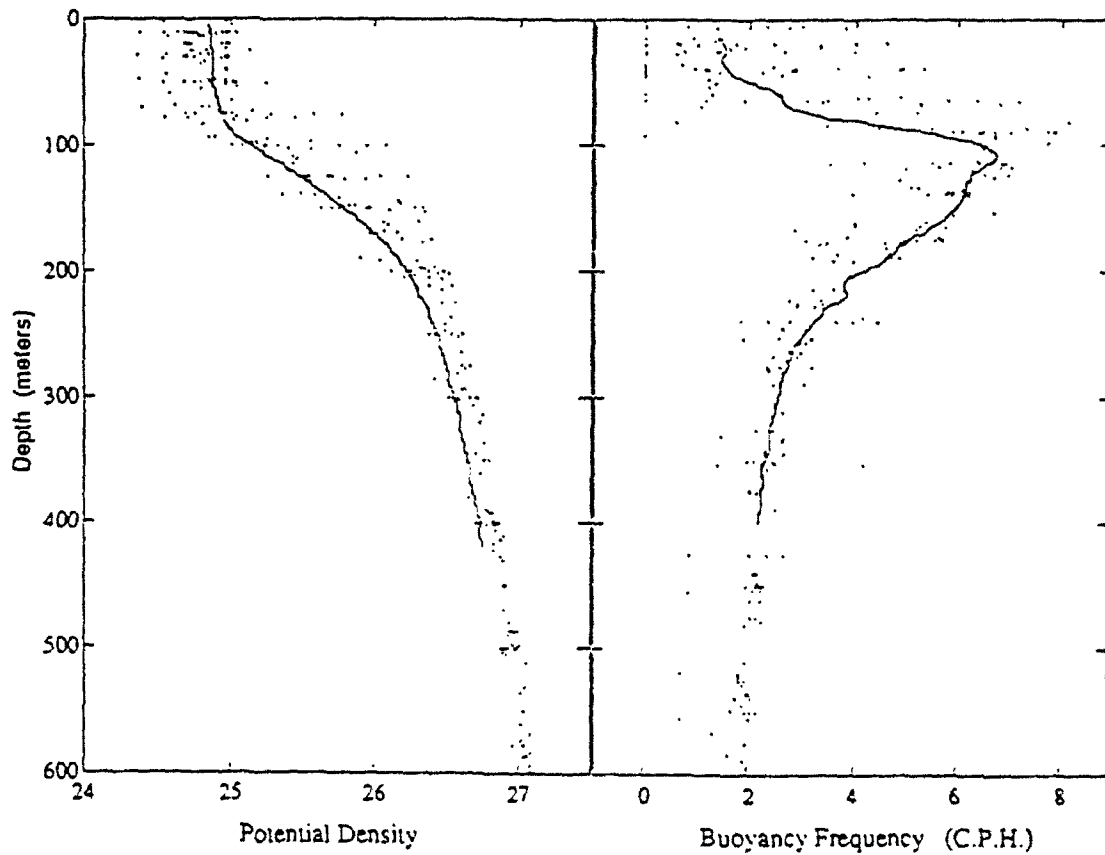


**Figure A.4 Historic Hydrographic data and Cruise Averaged Potential Density.** The historic hydrographic data is from J. Ried's hydrosearch on the computer 'nemo' which contains a database of physical-chemical oceanographic stations from around the world. 25 stations were found that occurred during February and March between the latitudes 34° N and 36° N and the longitudes 126° W and 128° W. The data spans 34 years from 1950 to 1984. Most of the stations extend to 600-1500m depth while 4 stations contain data to full ocean depths. Plotted here are the potential densities and buoyancy frequencies from the hydrographic data (dots) and the SWAPP cruise averaged profiles (solid line). The SWAPP data falls within the scatter of the historic data.

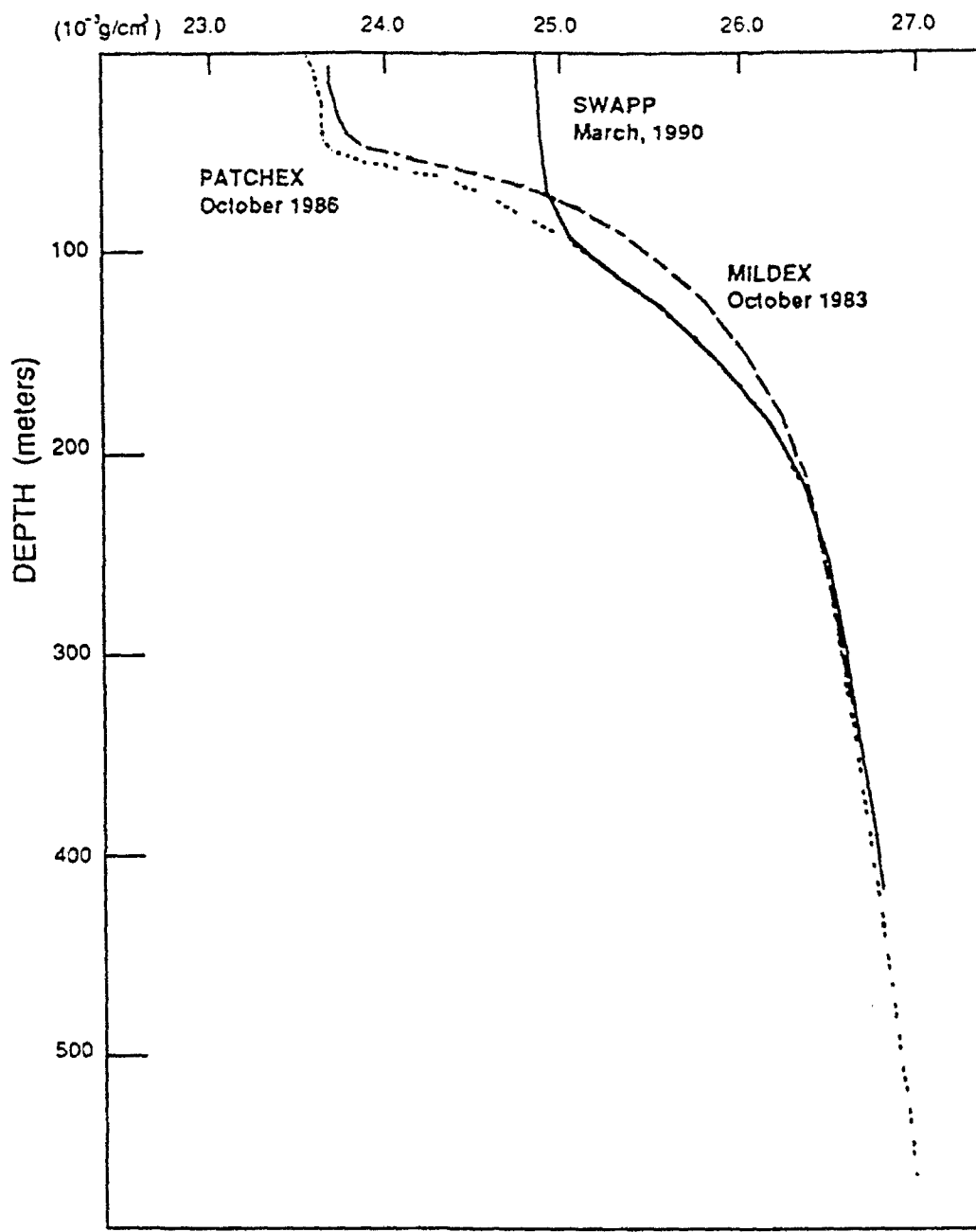


**Figure A.5 Cruise Averaged Potential Density.** The MILDEX data (dashed) was taken for 14 days during October/November 1983 while FLIP drifted near  $34^{\circ}\text{N}$ ,  $126^{\circ}\text{W}$ . The PATCHEX data (dotted) was taken for 21 days during October 1986 while moored at  $34^{\circ}\text{N}$ ,  $127^{\circ}\text{W}$ . The SWAPP data (solid) was taken for 20 days during February/March 1990 while moored at  $35^{\circ}\text{N}$ ,  $127^{\circ}\text{W}$ . Cruise averaged potential density is plotted versus depth. Note that MILDEX and PATCHEX both took place during the fall and have a much shallower mixed layer depth than SWAPP which took place in late winter.

## Appendix B

### Review of Linear Internal Wave Theory

#### B.1. Equations of Motion.

In this section, a review of linear internal gravity wave theory is presented. This will give a general framework for linear internal waves used in the discussion of the measured internal wave field.

It will be assumed the flow field is incompressible, inviscid, and continuously stratified. The continuity equation in this case is

$$\frac{\partial u}{\partial x} + \frac{\partial v}{\partial y} + \frac{\partial w}{\partial z} = 0 \quad (\text{B.1})$$

where  $u$ ,  $v$  and  $w$  are the components for the fluid velocity in the  $x$ ,  $y$  and  $z$  directions respectively. In a rotating fluid, the linearized momentum equations for small perturbations in pressure,  $p'$ , and density,  $\rho'$ , are

$$\begin{aligned} \frac{\partial u}{\partial t} - fv &= -\bar{\rho}^{-1} \frac{\partial p}{\partial y} \\ \frac{\partial v}{\partial t} + fu &= -\bar{\rho}^{-1} \frac{\partial p}{\partial y} \\ \frac{\partial w}{\partial t} &= -\bar{\rho}^{-1} \left( \frac{\partial p'}{\partial z} + \rho' g \right) \end{aligned} \quad (\text{B.2})$$

where  $\bar{\rho}(z)$  is the unperturbed density,  $g$  is the acceleration of gravity and  $f$  is the Coriolis parameter. The linearized pressure equation is

$$\frac{\partial p'}{\partial t} + w \frac{\partial \bar{\rho}}{\partial z} = 0 \quad (\text{B.3})$$

By making the Boussinesq approximation ( $w$  varies much more rapidly in the vertical than  $\rho_o$ ), linear traveling plane wave solutions to the above equations of motion can be found. The solutions are of the form

$$\begin{aligned}
w &= W_0 e^{i(kx+ly+mz-\omega t)} \\
u &= \frac{-m}{(k^2+l^2)} \left( k + il \frac{f}{\omega} \right) W_0 e^{i(kx+ly+mz-\omega t)} \\
v &= \frac{-m}{(k^2+l^2)} \left( l - ik \frac{f}{\omega} \right) W_0 e^{i(kx+ly+mz-\omega t)} \\
\rho' &= -\frac{i\rho_0}{g\omega} N^2 W_0 e^{i(kx+ly+mz-\omega t)}
\end{aligned} \tag{B.4}$$

with the linear dispersion relation

$$\omega^2 = \frac{(f^2 m^2 + N^2 (k^2 + l^2))}{(k^2 + l^2 + m^2)} \quad \text{for } f \leq \omega \leq N. \tag{B.5}$$

This highest frequency of oscillation is the Brunt-Väisälä frequency or buoyancy frequency,  $N$ , and is defined as

$$N(z)^2 = -g\bar{\rho}^{-1} \frac{d\bar{\rho}(z)}{dz}. \tag{B.6}$$

## B.2. Counter Clockwise to Clockwise Rotating Shear Ratio.

Consider an internal wave traveling in the positive  $x$  direction ( $l=0$ ), the phase is propagating in the positive  $z$  direction and energy is propagating in the negative  $z$  direction. If  $z=0$  at the ocean surface and  $z$  increases with increasing depth, then energy is traveling down from the surface. Since the interest here is to study the velocity field in time and depth, the horizontal coordinate,  $x$ , is set equal to zero. The Eulerian velocity field for this internal wave is defined by

$$\begin{aligned}
w &= W_0 \cos(mz - \omega t) \\
u &= -\frac{m}{k} W_0 \cos(mz - \omega t) \\
v &= -\frac{m}{k} \frac{f}{\omega} W_0 \sin(mz - \omega t) \\
\rho' &= -\frac{\bar{\rho}}{g\omega} N^2 W_0 \sin(mz - \omega t)
\end{aligned} \tag{B.7}$$

where the internal wave dispersion relation is

$$\frac{m}{k} = \left( \frac{\omega^2 - N^2}{f^2 - \omega^2} \right)^{\frac{1}{2}}, \quad \text{for } f < \omega < N. \tag{B.8}$$

Solving for the vertical shear field for this internal wave yields.

$$\begin{aligned}\bar{u}_z &= \frac{du}{dz} + i \frac{dv}{dz} \\ &= W_0 m \left( \frac{\omega^2 - N^2}{f^2 - \omega^2} \right)^{\frac{1}{2}} \left( \sin(mz - \omega t) - i \frac{f}{\omega} \cos(mz - \omega t) \right)\end{aligned}\quad (\text{B.9})$$

Solving for the vertical shear spectrum obtains

$$\Phi_{u_z}(\tilde{m}, \tilde{\omega}) = \frac{W_0^2 m^2}{4} \left( \frac{\omega^2 - N^2}{f^2 - \omega^2} \right) \left[ \left( 1 + \frac{f}{\omega} \right)^2 \delta(\tilde{m} + m) \delta(\tilde{\omega} - \omega) + \left( 1 - \frac{f}{\omega} \right)^2 \delta(\tilde{m} - m) \delta(\tilde{\omega} + \omega) \right] \quad (\text{B.10})$$

The counter clockwise (CCW) to clockwise (CW) shear variance for this case is

$$\frac{ccw}{cw} = \left( \frac{\omega - f}{\omega + f} \right)^2 \quad (\text{B.11})$$

For the high frequency waves,  $\omega \gg f$ , spectral energy is found equally at both  $(+m, -\omega)$  and  $(-m, +\omega)$ . As  $\omega$  approaches the inertial frequency, however, energy is only found only at  $(-m, +\omega)$ . Extending this to a full spectrum of upward and downward propagating internal gravity waves, near inertial energy is found only in the  $(+m, +\omega)$  (counterclockwise, upward propagating phase, downward energy) quadrant and the  $(+m, -\omega)$  (clockwise, downward propagating phase, upward energy) quadrant. High frequency waves fill energy throughout all the quadrants in  $(m, \omega)$  space.

### B.3. Shear Variance to Strain Variance Ratio

Strain is defined here as the vertical derivative of vertical displacement. The vertical displacement,  $\eta$ , can be found by integrating the vertical velocity field to yield

$$\eta = \int w dt \quad (\text{B.12})$$

From the linearized pressure equation,  $\eta$  is found in terms of the perturbation density

$$\eta(z, t) = \frac{\rho'(z, t)}{\partial_z \rho_0} \quad (\text{B.13})$$

The Eulerian strain is the vertical derivative of the displacement field with respect to the vertical coordinate,  $z$ , and is defined as

$$\eta_z = \frac{\rho'_z}{\bar{\rho}_z} = \frac{\rho_z}{\bar{\rho}_z} - 1 \quad (\text{B.14})$$

where the density field is determined by a mean state and a fluctuating component due to internal waves,  $\rho(z,t) = \rho'(z,t) + \bar{\rho}(z)$ . The Eulerian strain is calculated by first differencing density in depth, normalizing each profile by the first differenced mean density profile and subtracting 1.0. The Semi-Lagrangian strain is the derivative of the displacement field with respect to the Semi-Lagrangian coordinate

$$\zeta = z - \eta \quad (\text{B.15})$$

and is calculated by taking the instantaneous difference between isopycnal displacement and dividing by the mean depth

$$\eta_\zeta = \frac{\partial \eta}{\partial \zeta} = \frac{\eta\left(\zeta + \frac{\Delta \zeta}{2}, t\right) - \eta\left(\zeta - \frac{\Delta \zeta}{2}, t\right)}{\Delta \zeta} \quad (\text{B.16})$$

The Semi-Lagrangian strain is related to the Eulerian strain by

$$\eta_\zeta = \left( \frac{d\zeta}{dz} \right)^{-1} \frac{\partial \eta}{\partial z} = \frac{\eta_z}{1 - \eta_z}. \quad (\text{B.17})$$

Linear internal wave theory (using equation B.4b-d) predicts a buoyancy frequency normalized strain variance to shear variance ratio of

$$N^2 \frac{\Phi_{\eta_z}(\omega)}{\Phi_{u_z}(\omega)} = N^2 \frac{|\eta_z|^2}{|\bar{u}_z|^2} = \frac{N^2}{N^2 - \omega^2} \left( \frac{\omega^2 - f^2}{\omega^2 + f^2} \right) \quad (\text{B.18})$$

for a spectrum of linearly superimposed waves.

## Appendix C

### CTD processing

Fine structure density estimates are made using conductivity, temperature and pressure data collected with two repeat profiling CTDs. Sea-Bird Electronics (SBE) instruments were deployed during SWAPP experiment in a similar arrangement as has been used in past upper ocean experiments on FLIP (Williams, 1983; Sherman, 1989). The conductivity sensors are model SED 4-01 ( $5 \times 10^{-5}$  S/m resolution at 12Hz), and the temperature sensors are model SBE 3-01/F ( $5 \times 10^{-4}$  °C resolution at 12Hz). The CTD sensors and a pressure case containing sampling electronics are mounted in a streamlined cage with a 55 kg lead weight in front to allow for high fall rates. During the SWAPP deployment, a SBE dual needle conductivity probe was placed in front of each instrument. The shape of the cage allows profiling only in one direction since all the sensors are in the instrument wake while being pulled to the surface. The cycle period was 130 seconds from the start of one profile to the beginning of the next and fall rates were 3.65 m/s. The upper CTD profiled from 5-220 meters and the lower CTD profiled from 200-420 meters. The temperature, pressure and conductivity sensors are sampled at 24 Hz and the dual needle probe is sample at 96 Hz. The upper CTD was operated from February 26 to March 18, 1990 collecting ~12000 profiles and the lower CTD was operated from March 1 to March 16, 1990 collecting ~9200 profiles.

A pitot tube equipped pressure sensor, used to measure the static pressure during profiling and is used to estimate depths,  $z$ . A typical profile of first differenced pressure shows a high frequency fluctuation associated with water turbulence (Figure C.1). Using a simple transformation from frequency to wavenumber assuming constant fall rate, a spectrum for the first differenced pressure reveals a +1 power law above 0.1 cpm. This is likely due to water turbulence and does not reflect real fluctuations in fall rate. The pressure signal is low pass filtered below 0.14 cpm to remove the turbulent noise. Note the spectral peak at 0.022 cpm corresponding to a pressure signal from a surface wave swell period of 12.5 seconds. The pressure data was then resampled at half the data rate.

Following the procedure developed by Williams (1985) with one slight modification, the time response of the temperature (T) and conductivity (C) sensors are matched. The method assumes that the conductivity fluctuations at scales smaller than 10 meters are due mainly to temperature fluctuations. By computing the cross spectrum between temperature and conductivity, a transfer function phase and amplitude function can be estimated. The Fourier transform of measured temperature,  $t_m$ , and conductivity,  $c_m$ , are related to the true values by

$$\begin{aligned} t_m(m) &= t(m)G_T(m)e^{i\phi_T(m)} \\ c_m(m) &= c(m)G_C(m)e^{i\phi_C(m)} \end{aligned} \quad (C.1)$$

where  $m$  is the vertical wave number,  $G_T$ ,  $G_C$ ,  $\phi_T$  and  $\phi_C$  are the amplitude and phase responses of the sensors. The temperature spectrum is related to the cross spectrum (assuming no salinity contribution) by

$$\begin{aligned} \langle t^* t \rangle &= \alpha \langle t^* c \rangle \\ \langle t_m^* t_m \rangle G_T^2 &= \alpha \langle t_m^* c_m \rangle G_T G_C e^{i(\phi_C - \phi_T)} \end{aligned} \quad (C.2)$$

$$\text{where } \alpha = \frac{dT}{dC}.$$

The transfer function is found by

$$H(m) = \frac{\langle t_m^* t_m \rangle}{\alpha \langle t_m^* c_m \rangle} = \frac{G_C}{G_T} e^{i(\phi_C - \phi_T)} \quad (C.3)$$

$H(m)$  is estimated using 100 profiles from the upper and lower CTD's. The profiles are first differenced then Fourier transformed to compute temperature and cross spectra. The transfer function is modeled by fitting a fifth order polynomial to the estimated amplitude and phase (Figure C.2). All profiles of T and C are first differenced and Fourier transformed. The transfer function is applied to match the spectral response of T to that of C. Both T and C are then low pass filtered with a cut off of 1.3 c.p.m. before inverse Fourier transforming. T and C are then reintegrated and sampled at half the data rate to form corrected profiles. Salinity, potential temperature and potential density are estimated using the equation of state (Fofonoff and Millard, 1983). Examples of raw and corrected density profiles show that much of the density overturns from sensor mismatch is removed (Figures C.3 and C.4).

Upper CTD and lower CTD density profiles are combined using the overlap depths of 200-220 meters. A linear ramp is used in the region such that at 205m 100% of the upper CTD data is used, at 210m, 50% for each profile is used and at 215 m 100% of the lower CTD profiles is used. It should be noted that there is a 60 sec time lag between the sampling of this region by the lower CTD and sampling by the upper CTD. This time lag will bias strain variance. As an illustration, assume vertical advection moves a constant density gradient with no straining. The density field will be displaced between sampling by the lower and upper CTD. Advection towards the surface will appear as a positive strain and advection towards the bottom will appear as negative strain.

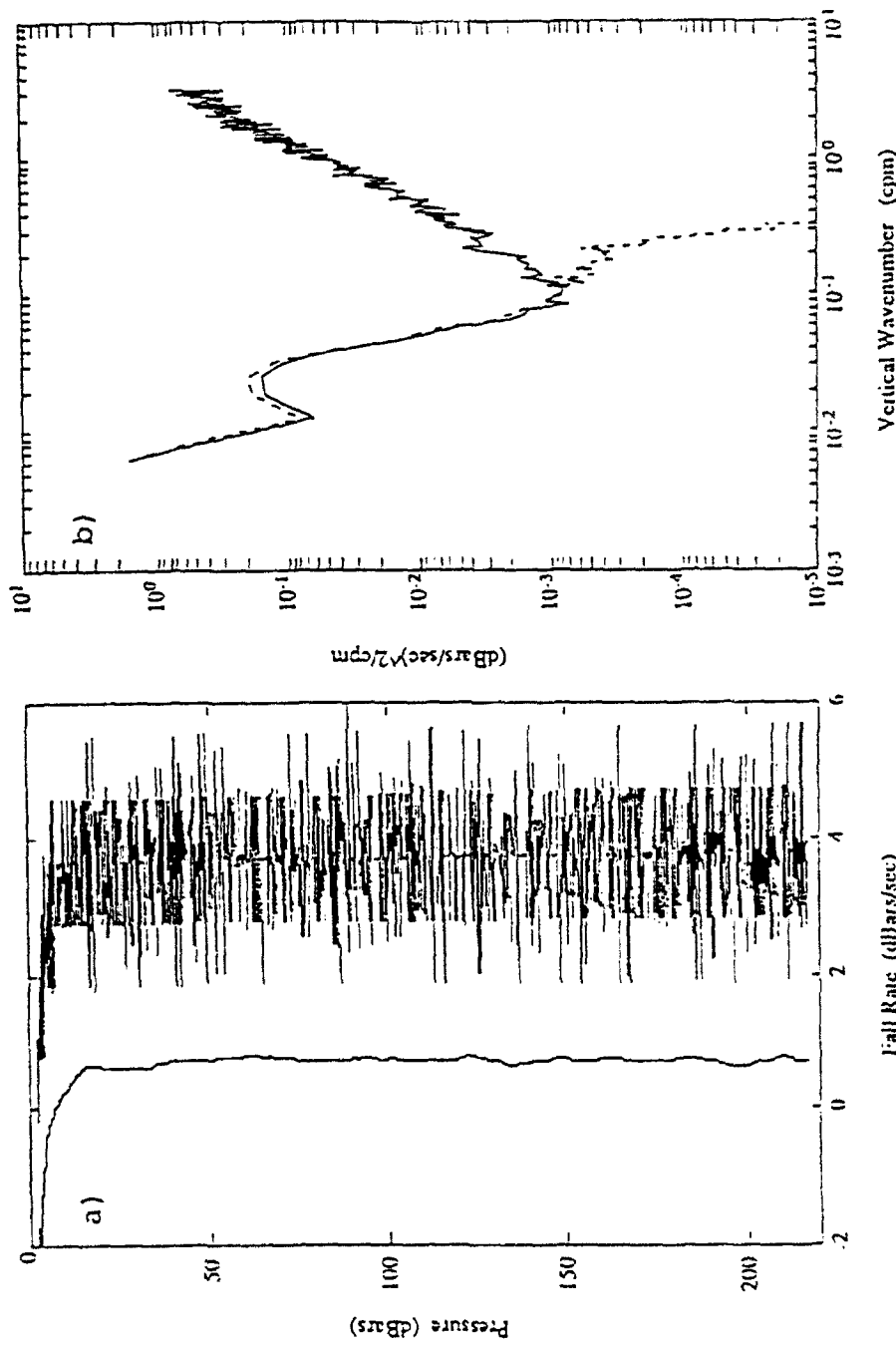


**Figure C.1. High Frequency Pressure Filtering.** A typical profile of fall rate as estimated from the first differenced pressure signal is shown in (a). Offset by 2 dBar/sec is the same profile low-pass filtered with a Hamming window based FIR filter with a cutoff at  $\sim 1.37$  cpm (.5 Hz). A power spectrum of fall rate calculated from 25 profiles is shown in (b). The raw signal power spectra (solid line) have a  $k^{-1}$  slope above  $10^{-1}$  cpm (0.36 Hz) which is likely caused by water turbulence at the pressure transducer. Also shown is the filtered pressure signal power spectra (dashed line.)

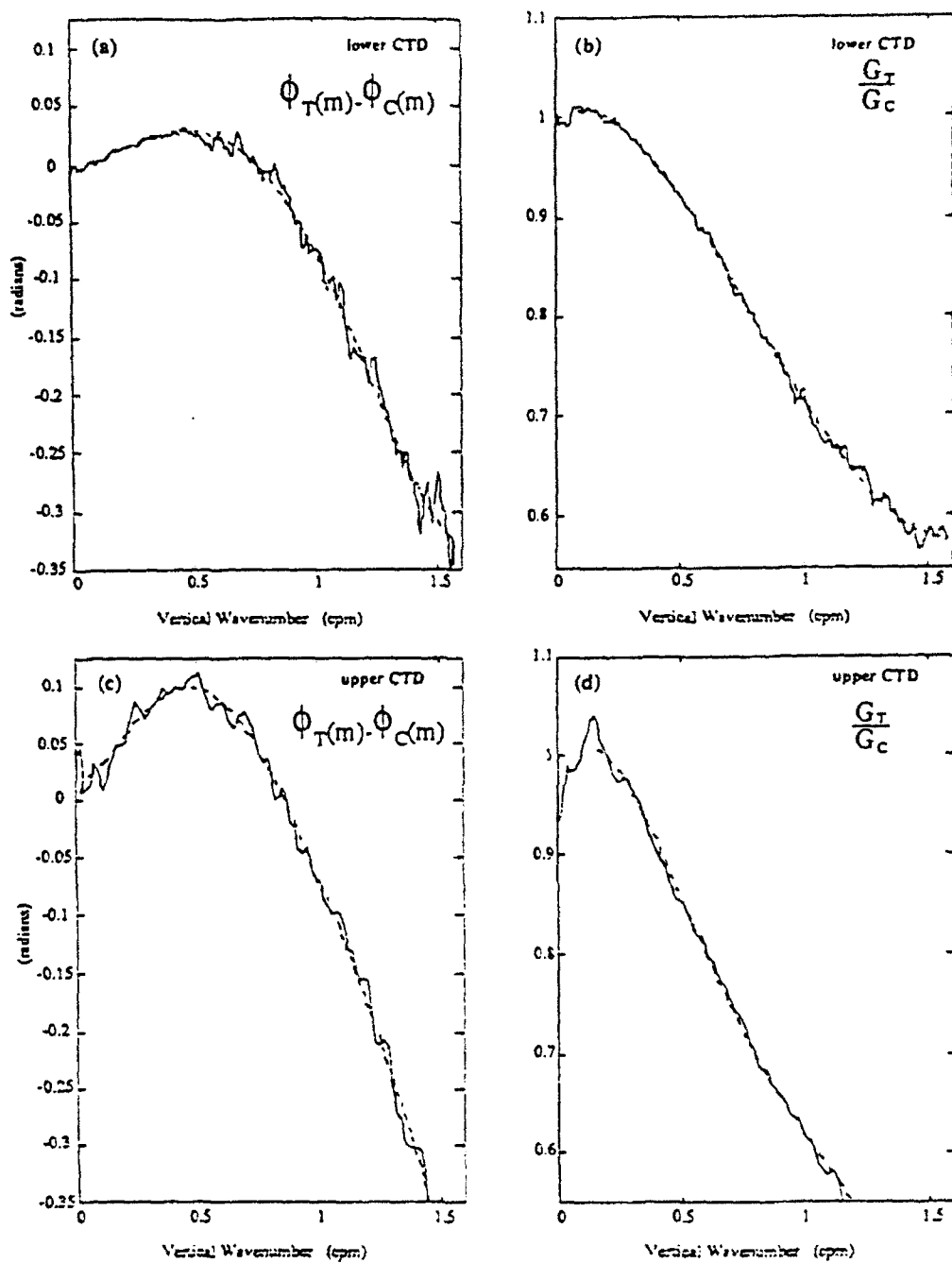


**Figure C.2** Temperature and Conductivity response matching. Transfer functions (solid lines) between temperature and conductivity are estimated from 500 profiles from both the upper and lower CTD. A fifth order polynomial is fit to the amplitude and phase of the estimated transfer function and is used to match the response of the two sensors prior to salinity calculations.

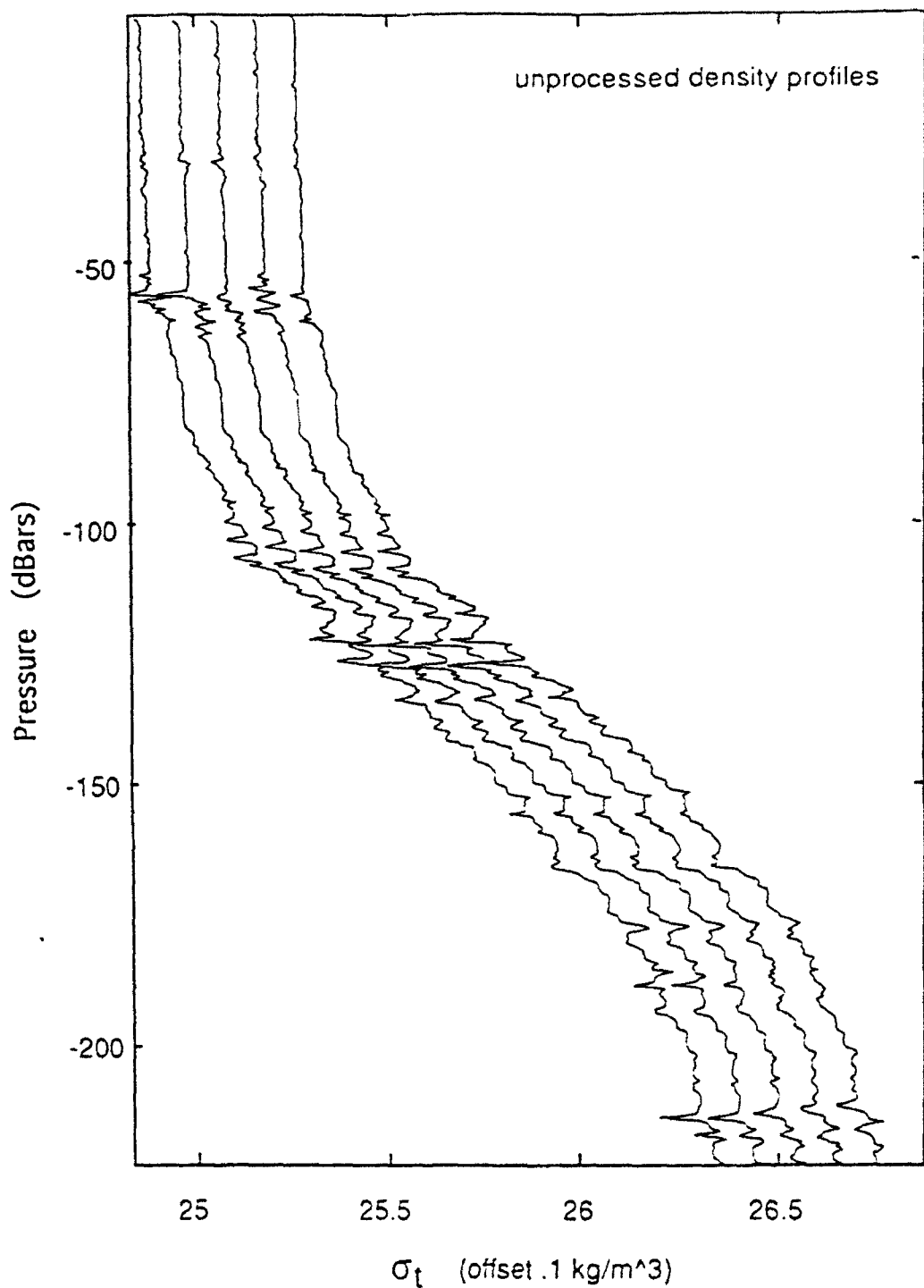


**Figure C.3 Uncorrected Density Profiles.** Five Density profiles, calculated from raw conductivity and temperature data, from the upper CTD are plotted. A mismatch between the spatial responses of the conductivity cell and temperature probe causes 'salinity spiking' leading to poor estimates of potential density.

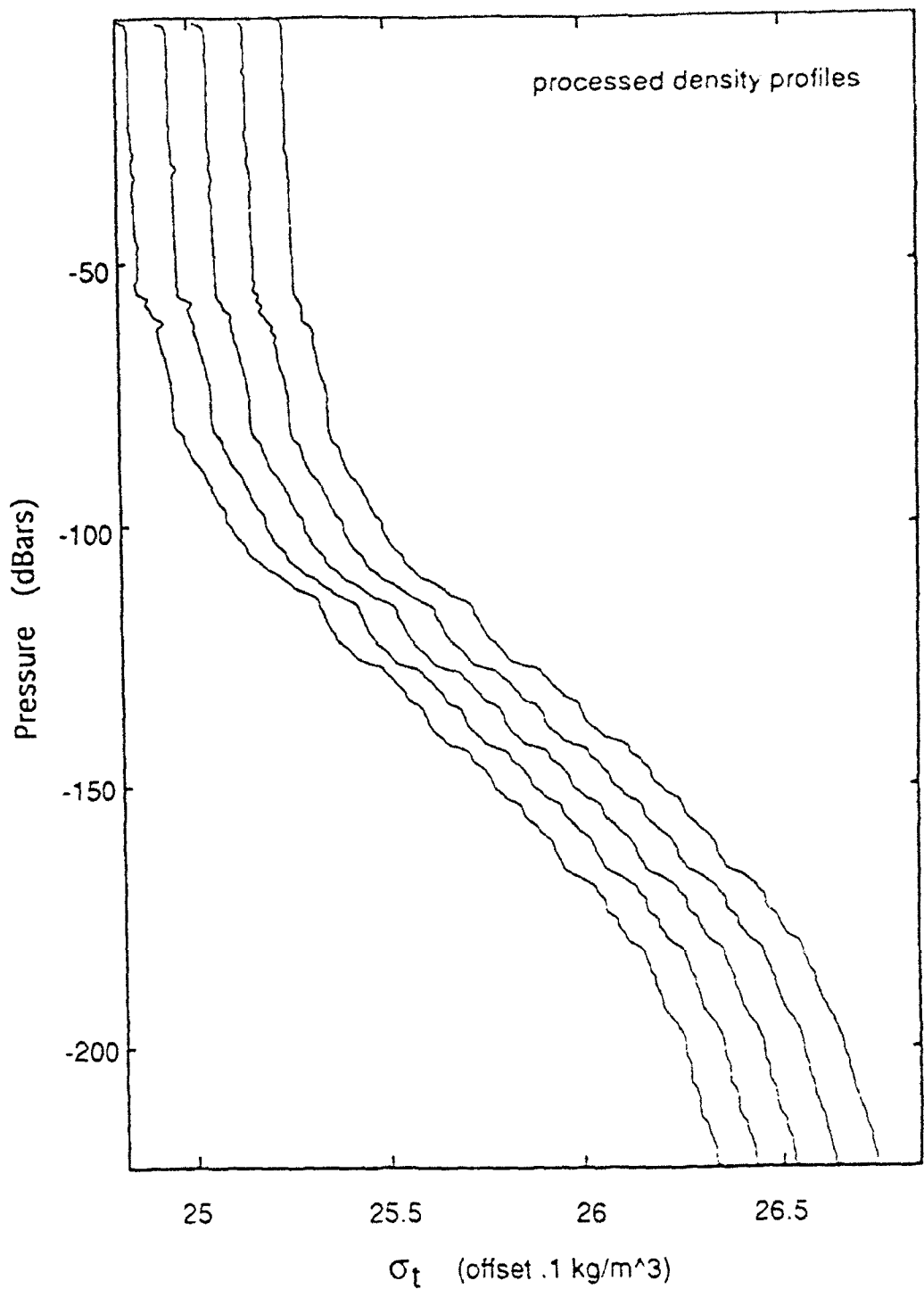


**Figure C.4 Corrected Density Profiles.** Same density profiles as plotted in Figure C.3 except now the spatial responses of the conductivity cell and temperature probe have been phase and amplitude matched.

## Appendix D

### Velocity Biasing Due to Horizontal Beam Separation

Horizontal velocity from Doppler sonar beams are obtained by comparing slant velocities from back to back beams. This velocity is only a good estimate of the true horizontal velocity if the horizontal wave scales are much longer than the horizontal beam separation (Sherman and Pinkel, 1991). The section estimates the expected spectral error as a function of vertical wavenumber and frequency. From linear internal wave theory, the vertical and east velocity components for a single internal wave are

$$\begin{aligned} w &= W_0 e^{i(kx+ly+mz-\omega t)} \\ u &= -\frac{m}{K} (\cos \gamma + i \frac{f}{\omega} \sin \gamma) W_0 e^{i(kx+ly+mz-\omega t)} \end{aligned} \quad (D.1)$$

where the horizontal wave numbers  $k=K\cos(\gamma)$  and  $l=K\sin(\gamma)$ . Assume that the sonar is located at the coordinates  $(x,y,z)=(0,0,0)$ . This wave is observed by the east and west beams of the sonar in the  $x-z$  plane with a beam down look angle of  $\theta$ . The slant velocity is found by taking the projection of the velocity field along each beam. The horizontal locations for each beam as a function of depth are  $x_e = z \cot \theta$  and  $x_w = -z \cot \theta$ . The measured slant velocities are then

$$\begin{aligned} v_e &= W_0 e^{i(mz-\omega t)} \left[ \cos \theta + \frac{m}{K} (\cos \gamma + i \frac{f}{\omega} \sin \gamma) \sin \theta \right] e^{iKz \cos \gamma \cot \theta} \\ v_w &= W_0 e^{i(mz-\omega t)} \left[ \cos \theta - \frac{m}{K} (\cos \gamma + i \frac{f}{\omega} \sin \gamma) \sin \theta \right] e^{-iKz \cos \gamma \cot \theta} \end{aligned} \quad (D.2)$$

The estimated horizontal velocity is obtained by

$$\bar{u} = \frac{v_w - v_e}{2 \sin \theta} = -W_0 e^{i(mz-\omega t)} \left[ \frac{m}{K} \left( \cos \gamma + i \frac{f}{\omega} \sin \gamma \right) \cos \phi + i \cot \theta \sin \phi \right] \quad (D.3)$$

where  $\phi = Kz \cos \gamma \cot \theta$ .

For a wave propagating in the north-south plane ( $\gamma=\pm\pi/2$ ), the estimated east velocity equals the true east velocity. For a wave moving in the east-west plane, there is a phase and amplitude shift in the estimated velocity field. This error is small for waves with horizontal wavelengths that are much larger than the beam spacing. The biasing of spectral estimates of the velocity field is assessed by comparing the measured variance to the expected variance. The bias at depth,  $z$ , for a single internal wave is given by

$$b(m, \omega, \gamma, z) = \frac{\bar{u}^* \bar{u}}{u^* u} \\ = \cos^2 \phi + \left( \frac{\cot \theta \sin \phi}{\cos^2 \gamma + (\frac{f}{\omega})^2 \sin^2 \gamma} \right) \left[ \left( \frac{f^2 - \omega^2}{\omega^2 - N^2} \right) \cot \theta \sin \phi + \frac{f}{\omega} \left( \frac{f^2 - \omega^2}{\omega^2 - N^2} \right)^{\frac{1}{2}} \sin \gamma \cos \phi \right] \quad (D2.4)$$

The total spectral bias for a horizontally isotropic wave field is determined by averaging  $b$  over the vertical length of the sonar beams and over all wave angles,  $\gamma$ . Averaging Equation D.4 over  $z = 1$  to 256 meters and  $\gamma=0$  to  $2\pi$ , and using  $N = 6$  c.p.h. and  $f=.0478$  c.p.h. yields Figure (D.1), the total spectral velocity bias as a function of vertical wavenumber,  $m$ , and frequency,  $\omega$ . The total spectral bias has a minimum of 0.5. There is very little bias found at low frequencies ( $\omega < 2f$ ) for all measurable wave numbers. As wave frequencies approach  $N$ , the waves have strong vertical velocities and short horizontal wavelengths leading to an overestimation of the horizontal velocity variance.

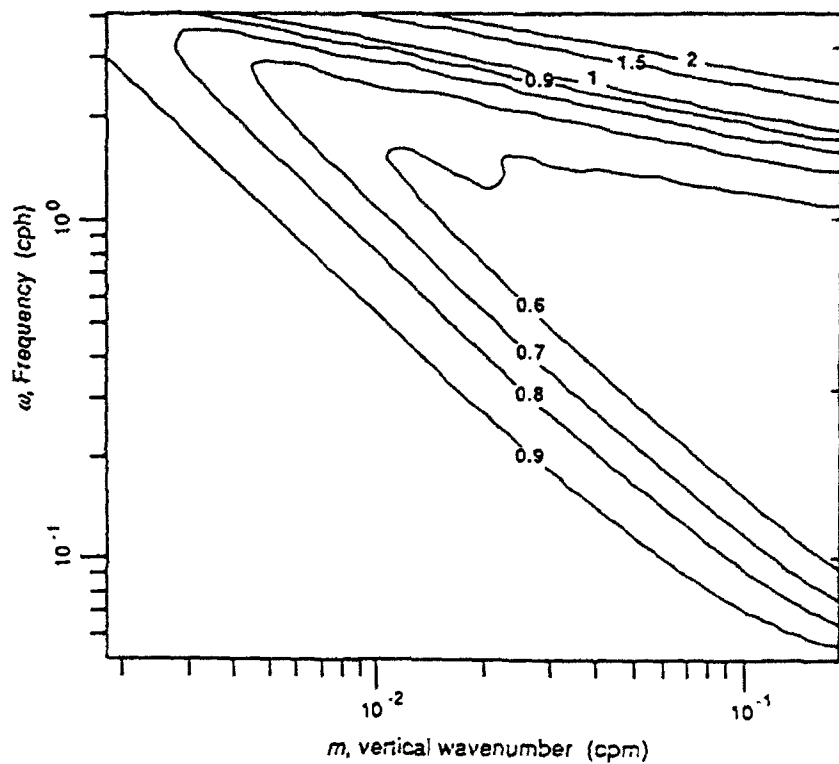


**Figure D.1 Estimated Spectral variance Bias Due to Beam Pair Separation.** Horizontal velocities determined by comparing back to back beams are biased estimates of the true velocity field due to horizontal beam separation. Assuming a horizontally isotropic internal wave field, the bias is averaged over all directions and over the vertical extent of the sonar measurements ( $z=0$  to 256 meters;  $f=.0478$  c.p.h.;  $N=6$  c.p.h.). At low frequencies ( $2f < \omega < 2f$ ), waves have long horizontal wavelengths and biasing is negligible. As  $\theta$  approaches  $N$ , waves have strong vertical velocities and short horizontal wavelengths and variances is overestimated. Variance is underestimated by as much as 50% at high vertical wavenumbers.

## Appendix E

### Sonar Data Processing

#### E.1. Doppler sonar background

To estimate water velocities, Doppler sonar systems transmit a pulse of sound and measure the Doppler frequency shift of the reverberation produced by acoustic scatterers in a volume of water. The acoustic scatterers in the upper ocean are biological and comprised mostly of zooplankton. To the extent that the scatterers are advected passively by the surrounding water, the frequency shift reflects the mean velocity of the interrogated volume of water. For a monostatic Doppler sonar, the sonar transducers are both the source and receiver. Assuming that the relative velocities between the water and the sonar are much smaller than the speed of sound,  $c$ , the reverberation frequency at the receiver,  $f_r$ , is determined by.

$$f_r = f_c \left[ 1 + \frac{2}{c} V \right] \quad (\text{E.1})$$

where  $f_c$  is the transmit frequency and  $V$  is the relative velocity of the interrogated water. Rewriting (E.1) to find the relative velocity in terms of the Doppler shift,  $f_d = f_r - f_c$ , obtains

$$V = \frac{c}{2f_c} f_d \quad (\text{E.2})$$

where  $V$  is positive if the volume is moving towards the sonar. For a simple Doppler system, a volume is interrogated with a pulsed transmission of the form

$$X_0(t) = A \cos(2\pi f_c t) G(t) \quad (\text{E.3})$$

where

$$G(t) = \begin{cases} 1 & \text{if } 0 \leq t \leq T_p \\ 0 & \text{otherwise} \end{cases}$$

and  $T_p$  is the pulse duration. The received signal at time,  $t$ , is defined as

$$X(t) = \text{Re} \{ Z(t) e^{i 2\pi f_c t} \} \quad (\text{E.4})$$

where  $Z(t)$  is the complex envelope. ( $X(t)$  is base banded with a reference signal and with the reference signal shifted in phase by  $90^\circ$  to remove the carrier frequency.) Then the complex envelope is sampled with two A/D converters with a sample interval of  $\tau$ . This results in the sampled complex envelope,  $Z(t_n)$ , where  $n = i$  is the sample number and  $t_n$  is zero at the start of the acoustic transmission sequence. To estimate a mean Doppler shift from the spectrum of shifts returned by various scatterers in the interrogated volume, a power weighted mean frequency of the complex envelope is found. This is done by estimating autocovariances using a technique developed by Rummel (1968). The autocovariance,  $C$ , is the product of the signal at sample  $t_n$  with its self at sample  $t_n+L$ , where  $L$  is the sample lag number. The autocovariance is then averaged in time to increase the stability of the autocovariance estimate. The averaging over consecutive autocovariances in time is called range averaging and the averaging intervals are called range bins. The average covariance over a range bin is found by

$$C(b_n) = \frac{1}{N} \sum_{t_n=Nb_n}^{N(b_n+1)-1} Z(t_n) Z^*(t_n + L) \quad (E.5)$$

where  $N$  is the averaging interval and  $b_n$  is the range bin number. This step is commonly referred to as range averaging. To increase the stability of the autocovariance estimates, several realizations from successive transmissions are averaged together which results in time averaging. Rummel showed that the estimated covariance is related to the power weighted mean frequency of the sampled complex envelope by

$$\bar{f}(b_n) = \frac{\arg\{C(b_n)\}}{2\pi L\tau}. \quad (E.6)$$

In a noise free sonar with a symmetric returned Doppler frequency spectrum, this is an unbiased estimate of the mean Doppler shift. In practice, for time lags much less than the inverse bandwidth,  $\bar{f}$  is a good estimate of the mean Doppler shift. Slant velocities are then found from  $\bar{f}$  using (E.2).

The optimum performance of a simple Doppler sonar in the limit of an infinite signal to noise ratio can be estimated using the Cramer-Rao bound (Theriault, 1986)

$$\Delta V \Delta R = \frac{c^2}{8\pi f_c \sqrt{P}} \quad (E.7)$$

where  $\Delta V$  is the rms velocity imprecision,  $\Delta R$  is the effective range resolution, and  $P$  is the number of independent transmit sequences averaged together. The effective range resolution is half the pulse length:  $\Delta R = \lambda c T_p$ .

Recently, repeat-sequence transmit coding has been used to increase the precision of Doppler sonars (Pinkel and Smith, 1992). Repeat-sequence codes are comprised of several repeats of a broad band subcode. The subcode is selected to have the smallest

possible autocorrelation except at zero lags and reverses the sign of the carrier signal at regulated time increments. In this case,  $G(t)$ , the transmit envelope, is no longer constant but takes on a value of +1 or -1. The subcode is made up of  $L$  bits each lasting a period length of  $\tau$ . The subcode is then repeated  $M$  times. An example of four repeats of a 7-bit Barker code is shown in Figure E.1. An ideal code is one that results in an autocovariance of nearly zero everywhere except at sample lags  $L$ . By transmitting codes instead of discrete pulses, the average transmit power is increased. Corresponding autocovariances are calculated at lags equal to the code length. Pinkel and Smith (1992) found performance is limited by

$$\Delta V \Delta R = \frac{c^{\frac{3}{2}}}{4\pi P^{\frac{1}{2}}} \left( \frac{V_{\max}}{f\Delta f} \right)^{\frac{1}{2}} \left( \frac{T_{\max}}{T_{\text{ovl}}} \right) \left( \frac{T_{\text{ovl}}}{T_{\text{avg}}} + \frac{1}{2} \right)^{\frac{1}{2}} \quad (\text{E.8})$$

where

$$V_{\max} \equiv \frac{c}{4f\tau L}, \text{ maximum unambiguous velocity estimate,}$$

$M$  ≡ number of repeats of the subcode,

$L$  ≡ number of bits in the subcode,

$T_{\text{avg}}$  ≡  $N\tau$ ,

$T_{\text{ovl}}$  ≡  $(M-1)L\tau$ , overlapped common range in the covariance estimate,

$\Delta f$  ≡  $\frac{1}{\tau}$ , maximum bandwidth.

$f$  ≡ the transmission frequency.

$T_{\max}$  ≡ the max of  $(T_{\text{avg}}, T_{\text{ovl}})$ .

Thus the rms precision of the sonar is enhanced roughly in proportion to the product of the bandwidth and the duration of the subcode. These coded pulses have now been used on several Doppler sonars at the Marine Physical Laboratory. Precision tests agree roughly with the predictions of (E.8).

## E.2. The MPL 161 kHz Doppler sonar system.

The MPL 161 kHz Doppler sonar system, designed and built originally for the CEAREX (1989) experiment, was mounted on the thruster of FLIP at a depth of approximately 15 meters for the SWAPP experiment. The system configuration parameters used for the FLIP deployment are listed in Table E.1. The system used a traditional four beam arrangement where the beams were spaced  $90^\circ$  apart horizontally (Figure E.2). Each beam pointed down with a downlook angle,  $\theta_0$ , of  $60^\circ$  from the surface. The slant velocity for each beam is the projection of the true velocity field onto that beam. The estimated horizontal and vertical velocities are found by comparing back to back beams such that

$$\begin{aligned} u_{02} &= \frac{(V_0 - V_2)}{2 \cos \theta_0} ; \quad u_{13} = \frac{(V_1 - V_3)}{2 \cos \theta_0} \\ w_{02} &= \frac{(V_0 + V_2)}{2 \sin \theta_0} \text{ and } w_{13} = \frac{(V_1 + V_3)}{2 \sin \theta_0} \end{aligned} \quad (E.9)$$

where  $V_0$ ,  $V_1$ ,  $V_2$ , and  $V_3$  are the slant velocity estimates from the four corresponding beams;  $u_{02}$  and  $u_{13}$  are the orthogonal horizontal velocities and  $w_{02}$  and  $w_{13}$  are the vertical velocities. Implicit in (E.9) is the assumption that the horizontal scales of the flow field are larger than the horizontal spacing between the sonar beams (Plueddemann, 1987). This beam configuration is typically called the Janus configuration and the estimated velocities from (E.9) are referred to as the Janus velocities.

### E.3. Variable Gain correction

To extend the dynamic range of the analog to digital converters, a variable gain circuit is used. The analog signal is sampled every 250  $\mu$ sec by a 12 bit A/D converter that has a dynamic range of 72 dB. Without any additional dynamic range, the sonar's potential profiling range would be limited by the decay in time of the acoustic return. The A/D converter samples the analog signal after the variable gain circuit actively amplifies the true receive signal. This extends the effective dynamic range to 102 dB. The profiling range is thus limited by system electronic noise. Here, a model of the variable gain circuit is used to correct the sampled covariance and intensity amplitudes.

The sampled acoustic return data,  $Z_s(t_n)$ , is related to the input signal,  $Z_0(t_n)$ , by

$$Z_s(t_n) = G^{(k)}(t_n) Z_0(t_n) \quad (E.10)$$

where  $G(t_n)$  is the variable gain function and  $t_n$  is the sample number from the start of the transmit sequence. The timing of the variable gain circuit is locked to the transmit pulse so that  $G(t_n)$  is applied identically to every received sequence. For the first 60 samples (15000  $\mu$ sec),  $G(t_n)$  is equal to one. For later samples, the gain is ramped up to 30 dB to a final value of 1000, with 60 steps of 0.5 dB (Figure E.3). Each step lasts 20 samples (5000  $\mu$ sec). The recorded intensity data,  $I_{ns}$ , which is range averaged over 9 samples and is related to the input signal by

$$I_{ns}(b_n) = \frac{1}{N} \sum_{t_n=Nb_n}^{N(b_n+1)-1} G(t_n) Z_0(t_n) Z_0^*(t_n) \quad (E.11)$$

where  $b_n$  is the range bin number and  $N$  is the range averaging. The true intensity data,  $I_{n0}(t_n)$ , is

$$In_0(b_n) = \frac{1}{N} \sum_{t_n=Nb_n}^{N(b_n+1)-1} Z_0(t_n) Z_0^*(t_n) \quad (E.12)$$

If  $G(t_n)$  is a constant over each range averaging interval then the true intensity is simply related to the sampled intensity by

$$In_0(b_n) = \frac{In_s(b_n)}{\bar{G}(b_n)} \quad (E.13)$$

where

$$\bar{G}(b_n) = \frac{1}{N} \sum_{t_n=Nb_n}^{N(b_n+1)-1} G(t_n). \quad (E.14)$$

The ideal gain would be constant over a given range bin. If there is a gain change over an averaging interval, there will be some biasing of the intensity that cannot be removed in post processing. (In the case of the 161 kHz sonar discussed here, the transmit pulse effectively smoothes the intensity profiles over a range bin. It is reasonable to assume that this biasing error will be small since  $Z_0(t_n)$  will be nearly constant over a range averaging interval.) Here, the biasing errors are neglected and the modeled variable gain function and estimated true intensities are found using (E.13) and (E.14). Figure E.4 shows a typical one hour averaged intensity profile with and without the variable gain correction and the full dynamic range of nearly 80 dB has been restored.

One side affect of the steps in the variable gain circuit is the addition of an intensity ripple due to the mismatch of the range averaging and gain step lengths. Figure E.5b shows a first differenced, hour averaged intensity profile. During the period of active gain change (bins 7 to 122) a high frequency ripple occurs even after averaging for one hour. This ripple can also be seen in the model variable gain function plotted in Figure E.5a. The same profile now corrected for the variable gain is plotted in Figure E.5c and shows much less variance.

The amplitude of the estimated covariance data is also affected by the variable gain function. The recorded covariance data is averaged over 9 samples and is related to the input signal by

$$C_s(b_n) = \frac{1}{N} \sum_{t_n=Nb_n}^{N(b_n+1)-1} (G(t_n) G(t_n + L))^* Z_0(t_n) Z_0^*(t_n + L) \quad (E.15)$$

where  $L$  is the lag number in samples. The true covariance data is defined as

$$C_0(b_n) = \frac{1}{N} \sum_{t_n=Nb_n}^{N(b_n+1)-1} Z_0(t_n) Z_0^*(t_n + L). \quad (\text{E.16})$$

If  $G$  constant and equal over each range averaging interval then the true covariance is obtained by

$$C_0(b_n) = \frac{C_s(b_n)}{\tilde{G}(b_n)} \quad (\text{E.17})$$

where

$$\tilde{G}(b_n) = \frac{1}{N} \sum_{t_n=Nb_n}^{N(b_n+1)-1} (G(t_n) G(t_n + L))^{1/2}. \quad (\text{E.18})$$

In the case where  $G$  varies over a range averaging interval, there will be biasing of the covariance data that cannot be removed with post processing. For the 161 kHz sonar, a  $L$  is 7 samples and a gain step length lasts 20 samples so only one step could occur over the averaging interval of 9 samples. Since the gain steps are small and the pulse length has smoothed  $Z_0(t_n)$ , it is assumed that the biasing will be small and the gain biasing errors will be neglected. The modeled variable gain function for the covariance and the estimated true covariance are found from (E.17) and (E.18). Figure E.6 shows a typical profile of both sampled and estimated true covariance amplitude.

#### E.4. Noise correction

The correction applied here assumes that band limited additive noise in the receiver causes biasing of the covariance estimates. The measured covariance is modeled as the sum of the signal covariance and the noise covariance,

$$C_m(b_n) = C_s(b_n) + C_n \quad (\text{E.19})$$

Estimates of  $\bar{f}$  from the measured covariance will be biased further away from the true mean Doppler shift as the signal to noise ratio gets small. The bias can be removed by estimating the true signal covariance. This is done by determining  $C_n$  from the return at far range where the signal has decayed away leaving only noise. The noise covariance is assumed to be constant over all ranges and is then subtracted from the measured covariance to find the estimated signal covariance. Then an unbiased estimate of the mean Doppler shift is found from the corrected covariance estimates. In practice, uncorrected slant velocity profiles will tend toward a non zero velocity at far range. (To remove this bias from the 161 kHz sonar data, the average covariance from the last 9 range bins for every profile is used as an estimate of the noise covariance,  $C_n$ , for each beam. The noise covariance is subtracted from the one minute averaged signal covariance prior to calculating slant velocities.)

shape as the wire spectrum in the surface wave band. However, at frequencies below the swell peak, the energy density increases towards lower frequency with a higher proportional energy than the corresponding wire spectrum. It is reasonable to assume that below .0167 Hz most of the accelerations are due to FLIP tilting. Tilt estimates used in the sonar processing are from 1 minute averaged accelerometer data.

### E.5.2. Transformation Matrix

There are three right-hand coordinate systems to consider. The first is the geovertical coordinates where  $\hat{k}$  points vertically upward parallel to gravity,  $\hat{j}$  points horizontally towards the bow of FLIP and  $\hat{i}$  points horizontally towards the starboard of FLIP. The other coordinate system is the ship coordinates and is defined by the unit vectors  $\hat{i}$ ,  $\hat{j}$ , and  $\hat{k}$  in Figure E.8. The third coordinate system is the geographic coordinate system where  $(i, j, k)$  correspond to (East, North, Up).

A vector in the ship coordinates can be related to the geovertical coordinates by a transformation matrix. Let  $\hat{r} = (\hat{x}, \hat{y}, \hat{z})$  be a vector in the tilted coordinates and  $r = (x, y, z)$  be the corresponding vector in the geovertical coordinates. The two vectors are related by

$$r = \begin{bmatrix} \cos \gamma_{11} & \cos \gamma_{21} & \cos \gamma_{31} \\ \cos \gamma_{12} & \cos \gamma_{22} & \cos \gamma_{32} \\ \cos \gamma_{13} & \cos \gamma_{23} & \cos \gamma_{33} \end{bmatrix} \hat{r} = M\hat{r} \quad (E.21)$$

The cosine angles,  $\gamma_{ij}$ , are the angles that the tilted unit vectors  $\hat{i}$ ,  $\hat{j}$ ,  $\hat{k}$  make with the geovertical unit vectors  $\bar{i}$ ,  $\bar{j}$ ,  $\bar{k}$ . It can be shown (Karamcheti, 1967) that if each of the coordinate systems is orthogonal, then

$$\sum_{j=1}^3 \cos \gamma_{ij} \cos \gamma_{kj} = 1 \text{ if } i = k \\ = 0 \text{ if } i \neq k \quad (E.22a)$$

and

$$\sum_{i=1}^3 \cos \gamma_{ij} \cos \gamma_{ik} = 1 \text{ if } j = k \\ = 0 \text{ if } j \neq k \quad (E.22b)$$

In order to relate the two coordinate systems, three angles must be given. This is often done using the *Euler angles* (Teichmann, 1969) where the rotation is carried out in three steps. First a rotation around the  $k$ -axis through angle  $\phi$ , then a rotation about the  $i$ -axis through angle  $\theta$  and finally a rotation about the new  $k$ -axis through angle  $\psi$ . The resulting transformation matrix is defined by

## E.5. Platform Motion Correction

There are four main steps to the tilt correction for the slant velocities. 1) mechanical alignment errors are determined using the translation correction method. 2) one-minute averaged slant velocity profiles are corrected for beam translation by interpolating velocities to common depth bins. 3) horizontal velocities are estimated subtracting the back to back beam translation corrected slant velocities. 4) geographic velocities are found by rotating the horizontal velocities using one minute averaged heading data. Included in this section is a discussion of the tilt rotation correction which is important in vertical velocity estimates and may sometimes be used to determine mechanical alignment errors.

### E.5.1. Platform Tilt and Accelerometer measurements

A three axis accelerometer package was mounted on the hull of FLIP and used as an inclinometer. The accelerometers were sampled at 10 Hz and averaged over 1 minute. Tilts are estimated by assuming that the horizontal accelerations measured are from the earth's gravitational field. The package is mounted such that the x-axis accelerometer, points starboard and the y-axis accelerometer points towards the bow. Note that the beams directions are rotated 45° with respect to the accelerometer (Figure E.2). The tilt angles are estimated by

$$\alpha = \sin^{-1} \left( \frac{a_x}{g} \right) \text{ and } \beta = \sin^{-1} \left( \frac{a_y}{g} \right) \quad (\text{E.20})$$

where  $a_x$  and  $a_y$  are the horizontal accelerations,  $\alpha$  and  $\beta$  are the x and y axis tilt angle estimates and  $g$  is the local gravitational vector. This approximation is only accurate for low frequency fluctuations in acceleration. In studies of a free drifting FLIP, Rudnick (1964) showed that in the surface wave frequency band, 0.05-0.2 Hz, most of the horizontal accelerations are due to the surface wave forcing while at lower frequencies horizontal acceleration variance decreased. Equivalent testing has not been performed on a moored FLIP.

During SWAPP, a two point mooring held FLIP in position. The tethering of FLIP above the water line causes a tilting moment when there is a near surface current. The strongest near surface currents occur at inertial currents and semi-diurnal frequencies which cause tilts of up to 2.5°. It is clear that for these low frequencies, the measured accelerations are due to tilt and not horizontal accelerations. At what frequency is the tilt signal masked? Capacitance wave wire data from the starboard boom (Figure E.7a) show that at higher frequencies, surface waves dominate the signal with a swell peak at 0.08 Hz and a typical wind wave spectral slope of  $\omega^{-5}$  (Philips, 1957). At frequencies below the swell, there is very little contribution of sea surface height due to surface waves. Instead the tilting of FLIP lifts the boom up and down causing apparent shifts in the surface height. Concurrent x-axis accelerometer spectrum (Figure E.7b) shows the same spectral

$$M_{\psi\theta} = \begin{bmatrix} (\cos \phi \cos \psi - \sin \phi \cos \theta \sin \psi) & (\sin \phi \cos \psi + \cos \phi \cos \theta \sin \psi) & \sin \psi \sin \theta \\ -(\cos \phi \sin \psi + \sin \phi \cos \theta \cos \psi) & (-\sin \phi \sin \psi + \cos \phi \cos \theta \cos \psi) & \cos \psi \sin \theta \\ \sin \phi \sin \theta & -\cos \phi \sin \theta & \cos \theta \end{bmatrix}. \quad (E.23)$$

The angles measured by the 3-axis accelerometer package are not the Euler angles. The horizontal tilt angles,  $\alpha$  and  $\beta$ , that are estimated from the accelerometers are the angles the tilted unit vectors  $\hat{i}$ ,  $\hat{j}$  make with the geovertical horizontal plane. The fact that there is no rotation about  $\hat{k}$  or  $\bar{k}$  allows the elimination of the third angle needed for the transformation of the tilted coordinates. Therefore, the tilt angles are related to the cosine angles by

$$\begin{aligned} \sin \alpha &= \cos(\alpha + 90^\circ) = \cos \gamma_{31} = -\cos \gamma_{13} \\ \sin \beta &= \cos(\beta + 90^\circ) = \cos \gamma_{32} = -\cos \gamma_{23}. \end{aligned} \quad (E.24)$$

Using (E.22) and (E.23), the resulting transformation matrix can be found in terms of  $\alpha$  and  $\beta$

$$M_{\alpha\beta} = \begin{bmatrix} \frac{\sin^2 \beta + \sin^2 \alpha (1 - \kappa)^{\frac{1}{2}}}{\kappa} & \frac{\sin \alpha \sin \beta ((1 - \kappa)^{\frac{1}{2}} - 1)}{\kappa} & \sin \alpha \\ \frac{\sin \alpha \sin \beta ((1 - \kappa)^{\frac{1}{2}} - 1)}{\kappa} & \frac{\sin^2 \alpha + \sin^2 \beta (1 - \kappa)^{\frac{1}{2}}}{\kappa} & \sin \beta \\ -\sin \alpha & -\sin \beta & (1 - \kappa)^{\frac{1}{2}} \end{bmatrix} \quad (E.25)$$

where  $\kappa = \sin^2 \alpha + \sin^2 \beta$ .

Thus a vector in the tilted reference frame,  $\hat{r}$  is related to the corresponding vector in the geovertical reference frame,  $r$ , by

$$r = M_{\alpha\beta} \hat{r}. \quad (E.26)$$

It is assumed that there is some mechanical misalignment between the accelerometer package mounted on the hull of FLIP and the 161 kHz sonar mounted about 20 meters above on FLIP's thruster. The Coordinate system of the sonar is defined by the measured tilt angles plus some constant tilt offset such that

$$\begin{aligned} \alpha' &= \alpha + \varepsilon_\alpha \\ \beta' &= \beta + \varepsilon_\beta \end{aligned} \quad (E.27)$$

The design tolerances in the mounting of the two sensors could result in misalignment errors of a few degrees. The beam directions, however, are built to much tighter tolerances. The sonar housing was machined from one piece of aluminum and the transducers are mounted rigidly in place. Orthogonality of the beams and the look down angles are fixed to within a fraction of a degree.

### E.5.3. Rotation Correction

Plueddemann (1987) showed that the rotation correction is only important for the vertical velocity estimates. Since the goal here is to study the horizontal velocities, the rotation correction is not directly used in the final velocity calculations but is presented here for completeness.

The rotation correction transforms the velocity vector into geovertical coordinates using (E.25). A velocity vector,  $\hat{V} = (\hat{u}, \hat{v}, \hat{w})$ , in the tilted reference frame is related to the corresponding vector in the geovertical reference frame,  $V = (u, v, w)$ , by

$$V = M_{\alpha\beta} \hat{V} \quad (E.28)$$

This correction is complicated by the fact that the sonar only estimates the along beam projection of the velocity field in the tilted coordinate system. A simple reparation is to use the uncorrected Janus velocity components. As shown before, the Janus velocities (for slant velocities positive towards FLIP) in this case are

$$u_{02} = \frac{(V_0 - V_2)}{2 \cos \theta_0} \quad (E.29a)$$

$$w_{02} = \frac{(V_0 + V_2)}{2 \sin \theta_0} \quad (E.29b)$$

$$u_{13} = \frac{(V_1 - V_3)}{2 \cos \theta_0} \quad (E.29c)$$

$$w_{13} = \frac{(V_1 + V_3)}{2 \sin \theta_0} \quad (E.29d)$$

where  $\theta_0$  is the downward beam angle. The sonar is rotated 45° from the accelerometer package (Figure E.2) and the estimated horizontal velocities in the coordinate system of the accelerometer package are found by

$$\hat{u} = \frac{\sqrt{2}}{2} (u_{02} - u_{13}) \quad (E.30a)$$

$$\hat{v} = \frac{\sqrt{2}}{2} (u_{02} + u_{13}) \quad (E.30b)$$

Substitution of (E.30) into (E.28) and solving for the vertical velocity component in the geovertical coordinate system yields

$$w'_{02} = -[\hat{u} \sin \alpha + \hat{v} \sin \beta] + (1 - \sin^2 \alpha - \sin^2 \beta)^{\frac{1}{2}} w_{02} \quad (\text{E.31a})$$

$$w'_{13} = -[\hat{u} \sin \alpha + \hat{v} \sin \beta] + (1 - \sin^2 \alpha - \sin^2 \beta)^{\frac{1}{2}} w_{13}. \quad (\text{E.31b})$$

#### E.5.4. Translation Correction

Let  $\hat{\mathbf{B}}$  be the unit vector along a beam in the rotated reference frame. Then, by using the dot product, the vertical coordinate in the tilted reference frame at range  $r$  along  $\hat{\mathbf{B}}$  is written as

$$\hat{z}(r) = r[\hat{\mathbf{B}} \cdot \hat{\mathbf{k}}] \quad (\text{E.32})$$

The vertical coordinate in the geovertical reference frame is found by using the transformation matrix and is written as

$$z(r) = r[(\mathbf{M}_{\alpha\beta}\hat{\mathbf{B}}) \cdot \hat{\mathbf{k}}]. \quad (\text{E.33})$$

Using the downward beam angle,  $\theta_0 = 60^\circ$ , the unit vectors in the four beam directions are

$$\hat{\mathbf{b}}_0 = -\frac{\sqrt{2}}{4}\hat{\mathbf{i}} - \frac{\sqrt{2}}{4}\hat{\mathbf{j}} - \frac{\sqrt{3}}{2}\hat{\mathbf{k}} \quad (\text{E.34a})$$

$$\hat{\mathbf{b}}_1 = +\frac{\sqrt{2}}{4}\hat{\mathbf{i}} - \frac{\sqrt{2}}{4}\hat{\mathbf{j}} - \frac{\sqrt{3}}{2}\hat{\mathbf{k}} \quad (\text{E.34b})$$

$$\hat{\mathbf{b}}_2 = +\frac{\sqrt{2}}{4}\hat{\mathbf{i}} + \frac{\sqrt{2}}{4}\hat{\mathbf{j}} - \frac{\sqrt{3}}{2}\hat{\mathbf{k}} \quad (\text{E.34c})$$

$$\hat{\mathbf{b}}_3 = -\frac{\sqrt{2}}{4}\hat{\mathbf{i}} + \frac{\sqrt{2}}{4}\hat{\mathbf{j}} - \frac{\sqrt{3}}{2}\hat{\mathbf{k}} \quad (\text{E.34d})$$

Using equation (E.26) to find the geovertical vertical coordinate from each of the beam vectors as a function of range and tilt yields

$$\begin{aligned} z_0(r, \alpha, \beta) &= r \left[ +\frac{\sqrt{2}}{4} \sin \alpha + \frac{\sqrt{2}}{4} \sin \beta - \frac{\sqrt{3}}{2} (1 - \sin^2 \alpha - \sin^2 \beta)^{\frac{1}{2}} \right] \\ z_1(r, \alpha, \beta) &= r \left[ -\frac{\sqrt{2}}{4} \sin \alpha + \frac{\sqrt{2}}{4} \sin \beta - \frac{\sqrt{3}}{2} (1 - \sin^2 \alpha - \sin^2 \beta)^{\frac{1}{2}} \right] \\ z_2(r, \alpha, \beta) &= r \left[ -\frac{\sqrt{2}}{4} \sin \alpha - \frac{\sqrt{2}}{4} \sin \beta - \frac{\sqrt{3}}{2} (1 - \sin^2 \alpha - \sin^2 \beta)^{\frac{1}{2}} \right] \\ z_3(r, \alpha, \beta) &= r \left[ +\frac{\sqrt{2}}{4} \sin \alpha - \frac{\sqrt{2}}{4} \sin \beta - \frac{\sqrt{3}}{2} (1 - \sin^2 \alpha - \sin^2 \beta)^{\frac{1}{2}} \right]. \end{aligned} \quad (\text{E.35})$$

As an example, let  $r = 200\text{m}$  and assume the tilt angles are both  $0.0^\circ$ . The corresponding vertical coordinate for each beam is  $z = -173.2$  meters. Now assume the tilt angles are both  $1.0^\circ$  so that all of the tilt is in the plane of beams 1 and 3. Beams 1

and 3 will both have the same vertical coordinate and a very small shift to shallower depths. Thus, solving for the vertical coordinates yields  $z_1 = z_2 = -173.1$  meters. Beams 0 and 2, however, have different vertical coordinates and a significant shift in depth. In this case, solving for the vertical coordinates yields  $z_0 = -168.2$  meters and  $z_2 = -178.1$  meters.

In the example above, Janus velocities calculated without tilt translation correction ... back to back slant velocities that are separated by 10 meters in depth. Since this ... near the resolution of the velocity estimates, significant errors will occur if there is any vertical shear in the velocity field. Besides Janus velocity errors, the absolute depth of the velocity estimates will be in error. This becomes important when velocity estimates are compared with density data from the profiling CTD. The tilt translation correction is a necessary step to the velocity data processing.

The algorithm for implementing translation correction proceeds as follows. A standard range bin vertical coordinate is set by the case of no tilt. Then 1 minute averaged accelerations are used to calculate an average tilt. New vertical coordinates based on (E.35) are calculated for each beam using the average tilt plus the mechanical alignment correction. Finally the slant velocities from each beam are interpolated to yield values at the standard range bins. (An example of corrected and uncorrected slant velocity profiles is shown in Figure (E.10).) At this point, Janus velocity estimates can be made from the slant velocities at the standard range bin depths.

#### E.5.5. Mechanical Alignment Error

The errors in mechanical alignment between the 161 kHz Doppler sonar and the accelerometer package are found using the translation correction. The method used is a straightforward search for the offset angles that result in the highest vertical correlation between back to back slant velocity calculations. The underlying assumption is that the horizontal velocity vertical finestructure has horizontal scales which are much larger than the horizontal separation between the sonar beams. If this is the case, then shear layers should lie on the same vertical coordinate from back to back beams and there will be a strong velocity correlation between the beams. If the beams are tilted, however, then the translation of the velocity estimates will shift the shear layers to different depths. This will tend to decrease the correlation between the back to back beams.

The data set used to find the mechanical alignment errors consisted of 990 consecutive slant velocity profiles and tilt angles averaged over one minute from year/day 72. The range bins 25 to 75 were used which correspond to depths of approximately 100 to 245 meters.

The tilt correction angles,  $\varepsilon_\alpha$  and  $\varepsilon_\beta$ , are allowed to vary over a range of possible values. For each combination of values, the translation correction is applied to each beam and 33 independent 30 minute averaged profiles are computed. The correlation between back to back, 30 minute averaged profiles is found from

$$Cor_{02} = \frac{\langle V_0 V_2 \rangle}{\sqrt{\langle V_0^2 \rangle \langle V_2^2 \rangle}}, \text{ and } Cor_{13} = \frac{\langle V_1 V_3 \rangle}{\sqrt{\langle V_1^2 \rangle \langle V_3^2 \rangle}} \quad (E.36)$$

This correlation is divided by the correlation between the same profiles with no tilt correction applied to create a correlation ratio. This correlation ratio will be greater than one if the translation correction has enhanced the corresponding vertical coordinate estimates and less than one if the vertical coordinate estimates are corrupted.

The average correlation ratio is found by averaging over the correlation ratio obtained from all 33 profiles and both pairs of back to back beams (Figure E.11). The mechanical alignment correction angles,  $\epsilon_\alpha$  and  $\epsilon_\beta$ , are varied from  $-2.25^\circ$  to  $2.25^\circ$ . The highest average correlation ratio is 1.022 and is found at  $\epsilon_\alpha = -1.55^\circ$  and  $\epsilon_\beta = -0.10^\circ$ . These are the mechanical misalignment correction angles used in the tilt correction processing.

An investigation is done to see if the rotation correction (E.28) can be applied to determine the mechanical alignment errors as well. This determination is based on the assumption that the depth-time average of the true vertical velocity is small compared to the magnitude of the errors. Minimization of the errors due to the translation of the sonar beams is accomplished by using depth averaged slant velocity estimates. Then time averaging removes the vertical velocities associated with high frequency internal waves. The remaining velocities are assumed to be due to horizontal currents measured in the tilted coordinate system. Mechanical misalignments are determined by minimizing the mean and the variance of the estimated depth-time averaged vertical velocities.

The data set for the misalignment investigation consists of slant velocity and tilt data averaged over 1 minute in time for 14 days from yearday 63 to 77. The slant velocity data were also averaged over 168 meters from 100 to 268 meters in depth. The uncorrected vertical velocities and the horizontal velocities are calculated using (E.29). The rotated horizontal velocities are calculated using (E.30). The resulting velocity estimates are then low pass filtered using a 5-pole Butterworth filter with a cutoff period of 20 hours and plotted in Figure (E.9a-c). The horizontal velocities have maximum amplitudes of 5 cm/sec. There is also a low frequency signal in the horizontal velocity data due to a front moving through which reverses the mean current almost  $180^\circ$  from day 63 to day 77. The tilt angles have maximum amplitudes of  $E.2^\circ$ . The tilting of FLIP at low frequencies is driven by near surface horizontal currents, near surface winds, ballasting and mooring line tension. It is apparent that much of the variance in both the horizontal velocities and the tilt angles is in the near inertial band ( $\sim 21$  hour period).

Since the vertical velocity correction is a function of both horizontal velocity and tilt angles, one would expect some variance in the uncorrected vertical velocities in the near inertial band. Theoretically, inertial waves have no associated true vertical velocities so this frequency band might be a suitable frequency to use in the determination of mechanical alignment errors. However, close examination of the low pass filtered vertical velocities (Figure E.9c) shows that is not the case. A diurnal signal (24 hour

period) with a velocity amplitude of 0.4 cm/sec dominates the uncorrected vertical velocity signal about a mean velocity of -0.3 cm/sec. Doppler shifts at this frequency are dominated by the nightly migration of plankton towards the surface to feed. This signal dominates over any rotation errors. (For example, a vertical velocity correction of magnitude 0.3 cm/sec needs a horizontal current of 4 cm/sec and a tilt of 4.3°.) An analysis of lower frequencies may not be useful since there may be strong daily variations in the migration of the plankton which is not correlated with the horizontal velocities and tilt angles. The rotation correction will not be used in the determination of mechanical alignment errors between the 161 kHz sonar and the accelerometer package. The strength of the diurnal plankton migration masks any estimation of vertical velocity errors.

#### E.5.6. Heading Correction

The heading of FLIP was constrained by a 2 point mooring which held the bow pointing between 210° and 275° TN. Wind, upper ocean currents and mooring retensioning all dynamically affected the heading. The heading correction consists of rotating the tilt corrected horizontal velocities to geographic coordinates. The geographic coordinate system is defined such that  $\mathbf{k}$  points vertically upward parallel to gravity,  $\mathbf{j}$  points horizontally towards the North and  $\mathbf{i}$  points horizontally towards the East. The rotation of the horizontal velocities is obtained by

$$\begin{aligned} \mathbf{u}_e &= \mathbf{u}_{13} \cos(\theta - 315^\circ) - \mathbf{u}_{02} \sin(\theta - 315^\circ) \\ \mathbf{v}_n &= \mathbf{u}_{13} \sin(\theta - 315^\circ) + \mathbf{u}_{02} \cos(\theta - 315^\circ) \end{aligned} \quad (\text{E.37})$$

where  $\theta$  is the compass heading,  $\mathbf{u}_e$  is the east velocity component,  $\mathbf{v}_n$  is the north velocity components and  $\mathbf{u}_{13}$  and  $\mathbf{u}_{02}$  are the horizontal Janus velocities. FLIP's compass supplied the heading data at a sample rate of 10 Hz. This heading is then averaged over one minute and the heading correction is applied to one minute averaged, tilt corrected horizontal velocities.

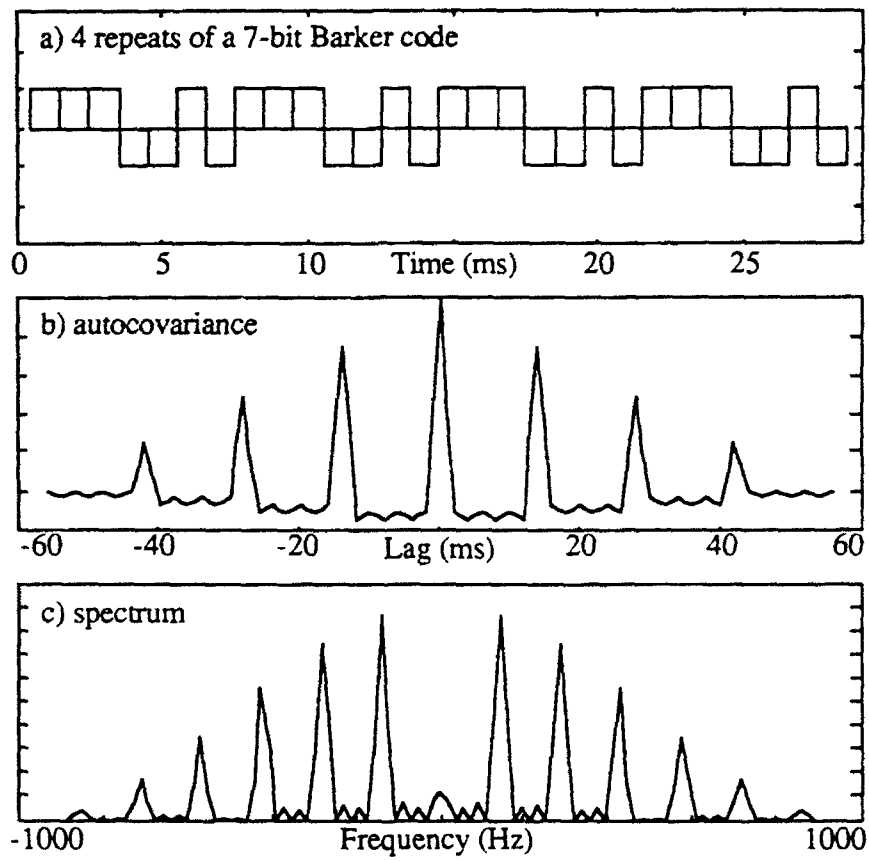


**Figure E.1** *Repeat Sequence Coded Transmit Pulse.* a) Schematic Representation of a repeat sequence code. The transmitted waveform consists of a seven bit Barker code repeated four times. b) The corresponding autocorrelation function. Values are small except at even multiples of the subcode length. c) The frequency spectrum of the code. The spectrum of an uncoded sinusoidal pulse of the same duration would consist of a single peak of width equal to the width of any individual peak in the above spectrum. (Pinkel and Smith, 1992)

**Table E.1 MPL 161 kHz Incoherent Doppler Sonar System Configuration Parameters.** Presented in this table are the Doppler Sonar system parameters as configured for the SWAPP deployment.

MPL 161 kHz Incoherent Doppler Sonar System Configuration Parameters

Transmit Frequency	$f_c$	161 kHz
Sample interval (bit length)	$\tau$	250 msec
Bandwidth	$\Delta f$	4000 Hz
Sequence Length		.75 sec
Sequence Averaging	$P$	80 seq/estimate
Range bin length, number of samples in covariance estimate	$N$	9 bits
Subcode	$G(t)$	7 Bit Barker code (1,1,1,-1,-1,1,-1)
Subcode Length	$L$	7 bits
Number of Repeats of Subcode	$M$	6 repeats
Averaging Length	$T_{avg} = N\tau$	.00225 sec
Overlapped common range in the covariance calculation	$T_{ovl} = (M - 1)L\tau$	.00875 sec
Sound Velocity	$c$	1485 m/sec
Maximum Unambiguous Velocity	$V_{max} = \frac{c}{4f\tau L}$	131.7 cm/sec
Averaging Length	$T_{max}$ $= \max(T_{avg}, T_{ovl})$	.00875 sec
Effective Range Resolution	$\Delta R = c \frac{T_{max}}{2}$	6.50 meters
RMS velocity imprecision	$\Delta V$	0.74 cm/sec
Beam Downlook Angle	$\Theta_0$	60°

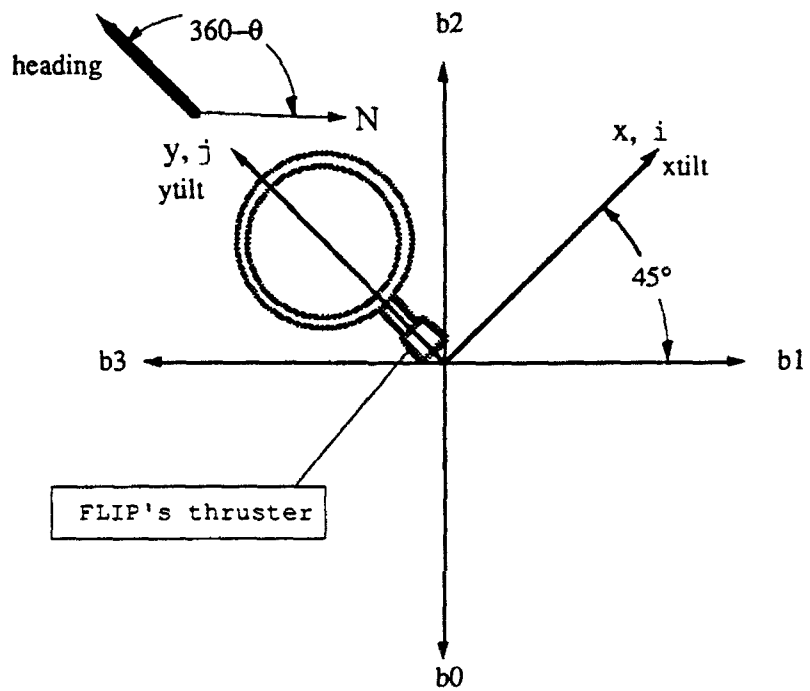


**Figure E.2 161 kHz Beam Directions and Accelerometer Tilt Axis Directions.** Looking down from above (with the z-axis coming out of the page), this diagram shows the direction of the four 161 kHz ADCP sonar beams. The ADCP was mounted on FLIP's direction thruster. FLIP was held in place by a two-point mooring and the thruster was never used during SWAPP. Q is the compass heading from FLIP and varied from 215° to 270°. The three-axis accelerometer package was mounted farther down the hull and was rotated 45° with respect to the sonar beams. The x-axis pointed towards starboard and the y-axis pointed towards the bow in the same direction as the heading vector.

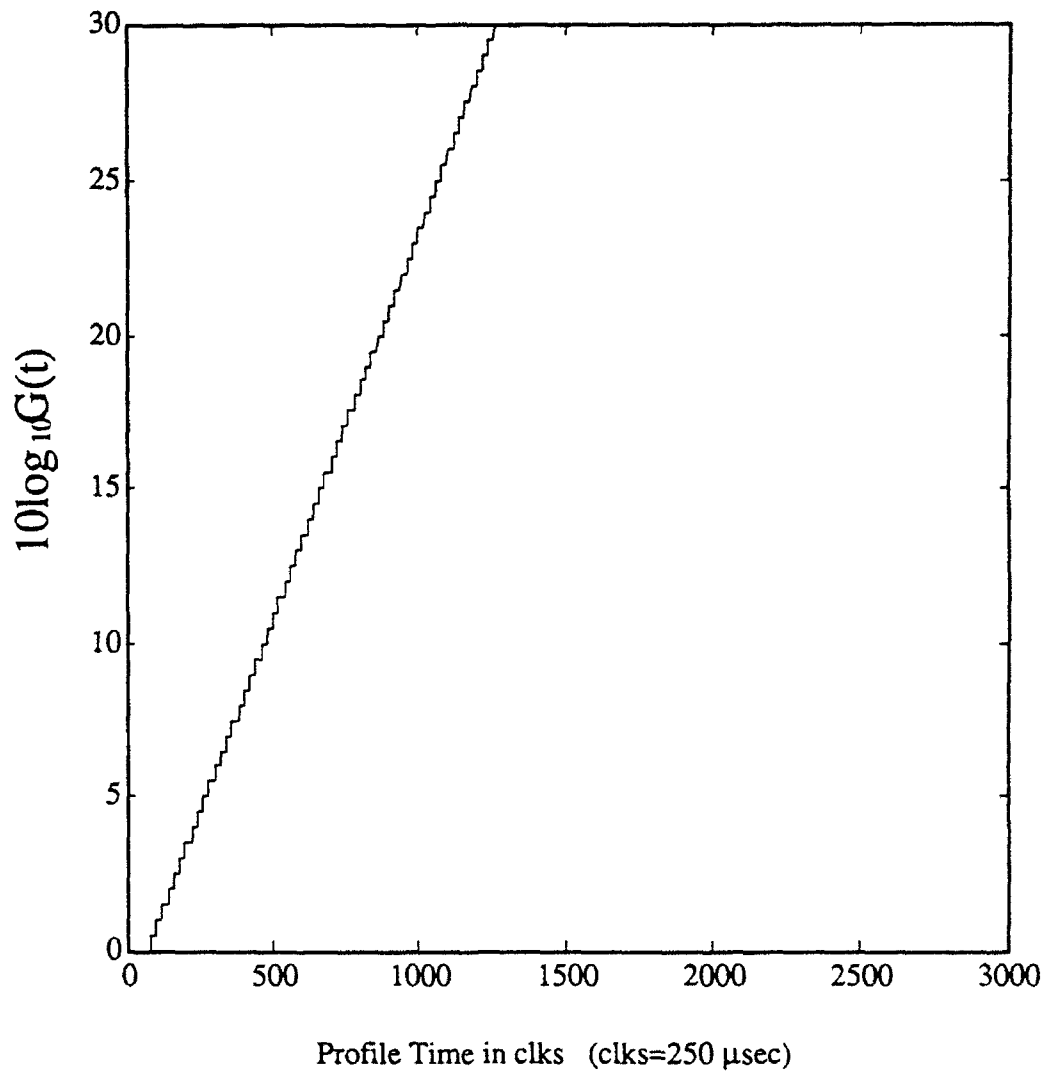


**Figure E.3** Variable Gain Correction. To extend the dynamic range of the analog to digital converters, a variable gain circuit is used. The gain was increased 30 dB with 60 steps of 0.5 dB each. The first step occurred at sample number 60 (15000 msec) and lasted 20 samples (5000 msec).

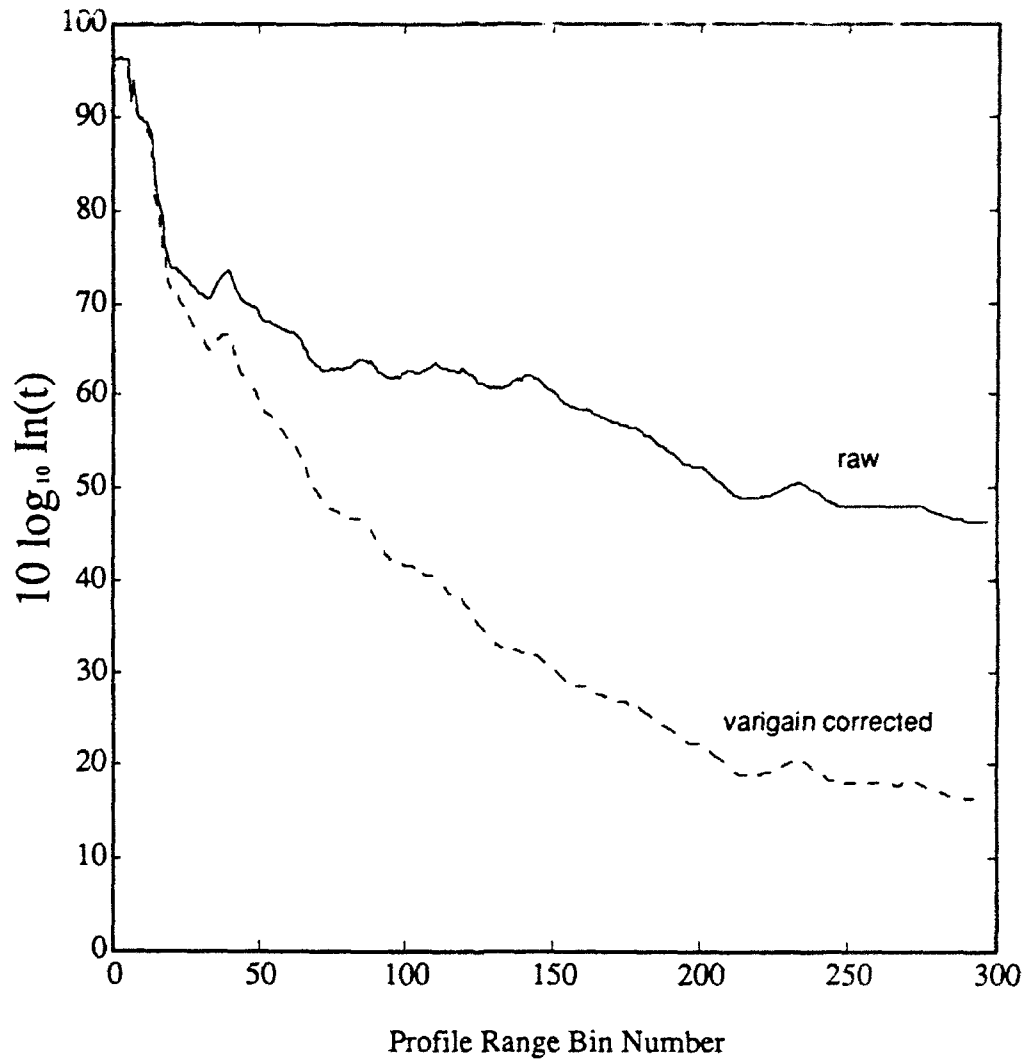


**Figure E.4 1 Hour Averaged Intensity Profile.** 1 Hour of raw intensity data from beam 0 is averaged and plotted. Also plotted is the variable gain corrected intensity data. The gain corrected profile shows nearly 80 dB of dynamic range.

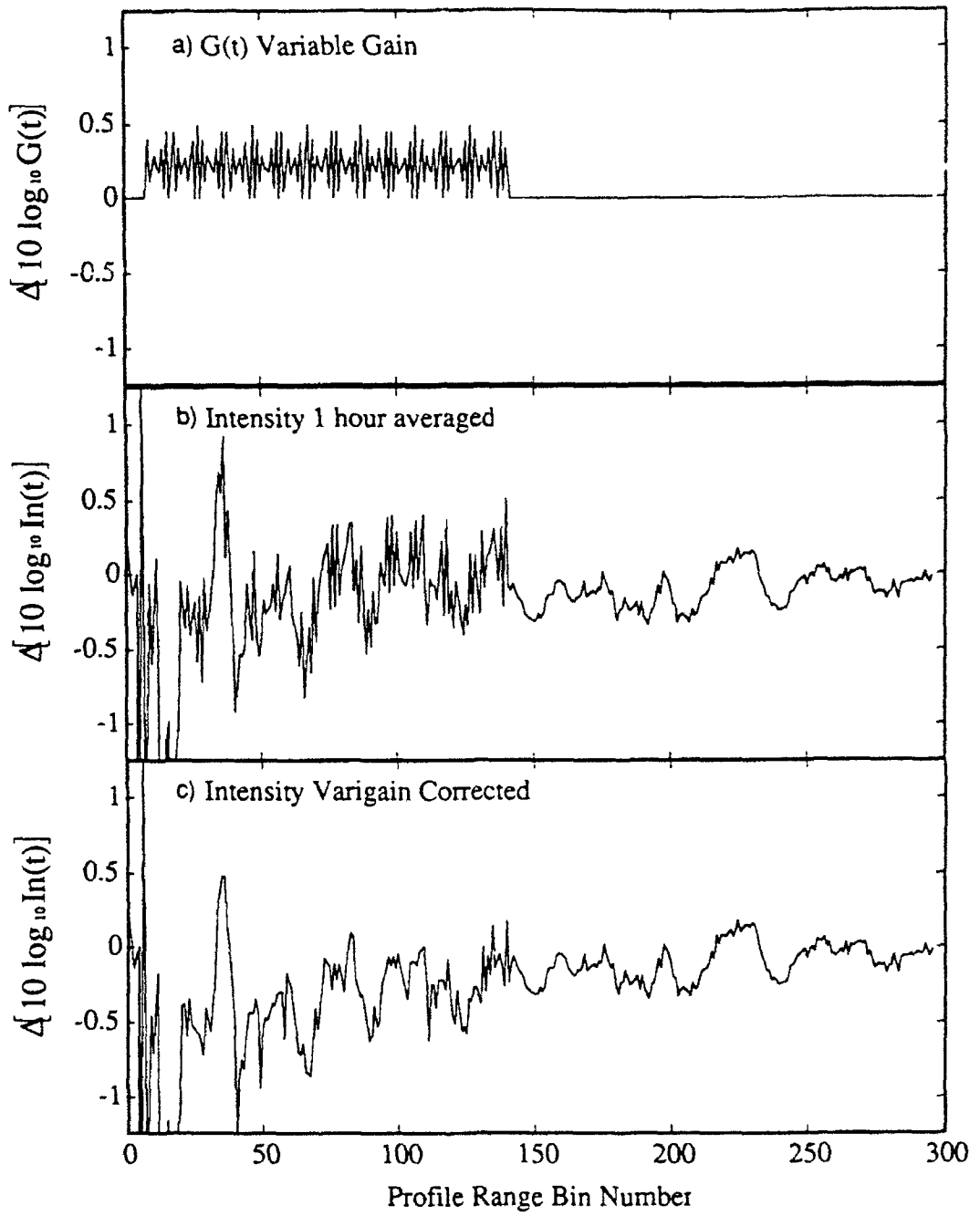


**Figure E.5 Hour averaged Intensity and Variable Gain First Differenced in Range.** The variable gain ramp consists of 60 gain steps which become more apparent in when first differencing is applied. The range bin averaged gain is plotted, (a), and shows a ripple during the gain ramp (bins 7 to 122). This ripple can also be seen in the 1 hour averaged intensity data, (b), during the gain ramp. When the variable gain correction is used, most of the ripple due to the gain steps is removed, (c).

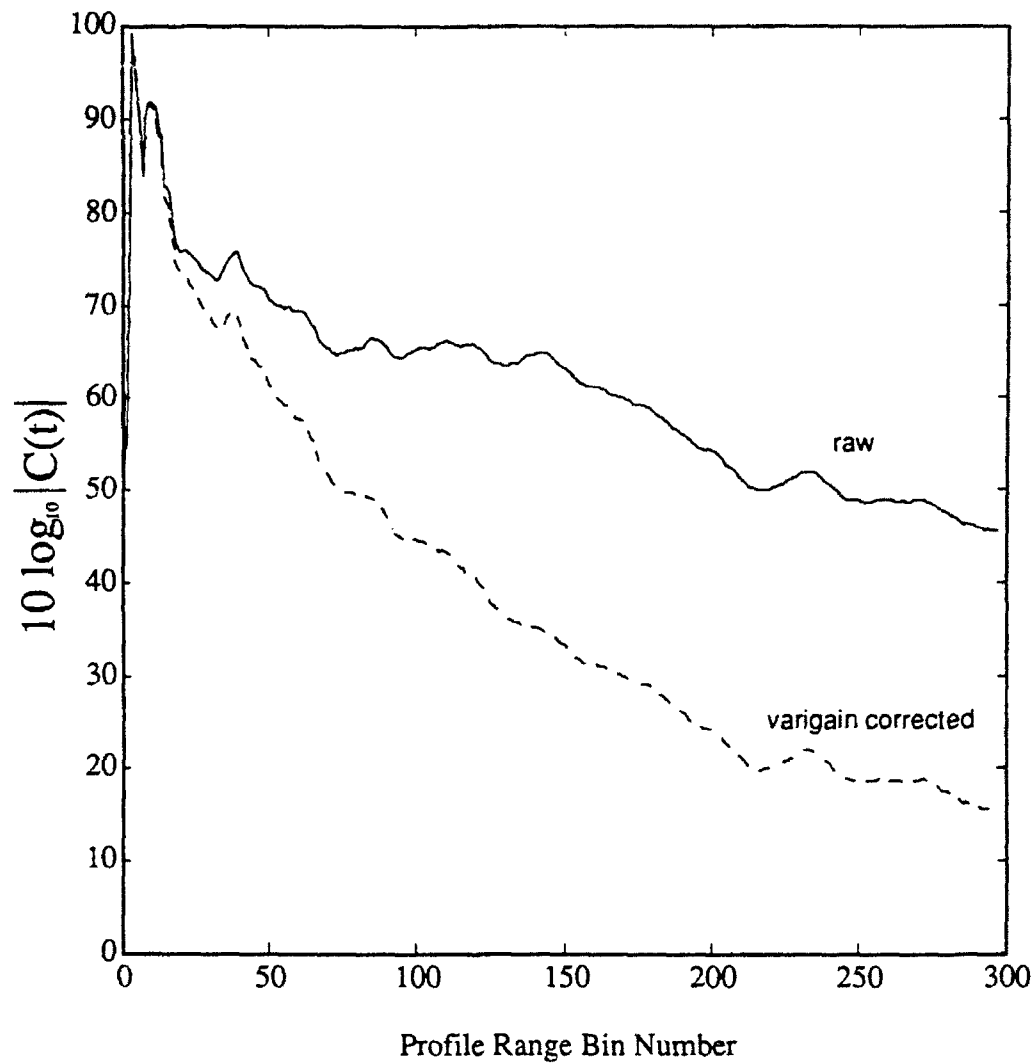


**Figure E.6 1 Hour Averaged Covariance Magnitude Squared.** One Hour of 1 minute averaged covariance data from beam 0 is averaged and plotted. Also plotted is the variable gain corrected covariance data. The gain corrected profile shows nearly 80 dB of dynamic range.

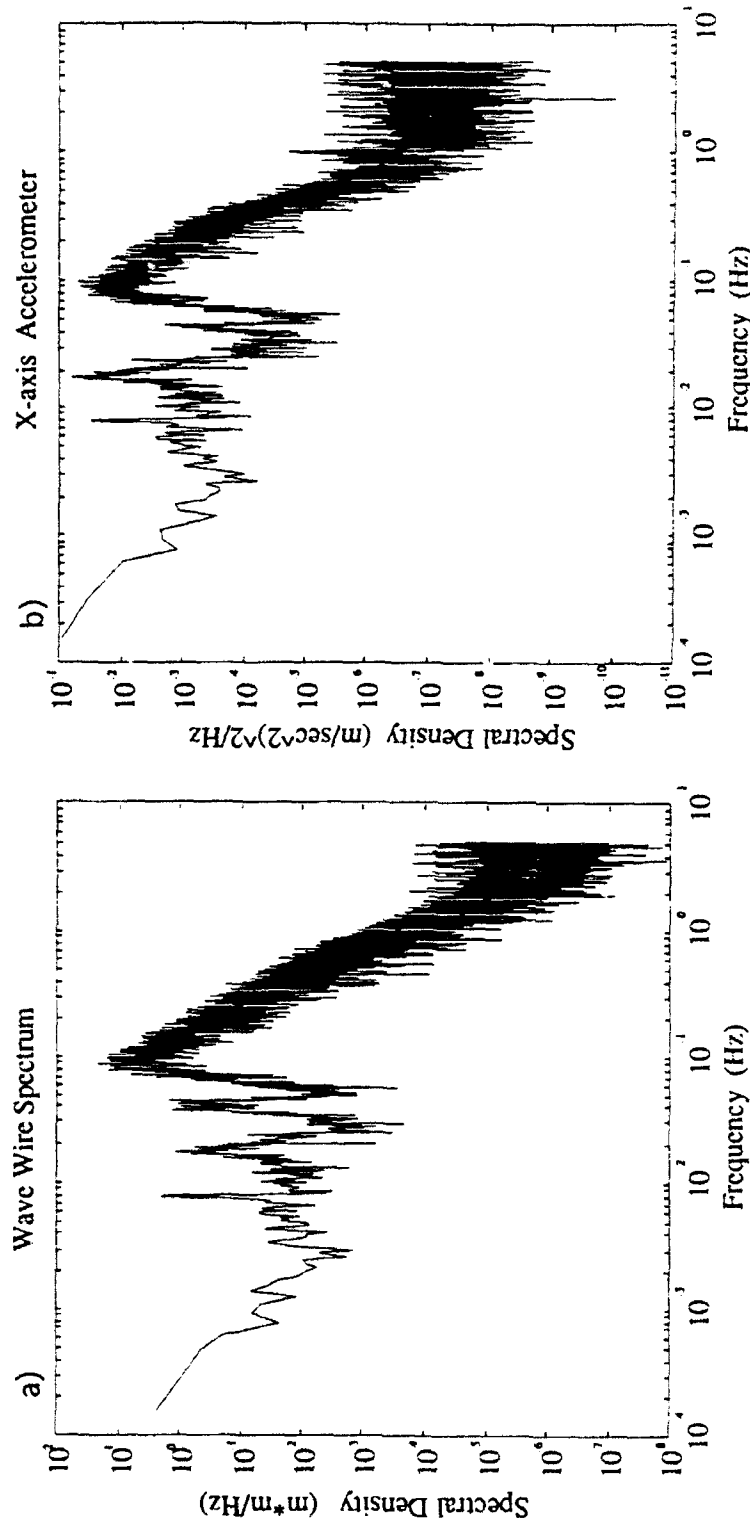


**Figure E.7 Wave Wire and Horizontal Acceleration Spectra.** The wave wire and x-axis accelerometer are sampled at 10 Hz. 3.6 hours of data is used in the spectra. The wave wire spectrum (a) is dominated by the surface wave variance at frequencies above 0.05 Hz with a peak at 0.08 Hz. At lower frequencies, surface wave contribution is small and instead the tilting of FLIP lifts the boom mounted wave wire up and down. The horizontal acceleration spectrum (b) is dominated at frequencies above 0.05 Hz by the horizontal forcing due to the surface waves with a peak at the swell frequencies. At lower frequencies, the accelerations are from the projection of the gravity vector onto the tilted accelerometer package. Note that the spectrum is rising towards lower frequencies. Most of the tilt variance is at the semidiurnal tide (not shown here) due to strong near surface currents pushing FLIP against the mooring lines.

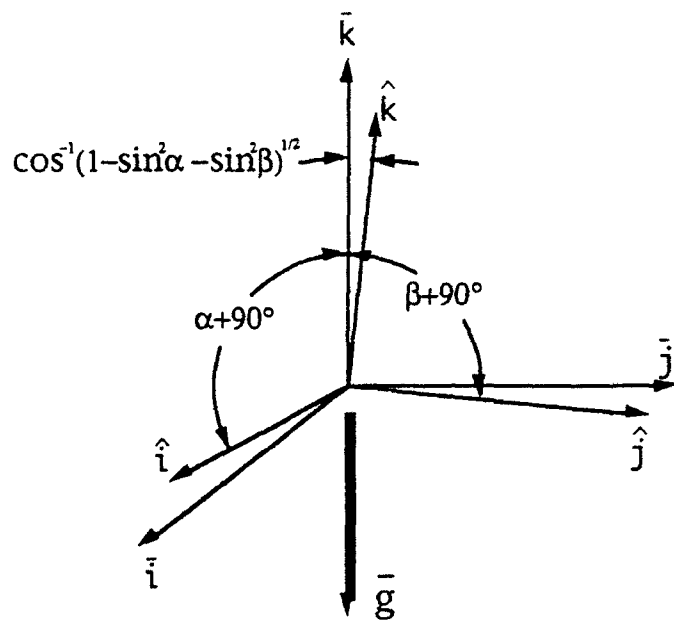


**Figure E.8 Geophysical and tilted coordinate systems.** The geovertical coordinate system,  $\bar{i}$ ,  $\bar{j}$ ,  $\bar{k}$ , is defined with the vertical coordinate parallel to gravity. The tilted coordinate system,  $\hat{i}$ ,  $\hat{j}$ ,  $\hat{k}$ , is one that rotates with the movements of FLIP and is defined by the tilt angles  $a$  and  $b$ . The tilt angles are inferred from horizontal acceleration measurements.

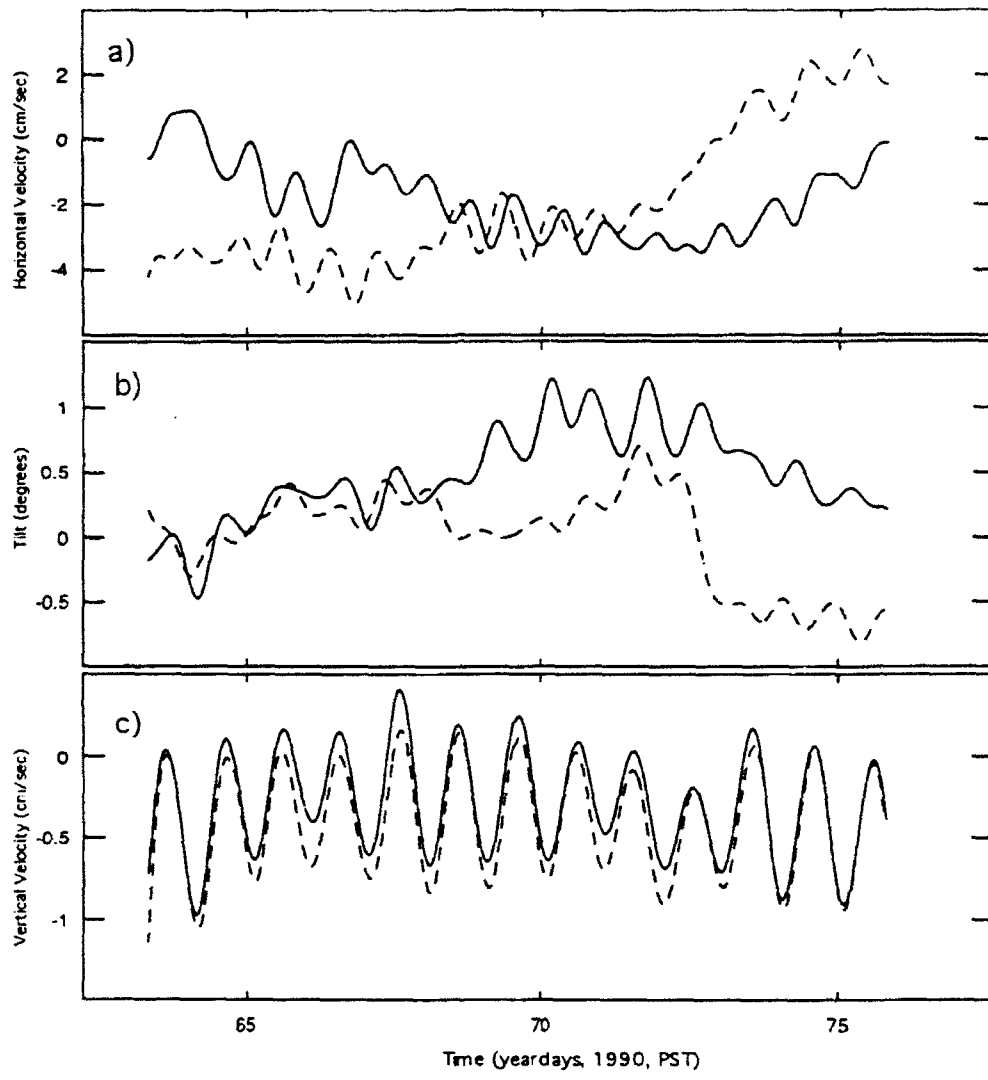


**Figure E.9 Low Pass Filtered Tilt Angles and Depth Averaged Velocities.** Slant velocities are depth averaged from 100 to 275 meters then Janus velocities are calculated. The data has then been low pass filter with a cutoff period of 20 hours. The estimated horizontal velocities in the coordinate system of the accelerometer package ( $\hat{u}$  solid;  $\hat{v}$  dashed), are shown in (a). The tilts (a solid; b dashed), are low pass filtered and shown in (b). Variance in the horizontal velocities and tilts is mostly in the inertial (21 hours) band. The estimated depth averaged vertical velocities ( $\hat{w}_s$  solid;  $\hat{w}_j$  dashed) are shown in (c). The dominated signal in the vertical velocities is in the diurnal (24 hour) band due to the vertical migration of the acoustic scatterers (plankton).

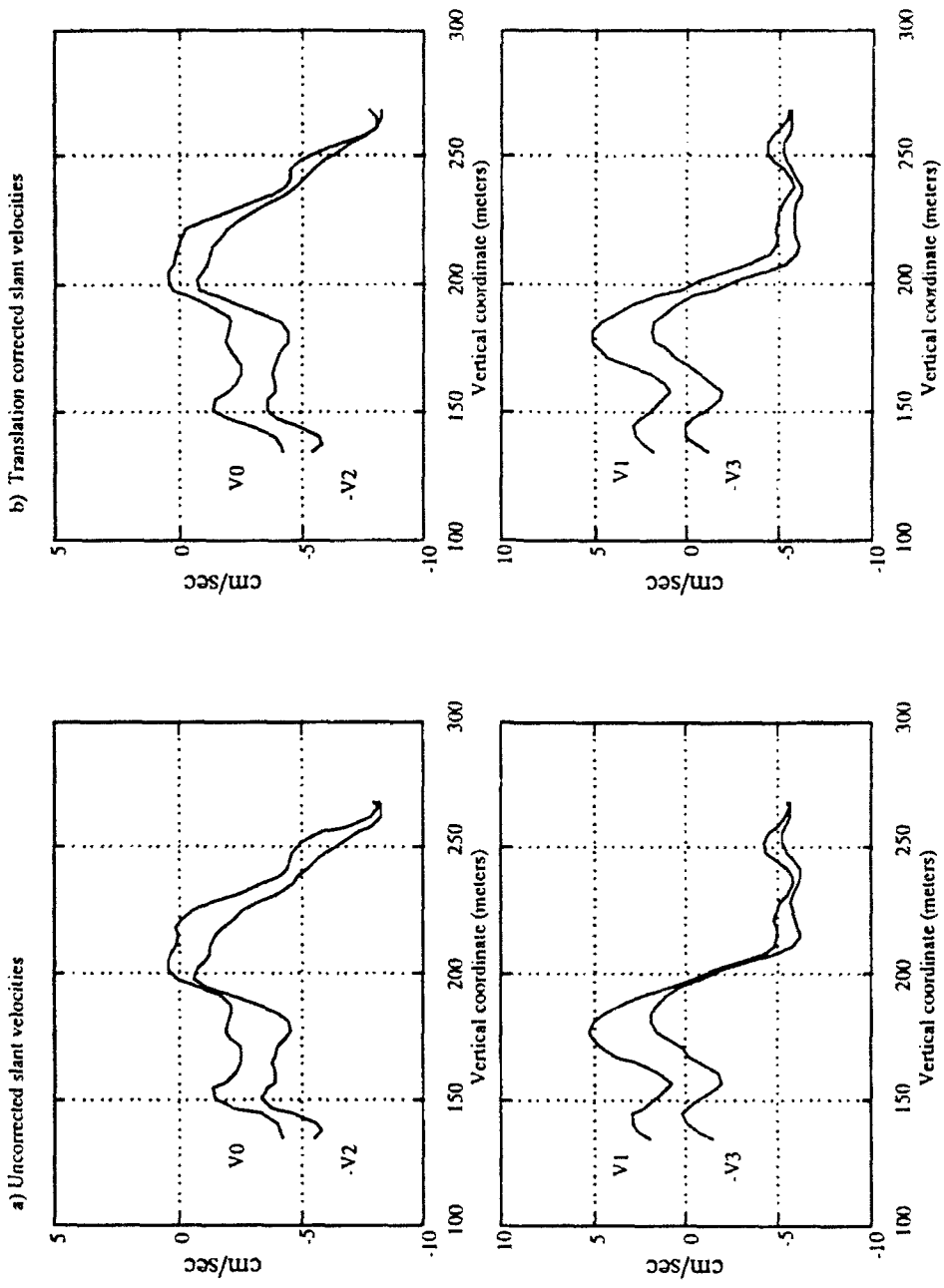


**Figure E.10 Translation Corrected Slant Velocities.** Slant velocity profiles and tilt angles are averaged over 1 minute. 60 profiles (1 hour) are averaged together before plotting versus the vertical coordinate. The average tilts plus the mechanical alignment adjustments are  $\alpha=1.124^\circ$  and  $\beta=0.189^\circ$ . No tilt correction has been applied to the profiles in (a). The tilt correction is applied to every profile before the one hour average is calculated. The tilt corrected profiles are shown in (b). Note that the vertical structure in the tilt corrected back to back beams is more correlated in depth than those without tilt correction.

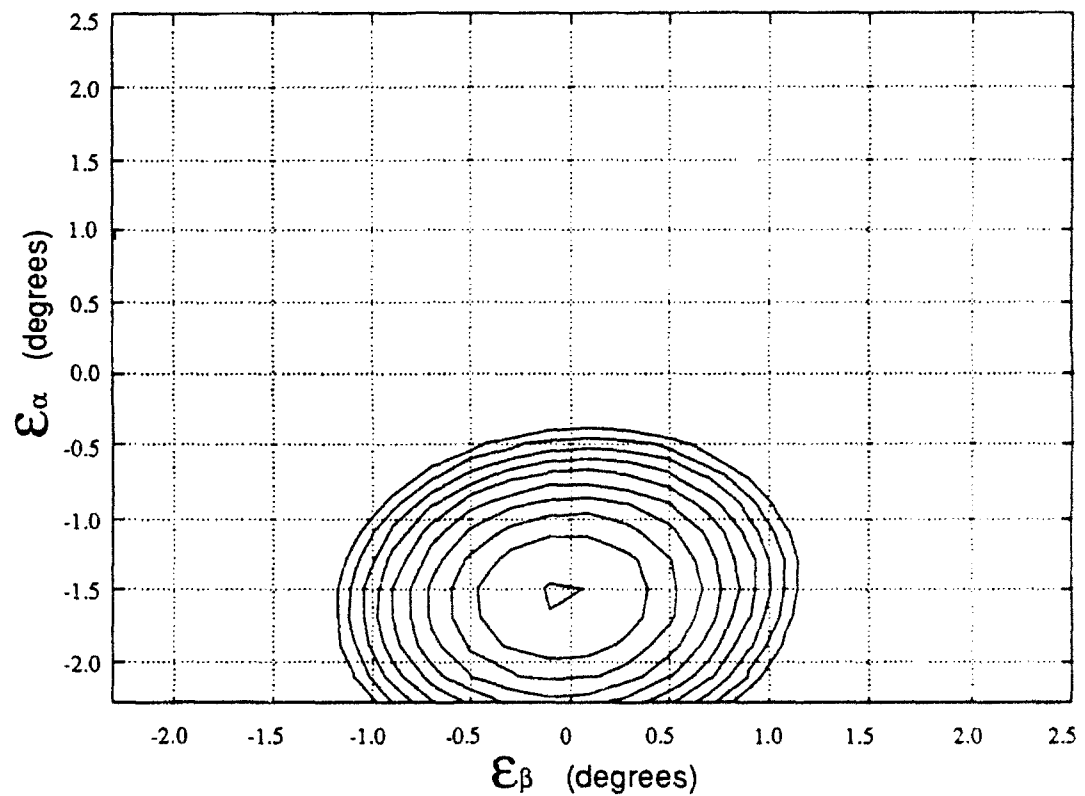


**Figure E.11** Contour of Correlation Ratio vs. Mechanical Misalignment Angles. The correlation ratio is tilt corrected, back to back beam, slant velocity correlation divided by the non corrected slant velocity correlation. This correlation ratio is calculated over a range of possible mechanical misalignment angles. Contour of correlation ratio is plotted with contour values starting at 1.000 and contour intervals of 0.002. The maximum correlation ratio is 1.022 and is located at  $\epsilon_\alpha = -1.55^\circ$  and  $\epsilon_\beta = -0.10^\circ$ . These are the alignment correction angles used in the translation correction.

## REFERENCES

- Allen, K. R. and R. I. Joseph, 1989. A Canonical Statistical Theory of Oceanic Internal Waves. *Geophys. Fluid Mech.*, **204**:185-228.
- Cairns, J. and G. Williams, 1976. Internal wave observations from a Midwater Float, 2. *J. Geophys. Res.*, **81**:1942-1950.
- Baker, M. A., 1985. Sampling turbulence in the stratified ocean: statistical consequences of strong intermittency. *Ph. D. dissertation*, Univ. of California, San Diego.
- Desaubies, Y. and M. C. Gregg, 1981. Reversible and irreversible finestructure. *J. Phys. Oceanogr.*, **11**:541-556.
- Desaubies, Y. and Smith, 1982. Statistics of Richardson number and instability in oceanic internal waves. *J. Phys. Oceanogr.*, **12**:1245-1259.
- Duda, T. F. and C. Cox, 1989. Vertical wave number spectra of velocity and shear at small internal wave scales. *J. Geophys. Res.*, **94**:939-950.
- Eriksen, C. C., 1978. Measurements and models of fine structure, internal gravity waves, and wave breaking in the deep ocean. *J. Geophys. Res.*, **83**:2989-3009.
- Fedorov, K. N., 1986. *The Physical Nature and Structure of Oceanic Fronts*. C. Garrett, Ed., Springer-Verlag, Berlin, 333 pp.
- Fofonoff, N. P. and R. C. Millard, Jr., 1983. Algorithms for computation of fundamental properties of seawater. *UNESCO tech. Pap. in Mar. Sci.*, No. 44, 53 pp.
- Gargett, A. E., 1978. Microstructure and fine structure in an upper ocean frontal regime. *J. Geophys. Res.*, **83**:5123-5134.
- Garrett, C. and Munk, W., 1972. Oceanic mixing by breaking internal waves. *Deep-Sea Res.*, **19**:823-832.
- Garrett, C. and Munk, W., 1972. Space-time scales of internal waves in the ocean. *Geophys. Fluid Dyn.*, **2**:225-264.
- Garrett, C. and Munk, W., 1975. Space-time scales of internal waves in the ocean: A progress report. *J. Geophys. Res.*, **80**(3):291-297.
- Gargett, A. E., S. Hendricks; T. Osbourn and A. J. Williams, 1981. A composite spectrum of vertical shear in the upper ocean. *J. Phys. Oceanogr.*, **11**:1258-1271.
- Georgi, D., 1978. Fine structure in the Antarctic Polar Front Zone: its characteristics and possible relationship to internal waves. *J. Geophys. Res.*, **83**:4579-3671.
- Gill, A. E., 1982. *Atmosphere-Ocean Dynamics*. Academic Press, New York, pp.662.
- Gregg, M. G., 1989. Small-scale mixing: a first-order process? *Parameterization of Small-Scale Processes, Proceedings of the 'Aha Huliko'a Hawaiian Winter Workshop*, P. Muller and D. Henderson, Eds., Hawaiian Institute of Geophysics, Honolulu, pp. 117-126.
- Gregg, M. G. and J. H. McKenzie, 1979. Thermohaline intrusions lie across isopycnals. *Nature*, **280**:310-311.
- Gregg, M. C. and Hess, 1985. Dynamic response calibration of Sea-Bird temperature and conductivity probes. *J. A. O. T.*, **2**:304-313.

- Gregg, M. C. and E. Kunze, 1991. Shear and strain in Santa Monica Basin. *J. Geophys. Res.*, **96**:16709-16719.
- Hines, C. O., 1991. The saturation of gravity waves in the middle atmosphere. Part I: critique of linear-instability theory. *J. of the Atmospheric Sciences*, **48**:1248-1359.
- Hines, C. O., 1991. The saturation of gravity waves in the middle atmosphere. Part II: developement of Doppler-spread theory. *Journal of the Atmospheric Sciences*, **48**:1248-1359.
- Holloway, G., 1983. A conjecture relating oceanic internal waves and small scale processes. *Atmosphere-Ocean* **21**, A- **21**:107-122.
- Horne, E. P., 1978. Interleaving at the subsurface front in the slope water off Nova Scotia. *J. Geophys. Res.*, **83**:3659-3671.
- Horne, E. P. and J. M. Toole, 1980. Sensor response mismatches and lag correction techniques for T-S profilers. *J. Phys. Oceanogr.*, **10**:1122-1130.
- Joyce, T. M., 1977. A Note on the Lateral Mixing of Water Masses. *J. Phys. Oceanogr.*, **7**:626-629.
- Joyce, T. M., W. Zenk and J. M. Toole, 1978. The Anatomy of the Antarctic Polar Front in the Drake Passage. *J. Geophys. Res.*, **83**:6093-6113.
- Karamcheti, K., 1967. *Vector analysis and cartesian tensors, with selected applications*. Holden-Day, San Francisco, 255 pp.
- Kunze, E., 1990. Observations of shear and vertical stability from a neutrally buoyant float. *J. Geophys. Res.*, **95**:18127-18242.
- Kunze, E., M. G. Briscoe, and A. J. Williams III, 1990. Interpreting shear and strain fine structure from a neutrally buoyant float. *J. Geophys. Res.*, **95**:18111-18125.
- Müller, P., D. J. Olbers, and J. Willebrand. The IWEX spectrum. *J. Geophys. Res.*, **83**:479-500.
- Munk, W., 1966. Abyssal recipes. *Deep-Sea Res.*, **13**:707-730.
- Munk, W., 1981. Internal waves and small-scale processes. *Evolution of Physical Oceanography*, B.A. Warren and C Wunsch, Eds., MIT Press 264-290.
- Papoulis, A., 1965. *Probability, random variables, and stochastic processes*. McGraw-Hill, New York, 583 pp.
- Phillips, O. M., 1958. The equilibrium range in the spectrum of wind-generated waves *J. Fluid Mech.*, **4**:426-434.
- Phillips, O. M., 1971. On spectra measured in an undulating layered medium. *J. Phys. Oceanogr.*, **1**:1-6.
- Pinkel, R., 1975. Upper ocean internal wave observations from FLIP. *J. Geophys. Res.*, **80**:3892-3910.
- Pinkel, R., 1981. Observations of the near-surface internal wave field. *J. Phys. Oceanogr.*, **11**:1248.
- Pinkel, R., 1984. Doppler sonar observations of internal waves: the wavenumber-frequency spectrum. *J. Phys. Oceanogr.*, **14**:1249-1270.
- Pinkel, R., 1985. A wavenumber-frequency spectrum of upper ocean shear. *J. Phys. Oceanogr.*, **15**:1453-1469.

- Pinkel, R., A. J. Plueddemann and R. Williams, 1987. Internal wave observations from flip in MILDEX. *J. Phys. Oceanogr.*, **10**:1737-1757.
- Pinkel, R., J. Sherman, J. Smith and S. P. Anderson, 1991. Strain: observations of the vertical gradient of isopycnal vertical displacement. *J. Phys. Oceanogr.*, **21**:527-540.
- Pinkel, P. and S. P. Anderson, 1992. Toward a statistical description of finescale strain in the thermocline. *J. Phys. Oceanogr.*, **22**:773-795.
- Pinkel, R. and J. A. Smith, 1992. Repeat-sequence coding for improved precision of Doppler sonar and sodar. *J. A. O. T.*, **9**:149-163.
- Plueddemann, A. J., 1987. Observations of the upper ocean using a multi-beam Doppler sonar. *Ph. D. dissertation*, Univ. of California, San Diego.
- Plueddemann, A. J. and R. Pinkel, 1991. Biasing of the covariance-based spectral mean estimator in the presence of band-limited noise. *J. A. O. T.*, **8**:172-178.
- Posmentier, E. S. and R. W. Houghton, 1978. Fine structure instabilities induced by double diffusion in the shelf/slope water front. *J. Geophys. Res.*, **83**:5135-5138.
- Rudnick, P., 1964. FLIP: An oceanographic buoy. *Science*, **146**:1268-1273.
- Ruddick, B. R., 1983. A practical indicator of the stability of the water column to double-diffusive activity. *Deep-Sea Res.*, **30**:1105.
- Ruddick, B. R. and J. S. Turner, 1979. The vertical length scale of double-diffusive intrusions. *Deep-Sea Res.*, **25A**:903-913.
- Rummier, W. D., 1968. Introduction of a new estimator for velocity spectral parameters. *Tech. Mem. MM-68-4121-5*, Bell Telephone Laboratories, Whippany, NJ.
- Sherman, J. T., 1989. Observations of fine-scale vertical shear and strain. *Ph. D. dissertation*, Univ. of California, San Diego.
- Sherman, J. T. and R. Pinkel, 1991. Estimates of vertical wavenumber - freq spectra of vertical shear and strain. *J. Phys. Oceanogr.*, **21**:292-303.
- Stern, M. E. 1967. Lateral mixing of water masses. *Deep-Sea Res.*, **14**:747-753.
- Teichmann, H., 1969. *Physical Applications of Vectors and Tensors*, G. G. Harrap and Co., London, 235 pp.
- Theriault, K. B., 1986. Incoherent multibeam Doppler current profiler performance. Part I: Estimae variance. *J. Ocean Eng.*, **OE-11**(1):7-15
- Toole, J. M. and D. T. Georgi, 1981. On the dynamics and effects of double-diffusively driven intrusions. *Prog. Oceanog.*, **10**:123-145.
- Turner, J. S., 1978. Double-diffusive intrusions into a density gradient. *J. Geophys. Res.*, **83**:2887-2901.
- Turner, J. S., 1981. Small scale mixing processes. *Evolution of Physical Oceanography*, B.A. Warren and C Wunsch, Eds., MIT Press 236.
- William, A. J., 1974. Salt finger observations in the Mediterranean Outflow. *Science*, **185**:941-943.
- Williams, R. G., 1985. The internal tide off southern California. *Ph. D. dissertation*, Univ. of California, San Diego.

## **ONR/MPL Report Distribution**

Office of Naval Research (3)  
Department of the Navy  
Ballastion Tower One  
800 North Quincy Street  
Arlington, VA 22217-5000  
Alan Brandt, Code 1122SS

Administrative Grants Officer (1)  
Office of Naval Research  
Resident Representative N66018  
University of California, San Diego  
(Mail Code 0234) 8603 La Jolla Shores Drive  
San Diego, CA 92093-0234

Director  
Naval Research Laboratory  
Atten: Code 2627  
Washington, D.C. 20375

Defense Technical Information Center (4)  
Building 5, Cameron Station  
Alexandria, VA 22314